




Universitat Autònoma de Barcelona

ADVERTIMENT. L'accés als continguts d'aquesta tesi queda condicionat a l'acceptació de les condicions d'ús establertes per la següent llicència Creative Commons:  http://cat.creativecommons.org/?page_id=184

ADVERTENCIA. El acceso a los contenidos de esta tesis queda condicionado a la aceptación de las condiciones de uso establecidas por la siguiente licencia Creative Commons:  <http://es.creativecommons.org/blog/licencias/>

WARNING. The access to the contents of this doctoral thesis it is limited to the acceptance of the use conditions set by the following Creative Commons license:  <https://creativecommons.org/licenses/?lang=en>



**Universitat Autònoma
de Barcelona**

**Nanoscale Study of Epitaxial Ferroelectric $\text{Hf}_{0.5}\text{Zr}_{0.5}\text{O}_2$
Thin Films and $\text{BaTiO}_3/\text{SrTiO}_3$ Superlattices**

Saúl Estandía Rodríguez

Doctoral Thesis in Materials Science

April 2021

Supervisors

Dr. Jaume Gázquez Alabart and Dr. Florencio Sánchez Barrera

Academic Tutor

Dr. Aitor Lopeandía Fernández

Department de Física, Facultat de Ciències

Laboratory of Multifunctional Thin Films and Complex Structures (MULFOX),
Institut de Ciència de Materials de Barcelona (ICMAB-CSIC)



Dr. Florencio Sánchez Barrera, research scientist at the Institut de Ciència de Materials de Barcelona - Consejo Superior de Investigaciones Científicas, **Dr. Jaume Gázquez Alabart**, tenured scientist at the Institut de Ciència de Materials de Barcelona - Consejo Superior de Investigaciones Científicas, and **Dr. Aitor Lopeandía Fernández**, associate professor at Universitat Autònoma de Barcelona – Physics Department

CERTIFY THAT

Saúl Estandía Rodríguez has carried out under their direction the doctoral research entitled “**Nanoscale Study of Epitaxial Ferroelectric $\text{Hf}_{0.5}\text{Zr}_{0.5}\text{O}_2$ Thin Films and $\text{BaTiO}_3/\text{SrTiO}_3$ Superlattices**”. This work has been developed within a PhD program in Materials Science at the department of physics of Universitat Autònoma de Barcelona.

For that record they sign this certificate. Bellaterra, April 2021

Dr. Florencio Sánchez Barrera Dr. Jaume Gázquez Alabart Dr. Aitor Lopeandía Fernández

Acknowledgements

To my supervisors, Dr. Jaume Gázquez and Dr. Florencio Sánchez, who have guided me through interesting research topics while allowing me enough independence. They have dedicated a lot of time to my education during the last years, and I am very grateful to them.

Thanks to all the members of the MULFOX group for interesting discussions during the weekly group meetings. I would also like to dedicate sincere thanks to Dr. Nico Dix, who has not only contributed to this thesis with useful and enriching discussions but has also made important contributions to the structural characterization of the $\text{Hf}_{0.5}\text{Zr}_{0.5}\text{O}_3$ thin films presented in this thesis. Special thanks to Dr. Ignasi Fina for sharing his expertise in the electric characterization of ferroelectrics, and to Dr. Jike Lyu, who instructed me how to perform ferroelectric measurements on the $\text{Hf}_{0.5}\text{Zr}_{0.5}\text{O}_2$ thin films. I acknowledge Prof. Rohan Mishra and Dr. Tengfei Cao for the density functional theory calculations included in this thesis.

I also thank the nice atmosphere created by the people who work at ICMAB and ICN2. I acknowledge the STEM group at Oak Ridge National Laboratory (ORNL) in the U.S. as well as the ICTS-Centro Nacional de Microscopía in Madrid for sharing their facilities and expertise to explore the bottom of the matter, making possible the present thesis.

Finally, I should acknowledge the funding provided by the scholarship (SEV-2015-0496-16-3) of the Spanish Ministry of Economy, Competitiveness and Universities and the European Social Fund.

Abstract

Ferroelectricity is a functional property that can be exploited in microelectronics devices such as non-volatile memories. In this thesis, the ferroelectric properties of nanometric thin films and superlattices have been studied by combining macroscopic and nanoscale characterization techniques. Firstly, the configuration of ferroelectric domains of BaTiO₃ has been studied in a set of BaTiO₃/SrTiO₃ superlattices of different periods by Scanning Transmission Electron Microscopy (STEM). A strong dependence of the superlattice period (layers' thickness) has been observed, with a decreasing polar distortion for longer periods, in agreement with the macroscopic polarization. Polarization rotations have been observed inside the BaTiO₃ layers of the superlattice with longest period (10 unit-cell thick BaTiO₃ layers), contrasting with the single oriented (out-of-plane oriented) domains in superlattices of shorter period. Secondly, Hf_{0.5}Zr_{0.5}O₂ thin films grown epitaxially on perovskite substrates have been studied. The films generally show a mixture of orthorhombic (ferroelectric) and monoclinic (non-polar) epitaxial crystallites, with more of one or the other phase depending on different conditions. The role of the bottom electrode on the stabilization of phases and the ferroelectricity of the films has also been studied. In order to stabilize the orthorhombic phase, the substrates require to be buffered with a manganite (i.e. La_{0.7}Sr_{0.3}MnO₃); otherwise, the amount of the orthorhombic phase is very small, and so is the ferroelectricity of the films. Besides, the effect of the epitaxial stress has been explored by growing Hf_{0.5}Zr_{0.5}O₂/La_{0.7}Sr_{0.3}MnO₃ films on a set of substrates with different lattice parameters, achieving pure orthorhombic films with enhanced ferroelectricity on films grown on those substrates that impose a tensile strain to the La_{0.7}Sr_{0.3}MnO₃ electrode. Furthermore, the epitaxy of Hf_{0.5}Zr_{0.5}O₂ on La_{0.7}Sr_{0.3}MnO₃ as well as the Hf_{0.5}Zr_{0.5}O₂/La_{0.7}Sr_{0.3}MnO₃ interface have been explored and described with atomic resolution by means of STEM.

Resumen

La ferroelectricidad es una propiedad funcional que encuentra aplicaciones en dispositivos microelectrónicos tales como las memorias no volátiles. En esta tesis se han estudiado las propiedades ferroeléctricas de capas finas nanométricas y superredes combinando técnicas de caracterización macroscópicas y nanoscópicas. En el primer bloque, se ha estudiado la configuración de dominios ferroeléctricos de BaTiO_3 en una serie de superredes de diferentes periodos (grosor de las capas) mediante microscopía electrónica de barrido en transmisión (STEM). Se ha observado una fuerte dependencia con el periodo, con una distorsión polar decreciente para periodos mayores, de acuerdo con la polarización macroscópica medida. Se han observado rotaciones de la polarización en las capas de BaTiO_3 de la superred de mayor periodo (con capas de BaTiO_3 de 10 celdas unidad de grosor), contrastando con los dominios con una única orientación (fuera del plano) en las superredes de menor periodo. En un segundo bloque se han estudiado capas finas de $\text{Hf}_{0.5}\text{Zr}_{0.5}\text{O}_2$ crecidas epitaxialmente sobre sustratos de perovskita. Las capas están generalmente compuestas de una mezcla de granos cristalinos de estructuras ortorrómbica (ferroeléctrica) y monoclinica (no polar), obteniendo más o menos de una fase u otra en función de distintas condiciones. También se ha estudiado el rol del electrodo inferior en la estabilización de las fases y la ferroelectricidad de las capas. Para estabilizar la fase ortorrómbica, se ha de depositar previamente una capa de manganita (i.e. $\text{La}_{0.7}\text{Sr}_{0.3}\text{MnO}_3$) sobre los sustratos; en caso contrario, la cantidad de fase ortorrómbica obtenida, así como la ferroelectricidad de las capas es muy baja. Por otro lado, el efecto del stress epitaxial también es evaluado depositando capas de $\text{Hf}_{0.5}\text{Zr}_{0.5}\text{O}_2/\text{La}_{0.7}\text{Sr}_{0.3}\text{MnO}_3$ sobre una serie de sustratos de distinto parámetro de red, obteniendo capas puras de fase ortorrómbica con mayor ferroelectricidad en aquellas capas depositadas sobre sustratos que incrementan el parámetro de red en el plano del $\text{La}_{0.7}\text{Sr}_{0.3}\text{MnO}_3$. Por otra parte, se ha explorado y descrito la epitaxia de $\text{Hf}_{0.5}\text{Zr}_{0.5}\text{O}_2$ sobre $\text{La}_{0.7}\text{Sr}_{0.3}\text{MnO}_3$ y la intercara de $\text{Hf}_{0.5}\text{Zr}_{0.5}\text{O}_2/\text{La}_{0.7}\text{Sr}_{0.3}\text{MnO}_3$ con resolución atómica mediante STEM.

General Motivation

Oxide materials offer a variety of functional properties appealing for microelectronics, such as ferromagnetism, superconductivity, or ferroelectricity; while these compounds are in general abundant and have good chemical stability. Ferroelectric perovskite oxides (the most common ferroelectrics) are being used in different electronic applications such as logic memory devices, pyroelectric energy conversion and pyroelectric and piezoelectric sensors,¹⁻³ or as high constant dielectrics.

BaTiO₃, a prototypical ferroelectric perovskite, is Pb-free, unlike the (Pb/Zr)TiO₃ currently used in memories and piezoelectric devices. BaTiO₃ has a spontaneous polarization of around 26 $\mu\text{C}/\text{cm}^2$ that can be increased by epitaxial lattice strain engineering through its coupling to the unit-cell structure. Epitaxial ferroelectric/paraelectric superlattices can induce and maintain epitaxial strain in the ferroelectric layers with thicknesses of several tens of nanometers, while the ferroelectric/paraelectric interfaces modify the electrical boundary conditions, which offers an additional degree of freedom to manipulate the polarization in the ferroelectric. As Aberration Corrected Scanning Transmission Electron Microscopy (STEM) has become ubiquitous during the last decade, it has allowed the observation of ferroelectric domain configurations with unit-cell resolution. The existence of exotic ferroelectric domain configurations in nanoscale heterostructures has been revealed by STEM, mostly in ferroelectric/paraelectric superlattices as PbTiO₃/SrTiO₃ superlattices, where the exotic domains were believed to arise due to the interplay of epitaxial strain and electrostatic boundary conditions. Inside the big field of ferroelectrics, the study of nanoscale domain configurations represents just an emerging research line, and could also lead to emergent functional properties.

Besides, (Hf/Zr)O₂ based materials are known to exist in a metastable ferroelectric phase since 2011.⁴ Ferroelectric (Hf/Zr)O₂ thin films show very promising properties, as their polarization remains strong in films of only a few nanometers and can be easily integrated with Si-based complementary metal-oxide-semiconductor, unlike ferroelectric perovskites. Due to these characteristics, (Hf/Zr)O₂ materials stand as promising candidates for ferroelectric random access memories or ferroelectric field effect transistors.^{5,6} The ferroelectric phase, believed to have an orthorhombic $Pca2_1$ space group, is usually found coexisting with the monoclinic ($P2_1/c$) phase, which is paraelectric and presents the lowest formation energy, and in some cases with the antiferroelectric tetragonal ($P4_2/nmc$) and the paraelectric cubic ($Fm3m$) phases.⁷

This thesis focuses in the experimental study of the ferroelectric oxides BaTiO₃ and Hf_{0.5}Zr_{0.5}O₂ (HZO). Since the ferroelectric properties are strongly determined by local features at the nanoscale level, including crystal structure, interfaces or defects, techniques able to probe the materials at the nanoscale, as STEM, are very appreciated and allow a deeper understanding of the materials'

properties. STEM, in combination with X-ray diffraction and electrical characterization are employed to address relevant questions of the ferroelectric oxides BaTiO₃ and HZO.

Objectives

This thesis' general objective consists in establishing links between the nanoscale features, as the crystalline structure (phases, lattice strain, distortions) of films, and the functional properties of ferroelectric oxides, allowing to ultimately gain useful knowledge about these systems. Specifically, this thesis is divided into two main blocks: one dedicated to the study of the configuration of ferroelectric domains in BaTiO₃/SrTiO₃ (BTO/STO) superlattices, and another devoted to the study of the microstructure and ferroelectric properties of Hf_{0.5}Zr_{0.5}O₂ (HZO) films.

In the case of BTO/STO superlattices, a local probe as STEM is required to observe with unit-cell resolution the configuration of polarization domains in BTO/STO superlattices as a function of the superlattice period. The observation of the configuration of domains will ultimately help us to understand the ferroelectric properties of these nanostructures, and to understand the effect of the boundary conditions on the configuration of domains.

In the case of HZO, understanding under which conditions the ferroelectric phase is more favorable than the competing phases is fundamental to gain control over the ferroelectric properties of the films. It is known that different factors such as doping, substrate or size can have an impact on the stabilization of the ferroelectric phase. In this regard, a second objective of this thesis is to study the stabilization of the ferroelectric HZO phase in thin films grown epitaxially on perovskite substrates. Specifically, we aim at understanding the effect that different epitaxial growth conditions can have on the stabilization of the ferroelectric phase of HZO and on the ferroelectric properties of the films. For that purpose, different sets of samples are synthesized and the macroscopic ferroelectric properties are analyzed alongside with the nanoscale structural information provided by x-ray diffraction and STEM. The combination of these complementary techniques is expected to be useful to unravel the different mechanisms governing the ferroelectricity of the HZO films.

Outline

The thesis is divided in six chapters, with different sections and subsections within each chapter. Chapter 1 introduces the physical concepts and materials relevant to this thesis. Chapter 2 describes the basics of the used experimental techniques. Chapters 3, 4 and 5 are dedicated to the experimental results and analysis carried out for this thesis. Chapter 3 explores the polarization domain configuration of BaTiO₃/SrTiO₃ superlattices of different periods. Chapters 4 and 5 are devoted to ferroelectric Hf_{0.5}Zr_{0.5}O₂ thin films. Finally, the conclusions are summarized and some final remarks are presented.

List of Acronyms

ABF	Annular Bright Field
AFM	Atomic Force Microscopy
BTO	BaTiO ₃
CMOS	Complementary Metal-Oxide-Semiconductor
COM	Center of mass
δ_{Ti}	Ti displacement
Δ	Crystal Field Splitting
DHM	Dynamic Hysteresis Measurement
DLCC	Dynamic Leakage Current Compensation
DFT	Density Functional Theory
EELS	Energy Electron Loss Spectroscopy
FFT	Fast Fourier Transform
GSO	GdScO ₃
HAADF	High Angle Annular Dark Field
HZO	Hf _{0.5} Zr _{0.5} O ₂
ICMAB	Institut de Ciència de Materials de Barcelona
ip	in-plane
LAO	LaAlO ₃
LNO	LaNiO ₃
LSAT	(LaAlO ₃) _{0.3} (Sr ₂ TaAlO ₆) _{0.7}
LSMO	La _{0.7} Sr _{0.3} MnO ₃
oop	out-of-plane
PLD	Pulsed Laser Deposition
PTO	PbTiO ₃
PUND	Positive-Up Negative-Down
PZT	(Pb,Zr)TiO ₃
RHEED	Reflection High Energy Electron Diffraction
RMS	Root Mean Square
RSM	Reciprocal Space Map
SPL	Superlattice
STEM	Scanning Transmission Electron Microscopy

STO	SrTiO ₃
TC	Topological Charge
XRD	X-Ray Diffraction
YSZ	Yttria Stabilized Zirconia

Table of Contents

Chapter 1. Introduction

1.1 Basics of Ferroelectricity	1
1.2 Investigated Materials: BaTiO ₃ and Hf _{0.5} Zr _{0.5} O ₂	2
1.2.1 BaTiO ₃	2
1.2.2 Fluorite Hf _{0.5} Zr _{0.5} O ₂	4
1.3 Engineering Ferroelectricity	6
1.3.1 Polarization Configuration in Ferroelectric Heterostructures	6
1.3.2 Strain Engineering	11
1.3.3 Engineering Ferroelectricity Beyond Electrostatics and Strain	13

Chapter 2. Experimental Methods

2.1 Pulsed Laser Deposition	15
2.2 Atomic Force Microscopy	16
2.3 X-Ray Diffraction	17
2.4 Electrical Characterization of Ferroelectric Thin Films	19
2.5 Scanning Transmission Electron Microscopy	22
2.5.1 Introduction	22
2.5.2 Imaging in STEM	25
2.5.3 Electron Energy Loss Spectroscopy	27
2.5.4 STEM Specimen Preparation	29
2.6 Computational Methods Based on Python	30
2.7 Other Computational Resources	39

Chapter 3. Rotational Polarization Nanotopologies in BaTiO₃/SrTiO₃ Superlattices

3.1 Introduction	42
3.2 Polarization Configuration in BaTiO ₃ /SrTiO ₃ Superlattices	44
3.2.1 Synthesis, Structural and Ferroelectric Characterization of the BaTiO ₃ /SrTiO ₃ Superlattices	44
3.2.2 Microstructure of the BaTiO ₃ /SrTiO ₃ Superlattices	47
3.2.3 Real Space Polarization Maps of the BaTiO ₃ /SrTiO ₃ Superlattices	50
3.2.4 Electronic Structure	68
3.2.5 Are the Polarization Configurations Stable under the Electron Beam?	71
3.3 Summary	75
Appendix 3	77

Chapter 4. The Epitaxial Stabilization of Ferroelectric Hf_{0.5}Zr_{0.5}O₂ Thin Films on Perovskites

4.1 Introduction	80
4.2 Stabilization of the Hf _{0.5} Zr _{0.5} O ₂ Ferroelectric phase on Different Electrodes	81
4.3 Insights into the Atomic Structure of the Hf _{0.5} Zr _{0.5} O ₂ /La _{0.7} Sr _{0.3} MnO ₃ Interface	89
4.3.1 STEM characterization of the Hf _{0.5} Zr _{0.5} O ₂ /La _{0.7} Sr _{0.3} MnO ₃ Interface	89
4.3.2 DFT calculations of the Hf _{0.5} Zr _{0.5} O ₂ /La _{0.7} Sr _{0.3} MnO ₃ Interface	97
4.4 The Atomic Structure of the Hf _{0.5} Zr _{0.5} O ₂ Interface with LaNiO ₃ and SrRuO ₃	101
4.5 Conclusions	107

Appendix 4-A Ferroelectric wake up of the HZO films on different bottom electrodes	108
Appendix 4-B Absence of the HZO tetragonal phase at the interface	110
Chapter 5. Engineering Ferroelectric Hf_{0.5}Zr_{0.5}O₂ Thin Films by Epitaxial Stress	
5.1 Introduction	114
5.2 HZO Thin Films on Strained LSMO Templates	115
5.2.1 Structural Characterization	115
5.2.2 Microstructural Characterization by STEM	122
5.2.3 Ferroelectric Hysteresis	125
5.3 Domain Matching Epitaxy of Hf _{0.5} Zr _{0.5} O ₂ grown on La _{0.7} Sr _{0.3} MnO ₃	129
5.3.1 Analysis of the plane matching at the Hf _{0.5} Zr _{0.5} O ₂ /La _{0.7} Sr _{0.3} MnO ₃ interface	129
5.4 Conclusions	138
Summary and Perspective	139
Bibliography	142
List of Publications	150

Chapter 1: Introduction

In this chapter, the theoretical background relevant to support the results of the thesis as well as the materials that are the subject of research are presented.

1.1 Basics of Ferroelectricity

Ferroelectrics are a subclass of dielectric polar materials that have two or more metastable states with a non-zero electric polarization. The electric polarization in a material represents the surface charge density that arises from a spatial separation of the centers of mass of negative and positive charges. For an ensemble of point-like charges it can be defined as: $\mathbf{P} = \sum_i \frac{\mathbf{d}_i \cdot \mathbf{q}_i}{V}$, where \mathbf{d}_i and \mathbf{q}_i are the position and charge value of charge i , and V is the volume of the ensemble of charges. This definition contains a problem of fundamental origin in a bulk piece of material. Unlike in a single molecule, which has a well-defined polarization, in the bulk region of a crystal the polarization is not well defined since the grouping of charges is arbitrary and different grouping yields different polarizations. Modern theory of polarization⁸ is the current framework that addresses such a problem and states that the polarization is not defined in bulk. Yet, it also states that changes in polarization (that is what is measured in the experiment) do have a well-defined value, and provides a formalism known as Berry-phase to quantify it.

Ferroelectrics possess a spontaneous polarization which in many cases is believed to arise when there is an appropriate balance of short-range repulsions between ions and long-range bonding interactions.⁹ Thus, the polarization arises without the necessity of an external agent, as an electric field. For a material to be classified as ferroelectric, it should be possible to switch between these metastable states by the coupling to an external electric field. This requirement leaves out of the ferroelectric group materials with permanent polar structures but that are not able to switch between different polar states under an external electric field. Switching of the polarization in a ferroelectric produces a hysteretic dependence of the polarization with the switching electric field, as shown in Figure 1.1 (c), as opposed to the linear dependence of an ideal linear dielectric Figure 1.1 (b). The properties of a dielectric crystal are intimately related to the symmetries of the unit-cell. In the case of ferroelectrics, their non-centrosymmetric structure confers them other interesting properties beyond ferroelectricity. All the non-centrosymmetric dielectrics have a coupling between the strain and the polarization, so that they get deformed under a bias or develop a change in their polarization if subject

to a mechanical stress. These materials are known as piezoelectrics. Furthermore, some of these piezoelectrics do have a unique polar axis so they have a spontaneous polarization. This group has the exclusive property of pyroelectricity, which entails a dependence of the spontaneous polarization with temperature. Finally, on top of the piezoelectric and pyroelectric properties, some materials can switch their polarization under an electric field, these are known as ferroelectrics. Thus, ferroelectrics have not only ferroelectric but also pyroelectric and piezoelectric properties. Figure 1.1 (a) shows the classification of dielectrics according to the mentioned properties. Important applications of ferroelectrics include memories, and also applications that exploit the pyroelectric and piezoelectric effects, as sensors and transducers, and the electro-optic devices. Different ferroelectric memory schemes exist, the most popular consisting in the non-volatile storage of positive or negative charges determined by the polarization direction in a ferroelectric capacitor, and the modulation of the conductance through a heterostructure determined by the polarization direction, known as ferroelectric tunnel junctions.¹⁰

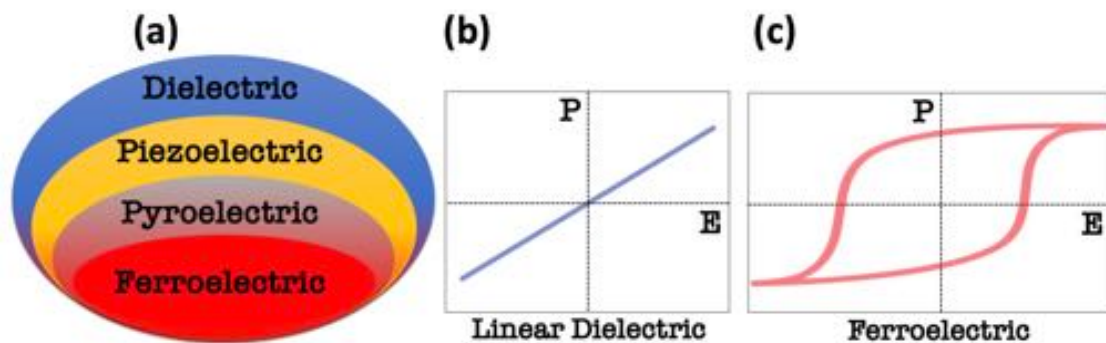


Figure 1.1: (a) As depicted, ferroelectrics belong to the group of dielectrics and have also piezoelectric and pyroelectric properties. Polarization-electric field behavior in an ideal linear dielectric (b) and a ferroelectric (c).

In the next section, the two ferroelectric oxides studied in this thesis are introduced.

1.2 Investigated Materials: BaTiO₃ and Hf_{0.5}Zr_{0.5}O₂

1.2.1 BaTiO₃

Perovskites are complex oxides with a general chemical formula ABO₃, where A and B are cations and O is oxygen. The unit-cell can be described as a body-centered cube with the A cations at the vertices, and the B cation at the center, and an O octahedra with O occupying the faces of the cube (see Figure 1.2). Among the different ferroelectric perovskites, some have been successfully used in

microelectronic devices, as it is the case of $\text{Pb}(\text{Zr},\text{Ti})\text{O}_3$;^{11,12} however, Pb toxicity concerns make desirable to find substitute materials. BaTiO_3 (BTO) is a good candidate to achieve Pb-free devices. BTO undergoes a series of phase transitions that lower the unit-cell symmetry as the temperature is decreased, as sketched in Figure 1.2. In bulk, the structure is cubic and the material shows a paraelectric behavior above 120 °C. Below it and down to 0 °C, the structure becomes tetragonal with the non-centrosymmetric $P4mm$ space group, while subsequent phase transitions further lower the symmetry to orthorhombic (below 0 °C) and to rhombohedral (below -90 °C).¹³ The phase transitions can be seen as peaks in the dependence of the dielectric constant with temperature, Figure 1.2. The non-cubic phases have a spontaneous polarization that arises as a consequence of the relative displacement of Ti and Ba from the positions occupied in the cubic phase, and to the displacement and distortion of the O octahedra, which occurs along the [001], [011] and [111] crystallographic axes in the tetragonal, orthorhombic and rhombohedral phases, respectively. More specifically, in the tetragonal phase the polarization can either point along [001] or $[00\bar{1}]$. Akin occurs in the rest of low symmetry phases, which make them ferroelectric. At room temperature the BTO bulk lattice parameters are $a=b=3.994$ Å and $c=4.038$ Å, and the spontaneous polarization reaches $26 \mu\text{C}/\text{cm}^2$.

Apart from ferroelectricity, BTO non-centrosymmetric phases can also show other valuable effects, as the Pockels effect (linear electro-optic effect that induces a birefringence controllable with an electric field) that can be exploited for photonics applications.¹⁴

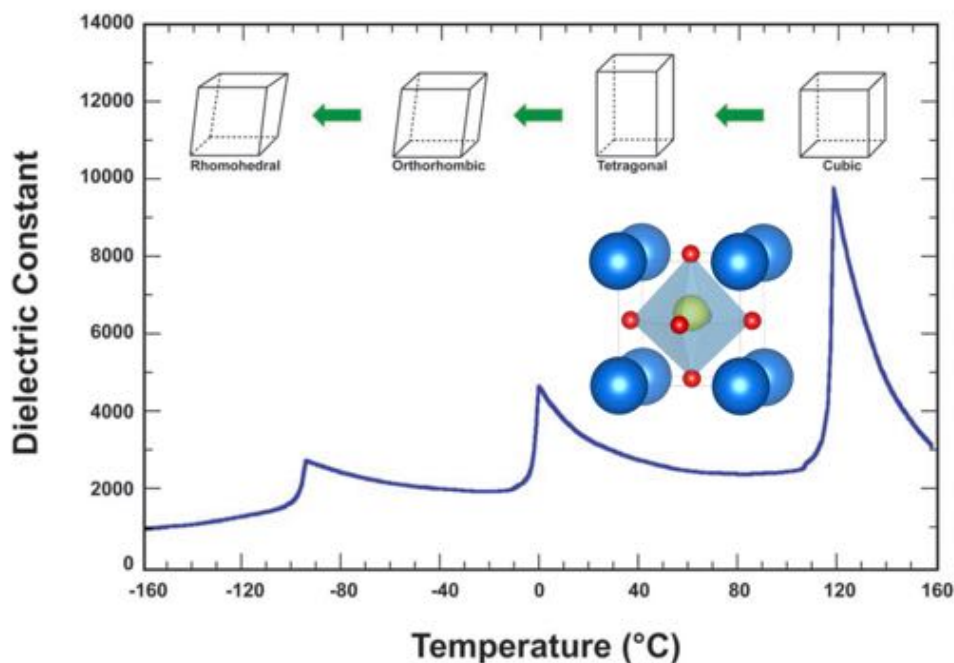


Figure 1.2: BaTiO_3 perovskite structure is shown at the center with Ba (blue) located at the corners, Ti (yellow) at the center and O atoms (red) at the faces. The different structural phases of BaTiO_3 at different temperatures are sketched at the top, while the dielectric constant-temperature dependence curve shows peaks of high dielectric constant at the phase transition temperatures. Adapted from ref.¹³

1.2.2 Fluorite $Hf_{0.5}Zr_{0.5}O_2$

$(Hf,Zr)O_2$ based materials are binary oxides with a fluorite-like structure (see the basic fluorite structure in Figure 1.3.) that have been used for years by the semiconductor industry as dielectric materials.

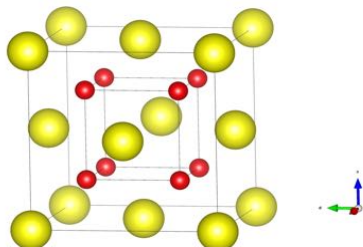


Figure 1.3: Cubic fluorite structure is depicted. The cations (in yellow) occupy the positions of a face-centered-cube, while the anions (in red) form a smaller simple cube and occupy interstitial sites.

Ferroelectricity in $(Hf,Zr)O_2$ based materials was found in 2011 in Si-doped HfO_2 .⁴ This discovery was unexpected, since the crystal structure of bulk HfO_2 and ZrO_2 oxides at room temperature and ambient pressure is a non-polar monoclinic phase (space group number 14, $P2_1/c$),¹⁵⁻¹⁸ and the predicted phases for different temperature and pressure conditions were also non-polar. The discovery of ferroelectricity in this family of materials has been a milestone for the development of technologies based on oxide ferroelectrics.

Ferroelectric perovskites have been studied for decades for their use in memories, in field effect transistors with ferroelectric gates, as well as in other applications. Commercialization success has been moderate, with mainly $Pb(Zr,Ti)O_3$ ferroelectric memories based on planar capacitors being commercialized for specific applications, where low energy consumption is crucial. Concerns over the Pb toxicity make desirable the use of other ferroelectrics. Other ferroelectric perovskites as $BaTiO_3$ or and $SrBi_2Ta_2O_9$ have been studied for Pb-free microelectronics. However, the family of ferroelectric perovskites present several fundamental limitations. Firstly, state of the art ferroelectric memories technology has achieved around 130 nm per node, while the DRAM or NAND flash memories used in computer circuitry and for data storage is one order of magnitude smaller.⁶ The ferroelectric properties get degraded in thin films, with a lowered polarization and high leakage currents, which limits the downscaling and the storage density. Secondly, the low compatibility with the complementary metal-oxide-semiconductor (CMOS) processes based on Si, which are indeed the paradigm of the microelectronics industry, requires the use of more complex synthesis processes.

The simpler binary oxides $(Hf,Zr)O_2$ are expected to overcome many of these difficulties. $(Hf,Zr)O_2$ materials are fully compatible with complementary-metal-oxide-semiconductor technology: they are compatible with the chemical composition and the deposition processes to obtain polycrystalline ferroelectric $(Hf,Zr)O_2$ films.¹⁹ Furthermore, the ferroelectricity shows an inverse

dependence with thickness to the one shown by the archetypal ferroelectric perovskites: it shows a strong tendency to become stronger at sizes of a few nanometers,²⁰ and allows integration in 3D architectures. This feature is very appreciated to achieve high density and lower energy consuming devices, where the scale is a fundamental parameter. The smallest memory node has been achieved with ferroelectric-Si:HfO₂ thin film, with a 22 nm technology node.²¹ Figure 1.4 shows the scaling gap between ferroelectric perovskites and HfO₂ memory nodes.

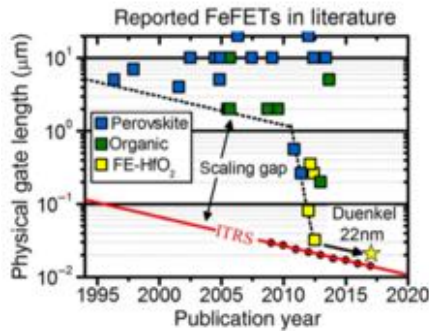


Figure 1.4: Size of the gate of field effect transistors reported for different types of ferroelectrics as a function of the publication year. The discovery of ferroelectric HfO₂ after 2011, leading to much smaller gate sizes in different publications. Adapted from ref.

21

(Hf,Zr)O₂ can be stabilized in different structural phases, both polar and non-polar. Ferroelectricity has been ascribed to the orthorhombic polar phase $Pca2_1$. The stable (Hf,Zr)O₂ non-polar phases include monoclinic (14, $P2_1/c$), tetragonal (137, $P4_2/nmc$), cubic (225, $Fm3m$) and orthorhombic (oI phase: 61, $Pbca$ or oII phase: 62, $Pnma$), depending on temperature and pressure.¹⁶ Figure 1.5 shows the main structural phases, with monoclinic, tetragonal and cubic paraelectric phases, and the polar orthorhombic phase $Pca2_1$. The identification of the $Pca2_1$ phase by x-ray diffraction is a challenging task due to the similar lattice parameters of the different polymorphs that produce degenerated reflections, so it is often assumed to be present considering the ferroelectric polarization of the films. Most often, coexistence of these phases is found. How different conditions affect the stabilization of the ferroelectric phase instead of the non-polar polymorphs is very relevant to achieve optimal ferroelectric properties; however, it is not well known. Factors as doping, deposition conditions and techniques, or surface energy and grain size (as suggests the higher polarization at reduced dimensions) can be relevant to the stabilization of the ferroelectric phase. Doping HfO₂ with Zr, Si, Y, Sr or La, has demonstrated to be a useful way of tuning properties as the polarization or fatigue. Hf_{1-x}Zr_xO₂ show good ferroelectric properties in a wide range of doping, reaching highest polarization at $x=0.5$.²² Epitaxial films have been much less investigated than polycrystalline ones. In this thesis, chapters 4 and 5 are dedicated to the study of epitaxial samples of Hf_{0.5}Zr_{0.5}O₂ grown on perovskites.

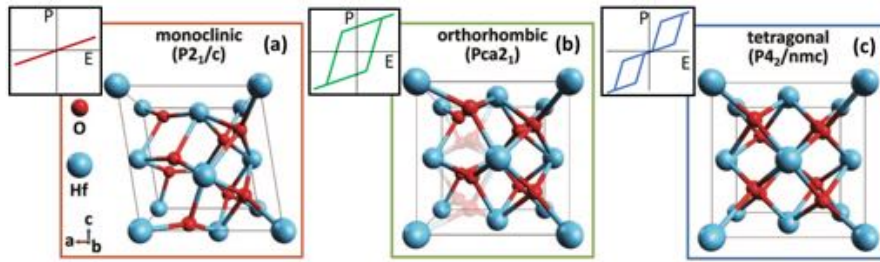


Figure 1.5: Sketch showing the paraelectric monoclinic (a), ferroelectric orthorhombic (b) and antiferroelectric tetragonal phases (c). The semitransparent O atoms in (b) represent the position for opposite polarization. Adapted from ref.²³

1.3 Engineering Ferroelectricity

1.3.1 Polarization Configuration in Ferroelectric Heterostructures

Ferroics like ferroelectric, ferromagnetic or ferroelastic materials are naturally found forming domain configurations (a domain being a region of approximately homogenous polarization) to reduce their energy. Hence, unless previously poled, a piece of ferromagnetic or ferroelectric material will normally show a negligible net magnetization or polarization. In ferroelectrics, the polar discontinuities found at interfaces and surfaces are at origin of domain formation. These polar discontinuities produce a net density of charge ρ that is related to the gradient of polarization ∇P through $\nabla P = -\rho$. The ferroelectric properties are governed by the internal arrangement of dipoles within the material, i.e. the polarization configuration, so the domain configuration is of great relevance. For example, the control over the polar axis orientation is relevant, since it can be used for different purposes, like controlling the conducting properties at the interface between a ferroelectric and a metal or semiconductor. Indeed, the possibility of stabilizing a single domain configuration is interesting for many ferroelectric applications since it allows to maximize the net macroscopic polarization that is exploited. To achieve it normally requires an effective screening of the ferroelectric charges. The integration with a conducting electrode serves as a screening mechanism; yet, even if the electrode is a good conductor, a dead layer can appear at the ferroelectric-electrode interface, with detrimental effects on the polarization. In certain cases, these depolarizing fields can also be sought for different purposes. For example, by using different top and bottom electrodes an asymmetric screening can generate an imprint field within the ferroelectric material, which can be used to increase the charge separation efficiency in photovoltaic cells by dragging the electron and hole of an electron-hole pair apart from each other.²⁴ In other cases, the depolarizing fields can be tuned to induce the formation of specific domain configurations, in which properties of technological interest may

arise.^{25,26} Hence, we can see how the electrostatic boundary conditions can alter the ferroelectric state and thus play a central role in the polarization configuration that is stabilized. An interesting approach consists in synthesizing epitaxial heterostructures combining ferroelectrics with paraelectrics. Similar to the case of the ferroelectric surface with air, the ferroelectric/paraelectric interface will provide little screening for the ferroelectric charges, creating an unstable state.

In order to present some basic domain configurations that can occur to reduce the energy of the system we shall consider the case of a simple uniaxial ferroelectric with polar axis along z . According to the Ginzburg-Landau theory, the electric part (omitting strain) of the free energy in a ferroelectric and paraelectric can be written as:

$$f_{FE} = \int_0^{d_F} \left(\frac{\alpha_1}{2} P_F^2 + \frac{\beta}{4} P_F^4 + \frac{\kappa_1}{2} \left(\frac{dP_F}{dz} \right)^2 - P_F \mathcal{E}_F \right) dz$$

$$f_{PE} = \int_0^{d_P} \left(\frac{\alpha_2}{2} P_P^2 + \frac{\kappa_2}{2} \left(\frac{dP_P}{dz} \right)^2 - P_P \mathcal{E}_P \right) dz$$

α_1 is a function of the temperature and becomes negative for $T < T_0$, which together with the term containing β (positive constant) produce the double-well ferroelectric energy profile (see Figure 1.6). Similarly, the term associated to α_2 (positive constant) describes the energy profile of the paraelectric, that has lowest energy at zero polarization. \mathcal{E}_F and \mathcal{E}_P are the electric field in the ferroelectric and paraelectric. The terms having κ_1 and κ_2 as positive constants represent the energy associated to polarization gradients inside each layer. The total electric energy of the system is obtained upon integration of these expressions along the thicknesses of the layers,^{27,28} and the ground polarization configuration by minimizing the total energy under a balance of the different terms at competition. In bulk, the electric fields and polarization gradients are zero, and the energy profiles look like the ones on the top panel of Figure 1.6. However, if the ferroelectric and paraelectric materials are brought together, at the ferroelectric-paraelectric interface the electric field created by the unscreened ferroelectric surface charges creates a polarizing electric field pointing towards the ferroelectric in the paraelectric, and a depolarizing field in the ferroelectric. Considering the internal energies and the electrostatic coupling $-P\mathcal{E}$ the energy profiles will be modified, as depicted in the lower panel of Figure 1.6.

Now, we shall consider how the electric coupling between layers and the balance of energy terms can result in different polarization configurations that minimize the total energy depending on the thicknesses of the layers. In this thesis, the case of a superlattice in which the electrostatic conditions become periodical by the repeated stacking of a bilayer made up of a ferroelectric and a paraelectric of specific thickness is considered.

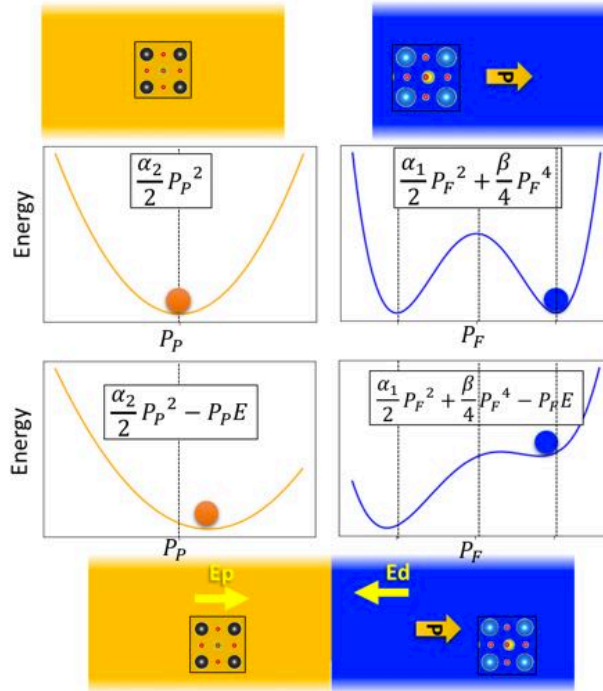


Figure 1.6: Top panel shows the electric energy terms and Energy-Polarization profiles of a bulk paraelectric and a bulk ferroelectric. Bottom panel shows the electric energy terms when a ferroelectric-paraelectric interface is considered. A non-zero polarization in the ferroelectric and zero polarization in the paraelectric creates polarizing (E_p) and depolarizing fields (E_d) in regions around the interface, putting the materials in an unstable state.

Two main regimes can be distinguished depending on the thickness of the layers: very thin layers in which the electrostatic coupling across layers is very relevant; and thicker layers, where the electrostatic coupling is weaker. In ferroelectric/paraelectric superlattices with very thin layers, polarization can be considered constant inside each layer thus eliminating internal polarization gradients. In this model, the energy can be written as follows^{29,30}:

$$E(P_F, P_P) = E_F(P_F) + E_P(P_P) + E_{F/P}(P_F, P_P)$$

where $E_F(P_F)$ and $E_P(P_P)$ are the energies of the bulk ferroelectric and paraelectric as a function of their polarizations, which depends on the polarization in each layer. $E_F(P_F)$ and $E_P(P_P)$ depend on the polarization as shown in the ferroelectric and paraelectric energy profiles and their dielectric constants. $E_{F/P}(P_F, P_P)$ represents the energy due to the coupling between the layers, and can be expressed as a function of the ferroelectric and paraelectric layer thicknesses (d_F and d_P) and polarizations by making some assumptions. First, the electric displacement D ($D = P + \epsilon_0 \cdot \mathcal{E}$) should be continuous across the interface: $P_F + \epsilon_0 \cdot \mathcal{E}_F = P_P + \epsilon_0 \cdot \mathcal{E}_P$. The potential drop (electric field integrated along the whole

thickness) should be zero for short-circuit boundary conditions, and $d_P \mathcal{E}_P = -d_F \mathcal{E}_F$. Then, the electric field in the ferroelectric (paraelectric) can be written as a function of the polarization in each layer and their thicknesses:

$$\mathcal{E}_{F(P)} = \frac{d_{P(F)}(P_{P(F)} - P_{F(P)})}{\varepsilon_0(d_P + d_F)}$$

As can be seen, the electric field vanishes if a constant polarization is developed across the layers. The energy associated to an electric field can be approximated in first order as $-d \cdot P \cdot \mathcal{E}$. Then, adding the energy in the ferroelectric and paraelectric ($-d_F \cdot P_F^0 \cdot \mathcal{E}_F - d_P \cdot P_P^0 \cdot \mathcal{E}_P$) the expression for the energy reads:

$$E_{F+P} = \frac{d_F \cdot d_P}{\varepsilon_0(d_F + d_P)} \cdot (P_F - P_P)^2$$

This energy term represents the energy associated to the electric fields created by the discontinuity in the polarization between the ferroelectric and paraelectric layers; and thus, it can be seen as a force favoring a constant polarization across layers. As can be inferred from this energy expression, the energy per unit of thickness remains constant when the thicknesses are increased, as long as the thickness ratio of both materials is kept constant. This result is valid for very thin films, where electric fields created by polarization can be considered to be constant across the layer (the ideal case sketched in Figure 1.7 (a)); in contrast, in the case of layers with a bigger thickness (bigger than the electric field penetration length), this assumption does not hold. For thicker layers, the electrostatic coupling between layers becomes weaker as an increasing part of each layer is away from the interface as the thickness of the paraelectric is increased. The coupling between ferroelectric layers also becomes much smaller. In this regime, the formation of domains in the ferroelectric (as sketched in Figure 1.7 (b)) is a common prediction.^{31,32} The formation of domains can decrease the depolarizing and polarizing electric fields in the ferroelectric and the paraelectric, decreasing the associated energies. This decrease will be larger for smaller domains. However, the domain walls have an energy cost associated to inhomogeneous polarization, so the size of domains is determined by the balance of these polarization, so the size of domains is determined by the balance of these competing energies. Kittel first addressed this question in ferromagnetic materials; and although the physical origins of domains is different in different ferroics as are ferromagnetics and ferroelectrics, the role played by magnetostatic and electrostatic energies is analogous, and so is the mathematical derivation. The depolarizing energy E_{DEP} ,³³ and the energy associated to polarization gradients present at domain walls E_{DW} are:

$$\left. \begin{aligned} E_{DEP} &\sim d_D \cdot (P_F)^2 \\ E_{DW} &\sim \Delta \cdot (P_F)^2 \cdot \frac{d_F}{d_D} \end{aligned} \right\}$$

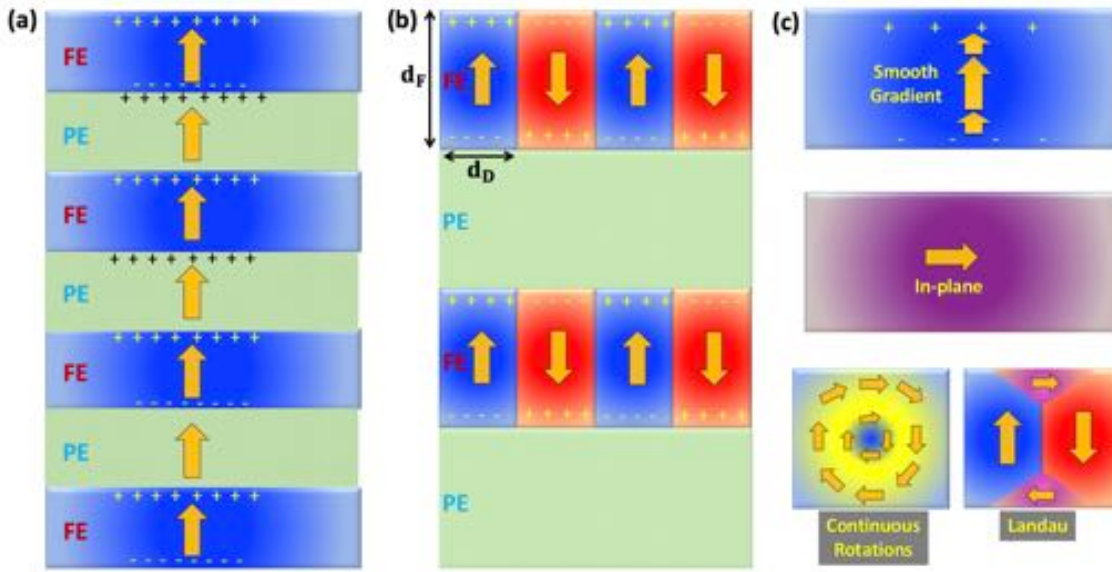


Figure 1.7: (a) Continuous Polarization Configuration is expected for thin enough paraelectric films. (b) Case of intermediate layers thickness showing Kittel up-down domains in the ferroelectric and a negligible polarization in the paraelectric. (c) Other polarization configurations in the ferroelectric are possible.

, where Δ is a constant that accounts for the width of the domain wall and d_D is the domain width. Minimization of the total energy with respect to the domain width (by taking the derivative with respect to d_D) yields the ground domain size³⁴:

$$d_D \sim \sqrt{\Delta d_F}$$

Thus, the domain size increases as the square root of the ferroelectric layer thickness d_F . From the last equation, the ground total energy per unit of thickness ($\frac{E_{DEP+DW}}{d_F}$) can be written as a function of P_F , d_F and Δ as: $\frac{E_{DEP+DW}}{d_F} \sim 2(P_F)^2 \sqrt{\frac{\Delta}{d_F}}$. This result indicates that the energy per unit of thickness increases as the size of the ferroelectric layer is reduced, which is due to the bigger relative contribution of the domain wall energy, accounted by Δ . Thus, domains may be energetically unfavorable below a certain thickness. These simplistic models can successfully account for many of the features observed in ferroics, as the formation of domains and the domain sizes, or the macroscopic polarization for different thicknesses of the ferroelectric and paraelectric layers. Yet, under the appropriate conditions and specially at the nanoscale, the polarization can produce more complex configurations by including smooth polarization gradients, as rotations of the polarization and a smoothly varying local polarization (with several examples sketched in Figure 1.7 (c)). At the nanoscale, ferroelectric behavior may be different from bulk not only due to the depolarizing fields but also because the long range

Coulombian interaction can be altered. More sophisticated models, as the ones based on the Ginzburg-Landau theory,^{28,35} are used to describe more complex polarization configurations. It is important to note that in the above analysis, the epitaxial strain has been omitted; however, together with the electrostatic boundary conditions it is one of the most relevant conditions influencing the ground polarization configuration in an epitaxial heterostructure such as a ferroelectric/paraelectric superlattice.

1.3.2 Strain Engineering

Modifying the crystal structure by the application of a suitable mechanical stress is another mature approach that allows to control the functional properties of oxides due to the relation/dependence of properties such as the ferroelectricity with the crystal structure. This technique, known as strain engineering, generally consists in the growth of a material onto a suitable substrate. As an example of its capabilities in ferroelectrics, the ferroelectric transition temperature can be driven to higher temperatures by straining the structure,³⁶ and the polar axis orientation can be favored to occur along a specific direction.³⁷ This technique is widely used to modify functional properties of crystalline materials beyond ferroelectrics, as can be ferromagnetic,³⁸ or semiconductor materials.³⁹ In the case of epitaxial films, the strain state of the film can be selected by growing it on a substrate with suitable lattice mismatch. In this 2D geometry, the film becomes strained in the plane of growth (biaxial strain), while the structure is free to relax along the other direction, as sketched in Figure 1.8. The lattice mismatch along a given direction between the film and the substrate is expressed as follows:

$$f = \frac{a_{SUBS} - a_{FILM}}{a_{FILM}}$$

, where a_{SUBS} is the lattice parameter of the substrate and a_{FILM} is the lattice parameter of the film in its bulk state. f can be understood as the number of times that the corresponding lattice parameter of the film would need to increase or decrease to perfectly match the substrate. Depending on whether the substrate lattice parameter is smaller or bigger than that of the film, the strain can be either tensile (positive f) or compressive (negative f), see Figure 1.8. Moreover, in general, the lattice mismatch can be different along different directions. For the specific case of perovskites, when considering cubic symmetries in the plane the strain is isotropic.

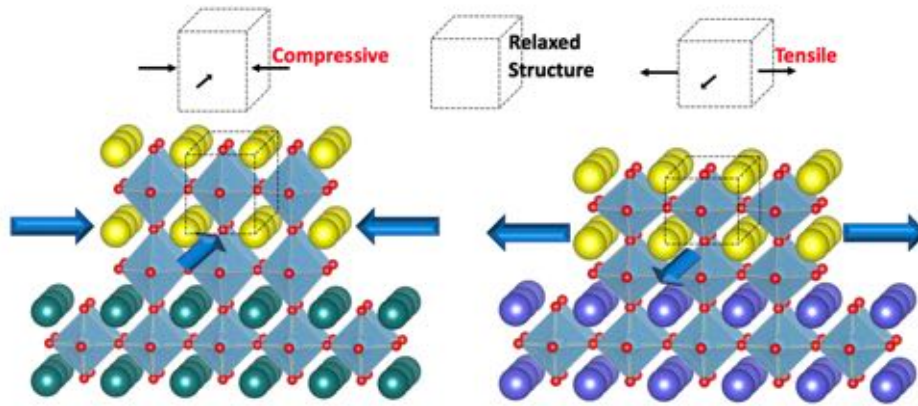


Figure 1.8: Compressive and tensile strain induced in a perovskite layer by using two perovskite oxides substrates with smaller and bigger lattice parameters, respectively. The deformations are exaggerated so that they are clearly visible.

Nevertheless, the lattice parameters of the substrate are not always transferred to the film. This is so mainly because the elastic deformation of the film comes with an elastic energy cost associated, which rapidly increases for increasing strains, and can result in a plastic relaxation by different mechanisms when the lattice mismatch is too big. Analogously to the lattice mismatch definition, the strain of a film can be written by comparing the lattice parameter of the strained film (a_{FILM}) with the bulk lattice parameter (a_{BULK}) as follows:

$$s = \frac{a_{FILM} - a_{BULK}}{a_{FILM}}$$

In the case of a layer fully strained onto a substrate the lattice parameters will be equal ($a_{FILM} = a_{SUBS}$) and s and m will have the same value. In the case of a partial relaxation the strain will be smaller than the lattice mismatch $|s| < |f|$. In general, for strains bigger than 3% the strained growth is often not feasible.⁴⁰ Moreover, even for low strain mismatches as films are grown thicker, the films tend to relax the elastic energy. This constitutes one important limitations of the strain engineering method. Other important limitations are present, as the limited possible stresses due to the limited availability of compatible substrates due to different symmetries and lattice parameters, or the impossibility to modify the strain post-growth.

In the case of ferroelectric BTO, strain can increase its polarization by increasing the asymmetry of the unit-cell, for example. This is, the spontaneous polarization can be increased in tetragonal BTO by increasing its tetragonality (though the piezoelectric effect). The polar axis orientation will be favored to be oriented out-of-plane (oop) if the in-plane (ip) lattice mismatch is

negative, while it will be favored to lay in plane if it is positive. These concepts will be used to in the analysis of BaTiO₃/SrTiO₃ superlattices presented in Chapter 3.

1.3.3 Engineering Ferroelectricity Beyond Electrostatics and Strain

There exist other methods of great relevance beyond the ones presented above, which combined can represent a breakthrough over the control functional properties of oxides. One of them consists in the generation of crystal defects, like oxygen or cation vacancies, dislocations or stacking faults. In Pulsed Laser Deposition (PLD), as well as in other synthesis methodologies, the defects can be controlled by adjusting the deposition parameters.⁴¹ PLD offers the possibility of tuning the growth rate and deposition temperature, for instance. Another very relevant approach is the addition of dopants or more generally the modification of the stoichiometry, a technique known as doping. Doping is well known to be fundamental in electronic components and devices using semiconductors, such as diodes. In oxides doping can permit the stabilization of different phases, as the ferroelectric phase of (Hf,Zr)O₂,²² or reduce the leakage current and fatigue of the material, among other effects.

In general, the combination of the different engineering methods that aim at different degrees of freedom can be used in combination to produce the required properties.

Chapter 2: Experimental Methods

In this chapter, the methodologies used to prepare and characterize the studied oxide thin films are presented. The different sections are ordered emulating the time ordering of the different processes that take place during the research, from the synthesis to the different characterization techniques and data analysis.

2.1 Pulsed Laser Deposition

The crystal growth laboratory at ICMAB possesses an ultra-high-vacuum cluster equipped with two Pulsed Laser Deposition (PLD) chambers and one sputtering chamber. PLD was used to grow epitaxially the oxide films studied in this thesis.

PLD is a physical vapor deposition technique that uses a pulsed laser (KrF excimer laser with a pulse of 25 ns and a wavelength of 248 nm was used) and focuses it onto the target that contains the elements and stoichiometry to be deposited (Figure 2.1 (a)). In this way, the laser light, that is directed to the selected PLD chamber by an optical system, transfers energy to the target, ablating a fraction of it and forming a plasma plume (see Figure 2.1 (a) and (b)). The plasma plume, which contains the elements to be deposited with the corresponding stoichiometry, expands inside the chamber and gets

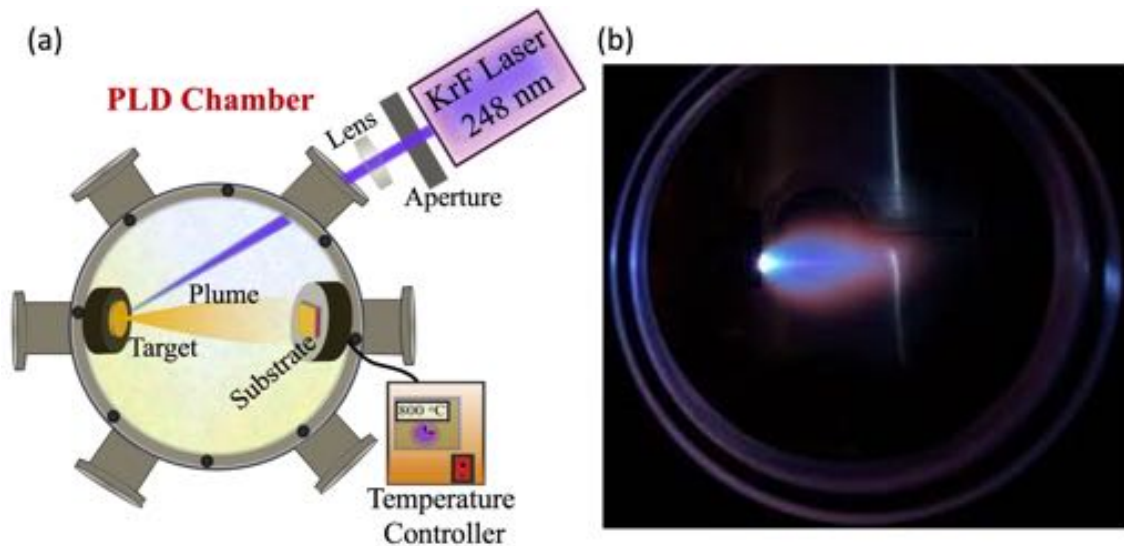


Figure 2.1: (a) simplified sketch of the PLD setup. (b) picture of the plume acquired through a window of one of the PLD chambers at ICMAB.

deposited on the substrate (normally in less than 10 μ s). The distance target-substrate can be varied by displacing the substrate holder. This deposition process is repeated as many times as laser pulses are

used, adding the specific amount of material that gets deposited in each pulse. The substrate temperature is measured by a thermocouple located at the center of the heater block and controlled by a heater that can reach up to 850 °C. The vacuum chamber is filled with oxygen at a given pressure (normally in the 10^{-4} - 0.3 mbar range), which can be used to control the energy of the atoms in the plume as well as to avoid oxygen deficiency in the film. The total number of pulses are set to obtain a specific film thickness. PLD permits to grow films as thin as a few atomic monolayers, allowing to grow for example superlattices with variable periods (see Chapter 3). Up to five targets can be held by the target holder, allowing to deposit different stoichiometries or materials in a single process. Besides, the amount and kind of defects as well as other aspects occurring during the growth can be indirectly controlled from the deposition parameters (substrate temperature, oxygen pressure and growth rate).

Moreover, one of the PLD chambers at ICMAB is further equipped with a Reflection High Energy Electron Diffraction (RHEED) system. RHEED is useful to track the growth process in-situ. It directs an electron beam towards the sample surface and collects the diffraction pattern on reflection, which provides real-time structural information of the sample surface during the growth.

2.2 Atomic Force Microscopy

Atomic Force Microscopy (AFM) has been used to study the surface topography after the synthesis of the different samples by PLD. The technique uses a cantilever provided with a tip that is scanned onto the sample's surface. AFM can be used in contact mode, in which the tip and the surface are in direct contact, in non-contact mode, or in intermittent contact mode (also known as tapping mode). The last mode was used. This mode makes the tip oscillate according to a driving signal, but its interaction with the sample's surface can modify the amplitude, frequency and phase of the tip oscillation. As is sketched in Figure 2.2, a laser beam is deflected by the cantilever and directed towards a four-pixel photodetector. When the cantilever oscillates it deviates the laser, modifying

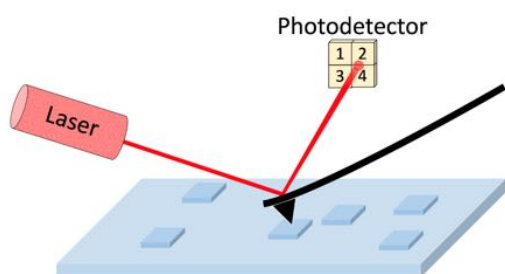


Figure 2.2: Sketch of the main components of the AFM, with the flexible tip that is scanned on the sample's surface and the laser beam being deflected by the tip towards the 4-pixels photodetector.

the laser intensity distribution on the photodetector and thus the intensity sensed by each of the four pixels, which is converted into a signal. By comparing the driving signal with the signal detected by the photodetector, information as the topography or height at each location of the sample's surface can

be extracted. An Agilent 5100 AFM device equipped with silicon tips was employed to scan areas (512x512 pixels) with sizes of $5 \times 5 \mu\text{m}^2$ and $1 \times 1 \mu\text{m}^2$.

2.3 X-Ray Diffraction

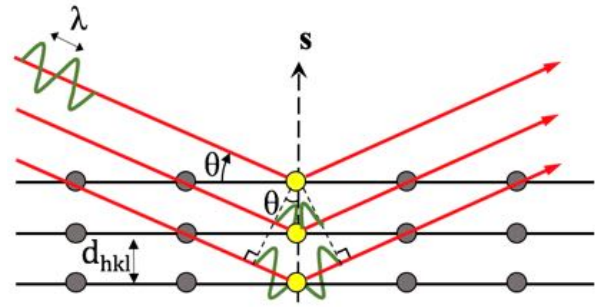
A powerful technique to characterize the crystal structure consists in recording and analyzing the signal produced by the diffraction (reciprocal space) of a beam of particles (electrons, photons, neutrons, etc) by a crystal. As a notable historical example, the DNA structure was finally solved with the help of x-ray diffraction. Here, x-ray diffraction has been extensively used to characterize the lattice of the samples, allowing to measure different plane spacings, the epitaxial relationship (relative orientation) between different layers or the layer thickness. X-Rays are highly energetic photons with short wavelengths approximately in the order of the Å. The diffraction equipment used at ICMAB use the K- α emission of a Cu source, which contains the K- α_1 (1.5406 Å) and the K- α_2 (1.5444 Å) emission lines. These wavelengths are very similar and sometimes are not resolved, in which case a weighted average is considered. Such small wavelengths are necessary to have sensitivity to the lattice spacings, which are about several Å. The x-rays are focused and diffracted at the sample's surface, providing structural information from the whole area of the sample (approximately $5 \times 5 \text{ mm}^2$).

Different scanning modes are used to explore different areas of the reciprocal space.⁴² The x-ray beam is directed towards the sample surface at an angle ω with the surface. After diffraction, the beam will subtend an angle with its initial direction denoted as 2θ . The diffracted beam fulfils the condition of constructive interference, which occurs only at specific angles. The Bragg law describes, for a given set of planes characterized by their reciprocal Miller indices (hkl), at which angle θ (with respect to the planes' surface) diffraction occurs. The difference in optical path between the waves diffracted in consecutive planes, which have a spacing d_{hkl} , should be an integer (n) of the wavelength (λ), thus:

$$n\lambda = 2d_{\text{hkl}}\sin(\theta)$$

Figure 2.3 shows a sketch of the diffraction geometry that leads to the Bragg law. As shown, the scattering vector, which is the variation in the wavevector between incident and diffracted beams ($\mathbf{s} = \mathbf{k}_f - \mathbf{k}_i$ with $|\mathbf{k}| = \frac{2\pi}{\lambda}$), is perpendicular to the diffracting planes when diffraction conditions are fulfilled.

Figure 2.3: sketch of diffraction satisfying the Bragg condition, with an incident wave with wavelength λ subtending an angle θ with a set of crystallographic planes with d_{hkl} spacing. s represents the scattering vector.



The simplest and most commonly used measuring mode is the symmetric ω - 2θ scan, Figure 2.4 (b). It is known as θ - 2θ and consists in varying the incidence angle ω of the beam and θ (detector) by maintaining $\omega = \theta$. This allows to observe diffraction of planes parallel to the sample's surface when the Bragg condition is met, which in turn allows to extract the d_{hkl} spacing from the values of θ and λ .

Asymmetric ω - 2θ is a variant of the symmetric scan in which $\omega \neq \theta$, Figure 2.4 (b). In this case, diffracting planes that are misoriented with respect to the sample normal by an angle χ can be observed by tilting the incidence and detector angles accordingly, so that the 2θ of the beam with the diffracting planes is maintained.

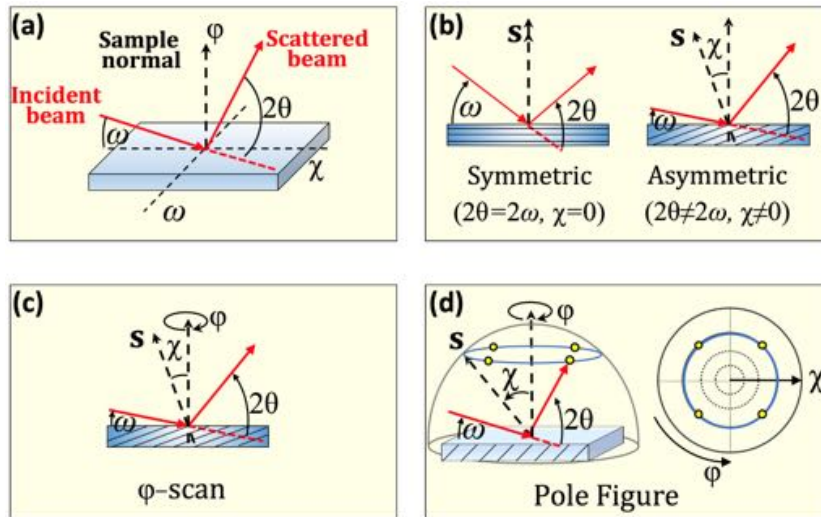


Figure 2.4: (a) Sketch of the measuring geometry and the angles involved. (b) Symmetric and asymmetric scans of ω and θ . (c) ϕ -scan with ω and 2θ of the detector fixed. (d) ϕ -scan is represented by the blue line, while diffraction directions on the ϕ -scan are given by the yellow dots. Pole figure involves scanning in ϕ and scanning in χ , which gives a 2D map that can be projected along the out-of-plane direction as shown at the right.

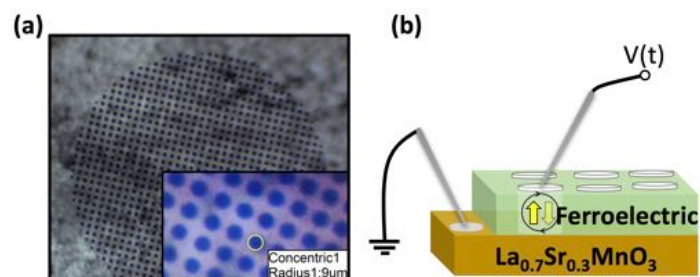
φ -scans are obtained by selecting and keeping fixed appropriate χ , ω and θ for a set of planes and scanning φ (rotating the sample around the φ axis), Figure 2.4 (c). It is a very useful measurement to find out the epitaxial relationship of the films or the crystallites contained in them. For example, for a cubic crystal with (001) orientation the {111} family of planes is equivalent due to the cubic symmetry of the crystal and the 4 planes of the unit-cell upper half ((111), (1 $\bar{1}$ 1), ($\bar{1}$ 11) and ($\bar{1}\bar{1}$ 1)) will have same θ and χ , showing the corresponding 4 {111} reflections for one full rotation. This φ scan will then indicate the in-plane orientation of the crystal. This case is sketched in Figure 2.4 (d) left.

Pole figures can be viewed as an extended case of φ -scan in which instead of rotating only in φ , the angle χ is also scanned, showing a map of the φ - χ plane. This case is sketched in Figure 2.4 (d).

2.4 Electrical Characterization of Ferroelectric Thin Films

Polarization hysteresis loops contain relevant information of a ferroelectric, such as the spontaneous and remanent macroscopic polarization, the coercive electric field and other parameters of interest. In order to measure the ferroelectric hysteresis of a sample, the domains are driven into a polarized state along the out-of-plane (oop) direction (either up or down), producing a non-zero macroscopic polarization, and then they are switched between the up and down states while this process is tracked. The polarization switching is achieved through the coupling of the polarization to an applied varying electric field applied along the oop direction, in a capacitor like configuration. $\text{La}_{0.7}\text{Sr}_{0.3}\text{MnO}_3$ was used as bottom electrode in most of the studied films. The $\text{La}_{0.7}\text{Sr}_{0.3}\text{MnO}_3$ and the other oxide layers in the studied heterostructures were grown by PLD in a single process. Metallic Pt contacts with circular shape and around 20 μm diameter were used as top contacts, and were deposited on the film's surface by magnetron sputtering through a stencil mask (Figure 2.5 (a)). The measuring scheme in which the film is electrically contacted at top and bottom, known as top-bottom configuration, is shown in Figure 2.5 (b). $\text{Hf}_{0.5}\text{Zr}_{0.5}\text{O}_2$ films (Chapters 4 and 5) were measured using

Figure 2.5: (a) optical microscope image of the contacts on the sample's surface. The contacts nominal radius is of 10 μm , but it can slightly vary; 9 μm is measured in the image. (b) Sketch of the top-bottom configuration.



this configuration, while the BaTiO₃/SrTiO₃ superlattices (Chapter 3) were measured in top-top configuration. The latter involves measuring two capacitors in series.

A net up/down polarization will produce accumulation of screening negative/positive charges at the top surface, and opposite charges at the bottom. Upon polarization switching, induced by the applied electric field, these screening charges are also reversed by flowing through the circuit. In an ideal ferroelectric film and considering an initial zero polarization, the polarization can be defined as:

$$P(t) = \frac{\int_0^t I(t)dt}{A}$$

where $I(t)$ is the current and can take positive or negative values, and A is the area of the contact. $I(t)/A$ is the current density, with units of charge/(area·time) and will be denoted as $J(t)$. According to the equation above, the hysteresis loop of a ferroelectric can be obtained by measuring the current associated to the switching of ferroelectric domains while switching is induced by an electric field. Ferroelectric hysteresis measurements were carried out by using *aixACCT* TFAalyzer 2000 (<https://www.aixacct.com>).

The most basic method used to measure hysteresis dynamically is known as Dynamic Hysteresis Measurement (DHM). It consists in applying four bipolar triangular voltage pulses with a time frequency ν and a delay time between the different pulses τ (normally 1 s), as sketched in Figure 2.6 (a). The first pulse serves to polarize the film in the down state, while the second pulse measures the switching from up to down. The third and fourth pulses do the same for the inverse polarity, completing the polarization hysteresis loop. If the triangular voltage pulses apply an electric field ⁱ bigger than the coercive field, switching of the polarization occurs, producing a ferroelectric current $J_{FE} = \frac{\partial P_{FE}}{\partial t}$, where P_{FE} is the ferroelectric polarization. However, other non-ferroelectric components will contribute to the measured current. Identify them is key to identify and isolate the ferroelectric current.^{43,44} Apart from the non-linear part associated to the ferroelectric switching J_{FE} , the material will produce a current associated to the linear part of the dielectric J_{ϵ} . Thus, rather than the polarization we are measuring the current associated to the electrical displacement $\frac{\partial D}{\partial t}$ ($D = \epsilon_0 E + P_{\epsilon} + P_{FE}$), known as displacement current, which includes a bigger amount of charge producing an overestimation of the polarization at non-zero fields. Furthermore, the ferroelectric film can be regarded as a lossy capacitor,

ⁱ The electric field E can be determined from the film thickness d and the voltage V as $E=V/d$

with a leakage current J_{LEAK} contribution, that can be very relevant in thin films due to the small thickness. Then, the total current will be: $J = J_{FE} + J_{\epsilon} + J_{LEAK}$. The resulting measured total current J at time t is the temporal convolution of the applied voltage signal and the measuring setup response, which can also be relevant in some cases, mainly depending on the frequency ν used, apart from sample and setup characteristics. Basically, the setup contribution can be described by an equivalent series resistance and an inductance that will delay the measured current with respect to the input signal.⁴³ At high frequencies, the setup contribution will be important while the leakage will be less relevant. Usually, the best option is to use a medium frequency (in the kHz range) where the ferroelectric and dielectric contributions are more important. Beyond an appropriate frequency, different strategies are used to identify and eliminate the non-ferroelectric contributions (Figure 2.6).

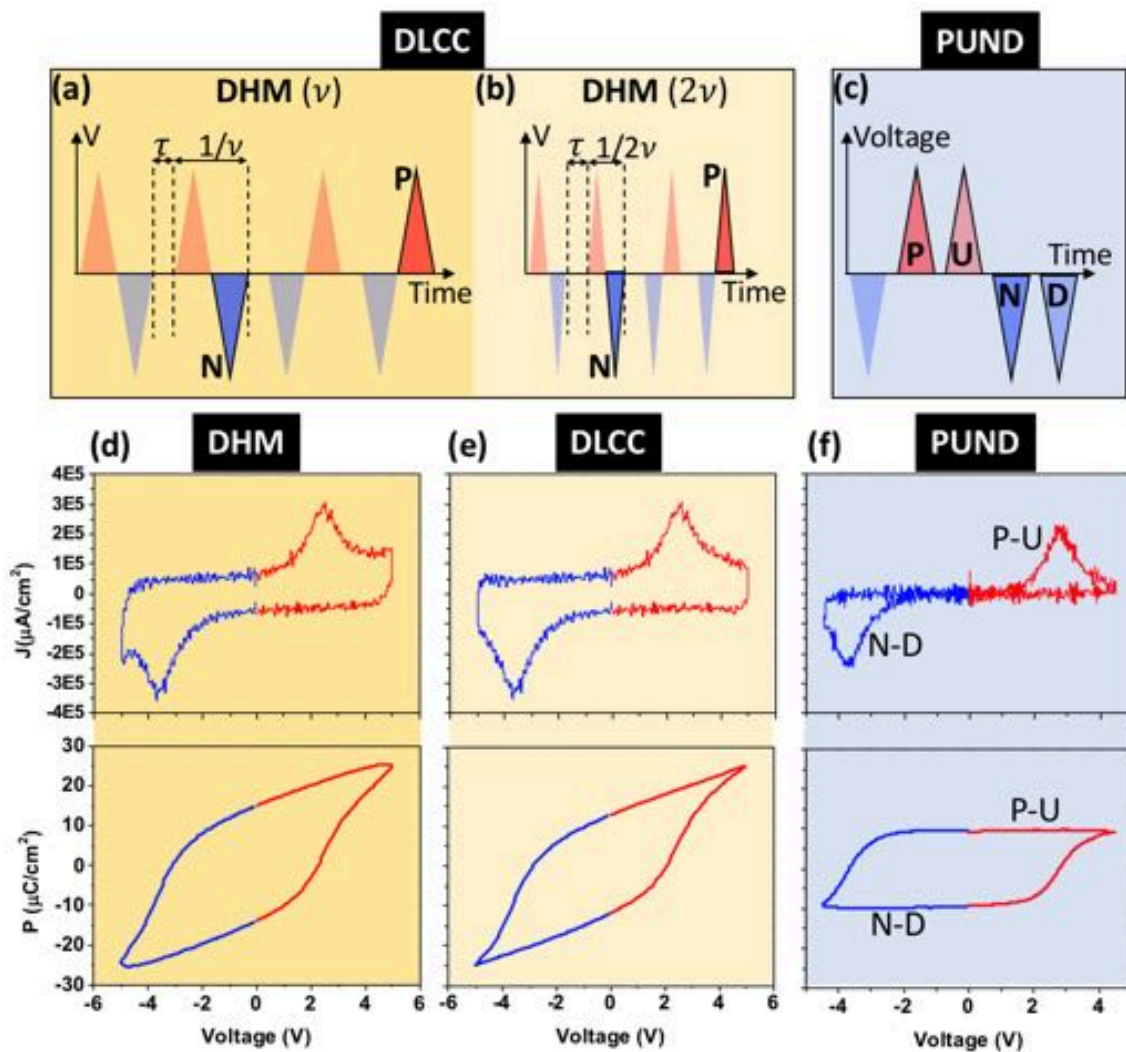


Figure 2.6: (a) DHM pulse sequence with frequency ν . (b) DHM at double frequency (2ν) than in (a). (a) and (b) are combined to obtain a DLCC hysteresis loop. (c) PUND pulse sequence. (d) DHM current and polarization loops. (e) DLCC of the same sample as in (d). (f) PUND current and polarization loops.

The Dynamic Leakage Current Compensation (DLCC) method, implemented in the measuring equipment, was used to subtract the leakage current J_{LEAK} . By assuming that J_{LEAK} is frequency independent and that the displacement current ($J_{FE} + J_{\epsilon}$) depends linearly on it, comparison of the measured current J at two different frequencies (ν and $\nu/2$) can serve, in an ideal case, to identify the leakage contribution and subtract it. The DHM, Figure 2.6 (d), shows the ferroelectric switching peak for positive voltage (in red) at around 2-3 V and an increasing current for higher voltages, corresponding to the leakage current. A similar current is observed for the negative side (in blue) of the loop. The leakage contribution widens the ferroelectric loop. As shown in Figure 2.6 (e), DLCC reduces the leakage current, observable at the highest voltages used, obtaining a narrower polarization loop after integration of the current J according to the above equation. Yet, DLCC still contains the other extrinsic contributions.

Another interesting measuring methodology known as PUND (Positive Up Negative Down) has also been used to measure samples with strong leakage and high coercive voltages, Figure 2.6 (c) and (f). It uses five triangular pulses and in principle, allows to obtain only the ferroelectric contribution. The first pulse polarizes the sample in a negative state, while the second (P) and third (U) are positive. P switches the domains to the positive state and contains the ferroelectric and non-ferroelectric contributions. U is positive as it is P but is applied after P, so no switching occurs and it only contains the non-ferroelectric contributions. Computing $I(P)-I(U)$ provides only the ferroelectric contribution. The same is done with the fourth and fifth pulses from the positive to the negative state, obtaining the whole hysteresis loop. This methodology is not perfect since it can produce an overestimation, the origin of which is not well understood.⁴⁴ As shown in Figure 2.6 (f), and unlike Figure 2.6 (d) and (e), the current is only non-zero at the ferroelectric switching peaks, obtaining a flat polarization at voltages smaller than coercive voltage.

2.5 Scanning Transmission Electron Microscopy

In this section we introduce a few basic principles of Scanning Transmission Electron Microscopy (STEM), as well as the techniques used for the structural and chemical characterization of the heterostructures studied in this thesis. More extensive details of STEM can be found elsewhere.⁴⁵⁻⁴⁸

2.5.1 Introduction

Aberration-corrected STEM has been used widely in this thesis for the characterization of materials. Specifically, a Nion UltraSTEM 200 located at *Oak Ridge National Laboratory* (United States) and a Jeol JEM ARM200CF located at *Centro Nacional de Microscopía* (Spain) were

employed. The electron microscope obtains structural and chemical information of materials from its interaction with an electron beam, and has been an outstanding characterization technique due to its unique spatial resolution, with state-of-the-art microscopes allowing to directly observe the atomic columns in a crystal. A specific crystallographic direction of the specimen needs to be aligned with the optical axis or electron beam direction, so that the projected structure shows the atomic columns. This alignment process is known as tilting.

An optical microscope is limited to spatial resolutions of the order of hundreds of nanometers (light wavelength), and photons of high energy as x-ray are sensitive to structural information in the Å scale but have a lower spatial resolution that is above tens of nanometers, limited by the minimum achievable area in which the photons can be focused. Unlike photons, electrons are electrically charged particles, so they can be easily accelerated, focused and scanned with electromagnetic lenses, as occurs in old cathode-ray displays. In a STEM microscope the electrons are first extracted from a gun (very thin and sharp tip) by the so called extracting voltage, and are accelerated by a high voltage (200 kV in this thesis) inside the high vacuum microscope column to high speeds. Secondly, the gun image is demagnified by the microscope optics composed of different electromagnetic lenses into a small electron probe onto the specimen. This probe is scanned later onto the specimen, generating a signal that varies with the probe position and ultimately producing a contrast that depends on the structure being probed.

The gun that emits the electrons plays a central role in the microscope capabilities. There are mainly two kind of emission guns: Schottky emission guns, which use the Schottky effect to enhance the thermionic emission of electrons, and cold field emission guns, which rely on a more intense extraction field and can emit at lower temperatures. The latter brings advantages over the Schottky guns, especially in that the energy spread of the electrons is smaller, which is beneficial in limiting chromatic aberration or improving the energy resolution, crucial for spectroscopy. The microscopes used in this thesis were equipped with cold field emission guns.

Regarding the electromagnetic lenses of an electron microscope, they are versatile since their focal length can be easily modified by adjusting the flowing current that controls the magnetic fields. Yet, these lenses suffer from different aberrations, that results in the spread of the electron probe intensity over a larger area and the corresponding loss of spatial resolution. The most relevant aberrations are geometric with rotational symmetry around the optical axis of the lenses, while the effect of the chromatic aberration, that produces a weaker deflection for higher electron energies, is kept low by the high monochromaticity of the electron beam. These rotationally symmetric aberrations depend on the angle θ with the optical axis, and can be expressed as a summation as follows:

$$\chi(\theta) = \frac{1}{2}C_1\theta^2 + \frac{1}{4}C_3\theta^4 + \frac{1}{6}C_5\theta^6 + \dots$$

, where C_1 is the defocus term, C_3 is known as spherical aberration, and C_5 is known as fifth order aberration. The function χ is known as the aberration function,⁴⁸ and represents the physical distance between the aberrated wavefront that converges onto the sample and the ideal wavefront of a system with no aberrations. Apart from these, other aberrations depend on the angle around the optical axis, as is the case of astigmatism and coma, common aberrations that are corrected while operating the microscope. These aberrations, specially the higher order ones, are very small close to the optical axis ($\theta \sim 0$), so the resolution can be increased by the use of apertures that limit the θ range; but this method is finally limited by diffraction and also entails an intensity loss. In order to reach the state-of-the-art spatial resolutions, that are below the Å, the electron microscope had to eliminate or reduce these aberrations (see Figure 2.7 (a)). The spherical aberration (C_3) is particularly relevant in the electron microscope since it is intrinsic to all round lenses (used to focus the electrons) due to their geometry, and it is always positive, as indicated by Scherrer in 1936. The use of non-round lenses, as the multipole lenses can produce a negative aberration. Aberration correctors use multipole lenses as quadrupoles, sextupoles and hexapoles, to produce a negative aberration on the incoming beam. By combining it conveniently with the spherical and the other aberrations of the round objective lens a net null aberration ($\chi \sim 0$) can be obtained. Since different aberration terms have different angular dependencies, net aberration cancellation will occur within an area around the optical axis.

Figure 2.7 (b) shows the Ronchigram of a corrected probe where the area free of aberrations (constant intensity) around the optical axis can be seen. A Ronchigram is the projection of the electron probe upon traversing the specimen out of focus as seen on a CCD detector or a screen. An aberration corrector uses an algorithm that measures the aberrations from images acquired at different values of defocus and calculates the aberration coefficients, passing them to the corrector.

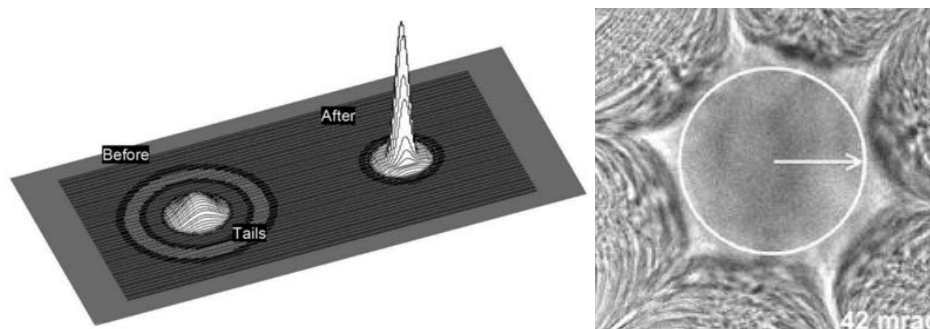


Figure 2.7: (a) *Uncorrected and corrected electron probes (adapted from ref.⁴⁹). Note how the intensity is greatly increased after correction due to the smaller spatial spread of the electrons.* (b) *Ronchigram showing the aberration free solid angle of an amorphous specimen (extracted and adapted from ref.⁵⁰).*

An electron microscope employed in characterization can be used both for imaging (real and reciprocal spaces) and spectroscopy. Upon traversing the specimen, the electrons can suffer different

scattering phenomena. Different signals and information can be obtained for electrons scattered at different angles, this being the reason for the ubiquitous use of annular detectors. Thus, there exist different imaging modes in STEM depending on the angle range covered by the detector. Detectors that collect electrons elastically scattered at low angles produce bright field images, while those subtending bigger angles than the angle range of the incoming electron beam are dark field imaging modes. Each of these detectors integrates all the electrons detected so they provide a single value for each probe position; although there exist segmented and pixelated detectors that can detect the distribution of scattered electrons on the detector used for other specific purposes (not used in this thesis). Basically, the bright field imaging modes are the Bright Field (BF) and the Annular Bright Field (ABF), and the dark field includes the medium angle annular dark field (MAADF) and high angle annular dark field (HAADF), see Figure 2.8 (a) and (b). Figure 2.8 (b) shows a sketch of the different detectors that subtend different angles with the incident beam direction. Each of these detectors provide a different and complementary kind of information. In addition, those electrons that suffer inelastic scattering upon traversing the specimen can also be collected and separated depending on their energy, which provides chemical information. This technique is known as Electron Energy Loss Spectroscopy (EELS). HAADF and ABF imaging modes and EELS have been routinely used during this thesis, and are introduced in the next.

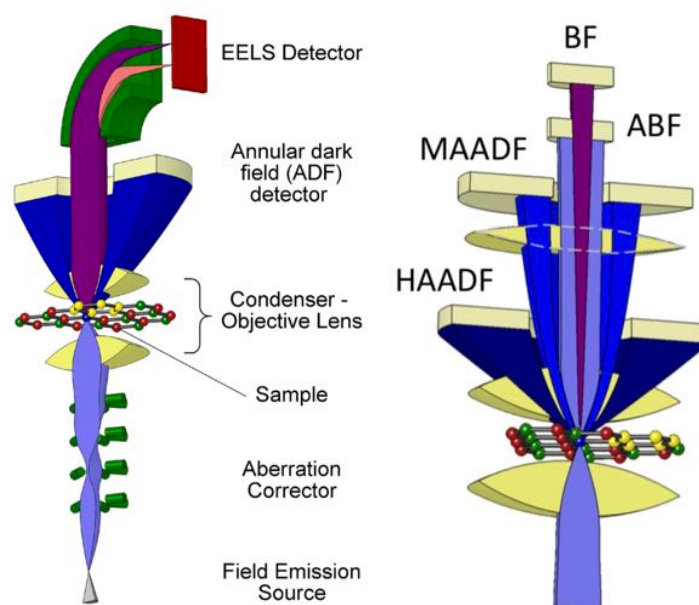


Figure 2.8: (a) simplified sketch showing the main components of an aberration corrected electron microscope. (b) different imaging modes with detectors subtending different angles with the TEM specimen. The sketches have been adapted from the Nion UltraSTEM User Manual.

2.5.2 Imaging in STEM

The HAADF image is formed by collecting electrons scattered by the specimen at high angles (100 to 200 mrad). Rutherford scattering with the nucleus is the main physical mechanism involved,

so electrons passing closer to the atomic nucleus will have a bigger probability of scattering. This occurs when the probe is centered onto an atomic column. This type of scattering can be considered to be mainly non-coherent, so it can be thought as the convolution of the electron probe intensity with the specimen intensity as follows: $I = |\varphi(\mathbf{R})|^2 \otimes |P(\mathbf{R})|^2$, where \mathbf{R} is the position on the specimen, and $\varphi(\mathbf{R})$ and $P(\mathbf{R})$ are the complex waves representing the specimen and the electron probe focused onto the specimen. This non-coherent character makes HAADF images straightforward to interpret, with bright spots representing the atomic columns on the darker background, Figure 2.9 (a). Moreover, the probability of being scattered by the nucleus by Rutherford scattering scales approximately with the square of the nucleus atomic number Z , thus as Z^2 . This is the case of an isolated element, but in a crystal, other aspects can influence the final intensity. During the transmission of the electron beam throughout a crystal of finite thickness, the beam interacts with the sample and the distribution of electrons is modified, with channeling and dechanneling processes playing an important role. Channeling occurs when the atomic columns attract the electrons close to them, while dechanneling refers to the processes by which electrons are scattered away from an atomic column, electrons that can end channeling along another nearby column. This propagation inside the crystal is complex and depends on the crystallographic direction, and makes that although heavier elements appear brighter, other factors can influence the intensity along an atomic column. Besides, the Z^2 dependence makes challenging to observe light elements such as oxygen, due to their weak atomic scattering. This generally translates into the impossibility to observe the oxygen sublattice, which can be much lighter than the cation elements to which it is bonded. Figure 2.9 (a) shows a HAADF image of a BaTiO_3 film imaged along the $[100]$ zone axis, where only Ba and Ti are visible.

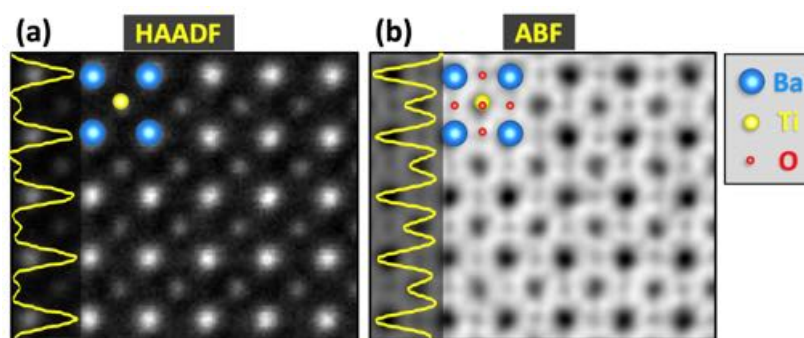


Figure 2.9: (a) and (b) show simultaneously acquired HAADF and ABF images of a BaTiO_3 film imaged along the $[100]$ zone axis. The BaTiO_3 unit-cell containing only cations (Ba and Ti) and all elements are superimposed on the HAADF and ABF, respectively. The intensity profiles of each imaging mode are superimposed at the left of the images.

ABF imaging mode is used to observe all the sublattices, including the oxygen one, Figure 2.9 (b). In ABF an annular detector is also used, although the images are recorded using an annular detector

in the outer area of the so-called bright-field region. The image is formed by collecting the electron scattered to angles in the range approximately from 10 to 20 mrad. The intensity contrast arises from interferences produced by the phase differences between the unscattered and the scattered beam. Thus, the intensity of ABF can be approximately expressed as the intensity of a coherent image: $I = |\varphi(\mathbf{R}) \otimes P(\mathbf{R})|^2$. Unlike the non-coherent case, the convolution is not between intensities (squared waves) but amplitudes (complex waves). In general, in absence of aberrations, the atomic columns produce such a phase shift in the scattered beam that they are seen as dark spots on a white background (representing the empty space between columns), so the contrast is inverted with respect to the HAADF imaging mode, see Figure 2.9 (b). Yet, the phase change can pass from destructive to constructive and viceversa by increasing the thickness, introducing aberrations, specimen tilt and other factors. This makes the interpretation of ABF less robust than HAADF, which makes comparison with a simulation advisable. Nonetheless, in most cases the simultaneous acquisition of HAADF to the ABF signal serves as a guide to verify what represents the contrast of the ABF image.

Nowadays with the improvement in computational and electronics performance, much more information can be acquired simultaneously by recording the full diffraction pattern, a technique known as 4D STEM, which not only contains all the information to reconstruct the different imaging modes as ABF or HAADF, but provides additional information.⁵¹

2.5.3 Electron Energy Loss Spectroscopy

Apart from imaging, EELS has also been widely used for the characterization of materials. EELS can be acquired simultaneously to imaging signals as the HAADF, as one can substitute the BF detector by the ELL spectrometer. The spectra obtained in EELS show the energetic distributions of the initially monochromatic electrons that undergo inelastic scattering after interacting with the specimen. Due to the energy conservation, the energy lost by each of the electrons reveals the energy transferred to the specimen, providing chemical information with the spatial resolution provided by the STEM microscope. In order to obtain the EEL spectrum, the electrons are collected after the specimen and dispersed in energy by a magnetic spectrometer, and later projected onto a detector, as sketched in Figure 2.10 (a). For each position of the probe, a spectrum is collected, which yields a multidimensional data set known as spectrum image, sketched in Figure 2.10 (b). The EEL spectrum has three distinctive regions: the zero-loss peak (unscattered or elastically scattered electrons), the low loss and the core loss. The low loss region (few eV) covers the energy range of plasmons or bandgap excitations. The core-loss includes transitions from the highly bounded electrons to empty states above the Fermi level of the material, which are typically separated by several hundreds of eV. Figure 2.10 (c) shows an EEL spectrum of the core-loss region with the La M-edge acquired in a $\text{La}_{0.7}\text{Sr}_{0.3}\text{MnO}_3$ layer deposited on a SrTiO_3 substrate.

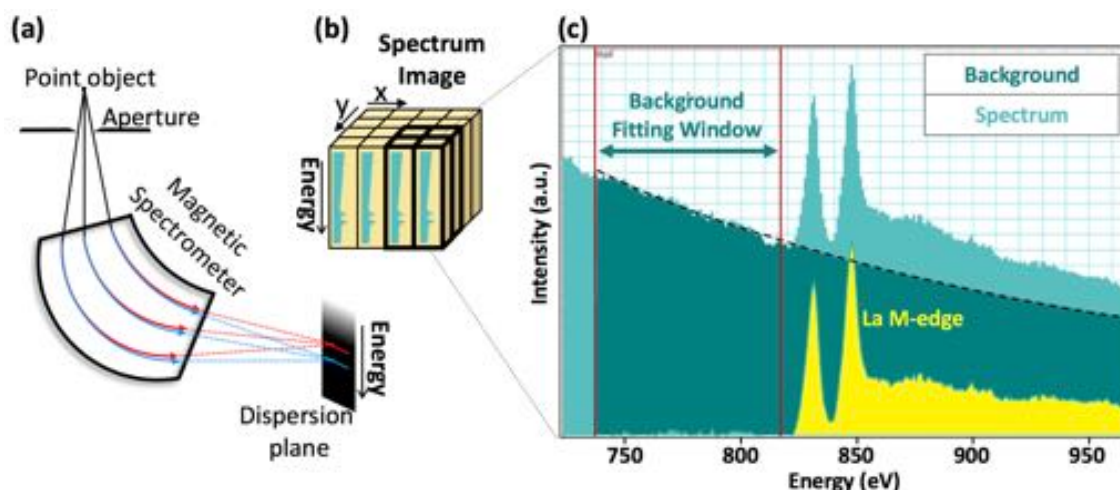


Figure 2.10: (a) Sketch of the energy dispersion in EELS, in which a point object produces lines separated in energy after traversing the magnetic spectrometer. The blue and red colored lines represent the paths followed by more and less energetic electrons, respectively. (b) The obtained multidimensional signal contains one spectrum (intensity vs energy) for each pixel of the spectrum image (corresponding to each position of the probe in the x-y plane). (c) One spectrum obtained after integrating the four spectra of the bold region in (b) is shown. The spectrum, obtained from a $\text{La}_{0.7}\text{Sr}_{0.3}\text{MnO}_3$ film, contains the La M-edge on the typical EELS background. The background is fitted in a window just before the La M-edge and extrapolated to bigger energies (dashed black line); then the background is subtracted from the spectrum, obtaining the La M-edge (shown in yellow).

In EELS, the multiple scattering processes that an electron can undergo produce a characteristic background that decays in intensity for increasing energies. The probability of undergoing multiple scattering, and therefore the background, increase with the specimen thickness, so thin specimens are desirable. In practice, background subtraction is required, which is achieved by fitting the background with a power law dependence. Figure 2.10 (c) shows the fitting of the background in a window before the La M-edge absorption edge and its extrapolation under the absorption edge, allowing subtraction.

Mainly two kind of analyses have been carried out with EELS in this thesis: the elemental mapping, and the study of the electronic fine structure. An elemental map is obtained by integrating, for each pixel, an available absorption edge of the corresponding element in a suitable energy range. This process will yield a single value per pixel, generating the elemental map. The fine structure requires studying the profile of the absorption edge in detail and with, normally, higher energy resolution (normally below 1 eV). In this way information as the type of bonding or the oxidation state of an element can be inferred. Moreover, STEM-EELS provides local information, which translates in the possibility to track changes of the fine structure of the absorption edge as the position is changed.

The EEL spectra are affected by noise, which affect the signal. The used tool to reduce the noise contribution known as Principal Component Analysis (PCA),⁵² which has been applied before the analysis of the EEL spectra.

2.5.4 STEM-Specimen Preparation

Electrons highly interact with matter; therefore, STEM specimens have to be thin enough to be electron-transparent. Conventional TEM-specimen preparation is a technique that destroys the samples and involves mechanical polishing followed by ion milling. The TEM observation occurs along a specific zone axis (or crystallographic axis) that should be chosen according to the experiment needs. In this thesis the observation was done always in cross-section mode, that gives access to one in-plane and the out-of-plane directions. The specimens were thinned down along either the [100] or [110] pseudocubic substrate zone axes, which, given the epitaxial relationships, allowed to access the convenient zone axes of the films.

The preparation procedure is as follows: the sample is cut in two equal pieces with a wire saw, and the pieces are glued together face-to-face forming a sandwich (Figure 2.11). The sandwich is cut in slices (normally around 200-300 μm thick), each of which is a potential TEM specimen; and are then stuck on a holder and thinned down to around 20 μm (or less if possible). A metallic grid (normally made of copper or molybdenum) is glued on the sample and an ion milling (using Precision Ion Polishing System from Gatan or Fischione Ion Milling equipments) is used to further thin the sample until a small hole is visible at the interest area. The ion polishing ensures smooth thickness gradients, so some areas around the hole edge will be electron-transparent. Occasionally, an alternative TEM-specimen preparation technique known as focused ion beam was also used.

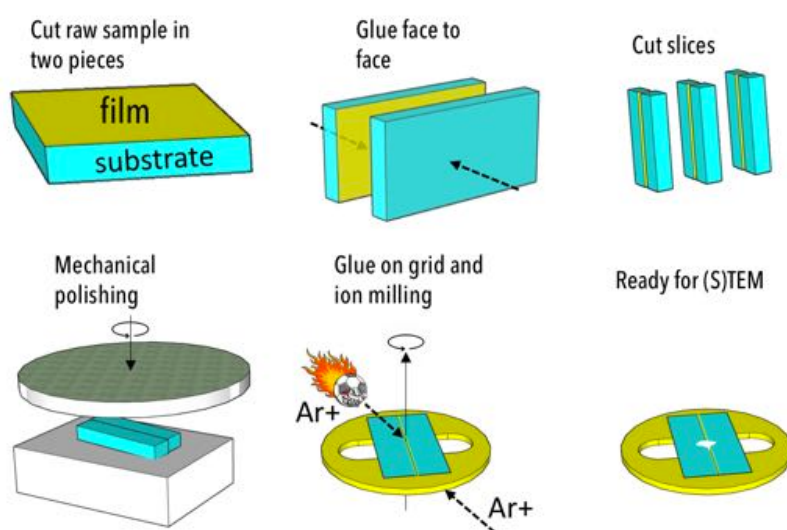


Figure 2.11: Sketch of the TEM cross-section specimen preparation process with relevant steps shown.

2.6 Computational Methods Based on Python

Python programming language was used for data analysis. The biggest effort was dedicated to program a software capable of computing and mapping, from STEM images with atomic resolution, ip and oop lattice parameters, different spacings, angles and structural distortions such as the ferroelectric distortion, thus being able to map ferroelectricity with unit-cell resolution. The basics of this software are presented in the following.

Determining Sublattices Positions from STEM images

The first step consists in finding the approximate location of intensity maxima (using Scipy library⁵³), which represent the projected atomic columns in HAADF, for instance. For a perovskite observed along [100] in HAADF mode, A and B sublattices are observed, as shown in Figure 2.12 (a). Under the condition of a minimum distance between local maxima (slightly smaller than the lattice parameters), only one maximum of intensity is detected per atomic column and only maxima corresponding to the heaviest sublattice are selected, yielding an array with the positions in the observation plane of each column of the A sublattice (see Figure 2.12 (b) and 2.12 (d)). Secondly, these initial positions are used to find more accurate positions of the atomic columns. To achieve that, each position is refined by iterative center of mass (COM) and 2D-Gaussian fitting (Figure 2.12 (c)). COM works by selecting those pixels inside a circular region centered at the non-refined positions (Figure 2.12 (c)) and performing:

$$r_{COM} = \frac{\sum_{i,j}^n I_{i,j} \cdot (i,j)}{\sum_{i,j}^n I_{i,j}}$$

, where i and j are the coordinates of each pixel inside the selected region, and $I_{i,j}$ is the intensity of the pixel i,j . Thus, COM is an average with the intensity at each pixel $I_{i,j}$ as weight. For the refinement of the A-sublattice positions by 2D-Gaussian fitting, the fitting module of the Atomap library⁵⁴ was employed, obtaining the final A-sublattice positions r_A . The position of the B-sublattice is found by first finding the center of the unit-cell r_X , which is defined as the position where the two diagonals connecting A columns at opposite corners meet (Figure 2.12 (f)), and is the location of the B column if the cell were non-polar. Another option to determine the center of the unit-cell (r_X) is to consider the average position of the 4 Ba columns, option that was also tried and yielded an almost indistinguishable output. This position r_X is then refined by COM and 2D-Gaussian fitting, converging into the actual B sublattice position r_B (in yellow, Figure 2.12 (e)). In the case of an ABF image, the O-sublattice can be found similarly to the B-sublattice by finding the center between vertically and horizontally connected A columns and converging to the actual position. All these positions can

ultimately be used to measure the ip and oop lattice parameters, or the ferroelectric distortion with a unit cell spatial resolution, for instance.

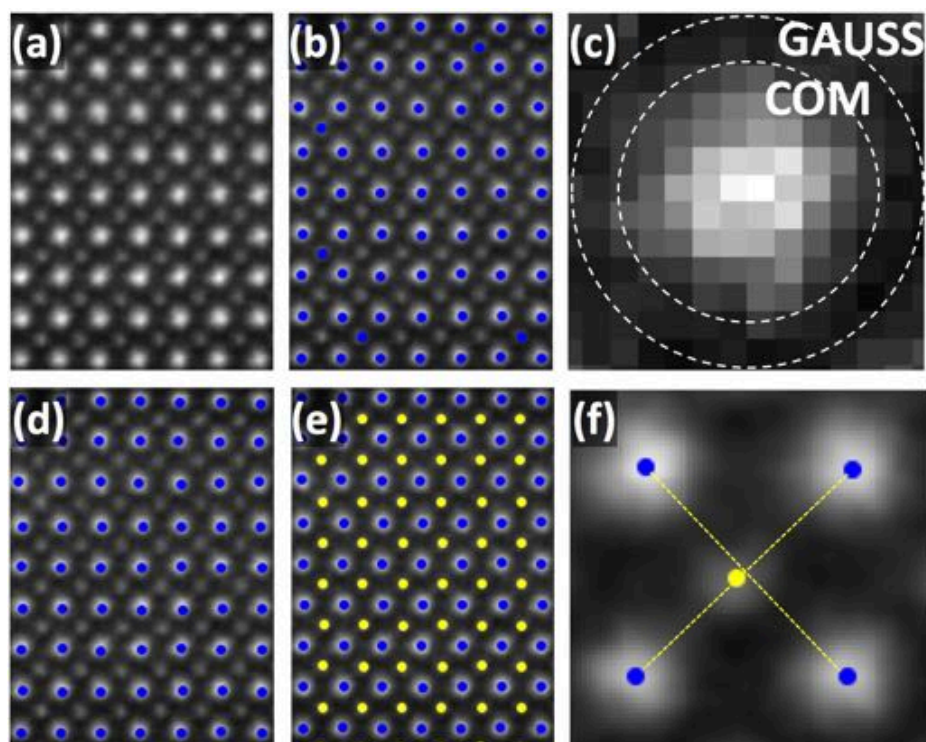


Figure 2.12: (a) HAADF image along the perovskite $[100]$ zone axis of a BaTiO_3 layer in the $\text{BaTiO}_3/\text{SrTiO}_3$ superlattice with 10 unit-cell thick layers (see Chapter 3). (b) Atomic column positions in blue contain the A-sublattice and positions of atomic columns not corresponding to the A-sublattice due to inadequate input conditions. (c) COM and 2D-Gaussian areas are sketched. (d) Correctly identified A-sublattice positions in blue. (e) A and B sublattices in blue and yellow. (f) Method to find the center of the unit-cell r_x and the B column position is depicted.

Dipole Maps

In order to determine the polarization configuration, it would be necessary to know the whole distribution of charge within each unit-cell. In perovskites with ionic bonding, the polarization can be approximately calculated from the locations of the ions and using the Born effective charge of each ion, which includes both the ion charge and the effect of its electron cloud. Even more, observation of the two cation sublattices may suffice to infer the polarization since a certain displacement of the B-sublattice with respect to the A-sublattice will correspond to a specific displacement of the O-sublattice.⁵⁵ This turns out to be useful in STEM, where it is challenging to observe the oxygen sublattice simultaneously to heavier elements by HAADF. In the case of $\text{BaTiO}_3/\text{SrTiO}_3$ superlattices, studied in Chapter 3, the polarization direction and magnitude in BaTiO_3 and SrTiO_3 can be inferred from Ti and Ba sublattices. More specifically, the polar distortion associated to the relative

displacement of Ti with respect to Ba (δ_{Ti}) can be calculated as the vector connecting the center of the unit-cell r_X as delimited by the Ba columns and the measured Ti position r_B (Figure 2.13 (b)).

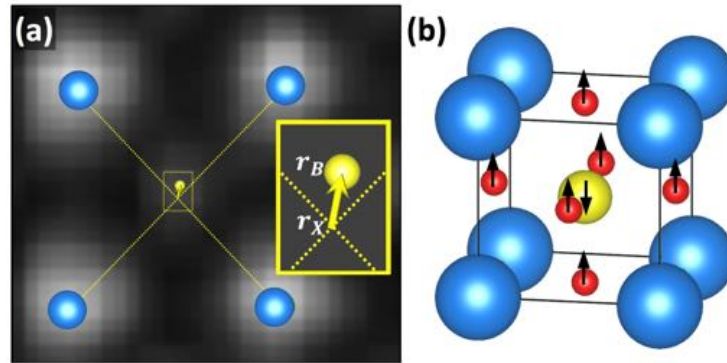


Figure 2.13: (a) Sketch of dipole associated to the Ti shift from the center of the unit-cell. (b) Distortion mode with Ti and O moving in opposite directions with respect to Ba.

The BTO Ti displacement δ_{Ti} associated to the ferroelectric distortion is expected to be around 9 pm in bulk, so higher sensitivity is needed; although the magnitude of the dipoles may be locally bigger due to the structural strain and other factors. The correct mapping of polarization in BaTiO_3 could be challenging compared to other displacive complex oxides ferroelectrics, like PTO, where the ions relative displacements are bigger. Under optimal image acquisition conditions, the resolution of the Nion UltraSTEM 200 is better than 1 Å (< 100 pm), which allows to determine the center of atomic columns with precision in the order of a few picometers by the methods presented above. The accuracy in measuring δ_{Ti} was determined to be around 4 pm, smaller than the pixel size in many images. Displacements of this magnitude and above (maybe up to 20 pm) are indeed difficult or not noticeable by eye in the images.

The fact that polarization in BTO is similar to that of PTO while the ion shifts are smaller in the system of reference of the A cation may be related to the different ferroelectric distortion modes present in these materials, with B and O sublattices moving in the same direction with respect to A sublattice in the case of PbTiO_3 , and Ti and O sublattices expectedly moving in opposite directions in BTO,⁵⁵ as sketched in Figure 2.13 (b). Other polar and non-polar distortion modes can be found in perovskites.^{56,57}

As mentioned before, the ionic bonding in perovskites allows the electric polarization to be calculated according to the ion displacements δ_n from the positions of the parent higher symmetry non-polar structure, as follows:

$$P = \frac{e}{V_{Cell}} \sum_n^N Z_n^* \cdot \delta_n = \frac{e}{V_{Cell}} \left(+ \sum_{n,Z>0}^N |Z_n^*| \cdot \delta_n - \sum_{n,Z<0}^N |Z_n^*| \cdot \delta_n \right)$$

, where Z_n^* is the Born effective charge of each ion, (which includes the effect of the displacement electron cloud of the ions and non-pure ionic bonding). The right side of the equation separates summation over negative charges and over positive ones. In the case of PTO, Ti and O terms will have different signs, given that they move in the same direction but have opposite electric charge. On the other hand, Ti and O shift in the same direction in BTO, and thus both contribute with the same sign. This can explain why for polarizations that are similar, the ion shifts are smaller in BTO as seen in the system of reference of the A cation.

In order to confirm the ferroelectric distortion mode in the BTO/STO SPLs, Annular Bright Field Imaging (ABF) was employed to image simultaneously the A, B and O sublattices. This imaging mode is less robust since it is a phase contrast and is more prone to show non-intrinsic distortions when there is presence of a residual off-tilt.^{58,59} These reasons led us to use mainly HAADF to image the polarization configurations. Figure 2.14 shows a representative area where Ti and O displacements are mapped across a BTO layer of a BTO/STO SPL, see Chapter 3. The oxygen displacement occurs in the opposite direction to Ti, as expected in BTO, while the same kind of distortion is generated inside the STO layers. Moreover, a smaller displacement for equatorial than for apical oxygens is seen, also expected in BTO. From this, it is noticeable that Ti and apical O have a similar displacement in BTO (25-30 pm). However, they do not exactly follow the same decreasing trend at the BTO/STO interfaces: at the bottom of the shown image, Ti displacements decrease faster than O displacements

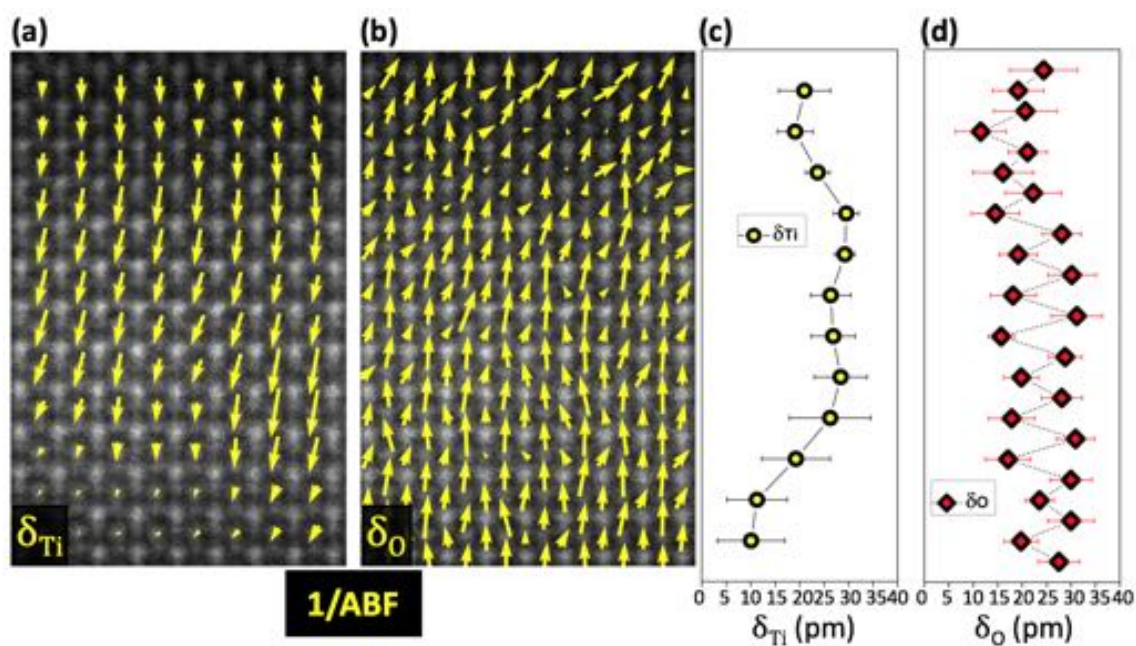


Figure 2.14: (a) and (b) show δ_{Ti} and δ_O superimposed on the contrast inverted ABF image of a BTO/STO superlattice. (c) and (d) show the corresponding oop profiles obtained by averaging the displacement values along each row.

do. A big variability in the relative displacements of Ti and O is observed in different areas, but their displacements are observed to occur in opposite direction in all the images explored.

Dipole Filter

In some cases, the δ_{Ti} dipoles seemed to have rather random orientations (see Figure 2.15 (a)), which was attributed to the fact that these dipoles were strongly affected by noise. A dipole filter was employed to decrease the noise effect, revealing the underlying polarization configuration (see Figure 2.15 (b)). The effect of the filtering is very noticeable in the resultant map, which shows that the dipoles are indeed not randomly distributed, but clearly have different preferential orientation in different areas, and that the orientation of dipoles smoothly varies as one moves across the dipole map. The justification for the use of this filter is provided in the following.

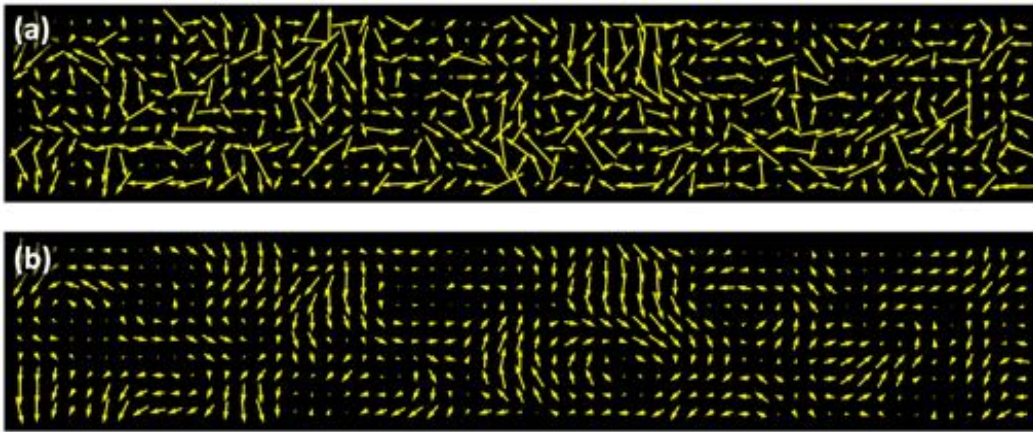


Figure 2.15: (a) Raw dipole map shows dipoles what seems to be a random distribution of the angle of the dipoles. (b) same map that is shown in (a) after filtering.

A measured dipole δ_{Ti} can be thought to have two contributions, one intrinsic and one coming from different noise sources, expressed as follows: $\vec{\delta}_{Ti} = \vec{\delta}_{Ti-Intrinsic} + \vec{\delta}_{Ti-Noise}$. The intrinsic contribution ($\delta_{Ti-Intrinsic}$) can decrease in some areas because the polar distortion/displacement on the STEM observation plane becomes smaller, but in these areas the amount of noise ($\delta_{Ti-Noise}$) will remain similar, producing a reduced signal/noise or $\delta_{Ti-Intrinsic}/\delta_{Ti-Noise}$ ratio that will increasingly mask the real Ti displacement ($\delta_{Ti-Intrinsic}$) as the modulus of $\delta_{Ti-Intrinsic}$ decreases. Starting from this point, the idea behind the filter is to take some neighbor dipoles and average them so that the random contribution of noise is averaged out. The noise component $\delta_{Ti-Noise}$ is expected to be mainly composed of random noise. If the dipole distribution is purely random the filter will dampen the dipoles; however, if the direction distribution is biased, the filter will dampen the random components ($\delta_{Ti-Noise}$) and keep the main direction. Of course, this occurs at the expense of averaging signals located at different locations, which can promote an artificial smoothness and decrease the spatial resolution. Thus, the best approach

is to find a good balance in the strength of the averaging in order to maximize the signal to noise/ratio; if the filter is too strong because the mask is too large and gives too much weight to the neighboring dipoles, it will not only average out noise ($\delta_{Ti\text{-Noise}}$) but also signal ($\delta_{Ti\text{-Intrinsic}}$) in a big amount. On the other hand, if the filter uses a mask that is too small, most of the signal will be kept but the same will happen to the noise. Then, to maximize the signal/noise ratio in the output dipole map, the size of the mask was limited by including only the eight first neighbors and the central dipole, and by properly adjusting the weight given to each dipole depending on its distance to the center of the mask. For a given position in the dipole map, the filtered dipole is calculated as follows:

$$\vec{\delta}_{Ti\text{filtered}} = \sum_i^9 w_i \cdot \vec{\delta}_{Ti}$$

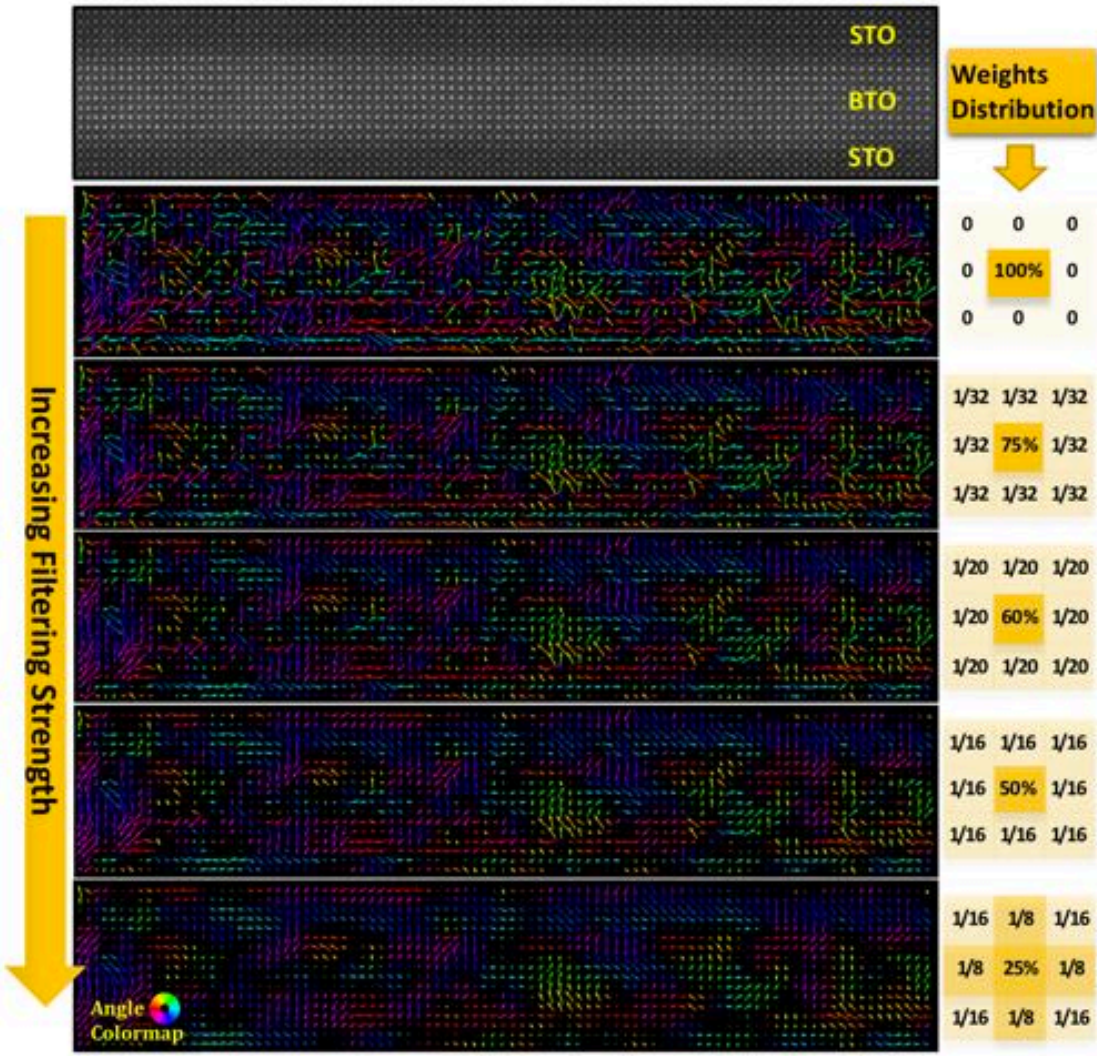


Figure 2.16: Series of dipole maps filtered with a different distribution of weights within the mask. The weights go from zero filtering strength (raw image) up to the largest filtering strength (the one used in Chapter 3). The series of increasing filtering strength highlights, helped by the employed dipole angle color map, that the dipole directions present in the raw dipole map are kept during the filtering process.

, where w_i is the weight given to each of the nine dipoles inside the mask. In Figure 2.16, the dipole map filtering process is sketched. It is shown a raw dipole map together with dipole maps filtered with a mask with different weights, going from softer to stronger filtering. Here, the dipoles are colored according to an angle-color map, which reflects the directions of the dipoles. This example is useful to realize that the dipole directions in filtered and raw images are basically the same, and to make sure the filtering is not introducing artefacts. The central dipole is given 25% of the weight of the output dipole (bigger than the one given to each of the other dipoles). The last set of weights was used in the calculation of the dipole maps in 10-SPL in Chapter 3.

The Role of the Specimen Thickness and the Depth of Field

Cross sectional TEM samples at the observation area are some nanometers thick along the observation direction (along with the beam direction), and typically show a negative thickness gradient along the sample growth direction. This gradient could favor different polarization configurations for thicker and thinner regions, since boundary conditions are modified. However, thickness changes are smooth and small in the inspected areas. The STEM specimens' thickness was measured with EELS, and it was kept in the 0.2–0.3 inelastic mean free path (25–30 nm) range. Moreover, the local variations in the dipole configuration of the different SPLs presented in Chapter 3 do not correlate with the thickness.

Besides, the thickness can also be relevant when it comes to our ability to observe the dipole configuration. The vector δ_{Ti} at one position is the resulting projection of several unit-cells along the beam direction, which can produce a decrease of the imaged δ_{Ti} if Ti displacements in different directions are present in the projected unit-cells (as probably occurs in the area with polarization rotations of 10-SPL). This effect can be slightly stronger for thicker TEM specimens, but even if the TEM specimen is thick, the limited depth of field of the aberration corrected electron beam (which is cone-like) ensures that a limited amount of unit-cells significantly contribute to the signal. With the illumination conditions used in our work (semi-angle of 30 mrad at 200 kV) the expected depth of field is 5.5 nm,⁶⁰ that is, mainly the 5.5 nm (around 14 unit-cells) around the focal point can be considered to remain in focus and contribute to the signal (Figure 2.17), while the rest of the specimen thickness will mainly contribute as background. This is only slightly more than the lateral size of the observed rotations in the BTO layers of 10-SPL. Therefore, the changes in the thickness are not expected to importantly impact the imaging of the polar domains. Since the depth of field is slightly bigger than the size of the domains observed in Chapter 3, a certain degree of overlapping between different domains along the zone axis could occur, however this is a minor effect in many of the observed areas. On the other hand, the directions of the projected dipoles within the depth of field,

which can depend on the relative orientation of the domains with respect to the projection direction, can be more relevant and can produce an averaging effect.

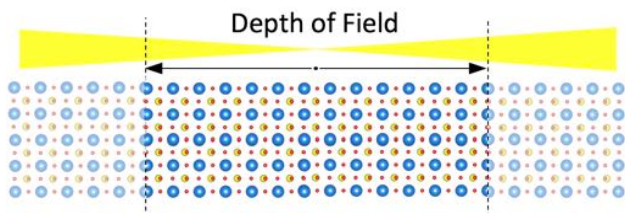


Figure 2.17: Depth of field accounts for the region around the focal point that can be considered in focus. Regions outside the depth of field region will mainly contribute as background.

Dipole Maps taking Ti columns as system of reference

A dipole map was also calculated taking the Ti sublattice as the system of reference ($\delta_{Ti}=0$) and measuring the relative Ba displacements (δ_{Ba}). Equivalent topologies are obtained, as can be seen in Figure 2.18. Notice that in this case, the Ba displacements point in opposite direction to the polarization.

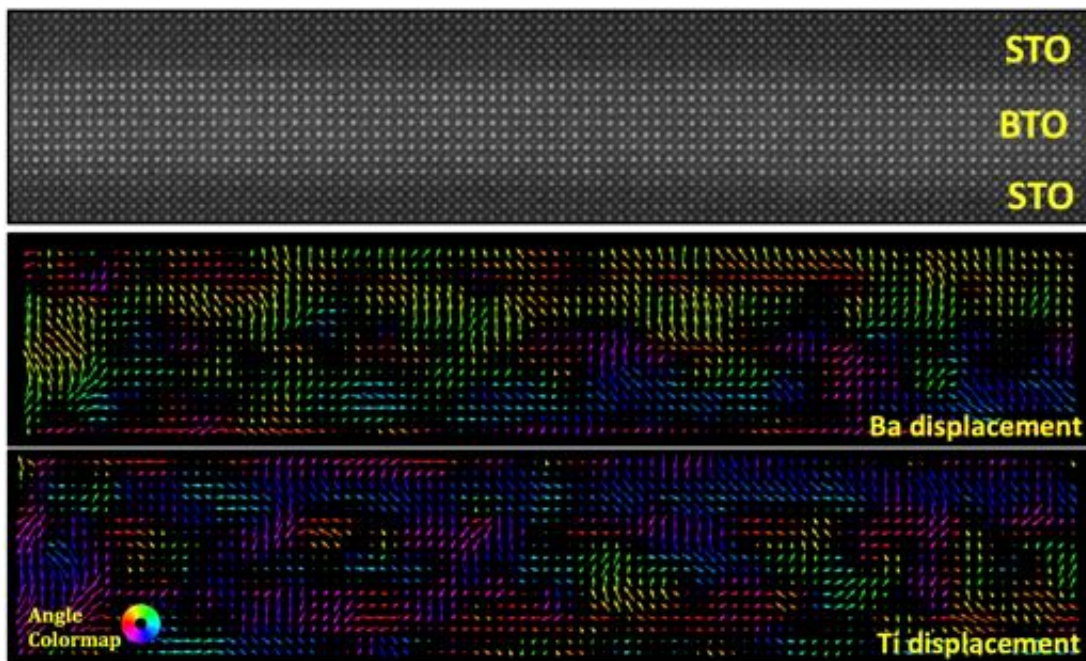


Figure 2.18. Dipole map for Ba displacement with respect to Ti sublattice (top map), and Ti with respect to Ba sublattice (bottom map). Similar nanotopologies are found in both maps. Arrows in the Ba displacement map point towards the barium from the center of four nearest Ti columns and therefore point in opposite direction to the polarization.

Distortion Correction: Flyback

The scanning acquisition mode can suffer from a distortion known as flyback, originated by a non-constant speed in the beam scanning, that squeezed the ratio of ip and oop distances. This distortion occurs along the scanning direction (corresponding to the ip direction in our

images) and does not affect the perpendicular direction. The distortion is stronger at the beginning of the scanning (left part of the images) and is reduced as the scan advances, disappearing towards the center or right areas of the image (Figure 2.19 (a)). Savitzky-Golay algorithm was used to interpolate between pixels along the ip direction and resize the images to correct this distortion (Figure 2.19 (b)). After flyback correction, changes in the dipole maps could barely be appreciated, even in those areas with stronger distortion (Figure 2.19 (c) and (d)), so this distortion is not something relevant for the correct calculation of the dipoles maps. This correction has been used to correct some images presented in Chapter 3. The right parts of the images were seen to be free of the flyback distortion, which could be checked by comparison with the STO substrate, which is and should appear cubic.

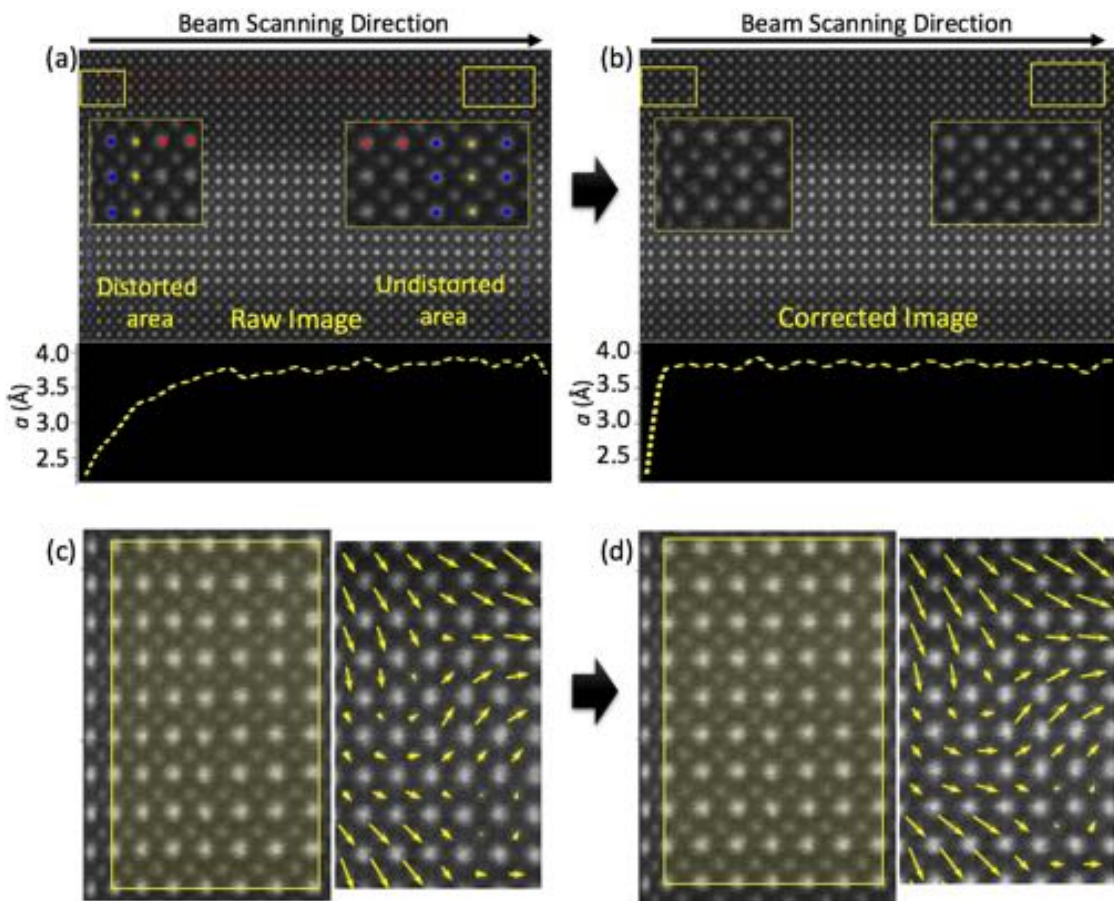


Figure 2.19: Raw (a) and corrected images (b) and the measured ip lattice parameter a profile (bottom panel) as a function of the lateral position. The atomic columns marked in blue and green were used to measure the a lattice parameter in the area to be corrected and reference (right) areas of the image, correcting a vertical slice at a time. Red columns mark the next areas to be corrected from flyback. Dipole maps extracted from an area suffering from flyback (c) and the map extracted from the same corrected area (d) show minor differences.

2.7 Other Computational Resources

Other computational resources were regularly used. The most relevant are briefly commented in the following.

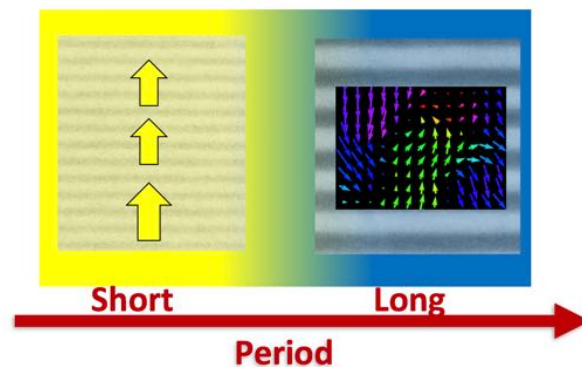
Digital Micrograph is the software used to acquire and analyze STEM images, and was used for visualization and analysis of the images.

Vesta⁶¹ is a free software for the visualization and analysis of molecules' and crystals' structures in 3D. A unit-cell can be created by introducing the symmetries and locations of each element, or, alternatively, the structure can be downloaded and directly opened with the software. In this thesis, it was mainly used to visualize the $\text{Hf}_{0.5}\text{Zr}_{0.5}\text{O}_2$ (chapters 4 and 5) structure, allowing to observe different crystallographic planes and zone axis. It was useful to compare the structural models with the STEM images, allowing to identify different phases and epitaxial orientations.

OriginPro was used for plotting data such as x-ray spectra, as well as for basic data analysis as model fitting to experimental data.

Chapter 3: Rotational Polarization Nanotopologies in BaTiO₃/SrTiO₃ Superlattices

In ferroelectrics, interfaces break the continuity of the polar crystal creating depolarizing fields, and can also induce lattice strain, which can bear tremendous effects in the ferroelectric state. In the last decade, exotic polar configurations have been revealed in ferroelectric superlattices and related nanostructures by using Scanning Transmission Electron Microscopy, envisaging new possibilities in ferroelectrics. Following this emergent research line, this chapter explores the effect of periodic interfaces as a mean to control the balance of elastic and electrostatic energies and tuning the polar configuration in BaTiO₃/SrTiO₃ superlattices grown on SrTiO₃(001). It will be shown that the superlattice period plays a critical role in the polar configuration that gets stabilized, evolving from an out-of-plane oriented polarization that is continuous across the ferroelectric and paraelectric layers in short period superlattices with 2 and 4 unit-cells thick layers, to the emergence of rotational topologies only in the ferroelectric in the longest period superlattice, with 10 unit-cell thick layers. The formation of such polar textures goes beyond what is generally expected to occur in a nominally tetragonal polar crystal whose tetragonal axis is fixed along the growth direction by the epitaxy on the SrTiO₃ substrate.



3.1 Introduction

Superlattices (SPLs) are a kind of artificial materials that combine two or more materials by stacking them periodically. The simplest and commonly used superlattice architecture consists of a stack of planar layers of A and B materials with similar structure, but more materials and more complex designs can be used. In general, the combination of materials in a superlattice can produce the coupling between the phenomena occurring in each material,⁶² as well as leading to properties not present neither in the parent compounds nor in the corresponding solid solutions.^{63,64} Some non-local properties, related to the formation of bandgaps, can arise from the superlattice periodicity too. For instance, in electronic or photonic devices based on semiconductors, control over the superlattice period is commonly employed as a mean to engineering from electronic to photonic properties as light propagation and emission/absorption processes,⁶⁵ or phononic properties as heat conductance.⁶⁶ Moreover, processes localized at the interfaces can also be very relevant, since the translational symmetry of the crystal is broken, modifying the mechanical, electric and chemical boundary conditions.⁶⁵ As an example, 2D conductance was found to emerge at the LaAlO₃/SrTiO₃ interface, which both are dielectric materials.⁶⁷ The fact that the physical properties of superlattices can be dominated by the interfaces makes of them a versatile system to engineer the physical properties of materials. In short, superlattices are one great example of artificial materials with a simple architecture that are successfully used in many branches of materials science and engineering, and ferroelectrics would not be less.

Ferroelectric superlattices, normally based on perovskites, have proven to be a promising method to manipulate ferroelectric and related properties, such as tuning of the dielectric constant or increasing the Curie temperature.^{56,68} Interestingly, in the last years, the advances leading to higher quality and more precise crystal synthesis methods have come together with advances in aberration corrected Scanning Transmission Electron Microscopy (STEM). This has permitted the direct observation of exotic polarization configurations in ferroelectric superlattices and other nanoscale heterostructures that would otherwise have been much more challenging to observe by other means. Unlike ferromagnetic domains, ferroelectric domains can be as small as a few nanometers, so observation of the smallest ferroelectric domains requires high spatial resolution techniques as STEM. Indeed, in 2016, nanosized vortices were observed in a PbTiO₃/SrTiO₃ (PTO/STO) SPL.⁶⁹ These vortices formed an ordered array configuration in which, as posterior studies indicated, the balance of competing energies was crucial.⁷⁰ Meanwhile, BaTiO₃/SrTiO₃ (BTO/STO) SPLs have been largely studied, given that BTO is a paradigmatic ferroelectric. This fact contrasts with the scarcity of STEM works on BTO SPLs, and more specifically BTO/STO SPLs. Some STEM experimental works have studied the polarization configuration of BTO heterostructures as epitaxial films,^{26,71–73} or BTO nanoparticles by using other experimental techniques;⁷⁴ but to the best of our knowledge, no works

have carried out unit-cell polarization mapping in BTO/STO SPLs, so it is unknown whether similar results to those found in PTO SPLs can occur.

Ferroelectric/paraelectric SPLs were originally studied as a mean to enhance the ferroelectric properties of the ferroelectric above those of the bulk compound.⁷⁵ A greater spontaneous polarization and dielectric constant were predicted in BTO/STO SPLs,⁷⁵ and experimentally demonstrated afterwards.⁷⁶ This potential polarization enhancement is determined in part by the electric coupling between the layers of the ferroelectric BTO and the paraelectric STO,^{31,75} that can induce a polarization in the STO; and in part due to the epitaxial strain exerted by the substrate and the layers that compose the SPL. BTO/STO SPLs have been commonly grown on STO(001), which fixes the polar axis along the out-of-plane (oop) direction and can increase the local polar distortions polarization, and hence the macroscopic polarization.

BTO tetragonal structure ($a=3.994$, $c=4.038$ Å) has a lattice mismatch with cubic STO ($a=3.905$ Å) of around -2.3%, allowing compressive epitaxial growth on a STO (001) substrate. In such a case, a and b axes of BTO will lay in the plane (given the lower lattice mismatch), while c will be oriented along the growth direction. In this way, the epitaxy not only can achieve a c oriented BTO but also an increased tetragonality and ferroelectricity, due to the fact that BTO tends to keep its unit-cell volume. The intercalation of STO layers in the BTO/STO superlattice can maintain the strained state avoiding plastic relaxation. However, when STO layers are inserted forming the BTO/STO SPL, another very relevant effect enters the arena. The dissimilarity in polar character of BTO and STO, with BTO being polar and STO non-polar, brings about the appearance of electric fields if the materials are considered in their bulk states. In order to diminish the energy associated to these electric fields, the system can adopt different polarization configurations (see Chapter 1), the most basic being the following:

- Constant polarization across BTO and STO layers.
- Up and down domains inside BTO and zero polarization in STO.

In a superlattice combining ferroelectrics and paraelectrics, the ground state or polarization domain configuration that minimizes the total energy is greatly influenced by the thickness of the layers, the polarization mismatch and the dielectric constants of the two materials. In very short period BTO/STO SPLs, of a few unit-cells, a strong electric coupling leading to a constant polarization bigger than that of BTO bulk is predicted for fractions of BTO over STO above 40% and an enhanced polarization than that of the bulk for bigger fractions of BTO.⁷⁵ Big dielectric constants, or highly polarizable materials, will favor the state of constant polarization. A decreasing interlayer coupling is predicted as the period or thickness of the layers is increased in a ferroelectric/paraelectric SPL,⁷⁷ which can trigger the formation of up and down domains.³¹ Beyond the role of energies, it is fair to mention that the chronology of events can play a relevant role in the configuration that finally gets

stabilized, by placing a kinetic barrier (metastability) between a local minimum and a lower energy minimum. Indeed, some studies^{78,79} have shown that, if the material is ferroelectric at the growth temperature, the depolarizing fields present during the growth may drive the polarization into a multidomain state that remains even after screening charges have become available at the end of the process. Apart from the simple and aprioristic configurations considered above, at the nanoscale, the delicate balance of energies together with different degrees of freedom that allow different unit-cell symmetries and lattice parameters, polarization orientation or different polar and non-polar distortion modes, can lead to more complex polarization configurations. This has been experimentally and theoretically revealed in the last years, both in PTO SPLs and other ferroelectric nanoscale heterostructures.⁸⁰

In this chapter, the polarization configuration of a set of symmetric BTO/STO SPLs of different periods is presented. The SPLs were synthesized with different periods and thicknesses: $M \times (\text{BTO})_n/(\text{STO})_n$, where M is the number of BTO/STO bilayers and n is the number of unit-cells in each BTO or STO layer. The considered SPLs have $n = 1, 2, 4$ and 10 , and $M = 60, 30, 15$ and 6 ; thus, all the SPLs have the same total thickness ($M \cdot n = 60$ unit-cells). For simplicity, in the following the SPLs are denoted as n -SPL, where n indicates the number of unit-cells of the BTO or STO layers and relates to the period (the SPLs periods are $2n$). The SPLs were grown on STO(001) TiO_2 terminated substrates buffered with a 10 nm thick $\text{La}_{0.7}\text{Sr}_{0.3}\text{MnO}_3$ (LSMO) electrode.⁸¹ The LSMO electrode, which given the structural compatibility, low mismatch (+0.8%) and low thickness, grows cube on cube and fully strained on the STO substrate, is used as bottom electrode for the ferroelectric characterization of the SPLs, given its conducting properties.

In the following, the question of which kind of polarization configuration is stabilized in BTO/STO SPLs is experimentally addressed with unit-cell resolution by making use of STEM, a technique that has demonstrated its tremendous capabilities in revealing polar configurations at the nanoscale. First, the SPLs microstructure and chemistry are presented, and secondly the results of the polarization configuration in each SPL are presented and discussed.

3.2 Polarization Configuration in $\text{BaTiO}_3/\text{SrTiO}_3$ SPLs

3.2.1 Synthesis, Structural and Ferroelectric Characterization of the $\text{BaTiO}_3/\text{SrTiO}_3$ SPLs

The superlattices studied in this chapter were synthesized and characterized prior to the beginning of this thesis research by our research group.⁸¹ The superlattices were grown by PLD, and the growth process was monitored in-situ by Reflection High-Energy Electron Diffraction (RHEED).

As an example, we show the intensity of the RHEED specular spot during BTO/STO deposition of the 4-SPL, Figure 3.1 (a), which shows intensity variations with an overall intensity decrease during BTO growth (in blue) and an increase during STO growth (in red). Figure 3.1 (b) is a zoom from Figure 3.1 (a) showing the intensity evolution during the growth of one BTO/STO period, with further zooms of marked areas shown in Figure 3.1 (d). Four intensity oscillations are seen for BTO and STO layers, indicating that layer-by-layer growth was achieved. Figure 3.1 (c) shows the RHEED patterns of the LSMO electrode before growth (left) and of the STO top layer after growth (right). Post-growth characterization included structural analysis by x-ray Diffraction (XRD) and Atomic Force Microscopy, and ferroelectric characterization, as well as STEM images and Electron Energy Loss Spectroscopy (EELS) chemical maps. XRD reciprocal space maps showed substrate and SPL reflections with same in-plane coordinate (Figure 3.1 (e)), indicating that the SPLs were fully strained on the STO substrate along the whole thickness. Cross-sectional STEM images confirmed the high crystalline quality growth of the SPLs and a strained structure across the SPL thickness, while the EELS chemical maps showed abrupt interfaces and low intermixing, see ref. ⁸¹.

By comparing SPLs with different periods, the roles of strain and electrostatics in the ferroelectric properties were separated. The electrostatic boundary conditions were found to play a main role in determining the ferroelectric properties, while the role of the strain was less relevant. This conclusion stemmed from the poor correlation observed between the oop parameter c and the polarization. The results showed that the largest spontaneous and remanent polarizations were measured in 2-SPL, being this SPL the one with the smallest c after 1-SPL (Figure 3.1 (f), (g) and (h)). For SPLs with bigger periods than 2-SPL, the polarization showed a decreasing trend. In contrast, the c parameter grew monotonically with n but decreased for the longest period SPL (10-SPL), as shown in Figure 3.1 (h), which was attributed to a possible partial strain relaxation.

It is remarkable that the spontaneous polarization surpassed that of bulk BTO for some short periods as $n=2$. This suggests that the enhanced strain of the BTO in the SPL on the STO substrate surpassed the detrimental effect of the polarization discontinuity.

These results, together with the previous knowledge in the field, led to propose the simple model of polarization configuration introduced in chapter 1 for the different superlattices (Figure 1.7 and Figure 3.2). Basically, a homogeneous polarization was proposed to be the ground state of short period SPLs (not considering 1-SPL), with this configuration evolving towards an up-down domains configuration in SPLs from some intermediate period and longer, and therefore 10-SPL would have an up-down configuration in the BTO (Figure 3.2). This basic model was useful to account for the measured ferroelectric properties, putting forward the main role of electrostatics in the form of specific polarization configurations. The experimental observations were compatible with the proposed model of domains; however, no direct experimental evidence of the domain configuration was provided at

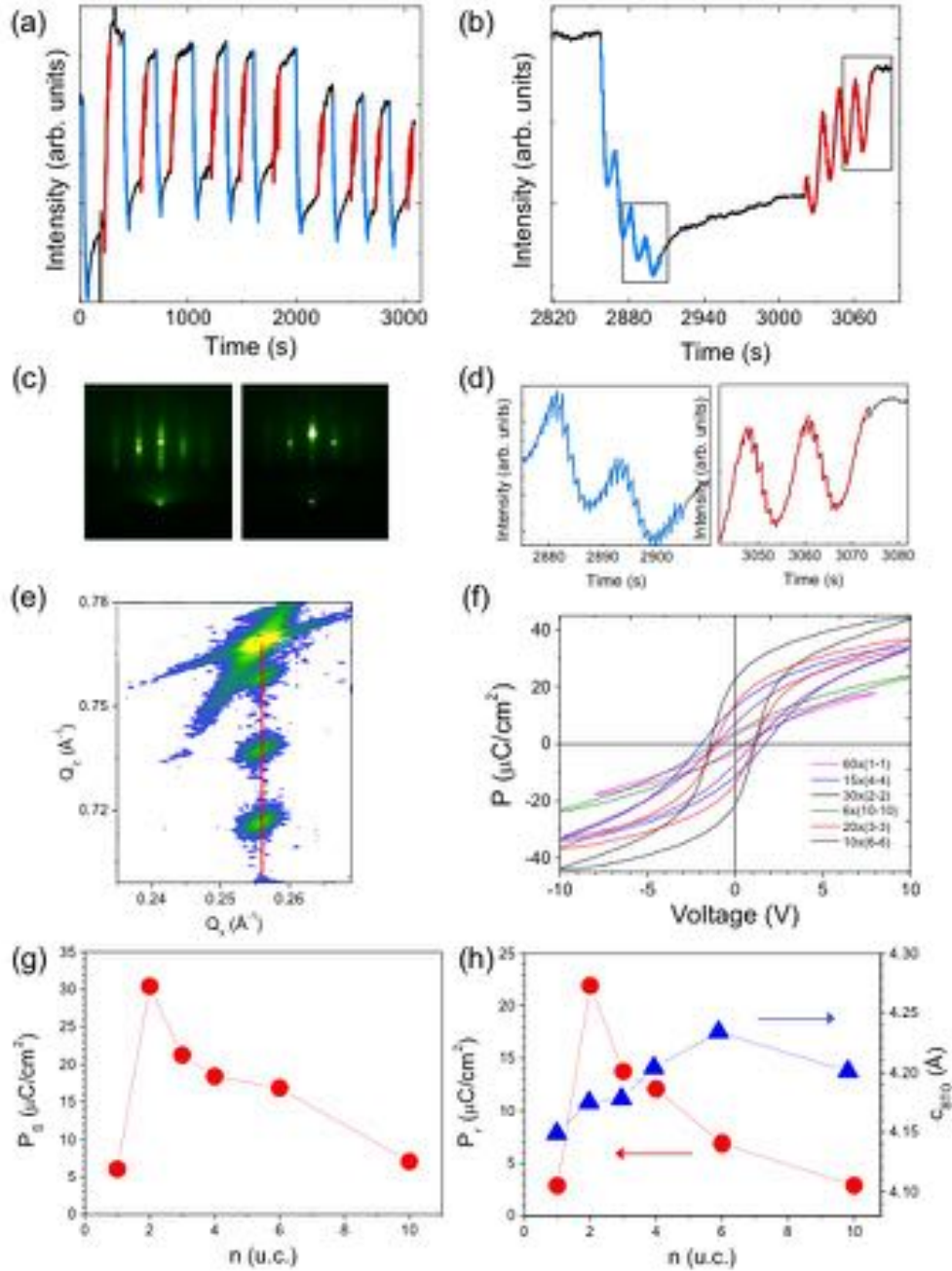


Figure 3.1: (a) Real time RHEED during the BTO/STO deposition of the 4-SPL shows an intensity decrease during BTO growth (in blue) and an increase during STO growth. (b) Zoom of (a) during the growth of one 4-SPL period shows 4 oscillations for each BTO and STO layer, indicating layer-by-layer growth mechanism. (c) RHEED patterns of the LSMO electrode before growth (left) and of the STO top layer after growth (right). (d) Zoom of oscillations marked in (b). (e) XRD reciprocal space maps show that the SPLs are coherent. (f) Polarization loops of the SPLs. (g) Spontaneous polarization as a function of the period n . (h) Remanent polarization and c of BTO as a function of n . This figure is adapted from ⁸¹.

the time. Yet, even if this model of domains turned to be broadly correct, the polarization could present significantly deviations and different local features. Therefore, the question of which kind of domain

configuration was present in each SPL remains unresolved. We have gone one step further in this thesis and, by characterizing the SPLs at the unit-cell level by means of STEM, we have revealed the polarization configuration in the real space.

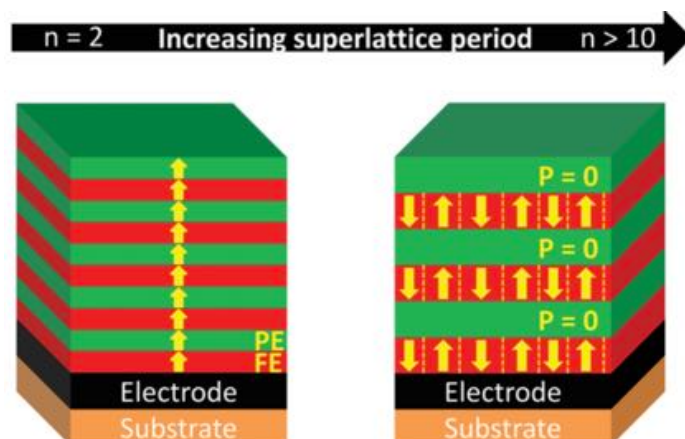


Figure 3.2: Proposed model of domains in the set of SPLs as a function of the period n .⁸¹ Ferroelectric and paraelectric layers are shown in red and green, respectively, and the yellow arrows represent the polarization. Figure extracted from ref⁸¹.

3.2.2 Microstructure of the BTO/STO SPLs

The SPLs have been imaged in cross-section along the $[100]$ zone axis, which is also the $[100]$ of the STO substrate. This zone axis is convenient for TEM-specimen preparation, given that the sides of the square sample mark the directions $[100]$ and $[010]$, while being a low-index zone axis, the distance between atomic columns is bigger and all the sublattices appear clearly separated, which facilitates the observation and analysis of the images. The observation of the heterostructure along a different zone axis could be useful to access features whose ordering is contained in the observation plane. This can be for example the case of a chemical ordering or the case of polarization domains. Particularly, in BTO/STO SPLs, different theoretical works suggested possible orderings of up and down domains along the $[110]$ zone axis or other directions, depending on the assumed conditions.^{31,82} However, observation along the $[100]$ zone axis entails the projection along this axis and therefore permits the observation of $[010]$ ip and $[001]$ oop directions of BTO and STO. We have followed this approach in this thesis.

In Figure 3.3, large field of view HAADF images of the four SPLs ($n=1, 2, 4, 10$) are presented, showing entirely the SPLs, the LSMO layer and a fraction of the STO substrate. The substrate and the LSMO electrode are clearly distinguishable due to the fact that the contrast in the HAADF imaging mode roughly scales with the square of the atomic number Z . Therefore, the LSMO layer ($Z_{La}=57$, $Z_{Sr}=38$, $Z_{Mn}=25$) appears brighter than the substrate (STO, $Z_{Sr}=38$, $Z_{Ti}=22$), and the same applies to the contrast of 2, 4 and 10-SPLs, where consecutive bright (BTO layer, $Z_{Ba}=56$) and dark (STO layer, $Z_{Sr}=38$) stripes are clearly visible. On the other hand, the BTO and STO layers are not distinguished

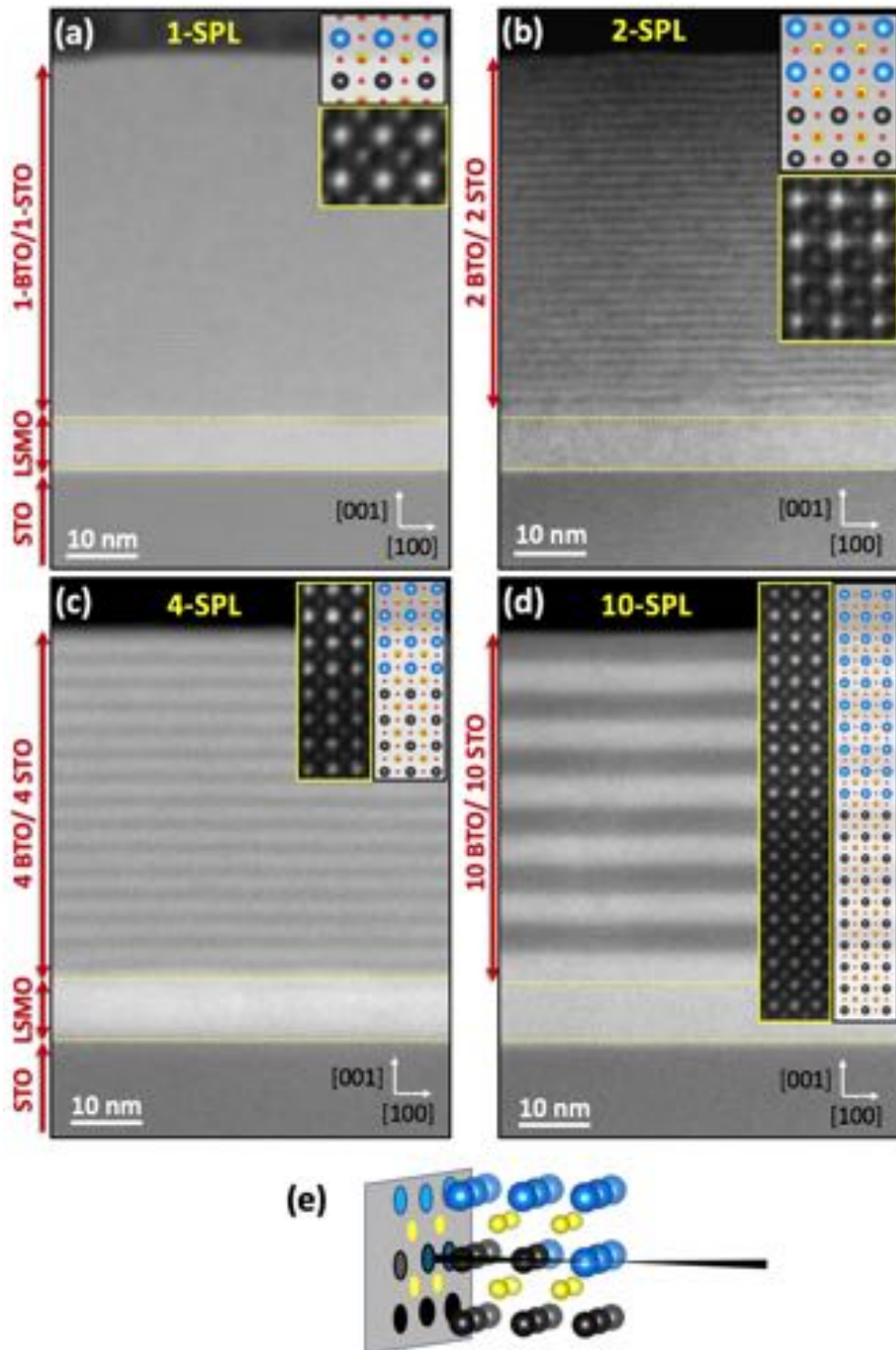


Figure 3.3: (a), (b), (c) and (d) low magnification HAADF images where the top part of the STO substrate, the LSMO electrode and the complete superlattice are visible for 1, 2, 4 and 10-SPL, respectively. The model of a period as seen along the [100] can be seen superimposed on the right part of each image (the model is magnified for clarity and the TiO₂ planes at the top/bottom boundaries are omitted for convenience, except in 1-SPL where they are shown). (e) Sketch of the averaging effect produced by the observation along an interface not completely sharp.

in 1-SPL. These Z-contrast images demonstrate a high crystal quality and low interfacial roughness, which is in the order of one unit-cell for these three SPLs.

The aforementioned roughness may be caused either by steps, that can be formed due to deviations from the layer-by-layer growth of BTO and STO and to a fewer extent to the miscut of the substrate.⁸³ Another possibility is a chemical intermixing at the interface. The roughness can be estimated based on the HAADF intensity variation at the interfaces, but EELS elemental maps are a more robust way of inferring sharpness at the interfaces. EELS allows to collect chemical information with the STEM resolution, so it can be used to study the distribution of elements (elemental maps) across the TEM-specimen (see Chapter 2). In the present case, these signals can reveal the degree of sharpness of the interfaces between BTO and STO layers. In order to obtain the elemental distribution, suitable absorption edges of the cations that compose BTO and STO were used: Ti L-edge, Ba M₄ and M₅ edges and Sr L-edge were first separated from the background and then integrated at each pixel of the image. The obtained chemical maps for 1-SPL, 2-SPL, 4-SPL and 10-SPL are presented in Figure 3.4. As it is expected from the low magnification HAADF images of the SPLs presented above, the chemical intermixing/steps is in the order of 1 unit-cell. Therefore, 1-SPL shows homogeneous Ba and Sr distributions, while 2-SPL, 4-SPL and 10-SPL show the expected distribution of Ba and Sr according to their periods. Ti distribution is continuous, as expected. Thus, the same features become obvious in the HAADF images and in the EELS chemical maps. Note also that the chemical profiles are slightly smoother at the bottom interface of STO/BTO (bottom of the STO layer-top of the BTO layer), which is most notable in the 10-SPL Sr and Ba maps (Figure 3.4 (d)).

The ideal 1-SPL has a BaO-TiO₂-SrO-TiO₂ stacking sequence, but due to the interfacial roughness the HAADF images (Figure 3.3 (a)) and EELS elemental maps (Figure 3.4 (a)) show a continuous contrast arising from a homogeneous distribution of Ba and Sr in the observation plane, meaning that 1-SPL is a different system from the one initially considered, and that 1-SPL is different from the rest of SPLs. For this reason, the analysis of 1-SPL will not be included in this thesis. In the next, the polarization maps extracted from HAADF images are presented along with structural characterization of 2, 4 and 10-SPLs. The analysis of short period SPLs (2-SPL and 4-SPL) is presented first, followed by the analysis of the 10-SPL.

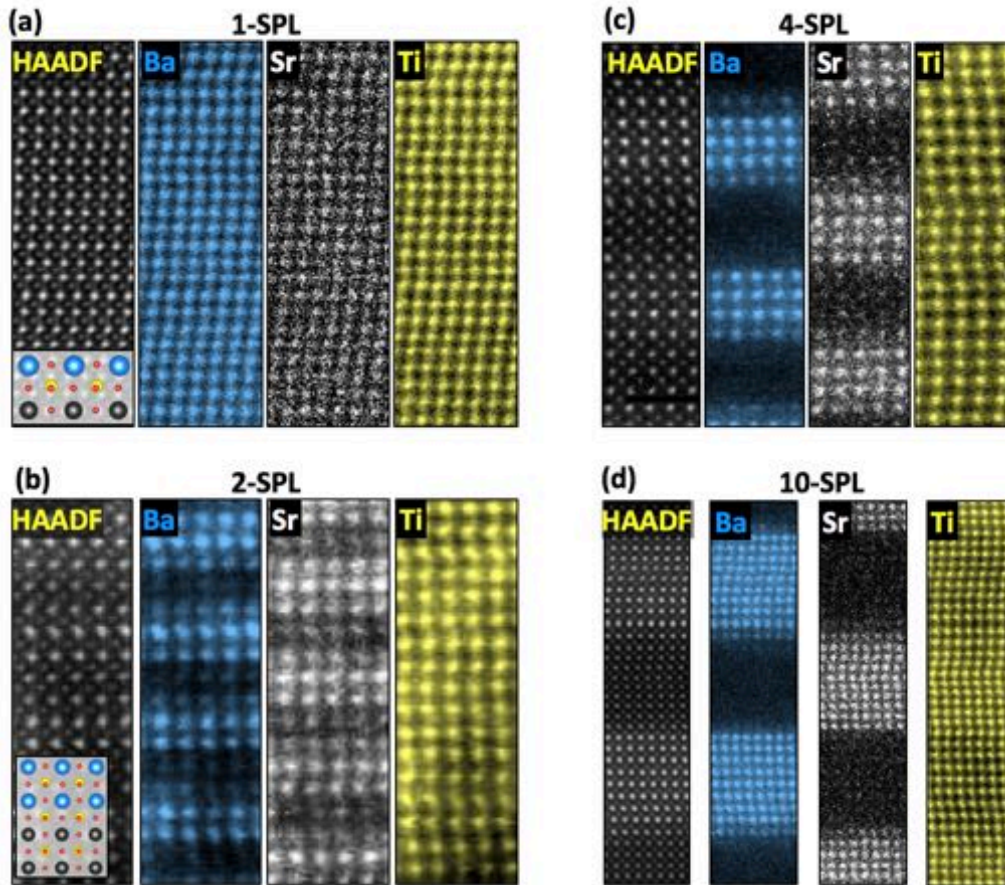


Figure 3.4: Chemical maps of Ba, Sr and Ti elements in the different superlattices obtained by integrating Ba M , and Sr and Ti L edges. (a) 1-SPL, (b) 2-SPL, (c) 4-SPL and (d) 10-SPL.

3.2.3 Real Space Polarization Maps of the BTO/STO SPLs

Short Period Superlattices (2 and 4-SPLs)

Short-period SPLs models predict a strong electric coupling between the BTO and STO layers,⁷⁵ and a homogeneous polarization across the SPLs can be expected. As will be shown in the following, the two short-period SPLs have similar domain and structural features; yet, they also have some revealing differences. Figure 3.5 shows the analysis of the 2-SPL lattice structure, in which the HAADF image shown in (a) has been used (a wider area than the one shown has been used). The analysis starts with the dipole maps (δ_{Ti}) and the ip and oop lattice parameters, a and c (see Chapter 2 for the procedure details), respectively. The a and c lattice parameters have been calculated using the Ba columns positions, although equivalent results are obtained by using Ti. The a and c maps, Figure 3.5 (e), show the a and c lattice parameter for each unit-cell. No variations across the thickness of the 2-SPL are observed in the a map, apart from the small stochastic variations within the measurement error that affect similarly a and c lattice parameters at any location. Hence, the STEM images show that 2-SPL is fully strained on the STO substrate, in agreement with the reciprocal space map presented

in Figure 3.1. The c parameter is modulated along the stacking/growth direction, as shown by the c map. This effect can also be seen as a modulation of the tetragonality, as shown in the tetragonality map (c/a), Figure 3.5 (f). c/a is calculated considering a fix a value of 3.905 Å, given that a constant value is experimentally observed (Figure 3.5 (c) and (e)). In a simple case considering only elastic energies, one would expect a cubic STO and a tetragonal BTO with the tetragonality axis oriented along the oop direction. However, the coupling between the structure and the polarization is also at play here. As shown by the dipole map (Figure 3.5 (b)), not only the BTO but also the STO is polarized, while the tetragonality c/a (Figure 3.5 (f)) shows that STO is not cubic but tetragonal. Figure 3.5 (c) and (d) show the average lattice parameters a and c , and the modulus of δ_{Ti} along each atomic row, respectively. The error bars in the profiles are calculated according to the definition of standard deviation from the average value along each row.ⁱⁱ

While a is 3.905 Å in STO, c is around 4.05-4.10 Å ($c/a \sim 1.04$). This STO tetragonality and polarization may appear bigger than it really is, since the layers thicknesses are only a bit bigger than the roughness, and the projection on the observation plane can produce an overlapping with BTO, thus averaging the c and δ_{Ti} values. However, the roughness is not big enough to account for the STO tetragonality. Theoretical calculations foresee polarized STO along with a tetragonal structure in BTO/STO superlattices, with a small tetragonality though.⁷⁵

Figure 3.5 (b) shows that the δ_{Ti} dipoles are found to be highly oriented along the oop direction, meaning that the polarization shows a strong tendency to point along the oop, which is the tetragonality axis. Indeed, δ_{Ti} ip components are much smaller than the oop components. δ_{Ti} is also found to be bigger in BTO than in STO, as it is the tetragonality c/a . Of course, it is the BTO/STO period that introduces this high spatial frequency modulation (adopting the stack BTO/STO period). The correlation between δ_{Ti} and c/a becomes clear by comparing together the lattice parameters and δ_{Ti} profiles, Figures 3.5 (c) and (d).

Interestingly, on top of the δ_{Ti} modulation caused by the BTO-STO alternation, the dipole map shows a clear variation that goes from the bottom to the top of the SPL. The dipoles at the lower part of the image, close to the LSMO electrode, point downwards while dipoles at the top part, closer to the surface, point upwards. These preferential directions can be originated by the availability of certain types of screening charges at the interfaces of BTO/STO bilayers with LSMO (lower) and with the virtual vacuum (upper), which would favor the observed orientations, or even by the presence of inhomogeneously distributed defects. The observed asymmetries between top and bottom regions of

ⁱⁱ The δ_{Ti} and a or c error bars are calculated as: $\sigma_{\delta_{Ti},row} = \sqrt{\frac{\sum_i^N (\delta_{Ti,i} - \bar{\delta}_{Ti})^2}{N}}$ $\sigma_{a(c),row} = \sqrt{\frac{\sum_i^N (a_i - \bar{a})^2}{N}}$, where N is the total number of dipoles or spacing sites along each row, i denotes the index of summation, and the top horizontal bar indicates the average value along each row.

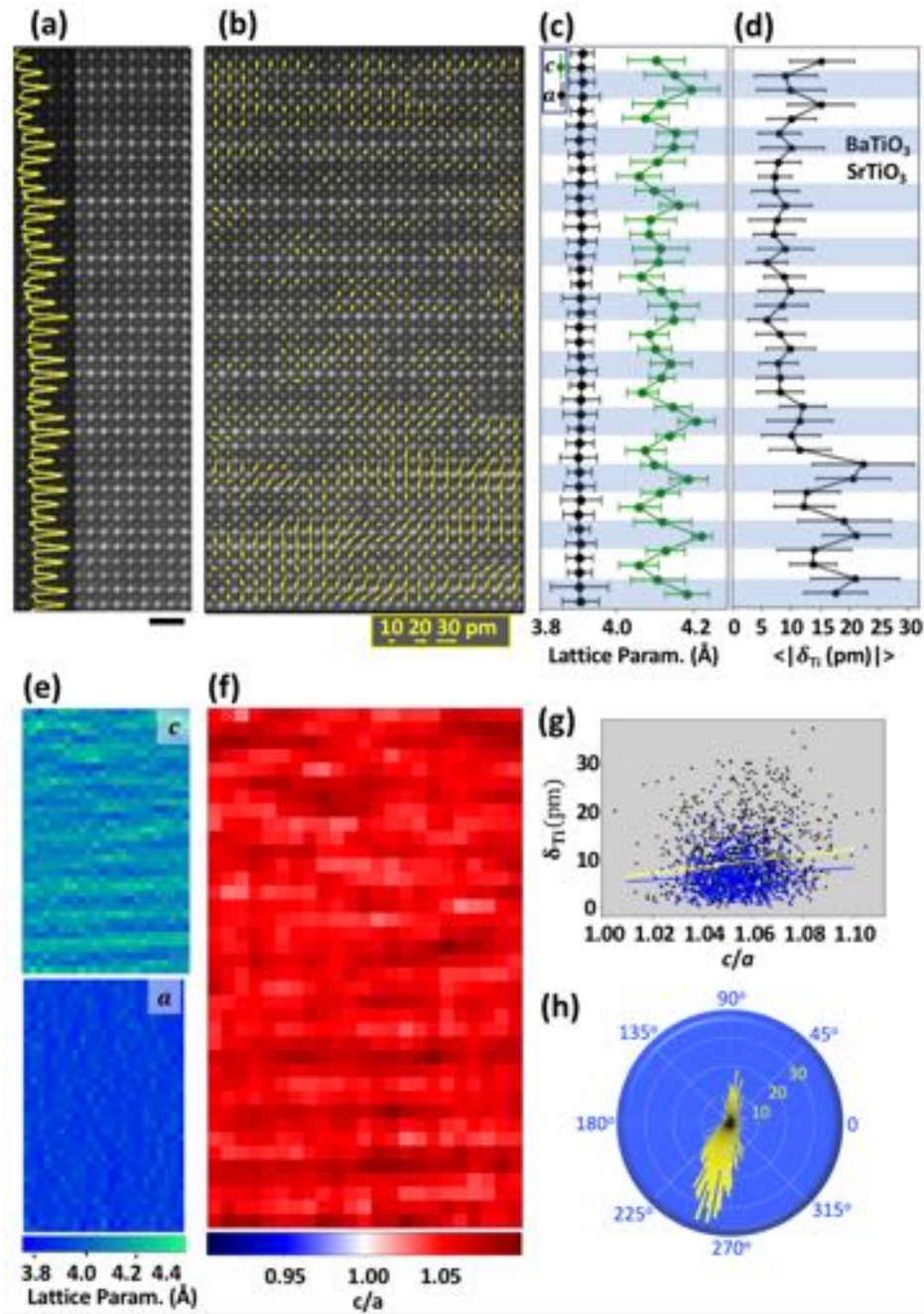


Figure 3.5: (a) Slice of the HAADF of the 2-SPL used to obtain the different panels. Scale bar: 1 nm. (b) Dipoles map extracted from the extended area shown in (a), superimposed on the corresponding HAADF. (b) dipoles map superimposed on the HAADF image. (c) Laterally averaged profiles of ip *a* and oop *c* lattice parameters. (d) Laterally averaged profile of the modulus of δ_{Ti} . Error bars in (c) and (d) indicate the dispersion of values along each row. (e) Maps of oop *c* (top panel) and ip *a* (bottom panel) lattice parameters. (f) Tetragonality *c/a* map, obtained by dividing maps in (e). (g) Data cloud obtained from plotting the δ_{Ti} modulus in each unit-cell as a function of the unit-cell tetragonality (yellow and blue lines correspond to black and blue data clouds, respectively). (h) Polar histogram representing the frequency of dipoles as a function of their orientation (2° step is used, so dipoles inside the same 2° step are grouped together).

the SPL can create an internal electric field that results in a preferential polarization orientation. This field is often present in ferroelectric heterostructures with asymmetric electrodes or inhomogeneously distributed charged defects. In the present case, at the top interface, it is possible that adsorbates provide screening charges that compensate the polarization charges. In fact, in the upper and lower areas of the analyzed area, the dipoles have much bigger values than in bulk (about 9 pm), where they can reach up to 20-30 pm displacement, so a big local polarization can be expected in those areas. Notice that towards the central area of 2-SPL, a decrease of the dipole modulus is seen, before flipping over.

The δ_{Ti} vs c/a correlation is further explored by explicitly plotting these, obtaining a data cloud, Figure 3.5 (g). In order to see if there exists a tendency, a linear curve is fit to the data cloud. When it is plotted this way, the effect of correlation looks weaker than when the oop profiles are compared. This is due to the LSMO screening effect that produces a larger δ_{Ti} close to it; and the fact that this effect is separated in the profiles but gets mixed when δ_{Ti} vs c/a are plotted as a cloud. The fitting indicates a tendency of δ_{Ti} to increase with c/a . However, the dispersion of data is bigger than the change introduced by this tendency, indicating that other factors prevail. In any case it is suggested that the data cloud should follow such a linear curve, but it is a simple way to discern whether a tendency exists or not, and to assess how strong it is. In the analyzed area, the best fit is $\delta_{Ti}=6.4+57(c/a - 1)$ pm, (yellow fit line, black and blue data points) with a standard deviation in the value of the slope of around 11 pm. That is, according to this fit the length of a dipole in a cell with $c/a=1$ would be 6.4 pm, while for $c/a=1.1$ it would be 12.1 pm. This result may be showing only that δ_{Ti} in STO, which also shows a lower c/a , tends to be smaller. As can be seen in Figure 3.5 (b) and (d), the area where the dipoles get flipped shows a lower δ_{Ti} . If only this central area is fitted separately, Figure 3.5 (g) (blue line and blue data points), and δ_{Ti} plotted against c/a , a smaller slope is obtained. This happens because the δ_{Ti} contrast between BTO and STO becomes smaller in the central area, while c/a stays unaltered across the whole SPL.

Apart from the induction of polarization in the STO, another possible way of reducing the polar discontinuity at BTO and STO consists in the rotation of the polar axis away from the axis along which the polar discontinuity is generated (that is, the growth direction or BTO/STO stacking direction), which reduces the discontinuity in the polarization oop component. This mechanism can reduce the polar discontinuity without reducing the polarization at each unit-cell, in coexistence with the other mechanisms. In order to assess this possibility, the dipole angles are plotted in a polar histogram that shows the frequency of dipoles to be oriented along a certain direction, Figure 3.5 (h). A clear tendency of the dipoles to point slightly away from the oop direction is found. The center of the distribution is offset towards an angle of around 14° . This tilt can be an additional mechanism that contributes to relax the electric energy in 2-SPL, as has been generally predicted in ferroelectric SPLs.⁸⁴

Finally, an area closer to the LSMO electrode was explored in order to assess the sensitivity of the δ_{Ti} polar distortions, and therefore of the polarization, of the SPLs to the electrostatic boundary conditions. This provided a more complete picture of these complex systems. Figure 3.6 shows the dipole map superimposed to the corresponding HAADF image of the inspected area. This dipole map shows, as previously, that δ_{Ti} becomes increasingly bigger towards the bottom, indicating that polarization is bigger next to the LSMO. In fact, δ_{Ti} reaches values above 40 pm in this area, which would translate into a local enhancement of the polarization in BTO of around a factor 4 with respect to bulk (assuming that the polarization scales linearly with δ_{Ti}).⁷⁰ Besides, the increase of δ_{Ti} as the LSMO is approached happens at a faster pace in BTO than in STO. This probably results in a bigger polarization contrast between the ferroelectric and the paraelectric next to the electrode. The big values of δ_{Ti} at the SPL bottom may be possible by the presence of screening free charges at the LSMO surface. The decrease of δ_{Ti} far from the LSMO should be attributed to the STO layers, that although they get polarized, they do not reach the BTO polarization values, which creates depolarizing fields in the BTO layers according to the BTO-STO polarization discontinuity.

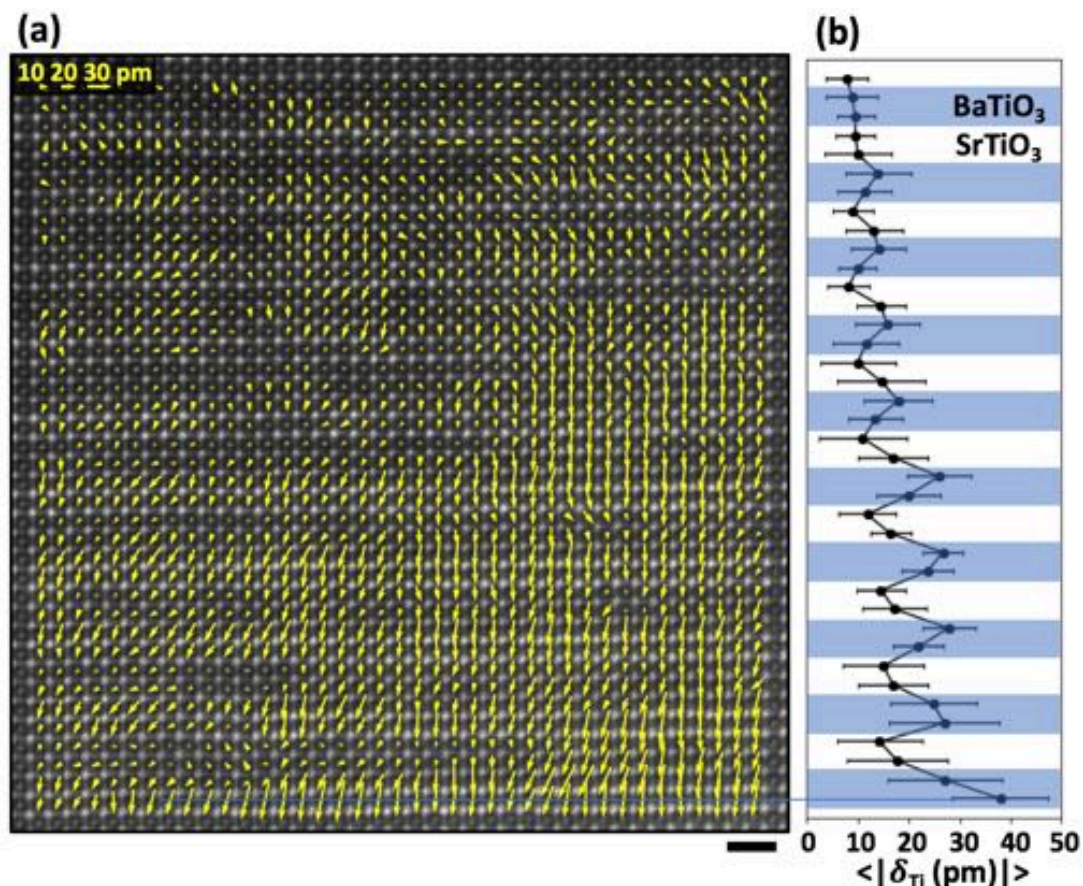


Figure 3.6: (a) δ_{Ti} dipole map obtained in 2-SPL in a region whose bottom area is right next to the LSMO electrode. Scale bar: 1 nm. (b) The profile across BTO and STO layers of the modulus of δ_{Ti} . The profile which shows a highly variable δ_{Ti} modulus depending on the distance to the LSMO electrode displacements of up to around 40 pm at the bottom area, which is directly next to the LSMO electrode.

Summing up, in 2-SPL, it is verified that the δ_{Ti} dipoles are preferentially oriented along the oop direction but keeping a tendency to be tilted away from this direction of around 14° , and there is a strong electric coupling between ferroelectric BTO and paraelectric STO that tends to impose a uniform polarization state, polarizing the STO. Yet, this state is not completely reached, producing a more complex configuration: the modulation created by BTO and STO stacking makes δ_{Ti} alternatively bigger and smaller in BTO and STO, respectively. In addition, a smoother variation that makes dipoles bigger near the LSMO electrode and progressively smaller far from it is observed.

The structural characterization of the 4-SPL, presented in Figure 3.7, reveals similar features to those found in the 2-SPL. Figure 3.7 (a) shows a slice of the analyzed HAADF image with its intensity profile shown in yellow. The dipole map, presented in Figure 3.7 (b), reveals a rather continuous polarization across both BTO and STO layers with a vast majority of dipoles oriented close to the oop direction. Figure 3.8 shows an extended version of the dipole map in Figure 3.7 (b), showing a wider area with bigger magnification in order to appreciate with greater detail the dipoles in each unit-cell. Figure 3.7 (c) shows the laterally averaged ip (a) and oop (c) lattice parameters. As in the 2-SPL, the non-zero δ_{Ti} in STO indicates that it becomes polarized as well. However, unlike in the 2-SPL, in the 4-SPL the STO unit-cells appear to be approximately cubic at the center in the STO layers. Tetragonality (c/a) in the STO of short period BTO/STO SPLs has been predicted to be around 1.008,^{75,76} which entails a difference of only 3 pm with respect to the cubic cell, smaller than the experimental error bars and therefore out of the sensitivity. The tetragonality shows a modulation as a result of the variations only in the oop lattice parameter, that alternates between a minimum $c \sim 3.9 \text{ \AA}$ in STO and a maximum $c \sim 4.1 \text{ \AA}$ in BTO. The ip lattice parameter a , as in 2-SPL, does not vary along the thickness and is equal to the STO substrate value $a = 3.905 \text{ \AA}$ indicating that no plastic relaxation takes place. Therefore, STO is almost cubic ($c_{STO}/a_{STO} \approx 1$) while BTO is tetragonal with a maximum tetragonality of $c_{BTO}/a_{BTO} \sim 1.05$ at the center of the BTO layers. Additionally, Figure 3.7 (c) reveals a smooth tetragonality gradient that starts at the interface and extends into the BTO layers, while in STO this gradient is restricted to the unit-cells right at the interface. The smooth tetragonality gradient also entails a unit-cell volume gradient inside BTO, since BTO unit-cells near the interfaces have a smaller oop lattice parameter than those in the center of the BTO layers. This smoothness is probably

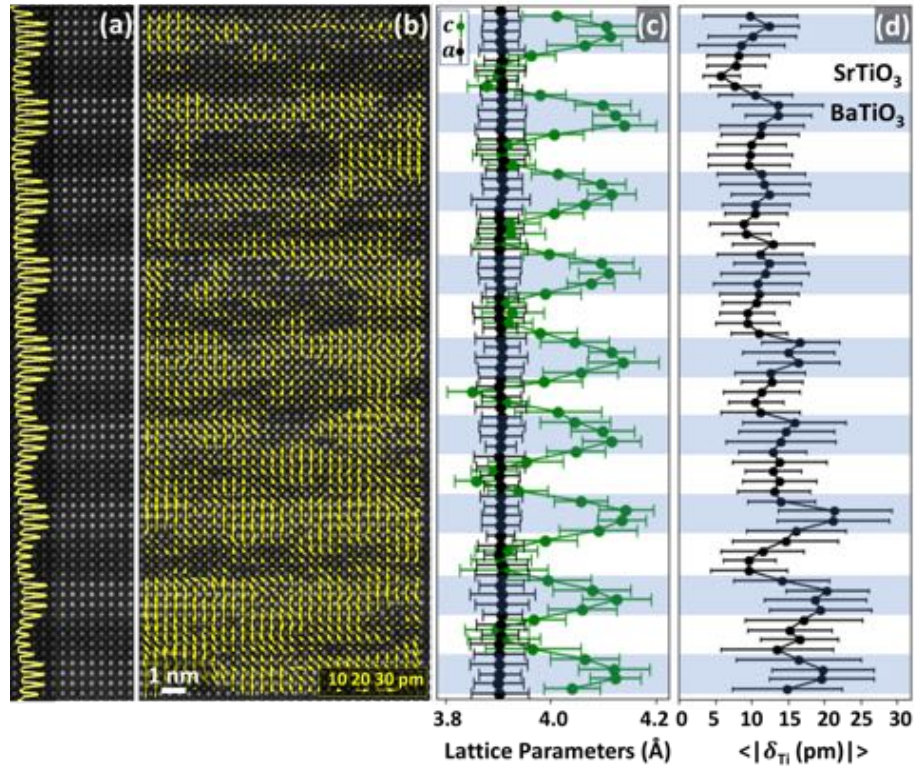


Figure 3.7: (a) slice of the HAADF of 4-SPL viewed along the [100] STO zone-axis, with its intensity profile along the oop direction superimposed. (b) dipoles map superimposed on the HAADF image. (c) laterally averaged profiles of ip and oop lattice parameters. (d) laterally averaged profile of the modulus of δ_{Ti} , defined as the distance of the Ti atomic column from the center of the unit-cell. For the sake of clarity, in (c) and (d) the BTO and STO slabs are indicated by colored stripes. Error bars in (c) and (d) indicate the dispersion of values along each row.

driven by an inverse piezoelectric coupling and could favor a smooth polarization variation through the dissimilar layers, thus reducing the energy associated with polarization gradients. In fact, comparison of the tetragonality profile with the HAADF intensity profile, Figure 3.7 (a), shows that the variation of lattice parameters across layers is smoother than the chemical variation (Ba-Sr) that is expected from the HAADF intensity. Similar smooth strain gradients have been observed in SPLs of PbZr_{0.2}Ti_{0.8}O₃/SrRuO₃ and PTO/ STO.^{85,86}

The laterally averaged δ_{Ti} modulus, presented in Fig. 3.7 (d), also shows modulations across the SPL. As in 2-SPL, a comparison of the profiles for the oop lattice c parameter and δ_{Ti} shows that they are correlated, as both the peaks and valleys coincide. Again, looking at the depth-wise changes of the δ_{Ti} modulus in Fig. 3.7 (d), one notices that BTO layers closer to the LSMO electrode present much larger δ_{Ti} values (~ 20 pm), and that δ_{Ti} gradually decreases with increasing distance from the LSMO electrode, to around 10 pm. This effect, as previously discussed, can be attributed to the metallic

character of LSMO, which would provide better screening of polarization charges, with a finite screening length though. In contrast, the less effective screening provided by the bare surface (upper

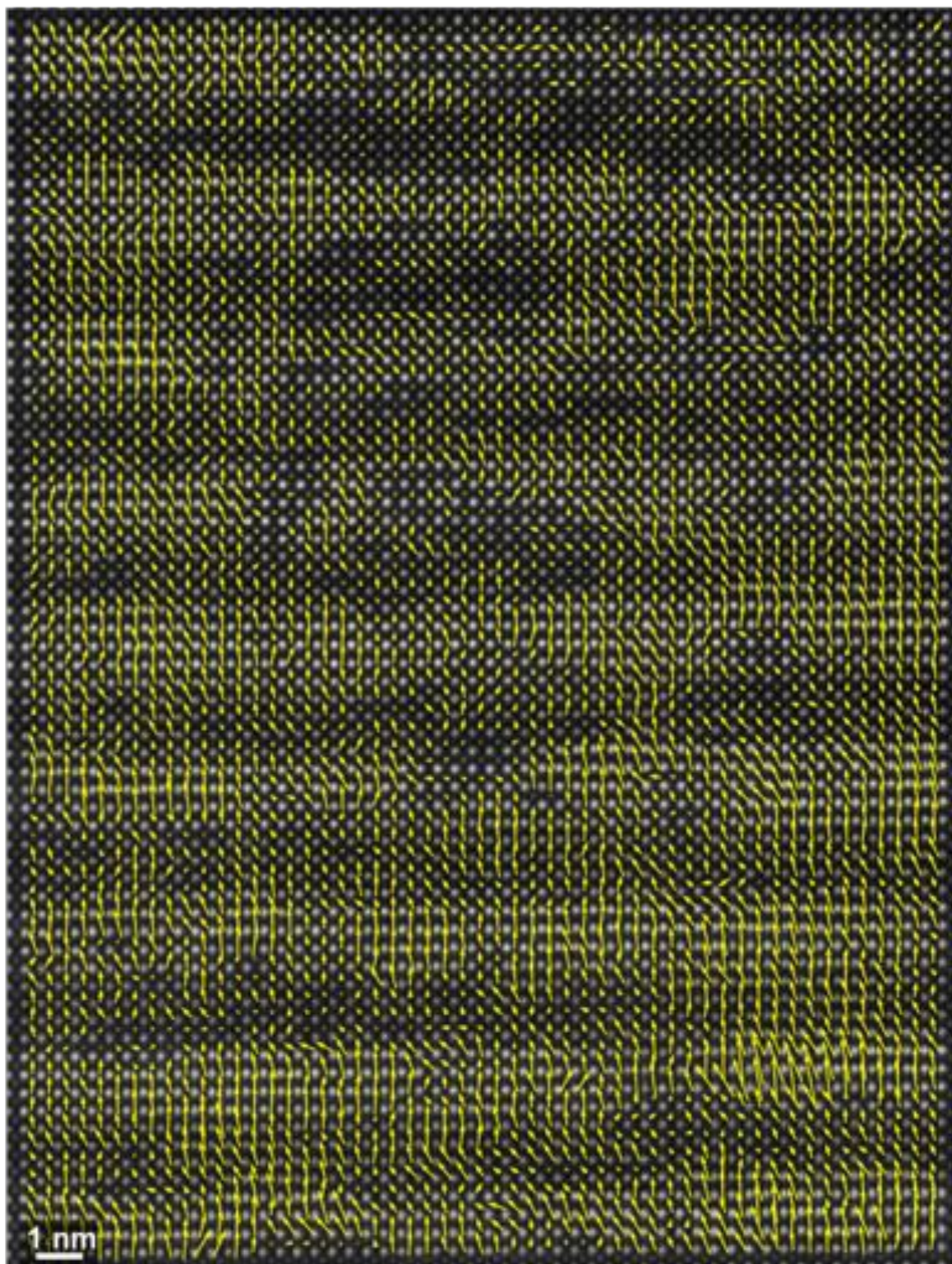


Figure 3.8: Extended version of the dipole map of 4-SPL shown in Figure 3.7 (b) with higher magnification and over a bigger area. The dipole maps is superimposed on the corresponding HAADF viewed along the $[100]$ zone-axis.

region of the image) and the presence of the paraelectric STO layers induce a sharper reduction of the polarization. Strikingly, the full dipole map in Figure 3.7 (b) also shows the presence of strong local variations of the imaged δ_{Ti} modulus, with regions in which δ_{Ti} is close to zero, which can be due to a decrease of the polarization or to a rotation off the observation plane (which would result in a smaller projection on the image's plane), but it can also be, in part, due to the finite signal/noise ratio of the image. These local variations may also be originated by the presence of local inhomogeneities such as steps at the interface, intermixing and other crystal defects.

Figure 3.9 (a) shows the c/a map of the corresponding HAADF presented in Figure 3.7. As in the 2-SPL, a positive tendency is seen in 4-SPL by plotting δ_{Ti} vs c/a , Figure 3.9 (b). The fitting of a linear model gives $\delta_{Ti}=9.2+87\cdot(c/a -1)$ pm, with a standard deviation of 4 pm in the slope. This can be also appreciated by comparing the δ_{Ti} and c/a profiles, where it can be seen that the dipoles are bigger inside the BTO layers, which also have a bigger tetragonality. Besides, statistics of the angular distribution of δ_{Ti} dipoles (polar histogram in Figure 3.9 (c)) show a tendency to be misaligned from

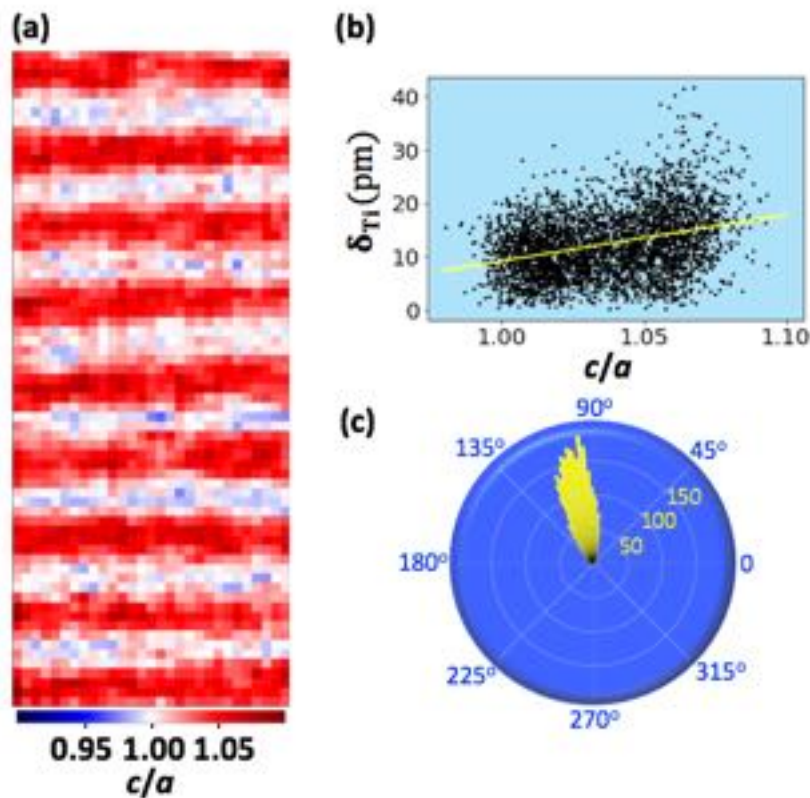


Figure 3.9: (a) Tetragonality (c/a) map of 4-SPL extracted from the same area as the dipole map in Figure 3.7. (b) Data cloud obtained from plotting the δ_{Ti} modulus in each unit-cell as a function of the unit-cell tetragonality. (c) Polar histogram representing the frequency of dipoles as a function of their orientation (2° step is used, so dipoles inside the same 2° step are grouped together).

the oop direction, with the center of the distribution being at an angle of around 14° , just like in the 2-SPL. The possibility of having a non-homogenous angle distribution yielding different angles inside the BTO and STO films, and at the interfaces was also explored by computing a map (not shown here) similar to the ones showing the cell parameters or tetragonality in each cell, but containing instead the angle of each dipole with respect to the oop direction. As can be also expected by looking at the δ_{Ti} dipole map, no systematic distribution is seen; that is, the angle distributions are similar in the inner of BTO and STO layers and interfaces. This contrasts with predictions of bigger dipole angles next to the interfaces,^{31,82} where the polarization mismatch has a greater effect. Another possibility is that the SPL is slightly tilted off the [010] zone axis, which can produce a virtual additional δ_{Ti} component.⁵⁸ The fact that the SPLs are grown on LSMO, which has a rhombohedral distortion with bulk angles around $0.2-0.3^\circ$ could originate a tilt of the SPLs with respect to the LSMO and the STO substrate.⁸⁷ Anyhow, these options are speculative, and the origin of the observed angle is not known.

Although some degree of correlation is found between the polarization (tracked by δ_{Ti}) and the tetragonality (c/a) in short period SPLs, it is far from the strong coupling expected in a ferroelectric material like BTO. Besides, this finding reasserts the thesis defended by Khestanova et. al.⁸¹ that states that the electrostatic boundary conditions play a main role in the polarization configuration, while the elastic would play a less important one.

In short, dipoles in 4-SPL are oriented close to the oop direction but keep a tendency to be tilted away from this direction, similarly to what is seen in 2-SPL. The electric coupling between ferroelectric BTO and paraelectric STO is smaller than in 2-SPL but still there is continuity across layers and the biggest dipoles are seen next to the electrode. In the 2-SPL, the dipoles can be as big as 40 pm near the LSMO, where a better screening of the polarization charges is expected. An analogous effect is seen in the 4-SPL, with dipoles reaching only 20 pm though. These results qualitatively agree with the dynamical measurements of the polarization presented in Figure 3.1, where polarization was found to be around twice as big in 2-SPL than in 4-SPL. The mapping of the local polarization by means of STEM implies observing the polar distortions at the unit-cell scale, while the dynamic hysteresis implies polarizing the heterostructure by an external electric field and measuring the change in the macroscopic polarization upon switching. Thus, these measurements are performed in different conditions. Yet, both sense the polarization and it seems reasonable that the different boundary conditions imposed by the SPL period allow to obtain the biggest polar distortions in 2-SPL (observed with STEM), and that this is reflected in the macroscopic polarization measured in the 2-SPL, which also the biggest among the different SPLs (as seen in the hysteresis measurements).

Long period superlattice: 10-SPL

An HAADF image showing the whole thickness of the 10-SPL is presented in Figure 3.10 (a). The area marked in yellow has been used for analysis and is shown with higher magnification in Figure 3.10 (b). Figure 3.10 (c) shows the tetragonality (c/a) map corresponding to the area shown in Figure 3.10 (b). A clear modulation of the tetragonality is seen, with BTO being tetragonal and STO being approximately cubic ($c/a \sim 1$).

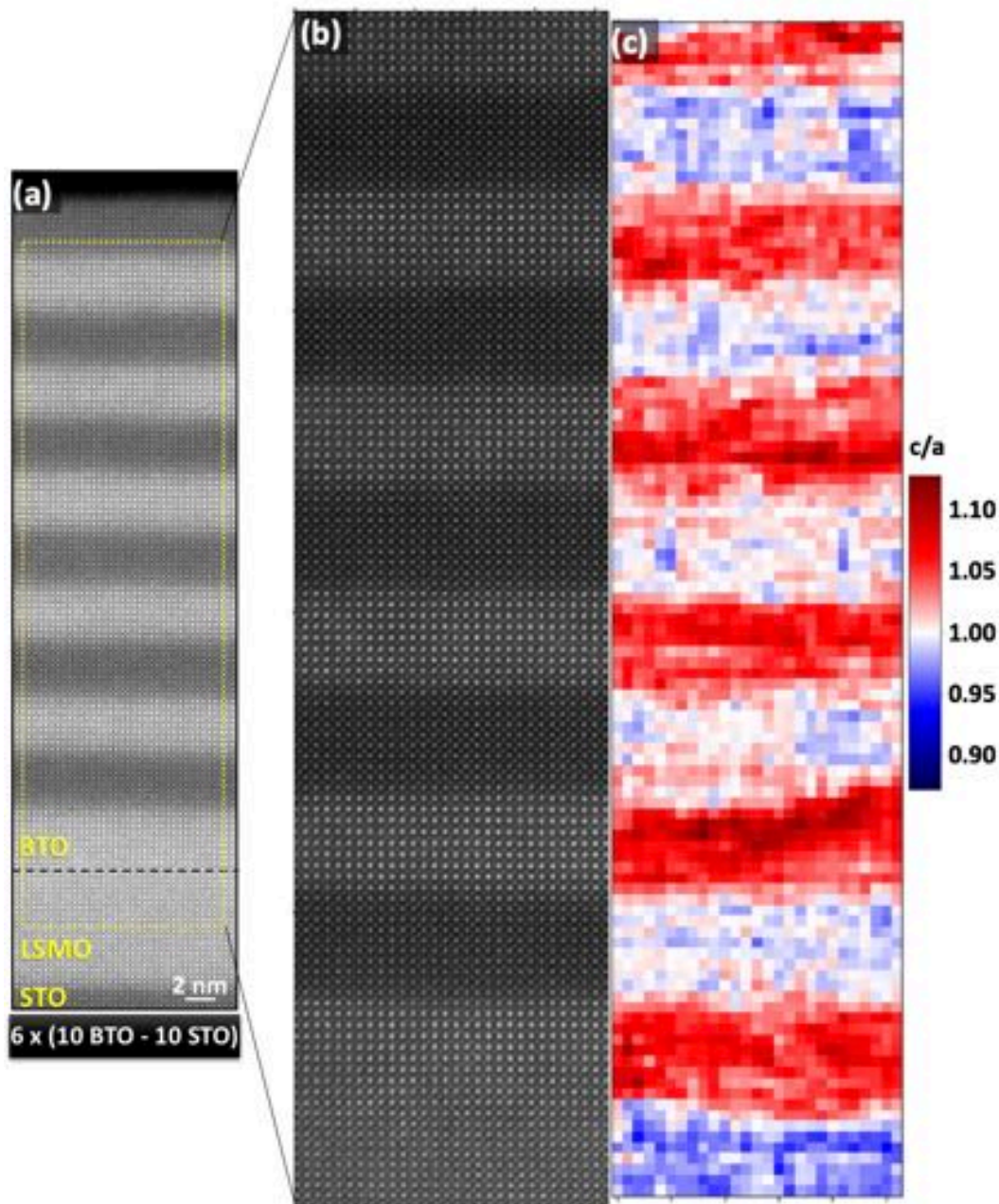


Figure 3.10: (a) Extended HAADF image of the 10-SPL where the analysis from where (b) and (c) are extracted. (b) HAADF of the analyzed area. (c) Tetragonality (c/a) map of the area shown in (b).

While the dipole maps of both short period SPLs (2-SPL and 4-SPL) show a configuration with dipoles highly oriented along the oop direction, a more complex scenario is found in the 10-SPL. First,

it is important to note that the dipole maps of 10-SPL show smaller dipoles (recall that unlike in 2 and 4-SPLs, 10-SPL showed a small macroscopic polarization (Figure 3.1)). Due to the smaller dipoles of 10-SPL, the dipoles are more affected by noise, so a filter was employed to reveal the underlying δ_{Ti} maps (review Chapter 2). With the help of this tool, the polar configuration in 10-SPL is analyzed. First, δ_{Ti} and a and c lattice parameters maps are computed in a HAADF image showing the entire 10-SPL structure. The whole HAADF image and the δ_{Ti} map superimposed on the analyzed HAADF area are shown in Figure 3.11 (a) and (b), respectively. So far, it is noticeable that the dipole configuration contrasts with the one found in 2 and 4-SPLs. Three different regions with distinctive dipole configurations can be distinguished in the δ_{Ti} map. The uppermost and lowermost BTO layers of the SPL show dipoles pointing along the oop direction. In particular, dipoles point towards the LSMO in the bottom area and towards the vacuum at the top area. Within the central region, comprising four BTO layers, the dipole map shows a configuration made of complex topologies with smooth dipole rotations, and thus having dipoles oriented along different directions. Moreover, the δ_{Ti} modulus is reduced in this central area. As was previously shown in Figure 3.1, the 10-SPL shows a polarization very diminished with respect to 2 and 4-SPLs. The observed δ_{Ti} configuration with rotational topologies could be difficult to transform into a configuration with polarization oriented along the oop direction, which would account for the reduced macroscopic polarization. Despite this reduced δ_{Ti} , the laterally averaged profile of c (Figure 3.11 (c)) and the c/a map (Figure 3.10 (c)) show a similar c modulation to the one observed in 4-SPL, alternating from a cubic STO to tetragonal BTO, but with strong local variations. As can be appreciated in Figure 3.11 (c), a is approximately constant but experiences a slight increase (smaller than 0.05 Å) towards the upper part of the 10-SPL, which might be due to a partial relaxation of the strain. Unlike in the 4-SPL, c and a profiles reveal broad regions of reduced tetragonality at the BTO/STO interfaces, extending around 3–5 unit-cells into the BTO layers. This effect produces a smooth volume gradient from the STO/BTO interface towards the center of the BTO layer. Moreover, the maximum differences between BTO and STO c parameters remain similar along the thickness of the SPL. Finally, notice that the lattice parameters of the LSMO layer show that it has a smaller c than a lattice parameter (Figures 3.11 (b) and 3.10 (c)), as expected from the in-plane tensile strain produced by the STO substrate.

A careful look at the δ_{Ti} map and its averaged profile, Figure 3.11 (b) and (d), respectively, also reveals that STO layers show a higher oop polarization in the bottom interface with the BTO than in the upper interface. The average δ_{Ti} measured in STO is mostly restricted to the oop direction, and it is rather small (5–9 pm) and only slightly above the noise level (3–4 pm) (see Appendix 3). The bigger polarization in STO layers at the bottom interface might be related to the fact that the lower and the upper interface with the ferroelectric have different polarization charges: EELS elemental maps and the HAADF profile in Figure 3.11 (b) show, in general, a more abrupt lower interface).

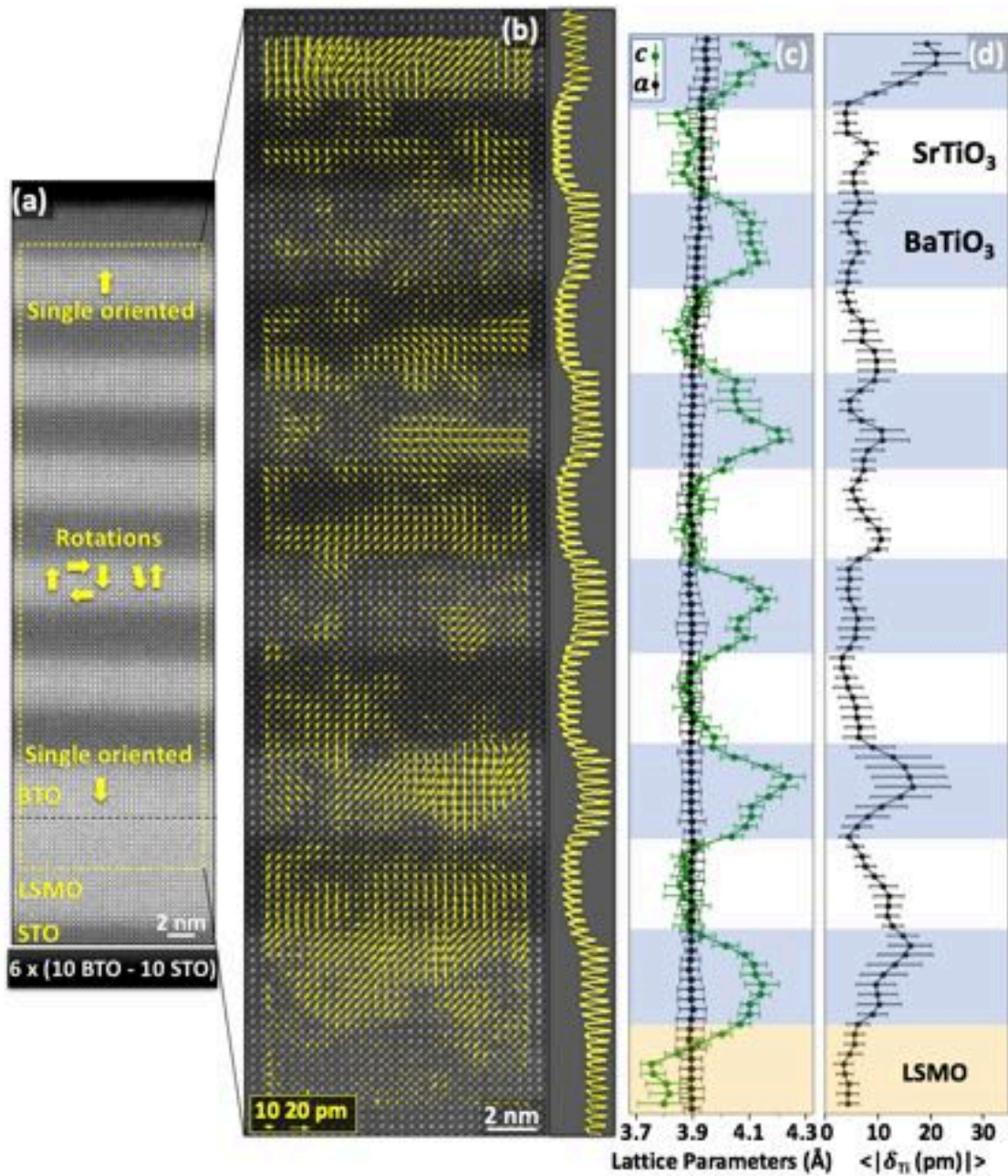


Figure 3.11: (a) High field of view HAADF image of the 10-SPL with superimposed schematics describing the polarization configurations at each location. The polar displacement map for the marked area in (a) is shown in (b), superimposed onto the HAADF image, and its intensity profile is shown at its right. (c) and (d) show the averaged profiles along the SPL thickness of oop and ip lattice parameters c and a and of the modulus of δ_{Ti} , respectively. The BTO, STO and LSMO locations are indicated by colored stripes.

Regarding the dipole angular distribution in the 10-SPL, Figure 3.12 (a), the polar histogram shows that the dipoles have a certain tendency to point along the oop direction (see also Figure 3.11 (b)), but not as strong as in 2 and 4-SPLs. The more spread distribution of dipole directions is due to

the formation of polarization rotations in the central BTO layers. Figure 3.12 (b) shows the δ_{Ti} as a function of c/a . The fitting to a linear regression gives: $\delta_{Ti}=6.04+30.77(c/a -1)$ pm, with a standard error in the slope of around 2 pm. The slope is significantly smaller than in shorter period SPLs, probably indicating a weaker correlation with c/a than in shorter SPLs. In fact, in the central area of the 10-SPL, where rotations are present, the measured δ_{Ti} does not correlate with c/a . The latter can be appreciated by comparing the δ_{Ti} and the c/a maps.

Different observed areas of 10-SPL show similar exotic dipole configurations in the BTO layers located in the SPL central region. Figures 3.13 and 3.14 provide a good display of the different kinds of rotational nanotopologies found in the BTO central layers with higher magnification. As can be seen in Figure 3.14 (a), STO present mainly oop oriented dipoles. The magnitude of δ_{Ti} in this central area where the rotational topologies

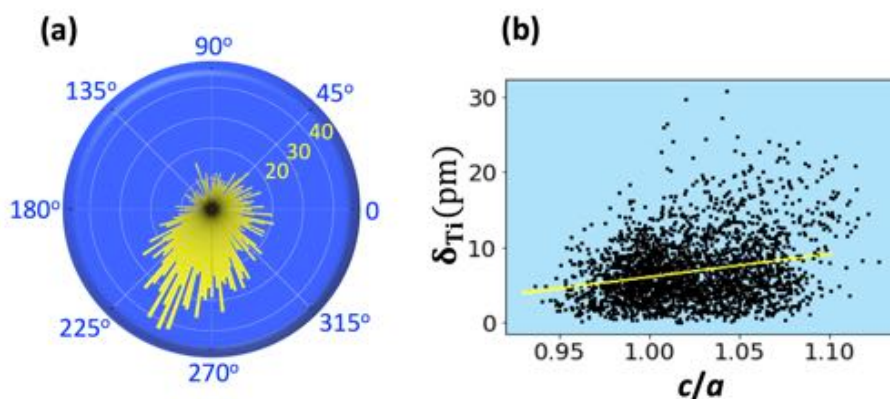


Figure 3.12: (a) Polar histogram representing the amount of dipoles as a function of their angle on the observation plane (2° step is used, so dipoles inside the same 2° step are grouped together). (b) Data cloud obtained from plotting the δ_{Ti} modulus in each unit-cell as a function of the unit-cell tetragonality.

are present is in general between 5 and 10 pm, which is substantially smaller than the δ_{Ti} from the uppermost and lowermost BTO layers of the SPL, where it can reach up to 20 pm. This result bears similarity to what is found in short period SPLs, where δ_{Ti} is smaller around the center and bigger at bottom and top areas of the SPLs. However, the δ_{Ti} is in general much smaller than in short period SPLs. Thus, this difference at bottom/top and central regions should be mostly due, as in short period SPLs, to the decrease of screening charges far from the LSMO electrode. Yet, the fact that in these regions with rotational topologies, δ_{Ti} may have an important component along the beam direction at some locations could also be a source contributing to the smaller δ_{Ti} observed. At the same time, δ_{Ti} at one position is the resulting projection of several unit-cells along the beam direction, which can produce a decrease of the imaged δ_{Ti} if Ti displacements with different directions are present in the projected unit-cells. However, this potential averaging effect is limited by the depth of field of the beam, provided that only a finite amount of unit-cells will significantly contribute to the image (see Chapter 2).

In BTO, smooth closed rotations can be appreciated, as the ones appearing in (a) and (b) panels of Figures 3.13 and 3.14, marked with red squares. These rotations contain a topological defect, that is, a discontinuity in the order parameter (electrical dipoles in the present case) at the core, where the change of polarization becomes more abrupt. A topological defect can be characterized by a topological charge or the closely related concept of winding number;^{88,89} in this case the close rotations bear a topological charge (TC) of +1. A +1 TC is obtained when, upon a clockwise contour loop around the defect core, a full clockwise dipole rotation is seen. Remarkably, all the observed +1 topological defects are found associated to other kind of defects with a TC of -1 (full counter-clockwise rotation upon a clockwise contour loop), marked with white squares. Thus, these defects form pairs with null net TC, and are compatible with vortices (defects with TC of +1) and antivortices (TC of -1). Interestingly, as we look from left to right of Figure 3.13 (b), it can be appreciated how the +1 defects make an up-down zigzag alternating clockwise and anti-clockwise rotation directions. An almost identical array of antivortices and vortices with alternating rotation directions was found in a BTO/STO SPL simulation,⁹⁰ but as a dynamic unstable configuration.

Other kinds of dipole configurations, such as waves and mushroom-like configurations are also found. Figure 3.13 (c) shows a domain wall separating up and down domains, while 3.14 (c) shows an example of a dipole wave ending in a mushroom-like configuration. At the base of the head of the mushroom-like configuration, dipoles become smaller on the observation, which could either indicate a bigger component out of the observation plane. The latter was argued to occur in PTO/STO SPLs,⁹¹ where very similar closed rotations, waves and mushroom configurations were observed.

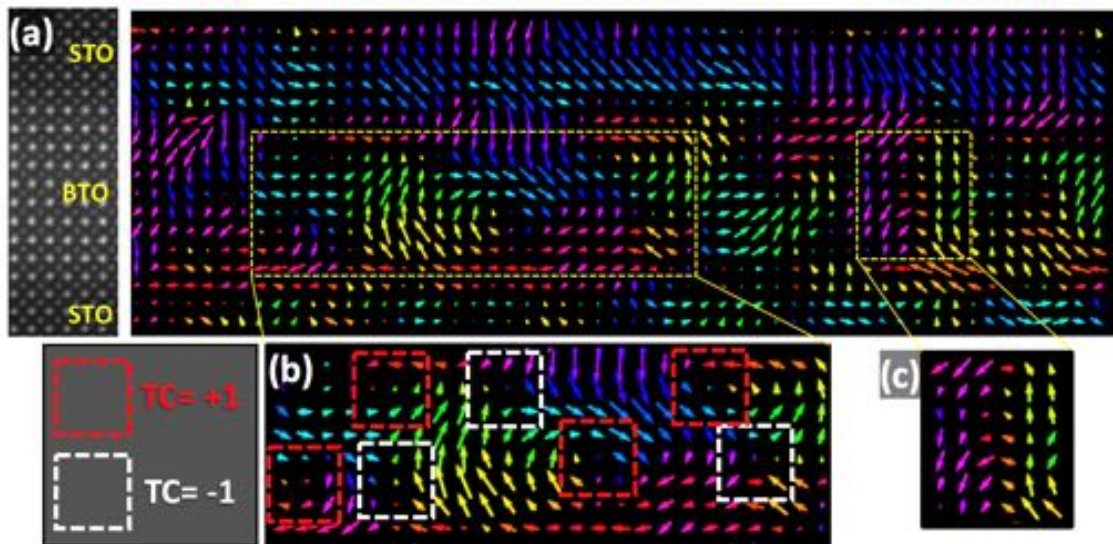


Figure 3.13: (a) Dipole map of the central area of 10-SPL. As a guide, a slice of the HAADF image from where the dipole map has been extracted is shown at the left of the dipole map. The dipoles are colored according to an angle color map with the aim of highlighting the different polarization directions. (b) shows a zoomed region where pairs of rotations containing topological defects with charges +1 and -1 are observed. (c) zoom of a domain wall separating up and down domains.

The +1 and -1 topological defects (dipoles around the defect cores) can interact with each other as particle-like objects, and share indeed many properties with elementary particles, reason why they can be considered as quasi-particles. The null net TC restricts the coupling range of the pair to dipoles located in its vicinity and allows homogeneous polarization far enough from the TC pair, where the dipoles do not discern the separated TC charges (as they screen each other). This is, a null TC pair can exist in a matrix of homogeneous polarization (*i.e.* surrounded by homogeneous downwards oop

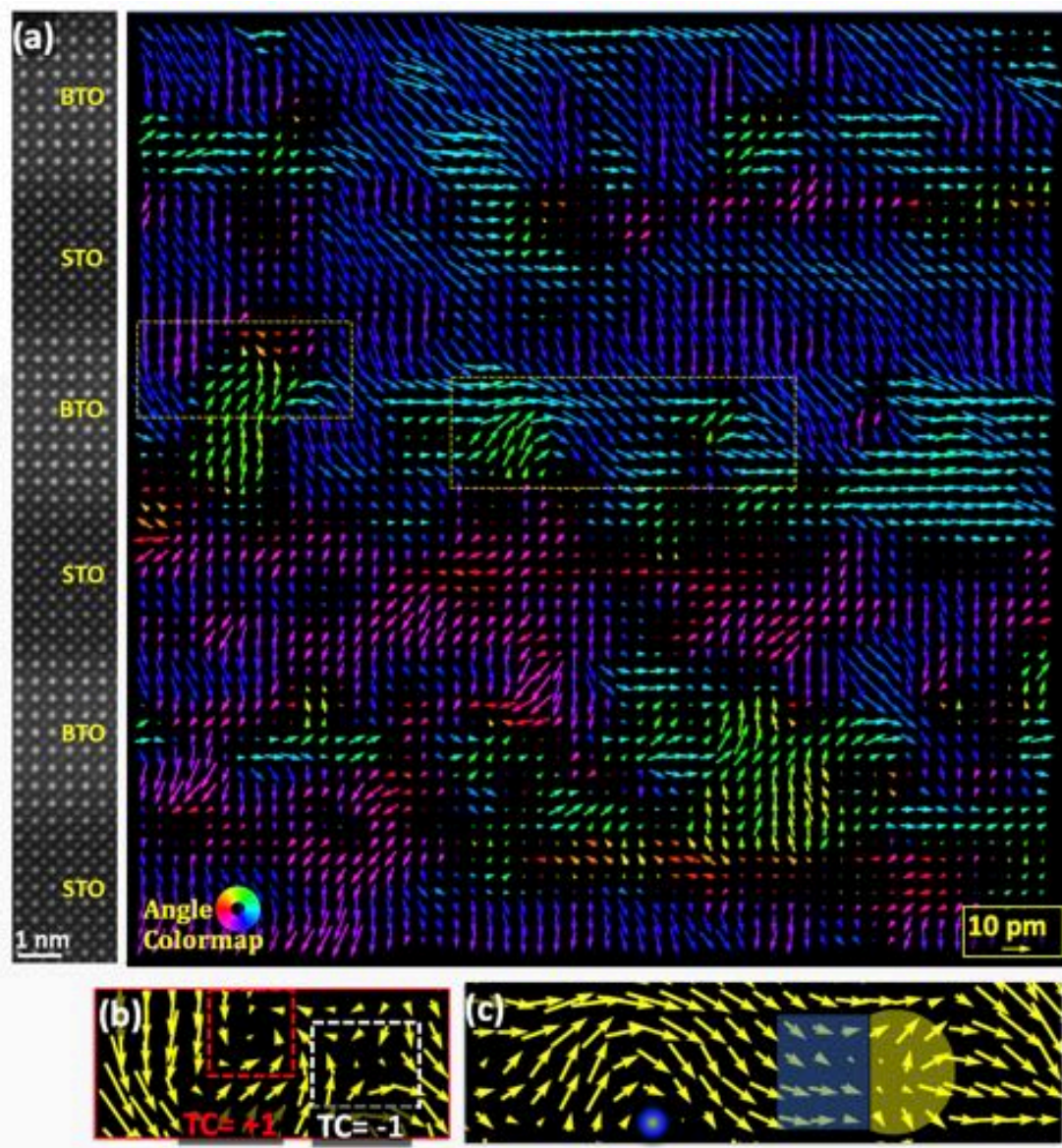


Figure 3.14: (a) Dipole maps of the central area of 10-SPL. As a guide, a slice of the HAADF image from where the dipole map has been extracted is shown at the left of the dipole map. The dipoles in (a) are colored as a function of their angle. (b) and (c) show different zoomed of selected areas marked in (a) (the angle colormap is not used in (b) and (c)). A pair of topological defects of opposite charge can be appreciated in (b), while (c) shows a dipolar wave ending in a mushroom-like dipole configuration.

polarization). Furthermore, this would make a null TC pair energetically favorable with respect to an isolated topological defect. This bonding of oppositely charged defects is described in the statistical xy model of a 2D lattice of rotors, in which dissociation is predicted to become energetically achievable above the Kosterlitz-Thoules transition temperature,⁹² which accounts for the phase transition of different physical systems such as lattices of magnetic spins, liquid crystals, superconductors or superfluids in systems of reduced dimensionality (2D).^{93,94} In the particular case of defects having opposite topological charge, the pair can annihilate if both defects converge after displacing towards each other.⁹⁵ The latter has been simulated in BaTiO₃^{96–98} and BTO/STO SPLs⁹⁰ subject to varying strain conditions and having up and down domains or other suitable initial configurations for the study of vortices dynamics. The presence of vortices in the aforementioned studies was not stable: either they were set as an initial configuration so that its evolution could be studied, or they arose in the process connecting initial and final configurations. Predictions of stable rotational topologies in BTO are restricted to confined stress-free nanostructures such as nanodots and nanowires,^{99,100} while up and down domains are generally predicted for BTO/STO SPLs. In PTO/STO SPLs, Aguado-Puente and Junquera found an up-down polydomain with smooth closed rotations at the domain walls to be a low-energy excitation of the system,⁷⁷ and thus to be probably feasible at room temperature. On the other hand, the transition from a single oriented polarization configuration to an alternating up and down domains configuration (both in BTO and STO) has been generally predicted for in-plane compressed BTO/STO SPLs for increasing periods,³¹ but no direct observation has been reported, as far as we know.

Unlike these predictions in BTO/STO SPLs, our results show that the transition to a polydomain configuration comes in the form of rotational nanotopologies that do not follow the anisotropy of the tetragonal unit-cell, suggesting that dipole–dipole interactions dominate over the anisotropy of the crystal allowing smooth polarization rotations.¹⁰¹ Alternatively, this could point to structural distortions of the tetragonal phase of BTO, provided that, expectedly, the BTO unit-cell symmetry strongly determines the dipole direction.¹⁰² Other BTO-based ceramics have shown that continuous rotations can form by acquiring a mix of unit-cell symmetries.¹⁰³ This means that the polarization direction at each unit-cell would be intimately related to that unit-cell symmetry. However, such symmetry variations are not favored in the SPLs considered here, which are not only clamped to the STO substrate with its in-plane 4-fold symmetry, but also compressively strained by it, which increases the tetragonal distortion and would further stabilize the oop polar axis. It is remarkable that while the single oriented configuration observed in short period SPLs shows a correlation between the tetragonality and the polarization, no correlation is evident in the areas where rotational nanotopologies are observed, obtaining always an oop tetragonality in BTO regardless of the presence

of ip or oop dipoles. This contrasts with the general understanding of how tetragonality and polarization are related,¹⁰⁴ and that is seen in here in short period SPLs to play a role. However, it seems that in both cases, with the tetragonal axis strongly fixed by the epitaxy, electrostatic effects are able to deviate or decrease the polar distortion without a systematic change in tetragonality. In tetragonal BTO the formation of topologies containing dipoles that considerably deviate from the crystal-axis direction was unexpected from the crystal anisotropy of a BTO/STO SPL clamped to a STO substrate.⁸⁶ A maximum dipole deviation of 45° at the BTO surfaces, where electrostatic conditions make more favorable rotations, was predicted.¹⁰⁵

Therefore, the observed rotational nanotopologies were, *a priori*, not expected to take place in BTO/STO SPLs, which begs the question of the underlying mechanism that permits such a deviation. Another point that should be noted is that simulations are generally performed at low temperature and considering perfect crystals, which implies absence of defects, and the existence of small off-stoichiometries cannot be discarded. The present SPLs were grown by pulsed laser deposition, which is a highly energetic technique that can cause the formation of defects.¹⁰⁶ Therefore, the existence of small off-stoichiometries and defects as vacancies is possible; which could assist the rotation of polarization in BTO, as was found to happen in BiFeO_3 .¹⁰⁷

More interestingly, the formation of different topological defects, as for instance bound vortices-antivortices pairs was recently predicted to occur in canonical BTO with different unit-cell symmetries (including tetragonal and orthorhombic) at a finite temperature through a new identified mechanism of topological protection.¹⁰⁸ The mechanism allows the stabilization of dipole configurations with dipoles deviating from the crystal anisotropy direction by relying on thermal entropy contributions, and although it was specifically studied in the case of BTO, the result should be generalizable to other proper ferroelectrics. Indeed, simulations are usually performed at low temperatures, so the effect of the thermal energy within the materials may be overlooked. Relying on this mechanism, stable rotational topologies might be feasible in strained canonical tetragonal BTO. It is remarkable that these theoretical predictions would fit well the experimental observations revealed in the present research work, as the bounding of opposite charged topological defects was also predicted.

Topological defects are powerful structures to engineer properties in solid state matter, since they can be controlled by external stimuli as a bias, with which they can be created, annihilated, or transported; all this while avoiding disruption of the host crystal lattice.^{25,109} Moreover, new properties have been found associated to topological defects in ferroelectrics, as the small regions around cores of polar vortices in PTO/STO SPLs in a stabilized negative capacitance state,¹¹⁰ or chirality associated to polarization vortices.¹¹¹ The negative capacitance state is achieved in these locations where the polar distortion becomes very small, driving the dipoles into the unstable region of negative capacitance that

is present in all classical ferroelectrics around the center of their double-degenerated energy landscape.¹¹² Another example is conductance at the core of topological defects.²⁵ The observed variety of rotational nanotopologies in tetragonal BTO at room temperature opens a potential window to address the feasibility to externally control the different topologies, as is being done with magnetic topological objects as the magnetic skyrmions.^{113–115}

3.2.4 Electronic Structure

Going further, the Ti-L edge and O-K edge fine structures were studied to assess possible further differences between the SPLs and within each SPL. In BTO, the Ti and O core edges are sensitive to bonding and structural distortions, while Ba is more stable and provides less information. The Ti L-edge contains electronic transitions from $2p^{1/2}$ (L_2) and $2p^{3/2}$ (L_3) states to the empty states in the partially filled 3d band, other bound states or the continuum. Due to the different interaction of the different 3d orbitals with the oxygen octahedra, the latter producing the crystal field, the Ti L_2 and L_3 transitions are split in energy, known as e_g and t_{2g} 3d sub-bands (see Figure 3.17 (a)). Similarly, the O-K edge accounts for electronic transitions from the 1s level to higher energy bound empty states or the continuum, but unlike the Ti L-edge, the O-K edge produces a non-trivial edge profile that generally needs of simulations to be understood. Ti L-edges and the O-K edges of 2, 4 and 10-SPLs, Figure 3.15, show very similar features in these three SPLs, suggesting that the chemical environment is equivalent in short period SPLs (2 and 4-SPL) and in the long period SPL (10-SPL) where continuous rotations are observed. Moreover, and importantly, these absorption edges are not different at different locations (bottom, center and top) within each SPL, which supports the idea that the observed differences in polarization at the bottom, center and top of each SPL are not driven by differences in the amount or

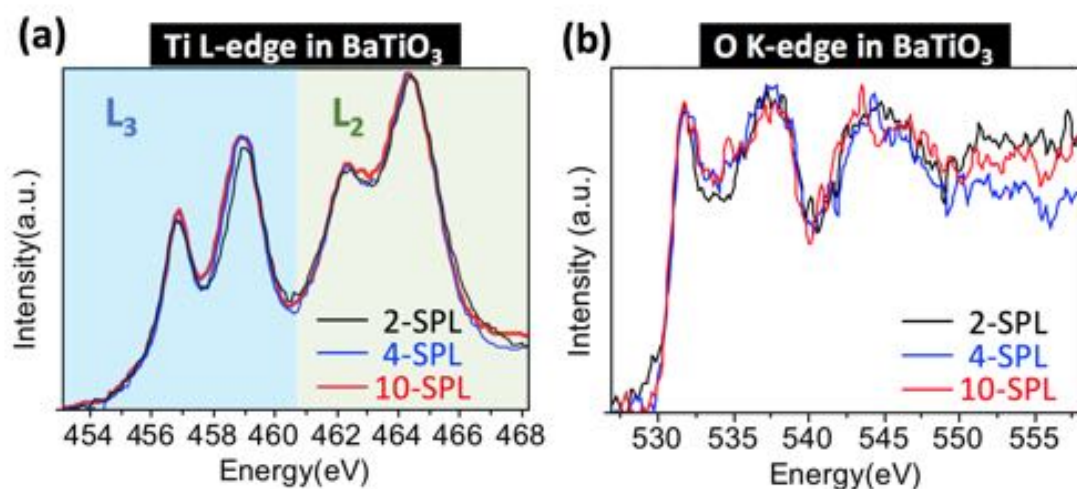


Figure 3.15: (a) Ti L-edges of 2, 4 and 10-SPLs showing the L_3 and L_2 transitions split in energy due to the crystal field. Similar features are found in all these SPLs. (b) O-K edges of 2, 4 and 10-SPLs showing similar features.

type of defects, that would probably leave a trace in the fine electronic structure.

Ti valency, which is expected to be +4 in BTO but can become +3 under certain circumstances, can be inferred from the ratio of L_3 and L_2 (L_3/L_2) transition intensities (denoted as L_{23} ratio). To do so, following a similar procedure to the one described in refs.^{116,117} the continuum contributions are subtracted (Figure 3.16 (a)). Then, the Ti L_2 and L_3 edge peaks, free now of the continuum contribution, are fitted to a Lorentzian model that allows to determine the center and area of each peak (Figure 3.16 (b)), and the L_{23} ratio as the ratio of areas of the corresponding peaks. The L_{23} ratio is calculated at different positions (BTO, STO and interface) in each of the different SPLs, obtaining a constant value (with fluctuations inside the measurement error bar) of 0.65 ± 0.05 , thus confirming that no changes in the Ti valence state occur in the SPLs, neither inside each SPL nor between the different SPLs. The error associated to the L_{23} ratio was estimated from the small fluctuations of the calculated Ti L_{23} ratio in different positions of the SPLs and by using different onset energies for the Hartree-Slater continuum cross-section. The Ti L_{23} ratio of 0.65 is very different from the value expected from the $2j+1$ degeneracy of the initial core states, $2p^{1/2}$ ($j=1/2$) and $2p^{3/2}$ ($j=3/2$), that would produce a 2/1 ratio (given that L_3 involves double number of electrons than L_2). Note that L_2 peaks have a greater total area than L_3 peaks (Figure 3.16 (b)), which corresponds to a L_{23} ratio smaller than 1. Indeed, the obtained value is much closer to the ones found in other works for Ti element, oxidized Ti, BTO and STO (0.7-1.0).^{116,118} In general, Ti and other 3d metals show a strong deviation from the statistical value 2:1, while 4d and 5d do not. Attempts to explain this deviation have pointed to the different exchange interactions or other mechanisms.¹¹⁶

In short, within the sensitivity of the technique, EELS measurements reveal expected electronic state for titanium and oxygen, suggesting that the smooth rotations of the polarization occur in canonical BTO.

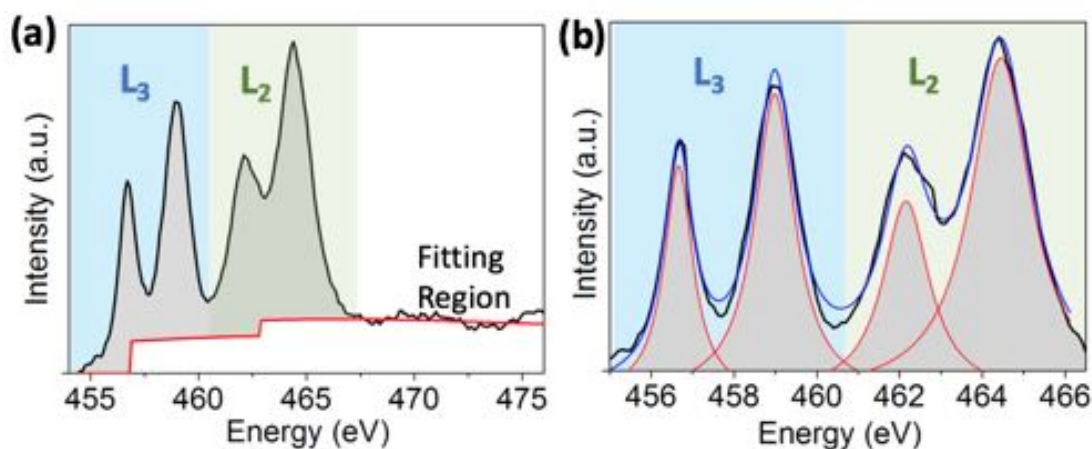


Figure 3.16: (a) Subtraction of the continuum contribution. (b) Fitting of L_3 and L_2 peaks by Lorentzian distributions yields the respective areas and an L_{23} ratio (L_3/L_2) of 0.65 ± 0.05 .

Going back to the dipole maps, recall that the averaged profile of the modulus of δ_{Ti} in 10-SPL showed gradients in the polarization across all STO layers (Figures 3.11, 3.13 and 3.14), which was argued to probably be originated from different polarization charges at lower and the upper interfaces with the ferroelectric (EELS elemental maps show a more abrupt lower interface) and to the different unit-cell volume at both interfaces. The latter can also be analyzed using the energy-loss near-edge structure (ELNES) of the Ti L-edge across the BTO/STO interfaces. In this direction, Figure 3.17 (b) shows the Ti L-edge spectra acquired in BTO (in red) and STO (in black) layers of the 10-SPL. Notice that the crystal field splitting Δ for the L₂ and L₃ are slightly bigger in STO than in BTO. The crystal field strength increases when the distance of Ti–O bonds is reduced (STO has a smaller unit-cell, thus

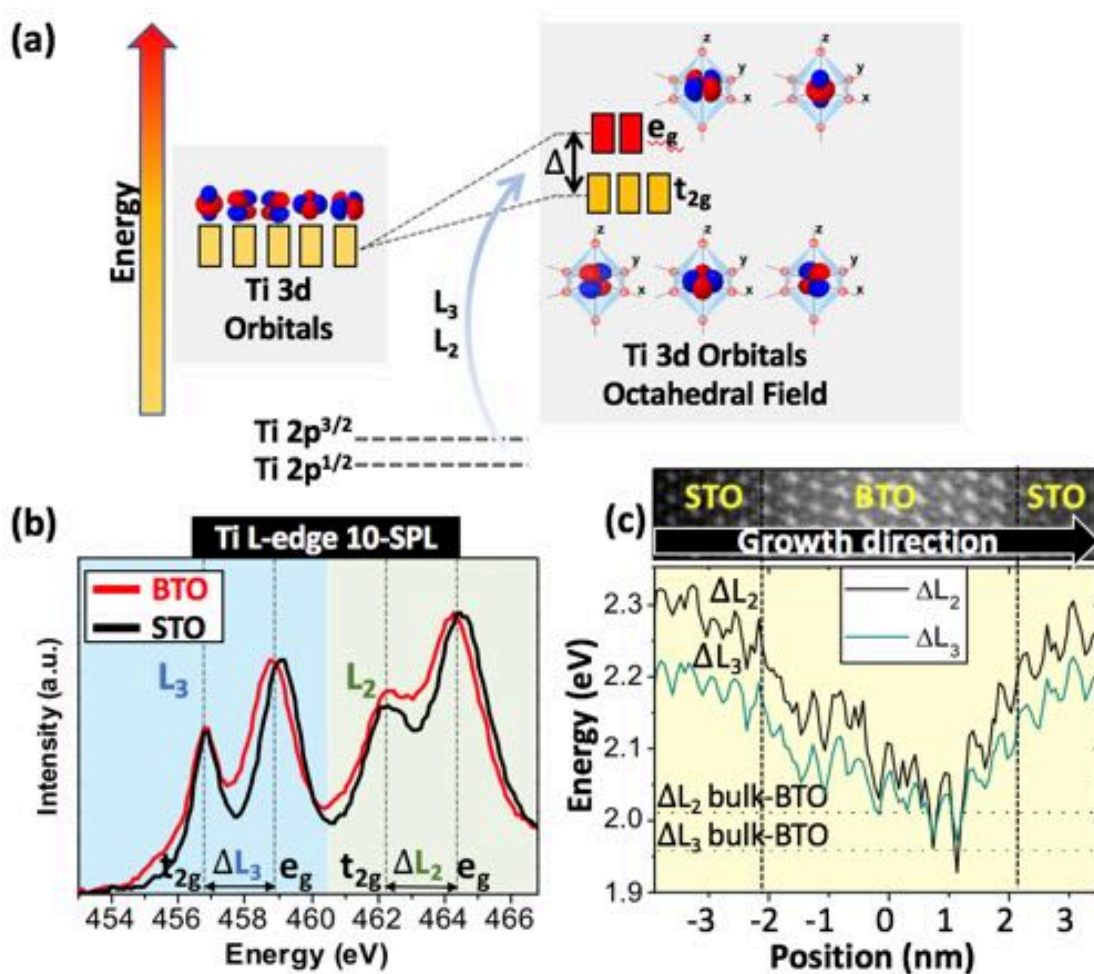


Figure 3.17: (a) Sketch showing the 3d orbitals of isolated Ti (left), and the 3d bands of Ti inside the oxygen octahedra split in energy due to the crystal field (right). (b) Ti L-edge spectra acquired in BTO and STO layers of the 10-SPL. Due to the oxygen octahedra crystal field, the Ti L₂ and L₃ peaks are split in energy and allow to obtain the e_g and t_{2g} 3d sub-bands. The crystal field splitting Δ for the L₂ and L₃ are indicated. (c) the upper panel shows the region of the 10-SPL from which a spectrum image was acquired. The lower panel shows the oop profile of the crystal field splitting ΔL_2 (in black) and ΔL_3 (in green) as a function of position across the BTO and STO layers of the 10-SPL (upper panel in (c)). Changes in the crystal field splitting indicate changes in the Ti–O bonds.

a bigger Δ), and therefore it is a useful parameter to track the strain state, assuming that a bigger tetragonality means a bigger unit-cell volume and therefore a larger Ti–O distance.^{86,119,120} Figure 3.17 shows a spectrum image across STO and BTO layers. The spectra were averaged along the lateral direction to obtain a the Ti L-edge BTO and STO with improved signal. Finally, from these spectra the ΔL_2 and ΔL_3 were calculated, obtaining the smooth profiles across BTO and STO shown in Figure 3.17 (c). This result agrees with the probed smooth tetragonality changes across the interfaces. Notice that the slope is greater in the lower part of the STO layer, which is where the STO presents a higher polarization (see Figure 3.11) and also where the BTO rapidly reaches the ΔL_2 and ΔL_3 values of the bulk. EELS elemental maps also show that this is the most abrupt interface. Therefore, dissimilar upper and lower interfaces become evident from both the polarization and the EELS analysis.

3.2.5 Are Polarization Configurations Stable Under the Electron Beam?

One can go further in the characterization and study the temporal stability of the polarization configuration in 10-SPL. To do so, two images of the same region within the 10-SPL are acquired, and the corresponding dipole maps are computed and compared.

It is important to verify that the polarization configurations observed are robust, especially given that some of these observations were never observed before in BTO. Indeed, one particular concern among some researchers has to do with the possibility of altering the polarization configuration by interaction with the electron beam, making the polarization evolve with time; or that specimen damage or charge accumulation produced by the beam could create spurious observations. In this regard, I believe that probing the same SPL region at different times and comparing the corresponding dipole maps is a simple and useful methodology to assess these possibilities. During the inspection of an area by STEM, several sequential images are normally acquired. In the time lapse between the acquisition of one image and the next, which is typically in the second time scale, the acquisition parameters may be readjusted to maximize the quality of the images. Two of these sequential images are analyzed and compared in the following.

Dipole maps from the two images acquired at times $t+\Delta t$ and t (with Δt being several seconds) are shown in Figure 3.18 (a) and (b), respectively. The inspected area is the same as the one presented in Figure 3.14. As can be seen, the same basic features are present in both dipole maps. On the one hand, finding the same basic features in both images confirms the robustness of the observations. On the other hand, it shows that the dipole configuration does not evolve significantly with time within the time scale of the experiment (several seconds). Even if the real dipole configuration did not change at all, a finite signal yields an image formed by finite statistics, which together with different possible noise sources (charge accumulation on the specimen supplied by the electron probe, instabilities of the

probe current or microscope optics, drift, heating, etc) can produce images that are slightly different; and so will be the dipole maps. Still, some of the observed changes could be originated from a real change in the polarization configuration, which would be assisted by the electron beam energy.

To quantify the changes, one could also calculate the difference between two dipole maps one unit-cell at the time. The difference map is calculated, at each ij site, as follows:

$$\Delta \mathbf{p}_{ij} = \mathbf{p}_{ij,t+\Delta t} - \mathbf{p}_{ij,t}$$

, where $\mathbf{p}_{ij,t}$ is the dipole at site ij and time t (first image) and $\mathbf{p}_{ij,t+\Delta t}$ is the dipole at site ij and time $t+\Delta t$ (second image). The resulting dipole derivative map, Figure 3.18 (c), shows the variation between the dipoles measured at t and $t+\Delta t$, at each atomic site ij , for the total number of sites N . It is visible that most of the dipoles suffer a variation, as indicated by the non-zero dipoles of the difference map. The difference between the dipole map at t and at $t+\Delta t$ can be synthesized in one single quantitative value by computing the average of the module of the $\Delta \mathbf{p}$ map, as follows:

$$|\overline{\Delta \mathbf{p}}| = \sum_{ij}^N \frac{|\Delta \mathbf{p}_{ij}|}{N}$$

If we do so, the measured $|\overline{\Delta \mathbf{p}}|$ results to be around 3.4 pm. This value can be considered as the average noise ground level in these images (considering that all the observed $\Delta \mathbf{p}_{ij}$ dipoles have an extrinsic origin). Indeed, the 3.4 pm value is very close to the 3.5 pm obtained in the STO substrate, where Ti displacement is expected to be zero. The value is also similar to the 5 pm standard deviation found by Aoki et. al.¹²¹ This would support the idea that the difference map is mostly made up of extrinsic effects.

By now, it has become evident that this derivative is useful to quantify similarity (or dissimilarity) between two dipoles maps. Leveraging it, the $\Delta \mathbf{p}$ map was also used to study the similarity between different areas within the two dipole maps. As can be appreciated in the dipole maps (Figure 3.18 (a) and (b)), on top of the different forms that the dipole maps can have locally, there is some degree of periodicity along the ip direction, as areas of up and down dipoles seem to hold a similar distance. To quantify this, we can shift one unit-cell along the ip direction dipole map at $t + \Delta t$ with respect to the one at t . Now the dipole maps are laterally shifted one unit-cell, and if $\Delta \mathbf{p}$ is calculated with the new position it is expected to increase, as the dipoles at each site $i+1,j$ and ij are expected to be more dissimilar. The maps are not only shifted one unit-cell, but n unit-cells (n being an integer) and $\Delta \mathbf{p}$ is calculated for each value of n and $|\overline{\Delta \mathbf{p}}|$ is plotted. The updated equation would simply include the dependence on n :

$$|\overline{\Delta \mathbf{p}_n}| = \sum_{ij}^N \frac{|\mathbf{p}_{i+n,j,t+\Delta t} - \mathbf{p}_{ij,t}|}{N}$$

$|\overline{\Delta p}|$ is related to the mathematical concept of correlation. A bigger $|\overline{\Delta p}|$ means a lower correlation or smaller similarity, while a smaller derivative means a bigger correlation or bigger similarity. Interestingly, $|\overline{\Delta p}_n|$ shows a modulation with maxima and minima when plotted as a function of the lateral shift n , Figure 3.18 (d). The valleys show the displacement n after which the dipoles match better again, since these maxima and minima are nothing else than the values of n for which correlation

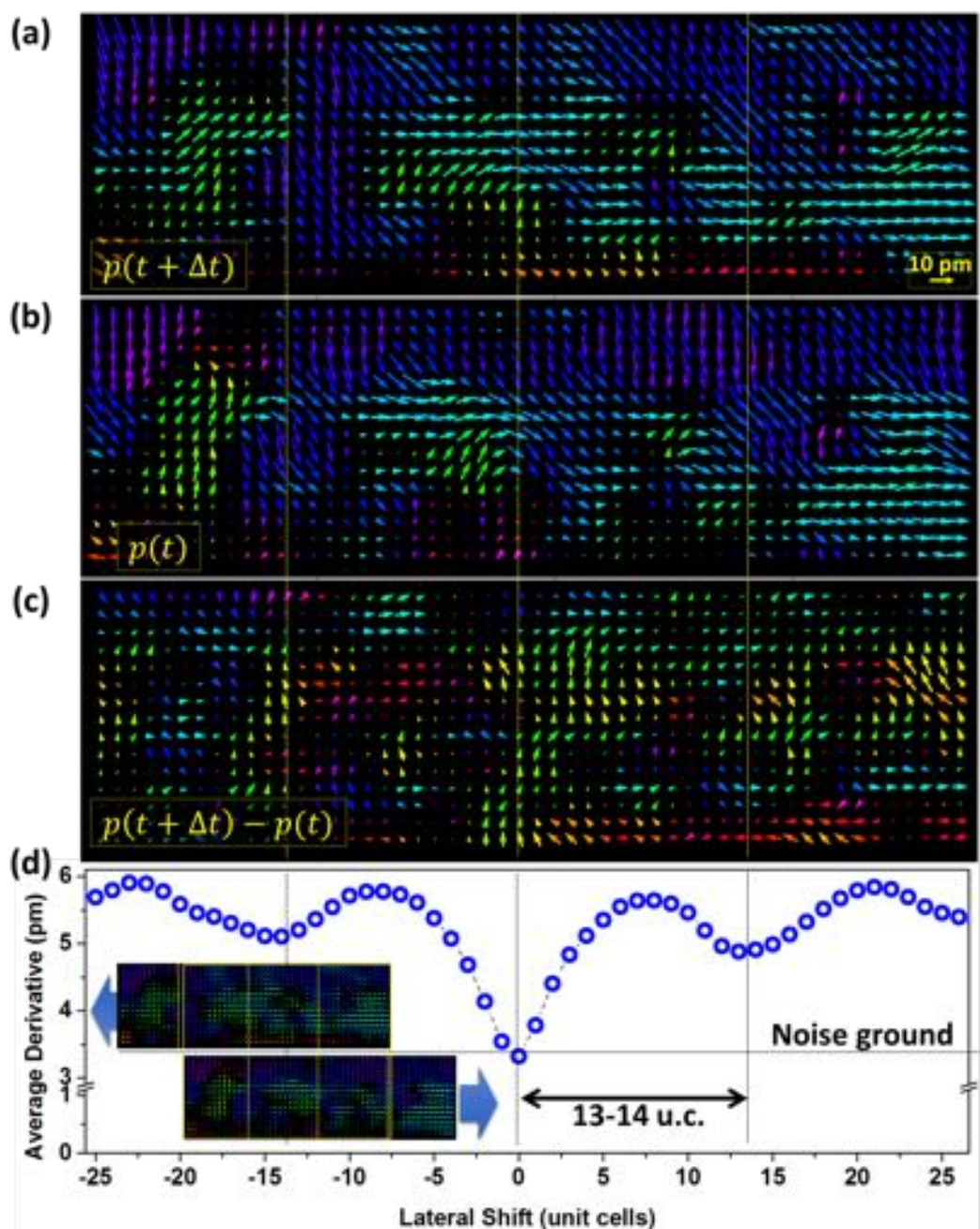


Figure 3.18: (a) Dipole map obtained from an image obtained at a time $t + \Delta t$ (where Δt is in the order of several seconds). (b) Dipole map of the same area as in (a) obtained from an image acquired at a time t . (c) Dipole map obtained as a result of subtracting dipole map in (a) and (b). (d) Average derivative as a function of the lateral shift of dipole maps in (a) and (b). The average derivative obtained from the dipole map in (c) corresponds to zero lateral shift and gives around 3.4 pm of average derivative, as can be seen.

is minimum and maximum, respectively. Moreover, maxima and minima are approximately equally separated, showing a lateral period of about 13 or 14 unit-cells, and demonstrating that there is some degree of periodicity. Periodic domains are expected since the minimum energy is obtained for a specific domain size. The observed period is, of course, the one associated to regions with up and down dipoles present in the dipole map. Since most of the features in the dipole map change smoothly, so does $|\overline{\Delta\mathbf{p}}|$ as a function of shift n . As a consequence of this smoothness, it was not obvious how to align the dipole maps of t and $t + \Delta t$ in the lateral direction (or set the same system of reference, given the images were extracted from images covering a wider area) to compute Figure 3.18 (c), that is to set $n=0$, since the dipole maps are extracted from images of bigger areas which are not exactly of same size. In other words, a lateral shift of one unit-cell makes only a small difference not obvious to identify by eye and, a priori, the shifts could be due to intrinsic variations in the dipole configuration. The value at which $|\overline{\Delta\mathbf{p}}|$ is smallest shows the match of $n=0$, also revealing that, for example, the center of the rotations are not displaced. If the same experiment was performed, but instead of using the two dipoles maps we used one and a copy of it, a similar $|\overline{\Delta\mathbf{p}}|$ versus n would be obtained; except that for $n=0$ $|\overline{\Delta\mathbf{p}}|$ would be zero, as they would perfectly match.

The methodology of analysis introduced here is simple but useful to extract information about periodicity and to assess the limit in the sensitivity to δ_{Ti} .

In short, these polar objects do not change spontaneously with time, nor do they change under the electron beam, which transfers energy to the material. These results indicate that the dipole configuration is indeed stable during the experiment. The stability observed under the electron beam is compatible with the reduced measured macroscopic polarization of the 10-SPL (Figure 3.1), since both indicate a polarization configuration that remains stable under external stimuli.

3.3 Summary

A set of symmetrical BTO/STO SPLs have been experimentally studied by using STEM. All the SPLs are strained to the STO substrates and all the interfaces can be considered to be chemically abrupt with a roughness that extends approximately one unit-cell, as seen in the STEM images and chemical maps. Different polarization domain configurations have been revealed in each SPL.

In short period SPLs, 2 and 4-SPLs, a strong electric coupling between ferroelectric BTO and paraelectric STO layers induces polarization in the STO, producing a smooth polarization across the SPLs layers. The dipoles are basically oriented along the oop direction, but show a

tendency to have a certain degree of tilting away from the oop direction, which can be a mechanism to reduce the polar discontinuity at the interfaces. Furthermore, the polarization is much stronger near the LSMO electrode, which we have argued to be due to the availability of screening charges at the LSMO surface. As expected, a smaller electric coupling between BTO and STO is observed for increasing periods. This decreasing coupling is reflected in a smaller polarization in the 4-SPL than in the 2-SPL and an approximately cubic STO in 4-SPL, while STO shows a big tetragonality in 2-SPL.

On the other hand, in the longest period SPL, 10-SPL, the even more reduced electric coupling triggers the formation of rotational topologies in the BTO layers that are not next to the LSMO or right at the top of the SPL. A variety of topologies of different character have been revealed. Remarkably, the smooth polarization rotations occur in these BTO layers while maintaining the tetragonality of the BTO unit-cells oriented along the oop direction. Thus, it has been experimentally shown that the polar axis can strongly deviate from the tetragonality axis, allowing polarization rotations in the strained BTO. This may suggest that different polarization textures are more feasible in ferroelectrics than previously thought. Furthermore, the stability of the polarization configuration has been studied in 10-SPL, finding a stable configuration within the considered time scale.

The dipole configurations in the different SPLs are compatible with the macroscopic ferroelectric and crystallographic characterization of the SPLs reported by Khestanova et. al., with analogous decreasing trends for increasing periods of the macroscopic polarization and the dipoles modulus.

The new knowledge presented in this chapter is potentially useful to better understand the processes that affect the polarization configurations in BTO/STO SPLs, and other ferroelectric SPLs and nanostructures, and might help to design superlattices with superior ferroelectric properties, as a higher switchable polarization, which is a central parameter for ferroelectric data storage. In fact, memories are one of the most pursued applications of ferroelectrics, since they are energetically very efficient compared to currently mass commercialized memory technologies, are very fast and have outstanding endurance properties. Despite these good characteristics, in practice, in the context of a market society, the use of perovskite ferroelectrics for memories has been restricted to niche applications in which low power consumption was primordial, due to limitations in downsizing and integration.

Yet, in the last decade, other kind of ferroelectric materials have been discovered and are standing as more promising candidates. Surfing this wave, the next two chapters are dedicated to the study of ferroelectric (Hf,Zr)O₂ based materials, materials that are believed to have the potentiality to overcome most of the limitations of perovskite ferroelectrics.

Appendix 3: δ_{Ti} Dipole Maps Measurement Accuracy

The measurement of δ_{Ti} may have different error sources associated, as a finite atomic column signal to noise ratio, different microscope instabilities, small specimen tilts, etc. In main of Chapter 3 this error was estimated by comparing dipole maps obtained in the same area but at different times. Apart from this method, the STO substrate was also used to estimate the measurement error. By assuming that the real δ_{Ti} in the STO substrate should be zero, given that it has a cubic centrosymmetric structure, the measured δ_{Ti} will represent the error.

The dipole maps extracted from HAADF images at the 10-SPL and at the substrate are compared for this purpose in Figures A3.1 and A3.2. BTO and STO layers can be distinguished based on the different intensity that Ba and Sr produce in the HAADF. Exploiting this, an intensity threshold was used to differentiate between BTO and STO layers (see light and dark stripes, Figures A3.1/A3.2 (b)). Dipoles inside the above-threshold-area (light area) are classified as BTO dipoles, while dipoles outside it (darker area) are classified as STO dipoles. As shown by the dipole modulus histogram in Figure A3.1 (c), the Root Mean Square (RMS), which indicates the typical δ_{Ti} , is 3.56 pm in the

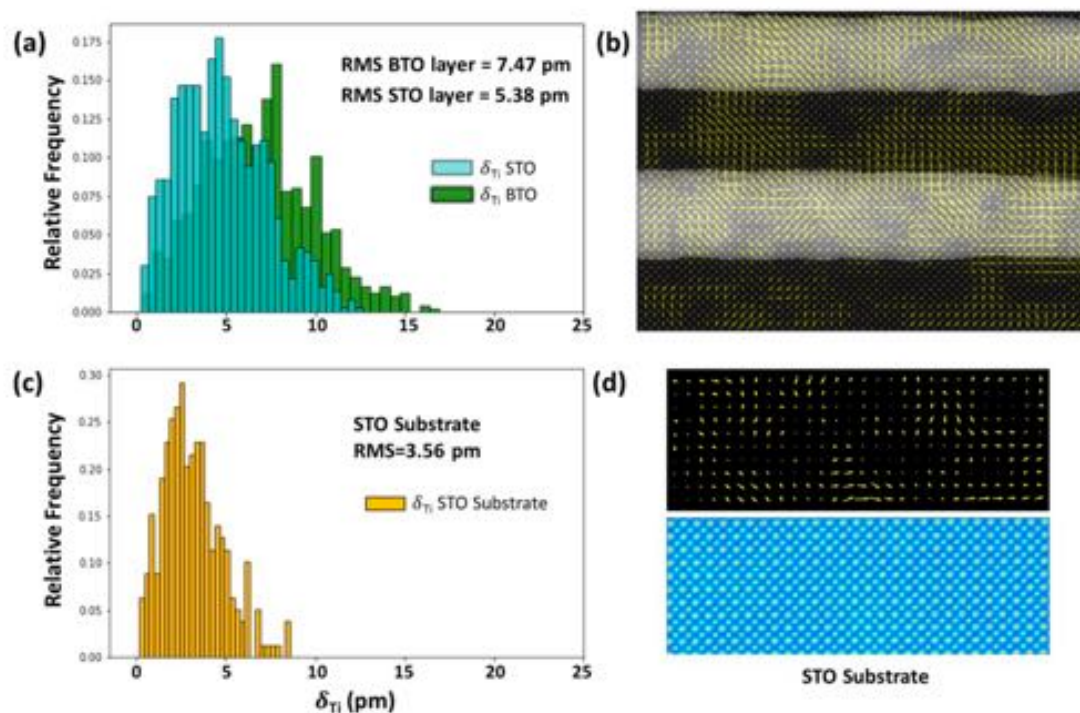


Figure A3.1: (a) shows the δ_{Ti} modulus histogram in BTO and STO layers. In (b), the dipole map on the HAADF image is shown with superimposed light and dark stripes that indicate the regions classified as BTO and STO, respectively. In (c) the δ_{Ti} modulus histogram in the STO substrate is shown, while (d) shows the corresponding dipole map and HAADF image.

STO substrate. An area with rotational topologies of the 10-SPL (Figure A3.1 (b)) is also analyzed, and the corresponding histograms are shown in Figure A3.1 (a). In this area the dipoles have a RMS of 5.38 pm in the STO and 7.47 pm in the BTO layers. Therefore, the δ_{Ti} in BTO layers is typically

double than the estimated error (δ_{Ti} in the substrate), while δ_{Ti} is even closer to the noise level in the STO layers.

Moreover, Figure A3.2 shows that the center of the distributions separated in ip and oop components are shifted from zero. This shift is very small in the STO substrate (<2 pm) and moderately bigger for oop in the STO layers (around 4 pm) and oop and ip in BTO layers (around 5 pm), indicating a smaller randomness in the δ_{Ti} distributions within the BTO and STO SPL layers than in the STO substrate. This analysis provides an assessment of the accuracy in the δ_{Ti} measurement, and allows to show that the measured δ_{Ti} dipoles are above the noise/error level in the area with polarization rotations. On the other hand, the fact that the dipoles are small and comparable to the noise level explains why the dipole maps of the 10-SPL are heavily affected by noise and needed to be filtered.

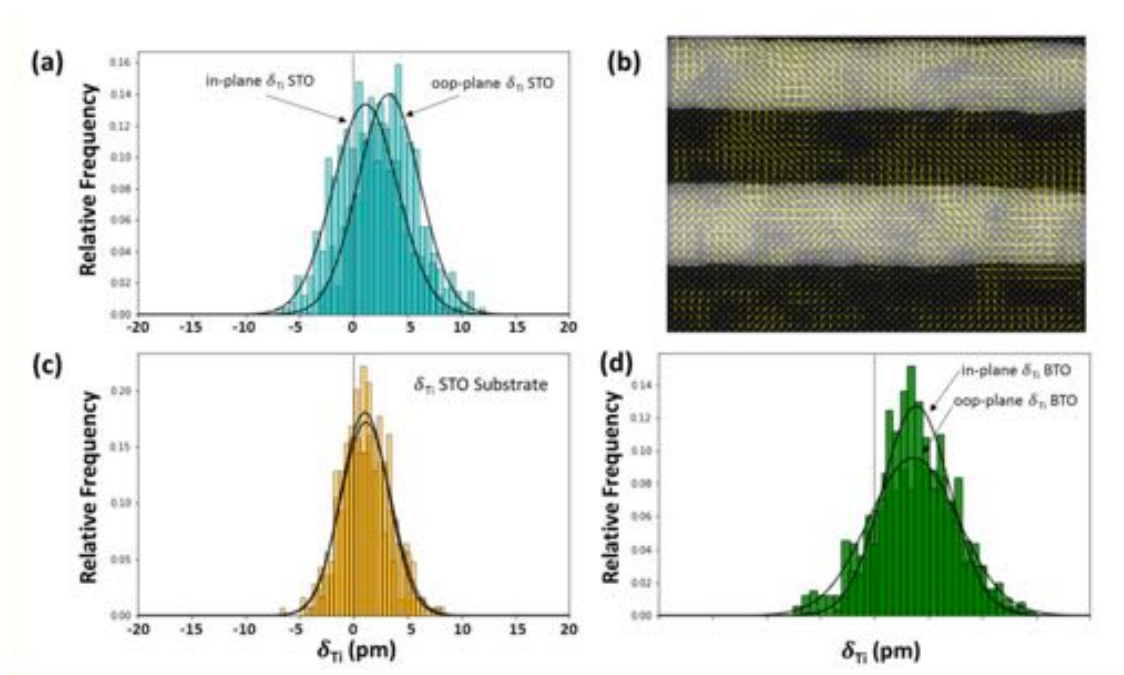
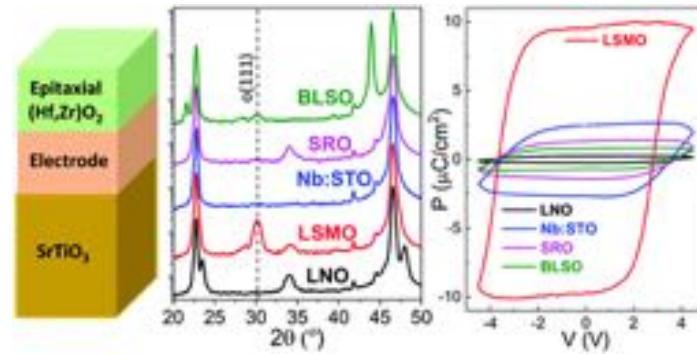


Figure A.3.2: In (a) and (d) the δ_{Ti} histograms of the ip and oop components in STO and BTO layers are shown, respectively. In (b) the dipole map on the HAADF image is shown with superimposed light and dark stripes that indicate the regions classified as BTO and STO, respectively. (c) displays the δ_{Ti} ip and oop components histograms at the STO substrate.

Chapter 4: The Epitaxial Stabilization of Ferroelectric $\text{Hf}_{0.5}\text{Zr}_{0.5}\text{O}_2$ Thin Films on Perovskites



Epitaxial orthorhombic $\text{Hf}_{0.5}\text{Zr}_{0.5}\text{O}_2$ (HZO) films on $\text{La}_{0.67}\text{Sr}_{0.33}\text{MnO}_3$ (LSMO) electrodes show robust ferroelectricity, with high polarization, endurance and retention. Meanwhile, reports of ferroelectric HfO_2 based films on perovskites other than LSMO are extremely rare, suggesting that LSMO is critical to ferroelectricity. In this chapter, HZO films grown on LSMO and other conducting perovskite electrodes are compared. A small amount of orthorhombic phase and low polarization is found in HZO films grown on La-doped BaSnO_3 and Nb-doped SrTiO_3 , while null amounts of orthorhombic phase and polarization are detected in films on LaNiO_3 and SrRuO_3 . While epitaxial stress is discarded as the cause, the chemistry at the interface appears to be critical. Indeed, engineering the HZO bottom interface on just a few monolayers of LSMO permits the stabilization of the orthorhombic phase. Furthermore, while the specific divalent ion (Sr or Ca) in the manganite is not relevant, reducing the La content causes a severe reduction of the amount of orthorhombic phase and the ferroelectric polarization in the HZO film. Inspection of a HZO/LSMO/ SrTiO_3 heterostructure, by STEM shows that the LSMO surface, expected to be mostly MnO_2 -terminated, undergoes a chemical reconstruction consisting of the substitution of the MnO_2 plane by a mixture of Hf and Zr cations with oxygen. Density-functional-theory calculations show that the substitution of Mn by Hf on the MnO_2 -terminated surface of LSMO is energetically favorable, as the higher electronegativity and valence of Hf with respect to Mn help to balance the surface charges.

4.1 Introduction

Most of the research on ferroelectric HfO₂ has been conducted with polycrystalline films, generally grown by atomic layer deposition. Epitaxial films, with more controllable microstructure, are better suited for studies aiming at understanding the ferroelectric properties as well as for prototyping devices. However, the epitaxy of ferroelectric hafnia is challenging because it requires the formation of a metastable orthorhombic phase instead of the paraelectric phase that is stable in bulk. Yet, the effort is worthy as examples of usefulness of doped HfO₂ epitaxial films include the achievement of coercive field (E_c) - thickness (t) $E_c \sim t^{-2/3}$ scaling,^{122,123} the separation of ionic and electronic transport contributions in ferroelectric tunnel junctions,¹²⁴ or the achievement of simultaneous high polarization, endurance and retention in films thinner than 5 nm.¹²⁵ For these reasons epitaxial films are being investigated now very actively. Several conducting or semiconducting substrates or templates, including Si wafers,¹²⁶ TiN,¹²⁷ GaN,¹²⁸ and indium tin oxide,¹²⁹ the fluorite yttria-stabilized zirconia (YSZ)^{127,130,131} and pyrochlore oxides¹³² have been used to deposit epitaxial films of ferroelectric doped HfO₂. In contrast, epitaxy of ferroelectric hafnia on perovskite-type oxide electrodes has only been reported on Nb-doped SrTiO₃ (Nb:STO)¹³³ and La_{0.67}Sr_{0.33}MnO₃ (LSMO).^{122,134–140} Epitaxy on other popular perovskite electrodes, such as SrRuO₃ (SRO) or LaNiO₃ (LNO), has not been achieved as far as we know. This is in stark contrast to conventional ferroelectric perovskites, which can be grown epitaxially on a large number of metal and oxide electrodes.^{1,141,142} It should be noted that the epitaxy of ferroelectric hafnia is challenging because it requires the formation of a metastable orthorhombic phase instead of the paraelectric phase that is stable in bulk.

In this chapter, the effect of the bottom electrode on the stabilization of orthorhombic and monoclinic Hf_{0.5}Zr_{0.5}O₂ polymorphs (o-HZO and m-HZO, respectively) in HZO thin films and on the ferroelectricity of the film is studied. In a first section, a systematic study of the impact of the lower electrode on the epitaxial stabilization of the ferroelectric hafnia is presented. First, a series of HZO films were deposited on a set of conducting epitaxial oxide thin films: LNO, LSMO, SRO and Ba_{0.95}La_{0.05}SnO₃ (BLSO) grown on STO(001). In addition, a Nb-doped STO substrate was also used as electrode. Secondly, HZO films were deposited on lower electrodes formed by two stacked conductive oxides; the one interfacing HZO being around only three unit-cells thick. Finally, we have also explored the use of manganite electrodes with a different chemical composition (LaMnO₃ doped either with Sr or Ca) and with different amount of doping (half-doped or optimally doped). This strategy is expected to reveal valuable information regarding the role of the interfacial chemistry in the stabilization of ferroelectric hafnia on perovskites. In a second and third sections, the structure and

chemistry of the o-HZO/LSMO, m-HZO/LSMO, m-HZO/LNO and m-HZO/SRO are studied with atomic resolution by STEM.

4.2 Stabilization of the Ferroelectric Phase on Different Electrodes

In a first series, bottom conducting LNO, LSMO, SRO and BLSO layers and top 9.5 nm thick HZO films were deposited in a single process on STO(001) (Figure 4.1 (a)). A HZO film was deposited also on a bare conducting Nb:STO(001) substrate. The lattice parameter of the electrodes in bulk (Figure 4.1 (b)) varies within a wide range from 3.86 Å (LNO) to 4.11 Å (BLSO), while the lattice parameter of the STO substrate is 3.905 Å. Figure 4.1 (c) shows XRD 2θ - χ frames (2θ from 20° to 50° , χ from around -20° to $+20^\circ$ for the smallest 2θ values) of the five samples. The highest intensity spots in all samples, located at $\chi = 0^\circ$ (corresponding to the surface normal) and 2θ around 22.8° and 46.5° , correspond to (001) and (002) reflections of substrates and electrodes. The other spots are reflections from the HZO film. The film on LSMO exhibits a very bright spot at $\chi = 0^\circ$ and $2\theta \sim 30.2^\circ$, corresponding to the o-HZO(111) reflection. There is also a weaker intensity spot, centered at $\chi = 0^\circ$ and elongated from around $\chi = -5^\circ$ to $+5^\circ$, at $2\theta \sim 34.1^\circ$, corresponding to the position of the monoclinic (002) reflection. Thus, the HZO film on LSMO presents (111)-oriented orthorhombic phase along with a minority monoclinic (001)-oriented phase. This finding can be appreciated also in the θ - 2θ scan obtained by integration around $\chi = 0^\circ$ (Figure 4.1 (d), red line). A detailed structural characterization of equivalent samples confirmed that both phases are epitaxial.^{122,134,139} In contrast, the films on LNO and SRO do not show the reflection from the orthorhombic phase, but they also exhibit the elongated monoclinic (002) spot at $2\theta \sim 34.1^\circ$. The integrated scans are shown in Figure 4.1 (d) (black and pink lines for LNO and SRO, respectively). On the other hand, the frames of the HZO films on Nb:STO and BLSO do not display evident symmetric reflections ($\chi = 0^\circ$) from the film. The integrated scans around $\chi = 0^\circ$ in Figure 4.1 (d) show no HZO peaks for the film on Nb:STO (blue line) and a tiny o-HZO(111) peak for the film on BLSO (green line). However, the XRD frames of the two films exhibit asymmetrical reflections that did not appear in the other samples. In the film on Nb:STO, there is a pair of spots at 2θ around 30.2° , corresponding to o-HZO(111), and $\chi = -15^\circ$ and $+15^\circ$. This finding indicates tilted epitaxy,¹⁴³ with o-HZO(111) crystallites tilted $\sim 15^\circ$ with respect to the normal direction. A similar pair of tilted o-HZO(111) spots are present in the film on BLSO, but this time at $\chi = -19/+19^\circ$ and having weaker intensity.

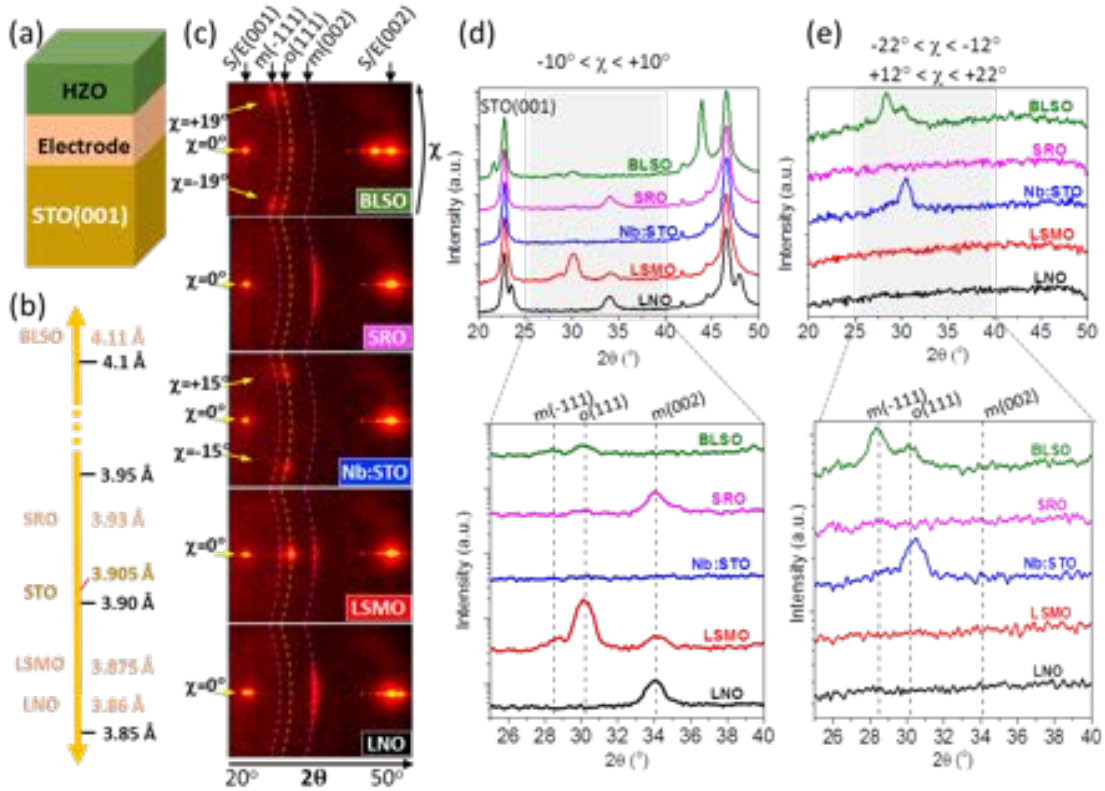


Figure 4.1: (a) Sketch of the epitaxial HZO/electrode heterostructures on STO(001). (b) Lattice parameters (bulk) of the perovskite electrodes. (c) XRD 2θ - χ frames. The electrode is indicated at the bottom right of each frame. Dashed yellow and pink lines mark the 2θ positions of the observed orthorhombic and monoclinic reflections, respectively. These reflections, as well as the (001) and (002) reflections of substrate (S) and electrode (E), are marked also by arrows in the top of the panel. The 2θ range is indicated in the frame shown in the bottom. (d) θ - 2θ scans obtained by integrating χ in the -10° to $+10^\circ$ range, or a smaller range with the aim of maximizing the signal/background ratio. Bottom: zoomed scans around orthorhombic o-HZO(111) and the monoclinic m-HZO(-111) and (002) reflections. (e) Equivalent θ - 2θ scans obtained by integrating χ in the -22° to -12° and $+12^\circ$ to $+22^\circ$ ranges, or smaller ranges to maximize the signal/background ratio.

Moreover, these spots are accompanied by another couple of spots, at the same $\chi = -19^\circ/+19^\circ$ and $2\theta \sim 28.5^\circ$ that corresponds to monoclinic HZO(-111), having greater intensity on BLSO. The θ - 2θ scans obtained by integration around $\chi = -19^\circ$ (from -22° to -16°) and $+19^\circ$ (from $+16^\circ$ to $+22^\circ$), Figure 4.1 (e), evidence the presence of these asymmetrical reflections in the films on Nb:STO (blue line) and BLSO (green line), and its absence in the other samples.

PUND measurements were conducted to evaluate the ferroelectricity of the HZO films (Figure 4.2). The current-voltage (I-V) curves (Figure 4.2 (a)) and the corresponding polarization loops (Figure 4.2 (c)) confirm the ferroelectricity of the film on LSMO, with remanent polarization $P_r \sim 10 \mu\text{C}/\text{cm}^2$ and coercive electric field $\sim 3.4 \text{ MV}/\text{cm}$. Zoomed I-V curves and polarization loops of the other

samples are depicted in Figure 4.2 (b) and Figure 4.2 (d), respectively. The films on Nb:STO (blue curve) and BLSO (green curve) show ferroelectric switching peaks at around 4 V (Figure 4.2 (b)), signaling ferroelectric nature of the samples. Note that loops in Figure 4.2 (b) are not saturated, so accurate polarization values cannot be given. The film on SRO shows a hysteretic I-V curve, but without a peak. This result could be in agreement with a minor I-V loop (where $V_{\max} < V_c$) of a ferroelectric material. However, I-V curves collected at higher voltages result in device failure before observing any current peak. The absence of ferroelectric current switching peak and the absence of orthorhombic phase traces in the sample (Figure 4.1) are indicative that switchable current results from non-ferroelectric contributions, most probably intrinsic electroresistance. The I-V curve of the film on LNO is similar to the one on SRO, but with significantly lower current values. The ferroelectric measurements are thus in agreement with the distinct presence of the orthorhombic phase in the samples (Figure 4.1), confirming the critical effect of the LSMO electrode in the epitaxial stabilization of the orthorhombic phase.

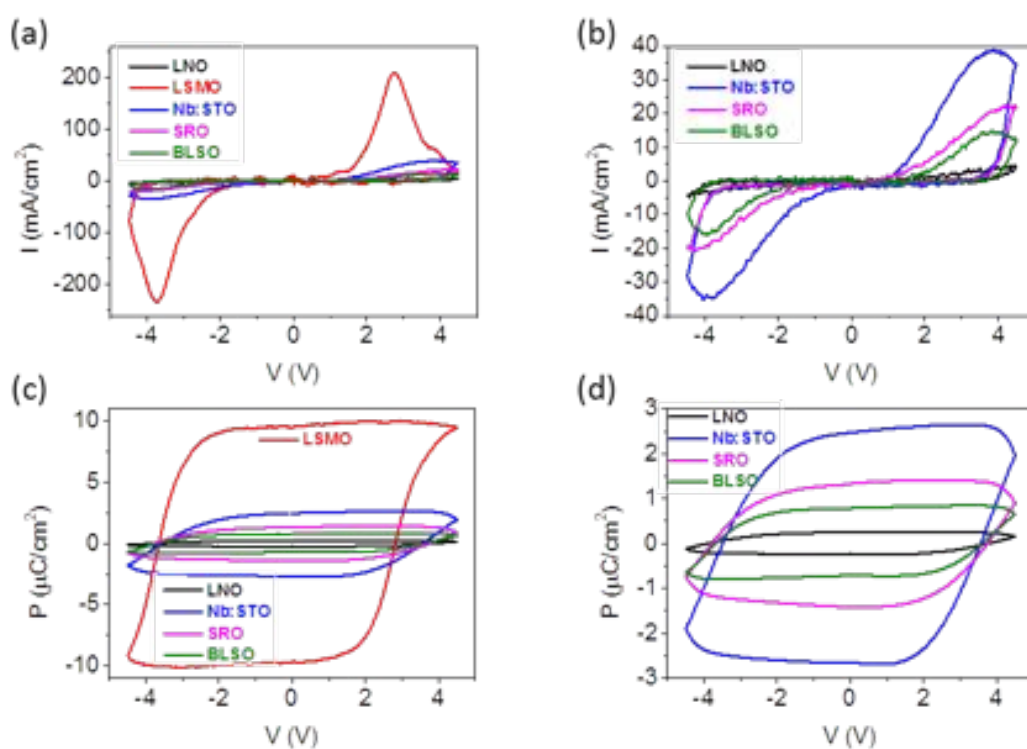


Figure 4.2: (a) I-V curves of the HZO films grown on the different perovskite electrodes. The I-V curves of the four films with lowest current are zoomed in (b). (c) Polarization loops, with zooms of the four films with lowest polarization in (d). Polarization loops were collected after 10 cycles. Figure A.4.1, Appendix 4-A compares the loops in pristine state and measured after 2 and 10 cycles.

Epitaxial stress has a major influence on the stabilization of the orthorhombic phase on LSMO electrodes (see Chapter 5).¹³⁹ However, the notorious differences in stabilized phases and orientation of the HZO films on the set of five electrodes do not correlate with the bulk lattice parameter of the

electrodes (Figure 4.1 (b)). Nevertheless, the electrode thin films could be strained. To estimate accurately the out-of-plane lattice constant of the thin film electrodes, not only the 2θ values from the values extracted from Figure 4.1 were used, but also those from θ - 2θ scans around symmetrical reflections acquired with point detector¹⁴⁴ (not shown here) were used. The out-of-plane lattice parameters, determined from the position of the corresponding (002) diffraction peaks, are $d_{\text{LNO}} = 3.79 \text{ \AA}$ (3.86 \AA in bulk), $d_{\text{LSMO}} = 3.86 \text{ \AA}$ (3.875 \AA in bulk), $d_{\text{SRO}} = 3.94 \text{ \AA}$, value extracted from the fit of two Gaussian curves to STO(002) and SRO(002), (3.93 \AA in bulk), and $d_{\text{BLSO}} = 4.12 \text{ \AA}$ (4.1 \AA in bulk), indicating that LNO, LSMO and SRO are strained, and BLSO is plastically relaxed. The in-plane lattice parameter of LNO, LSMO and SRO is expected to be coincident with the lattice parameter of the STO substrate (as measured in refs.^{139,145}), very similar to that of the conducting Nb:STO(001) substrate, and significantly smaller than the in-plane lattice parameter of relaxed BLSO. Therefore, a completely different epitaxial stabilization in this series of films takes place despite the almost coincident in-plane lattice parameter (and thus the lattice mismatch with HZO polymorphs) of four of the samples in the series.

Since the critical impact of the electrodes on the epitaxial stabilization of the ferroelectric phase is not caused by differences in the epitaxial stress, other factors that can modify the interface energy and therefore the epitaxial stabilization need to be considered. To evaluate if the different chemical composition and atomic structure of the surface of the electrodes is a relevant factor, HZO films were deposited on SRO and LNO electrodes covered by an ultra-thin ($\sim 1.2 \text{ nm}$) LSMO layer, and on LSMO electrodes covered by an ultra-thin ($\sim 1.2 \text{ nm}$) LNO or SRO layer (Figure 4.3 (a)). The XRD 2θ - χ frames (Figure 4.3 (b)) demonstrate that the effect of the ultra-thin layer interfacing HZO is huge. While HZO films grown on bare SRO or LNO are purely monoclinic, the films on either LSMO/SRO or LSMO/LNO are mostly orthorhombic, being in fact the frames very similar to those of the HZO film grown on bare LSMO. In contrast, the o-HZO(111) reflection is very weak in the film on SRO/LSMO, and in the film on LNO/LSMO there is only a high intensity spot corresponding to the monoclinic (002) reflection. The integrated θ - 2θ scans in Figure 4.3 (c) summarize the effect of the 1.2 nm thick layers on the stabilization of the different HZO polymorphs.

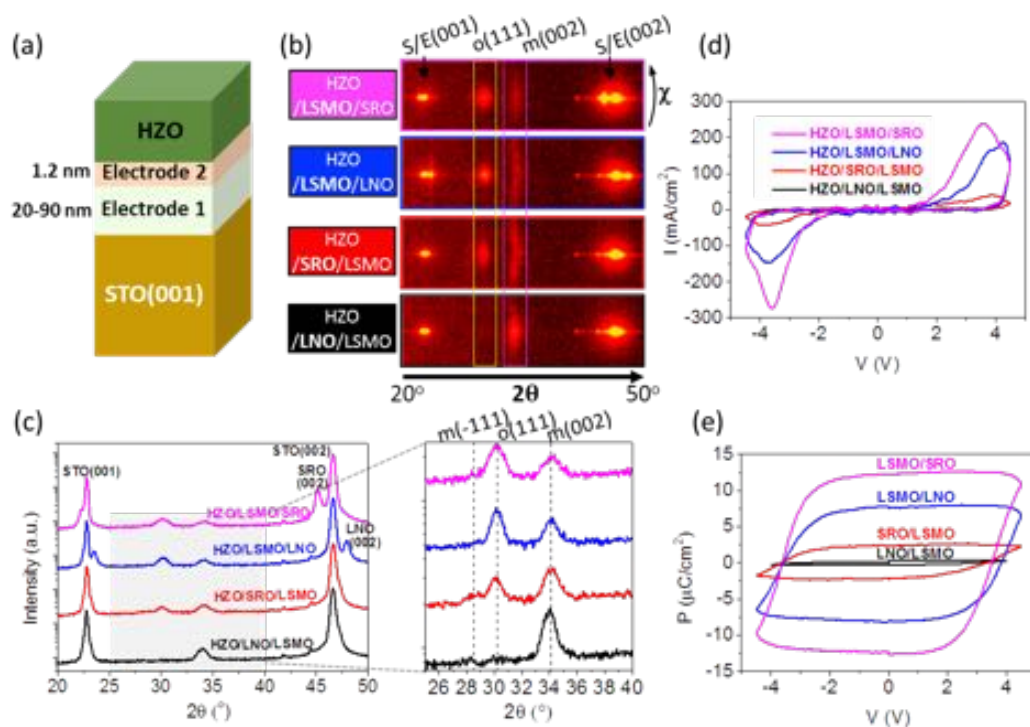


Figure 4.3: (a) Sketch of the epitaxial HZO/bilayer electrode heterostructures, in which the electrode interfacing HZO is 1.2 nm thick. (b) XRD 2θ - χ frames of the samples. The bilayer electrode is indicated at the left of each frame. Vertical yellow and pink rectangles mark the orthorhombic *o*-HZO(111) and monoclinic *m*-(002) reflections. The (001) and (002) reflections of substrate (S) and electrodes (E) are marked by arrows. (c) θ - 2θ scans obtained by integrating the XRD 2θ - χ frames in the χ - 10° to $+10^\circ$ range. Right: zoomed scans around the monoclinic *m*-HZO(002) and *m*-HZO(-111), and orthorhombic *o*-HZO(111) reflections. (d) I-V curves and (e) corresponding polarization loops of the HZO films

The I-V curves (Figure 4.3 (d)) and the corresponding polarization loops (Figure 4.3 (e)) confirm the huge effect: polarization is high when the ultra-thin layer interfacing HZO is LSMO, very small when this layer is SRO, and null when the layer is LNO. It is important to note that the non-negligible amount of orthorhombic phase present in the film on SRO/LSMO most probably originates from an incomplete coverage of the LSMO surface by SRO, as shown by cross-sectional scanning transmission electron microscopy images of the interface. This is because minority $\text{La}_{0.67}\text{Sr}_{0.33}\text{O}$ and majority MnO_2 chemical terminations coexist in LSMO, and SRO only nucleates on MnO_2 termination due to the high vapor pressure of Ru.¹⁴⁶ Figure 4.4 (a) and (b) show high field of view cross-sectional Z-contrast images of the HZO films on bilayer electrodes with ultra-thin SRO and LNO layers in contact with the HZO, respectively. As can be appreciated in the corresponding high magnification images presented in Figure 4.4 (c) and (d), SRO tends to accumulate in 3-D grains leaving areas of the LSMO surface uncovered. On the other hand, LNO forms a thin continuous layer of homogeneous thickness that fully covers the LSMO surface. Note that the LNO layer can be easily identified due to the higher intensity of the atomic columns of LNO compared to those of the LSMO layer (Figure 4.4

(d). This difference arises from the larger La content (which is a heavier element $Z_{\text{La}}=57$, $Z_{\text{Sr}}=38$) of the LNO layer. While the high-resolution Z-contrast images of the inspected areas revealed monoclinic grains with both (100) and (001) out-of-plane orientations in both samples, XRD (Figure 4.3) indicate that (001) is the dominant orientation.

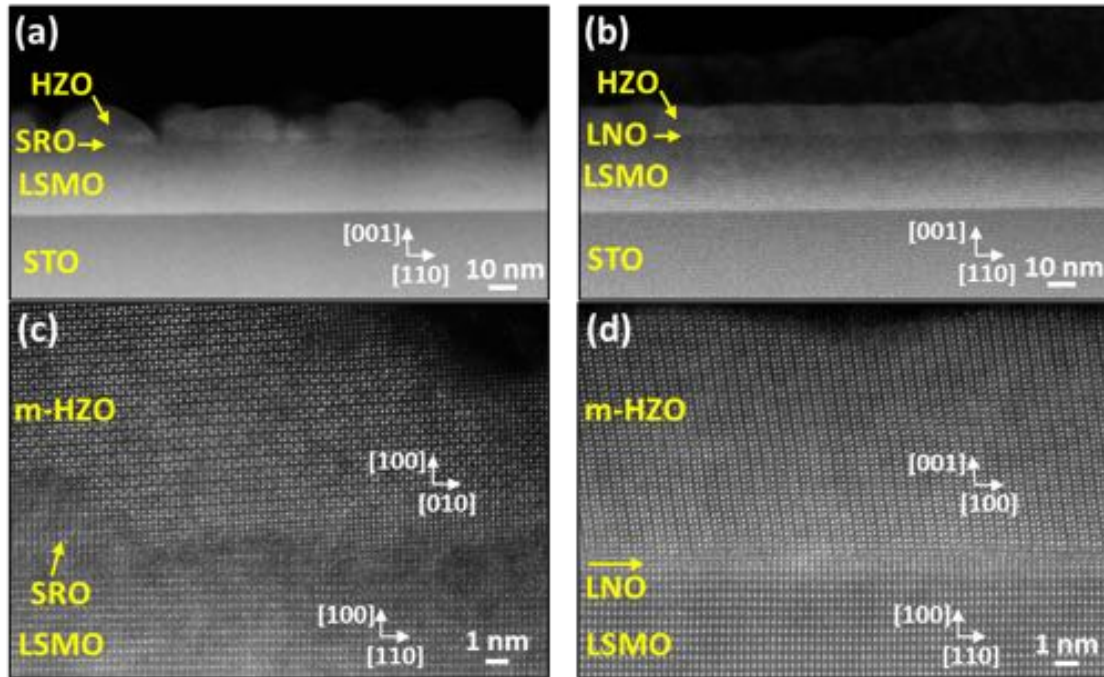


Figure 4.4. (a) and (b) show high field of view cross-sectional Z-contrast images of the HZO films on bilayer electrodes with ultra-thin SRO and LNO layers in contact with the HZO, respectively. (c) and (d) exhibit the atomic resolution images corresponding to the LSMO electrode, the SRO (c) and LNO (d) ultra-thin layers, and the HZO film.

It is demonstrated that LSMO has to interface HZO to stabilize the orthorhombic phase, and, as reported in ref.¹³⁹, the amount of orthorhombic phase depends on the strain of the LSMO when different substrates are used (see Chapter 5). Probably, the chemical composition and crystal structure of the LSMO surface reduces the energy at the interface between the electrode and the orthorhombic phase, favoring its formation instead of the other HZO polymorphs with lower energy in bulk. To gain insight about this phenomenon, a series of four HZO/manganite/STO(001) samples (Figure 4.5 (a)) were prepared using manganite electrodes with different chemical composition, $\text{La}_{1-x}\text{A}_x\text{MnO}_3$ ($\text{A} = \text{Sr}, \text{Ca}; x = 0.33, 0.5$). The XRD 2θ - χ frames scans in Figure 4.5 (b) and the integrated θ - 2θ scans in Figure 4.5 (c) show that there are no significant differences between the two films grown on optimally doped manganites ($x = 0.33$): a bright o-HZO(111) and a low intensity elongated monoclinic (002) spot, indicating that the epitaxial orthorhombic phase constitutes the majority for films on both Sr and Ca optimally doped manganites.

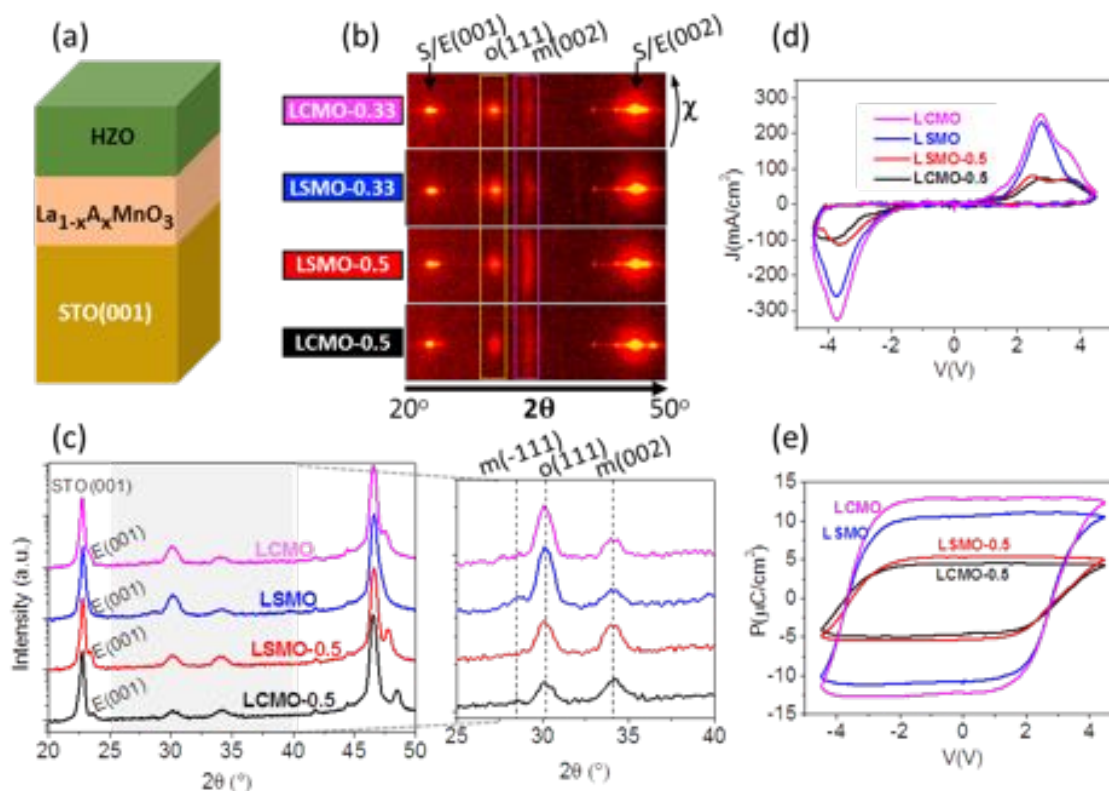


Figure 4.5: (a) Sketch of the epitaxial HZO/ $\text{La}_{1-x}\text{A}_x\text{MnO}_3$ heterostructures. (b) XRD 2θ - χ frames of the samples. The $\text{La}_{1-x}\text{A}_x\text{MnO}_3$ composition ($A = \text{Sr}$ or Ca , and $x = 0.33$ or 0.5) is indicated at the left of each frame. Vertical yellow and pink rectangles mark the orthorhombic o -HZO(111) and monoclinic m -(002) reflections, respectively. The (001) and (002) reflections of substrate (S) and electrodes (E) are marked by arrows. (c) θ - 2θ scans obtained by integration in χ between -10° and $+10^\circ$. Right: zoomed scans around the monoclinic m -HZO(002), and orthorhombic o -HZO(111) reflections. (d) I-V curves and (e) corresponding polarization loops of the HZO films.

In contrast, the frames of the two films on half-doped manganites ($x = 0.5$) show weaker o -HZO(111) diffraction spots, particularly on the Ca-doped electrode, whereas the intensity of the elongated monoclinic (002) spot is increased in both films. The I-V curves and polarization loops (Figure 4.5 (d) and (e)) confirm that the four films are ferroelectric. The remanent polarization on both optimally doped electrodes ($x = 0.33$) is more than $10 \mu\text{C}/\text{cm}^2$, whereas the films on half-doped manganites ($x = 0.5$) have much lower polarization (Figure 4.5 (e)), in agreement with the smaller amount of orthorhombic phase observed. Small differences in the I-V curves and polarization loops have been observed during the first cycles, as shown in Figure A.4.2 (Appendix 4-A).

The results shown in Figure 4.5 prove that epitaxial stabilization of the ferroelectric HZO phase is reduced in films on manganite electrodes with lower La content. This finding can be due to a dependence on the La content of the interface energy between the manganite and orthorhombic HZO.

Differences in the electrical conductivity of the manganites could be also a factor to be considered. In bulk, half-doped manganites have much lower room-temperature conductivity than the corresponding optimally doped compounds. However, the conductivity of half-doped manganites increases extremely in high enough tensely strained films, and the electrical resistivity of elastically strained $\text{La}_{0.5}\text{Sr}_{0.5}\text{MnO}_3$ and $\text{La}_{0.5}\text{Ca}_{0.5}\text{MnO}_3$ epitaxial films on $\text{STO}(001)$ is around 10^{-3} and $1 \text{ } \Omega \cdot \text{cm}$, respectively.¹⁴⁷ The resistivity of the former is thus low enough to be used as electrode, while the higher resistivity of the latter could cause a depolarization field. However, the ferroelectric polarization of HZO on these electrodes is similar, despite the large difference in the electrode resistivity, thus disregarding the possibly relevant role of the electrostatic boundary conditions in the formation of the ferroelectric HZO phase. Therefore, the higher polarization of the films grown on optimally doped electrodes is the result of the greater amount of orthorhombic phase, likely due to an enhanced epitaxial stabilization on manganite electrodes with larger La content, regardless of whether the divalent atom is Sr or Ca.

Overall, this study confirms that the interface chemistry influences critically the stabilization of the metastable orthorhombic phase and consequently the ferroelectric polarization in epitaxial HZO films. Manganite electrodes are critical to epitaxially stabilize the ferroelectric orthorhombic phase of hafnia. Films deposited on other investigated conducting perovskite electrodes present low (on $\text{Nb}:\text{SrTiO}_3$ and $\text{Ba}_{0.95}\text{La}_{0.05}\text{SnO}_3$) or null (on LaNiO_3 and SrRuO_3) orthorhombic phase and ferroelectric polarization. We show that engineering the interface with a few LSMO monolayers permits stabilizing the ferroelectric phase. Yet, while the effectivity of the $\text{La}_{1-x}\text{A}_x\text{MnO}_3$ manganites does not depend on the divalent ion A, being that either Sr or Ca, it is found to be greater for optimally doped manganites ($x = 0.33$) than for manganites with lower La content. In the case of ferroelectric perovskites, the effects of the interface chemistry on the polarization are known. In particular, the chemical termination of the LSMO bottom electrode, can have huge effect on the polarization, as demonstrated in BiFeO_3 ¹⁴⁸ and PbTiO_3 ¹⁴⁹ films. The orthorhombic phase of HZO forms on manganite electrodes, and its formation is favored on $\text{La}_{1-x}\text{A}_x\text{MnO}_3$ with greater La content, while HZO on LNO is monoclinic despite the presence of La atoms. $\text{La}_{1-x}\text{A}_x\text{MnO}_3$ and LNO are grown on STO substrates, which present majority of TiO_2 -termination, and therefore $\text{La}_{1-x}\text{A}_x\text{MnO}_3$ and LNO are expected to be mostly MnO_2 and NiO_2 terminated, respectively. Thus, the impact of La content in the manganite electrode on the epitaxial stabilization of the orthorhombic phase points to a complex interface. Detailed studies of the atomic structure at HZO/LSMO interface may help to understand the intriguing mechanisms of the epitaxial stabilization of the orthorhombic phase. In this spirit, a detailed characterization of the HZO/LSMO interface is carried out with STEM in the next section.

4.3 Insights into the Atomic Structure of the $\text{Hf}_{0.5}\text{Zr}_{0.5}\text{O}_2/\text{La}_{0.7}\text{Sr}_{0.3}\text{MnO}_3$ Interface

The use of a $\text{La}_{2/3}\text{Sr}_{1/3}\text{MnO}_3$ (LSMO) buffer layer directly in contact with HZO seems to be essential to stabilize the metastable ferroelectric phase on the perovskite substrates. These results suggest that the chemistry may play a fundamental role in the competing stabilization of the different polymorphs. However, the precise atomic structure of the HZO/LSMO heterointerface remains unknown. In this section, we provide insights into the structure and chemistry of the HZO/LSMO interface in the HZO/LSMO/STO heterostructure by combining STEM and density-functional-theory (DFT) calculations.

4.3.1 STEM characterization of the HZO/LSMO Interface

As shown in the previous section, o-HZO (111)-oriented o-HZO coexists with non-ferroelectric monoclinic HZO,¹³⁹ both phases being epitaxial to LSMO (see Chapter 5 for more details). Herein, we focus on the interface between the ferroelectric o-HZO and the LSMO buffer layer. The interface between the paraelectric monoclinic phase of HZO and the LSMO buffer is also studied in detail, revealing small differences with the orthorhombic phase that will be shown later. Figure 4.6 (a) and (b) show two Z-contrast images of the interface between (111) o-HZO and the LSMO layer viewed along the [100] and [110] LSMO zone axis, respectively (as a consequence, o-HZO is also viewed along two different zone axes). The (111) o-HZO crystallites are twinned on the four-fold LSMO surface, being the o-HZO grains aligned with either [0-22] or [-211] directions to [110] of LSMO (see more about this in Chapter 5).¹⁴⁰ The o-HZO (111) grain in Figure 4.6 (a) is not viewed along a major crystallographic direction. As a result, the Z-contrast image shows only bright stripes corresponding to the out-of-plane (111) HZO cation planes. On the other hand, the crystal structure of [0-22] and [-211] HZO grains, shown in Figure 4.6 (b) and 4.6 (c), respectively, become visible when the heterostructure is viewed along the substrate's [110] zone axes.

We observe rather striking features at the uppermost plane of the LSMO electrode (denoted with an “x” and marked with a yellow arrow in Figures 4.6 (a), (b) and (c)) and at the lowermost plane of the HZO layer. The intensity in a Z-contrast image is approximately proportional to the squared atomic number (Z^2) of the columns. Hence, the heavier cation columns appear brighter than the lighter cation columns. The anion columns (oxygens) are not visible due to dynamic range limitation of the detector. Accordingly, the Z-contrast images shown in Figure 4.6 give the expected contrast of an AMO_3 perovskite, such as the LSMO. The most intense atomic columns correspond to the mixed La/Sr sublattice ($Z_{\text{La}} = 57$, $Z_{\text{Sr}} = 38$), whereas Mn ($Z_{\text{Mn}} = 25$) atomic column appear slightly dimmer. While this holds true for both [100] and [110] zone axes, the uppermost plane with LSMO structure (denoted as “x”) shows a more intense atomic column than expected. Had the LSMO buffer layer ended with a

MnO_2 plane, its intensity would have been lower. This is clearly evidenced by tracing the profile intensity across the interface and comparing the intensity of the atomic plane x in both images, which is much higher than expected for the MnO_2 planes. Indeed, it suggests that Mn has been substituted by a much heavier atom, even heavier than La. Strikingly, the intensity of the first atomic plane of the HZO layer, named i in Figure 4.6, is lower than expected, which implies that the concentration of the heavy Hf ($Z_{\text{Hf}} = 72$) and to an extent Zr ($Z_{\text{Zr}} = 40$), is lower in this plane.

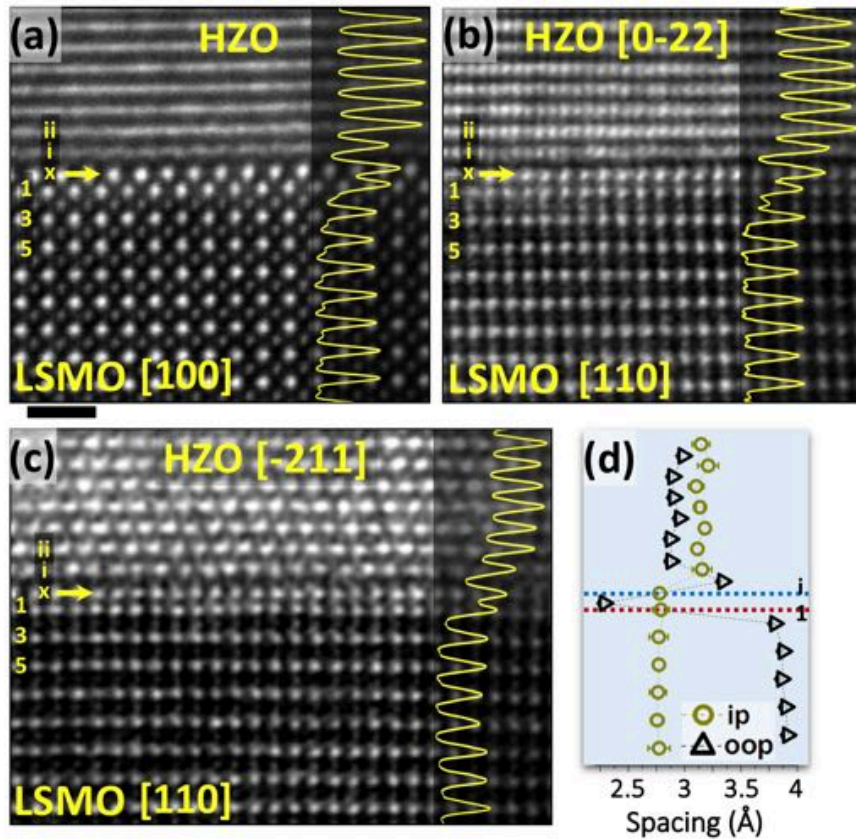


Figure 4.6. (a) Z-contrast image of the HZO/LSMO interface along the [100] LSMO zone-axis. (b) and (c) show images along the [110] LSMO zone-axis, displaying the two possible zone axes (according to the in-plane HZO twins) for the o-HZO grains. No HZO zone axis is close to the substrate [100] zone-axis in (a), and as a result, the HZO atomic columns are visible as bright horizontal stripes. The interface monolayer is denoted as x and it is indicated by a yellow arrow in both images, while the first atomic plane of the HZO layer is marked with an i . The averaged intensity profiles across the interface (along the out-of-plane direction) are shown at the right sides of (a), (b) and (c). The scale bar is the same for (a-c), corresponding to 1 nm. (d) in-plane and out-of-plane spacings between planes as seen along [110] of LSMO in the HZO twin variant shown in (c). The distance between consecutive $\text{La}_{0.67}\text{Sr}_{0.33}\text{O}$ planes is around $3.9 \pm 0.1 \text{ \AA}$, and that between plane x and i is around $2.3 \pm 0.1 \text{ \AA}$.

Further insights into this interface can be extracted by analyzing the spacings across the interface. For that, Gaussian curves were fitted to each atomic column in the observation plane of Figure 4.6 (c). Then, the distances between the centers of first neighbor Gaussians are taken as in-

plane and out-of-plane spacings and the averaged values are plotted as a function of the out-of-plane position, as shown in Figure 4.6 (d). The results show that the in-plane and out-of-plane spacings are, for both HZO and LSMO layers, constant beyond the interface and coinciding with the expected values,¹³⁹ 3.14 and 2.96 Å for HZO in-plane (distance equal to 3/2 of the distance between [-211] planes) and out-of-plane (111) spacings, respectively, and 2.76 and 3.9 Å for LSMO. Recall that the LSMO layer is fully strained on the STO substrate, thus replicating the in-plane lattice parameters of 3.9 Å for STO. However, the out-of-plane spacings at the interface deviate from the expected ones. Indeed, the distance between plane x and i (the first plane with HZO structure) is larger than the (111) HZO spacing (3.35 Å vs. 2.96 Å), and the distance from plane x to La (plane 1 in the image) is greater than the distance from La_{0.67}Sr_{0.33}O to MnO₂ planes (half the distance between La_{0.67}Sr_{0.33}O planes), 2.3 Å vs. 1.95 Å, respectively. The 2-D mapping of ip and oop spacings of the same area as Figure 4.6

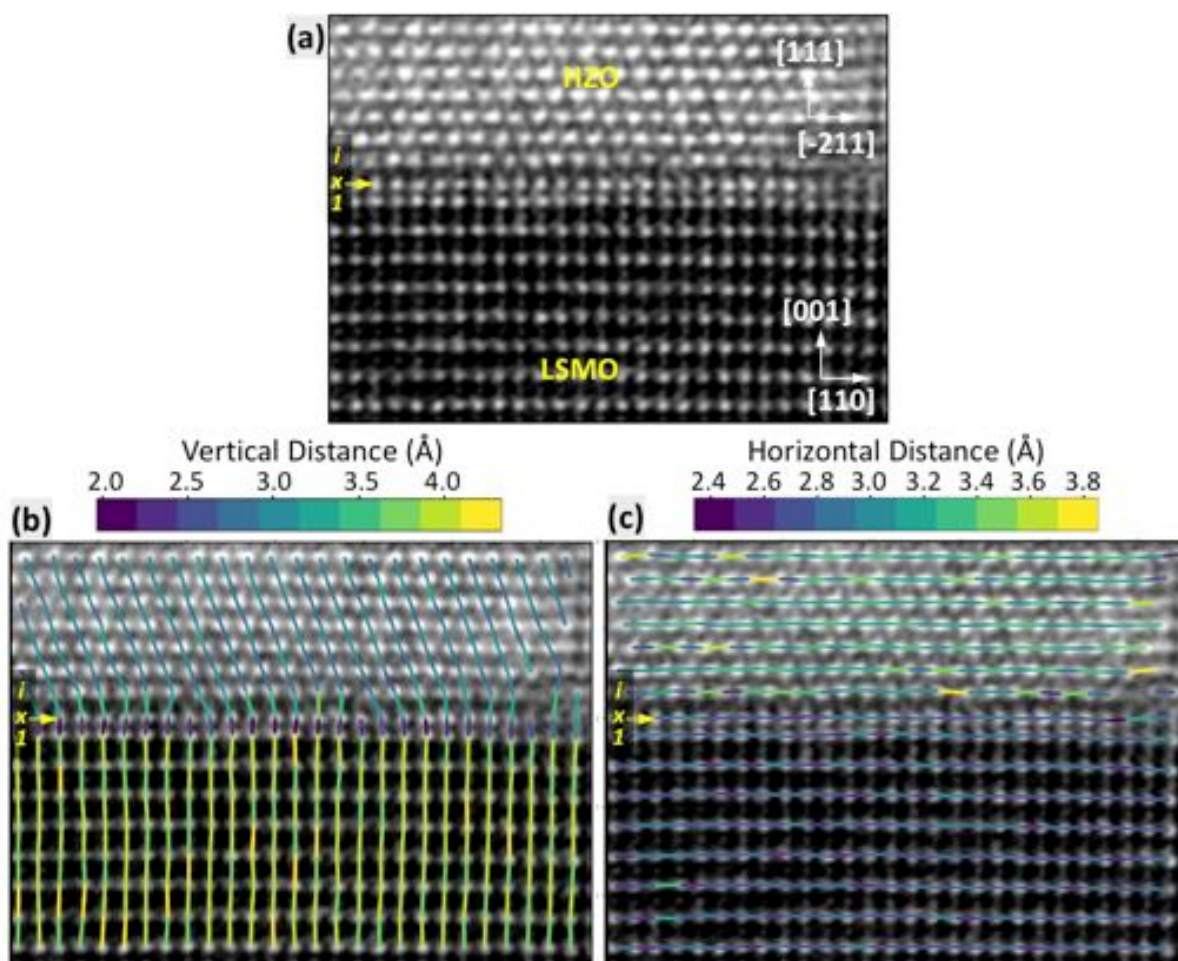


Figure 4.7: (a) HAADF image of the *o*-HZO(111)/LSMO interface. (b) corresponding map of the vertical atomic column distance across the *o*-HZO interface ((001) spacing in pseudocubic LSMO and (111) in the HZO film). Note that the atomic columns in HZO in (b) are connected along the diagonal but only the vertical component of the distance is represented by the colors. (c) map of the horizontal atomic column distance across the interface (distances corresponding to (110) spacing in pseudocubic LSMO and 3/2 of (-211) in the HZO film).

(c) is shown in Figure 4.7. Figure 4.7 (b) shows that oop spacings are constant in the LSMO below plane 1 and constant in the HZO above plane i, with different spacings between layers 1-x and x-i. In-plane spacings are constant in the LSMO up to layer x, acquiring in layer i and above the expected HZO spacings. It is worth noting that the out-of-plane spacings of the HZO twin variant shown in Figure 4.6 (b) across the interface follow the same trend (spacings profiles not shown here). These results show the presence of a sharp interface, ruling out the presence of a strain gradient in such dissimilar interface structures, as opposed to interfaces involving different perovskites such as $\text{LaAlO}_3/\text{SrTiO}_3$.⁵⁷

To reveal the chemistry at the interface, we used electron energy loss spectroscopy (EELS) to obtain chemical maps with atomic resolution. Figure 4.8 (a) shows a Z-contrast image of the interface. Figure 4.8 (b), (c), (d), (e) and (f) show elemental maps of La-M, Sr-L, Mn-L, Hf-M and Zr-L edges, respectively, from an EEL spectrum image that was acquired simultaneously with the Z-contrast image. The atomic resolution elemental maps reveal that the last plane that can be considered chemically LSMO is a $\text{La}_{0.67}\text{Sr}_{0.33}\text{O}$ plane. In contrast, the termination of the LSMO is expected to be

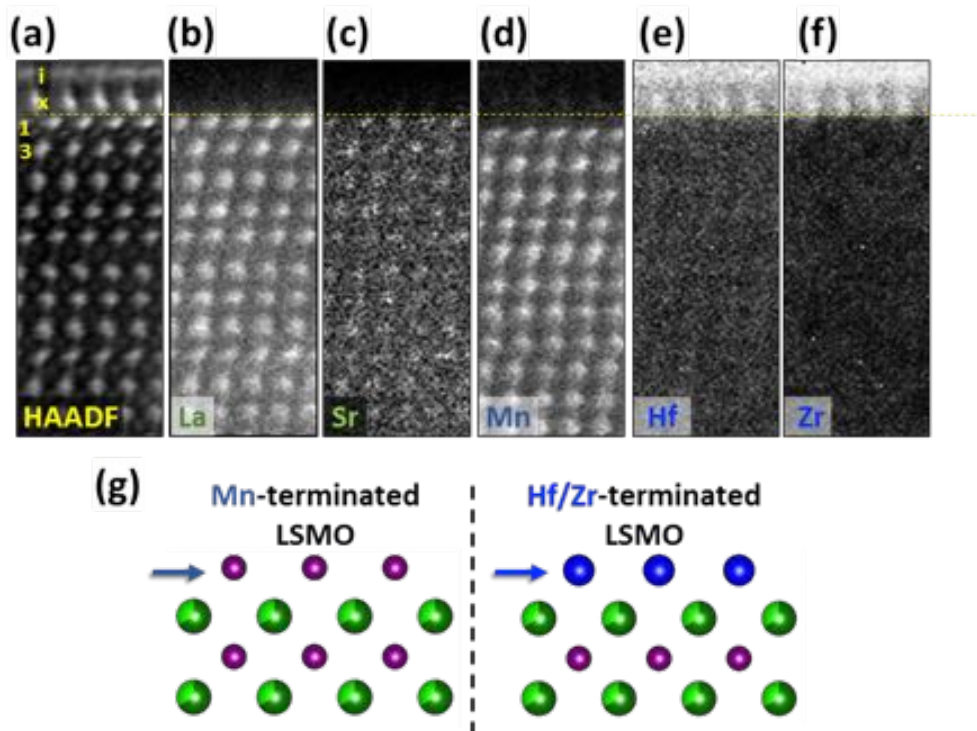


Figure 4.8: (a) HAADF image acquired simultaneously to the spectrum image along the $[100]$ zone axis. (b), (c), (d), (e) and (f) elemental maps of La-M, Sr-L, Mn-L, Hf-M and Zr-L edges, respectively. (g) Sketch of the uppermost region of the LSMO layer illustrating the substitution of the terminating Mn plane by Hf/Zr cations. Mn (purple), Hf/Zr (blue), La (dark green) and Sr (light green) atoms are shown.

primarily MnO_2 , with minor areas having $\text{La}_{0.67}\text{Sr}_{0.33}\text{O}$ termination.^{148,150} Different areas within the TEM specimen as well as different TEM specimens were inspected by EELS; they all revealed $\text{La}_{0.67}\text{Sr}_{0.33}\text{O}$ to be the last plane with LSMO chemical composition. Indeed, the Mn expected to be present at the upper surface of LSMO has been substituted by Hf/Zr atoms, as sketched in Figure 4.8 (g). In addition, the dimmer intensity of the first atomic plane shown by the Hf and Zr elemental maps suggests a lower concentration of these two elements right at the HZO/LSMO interface. These results

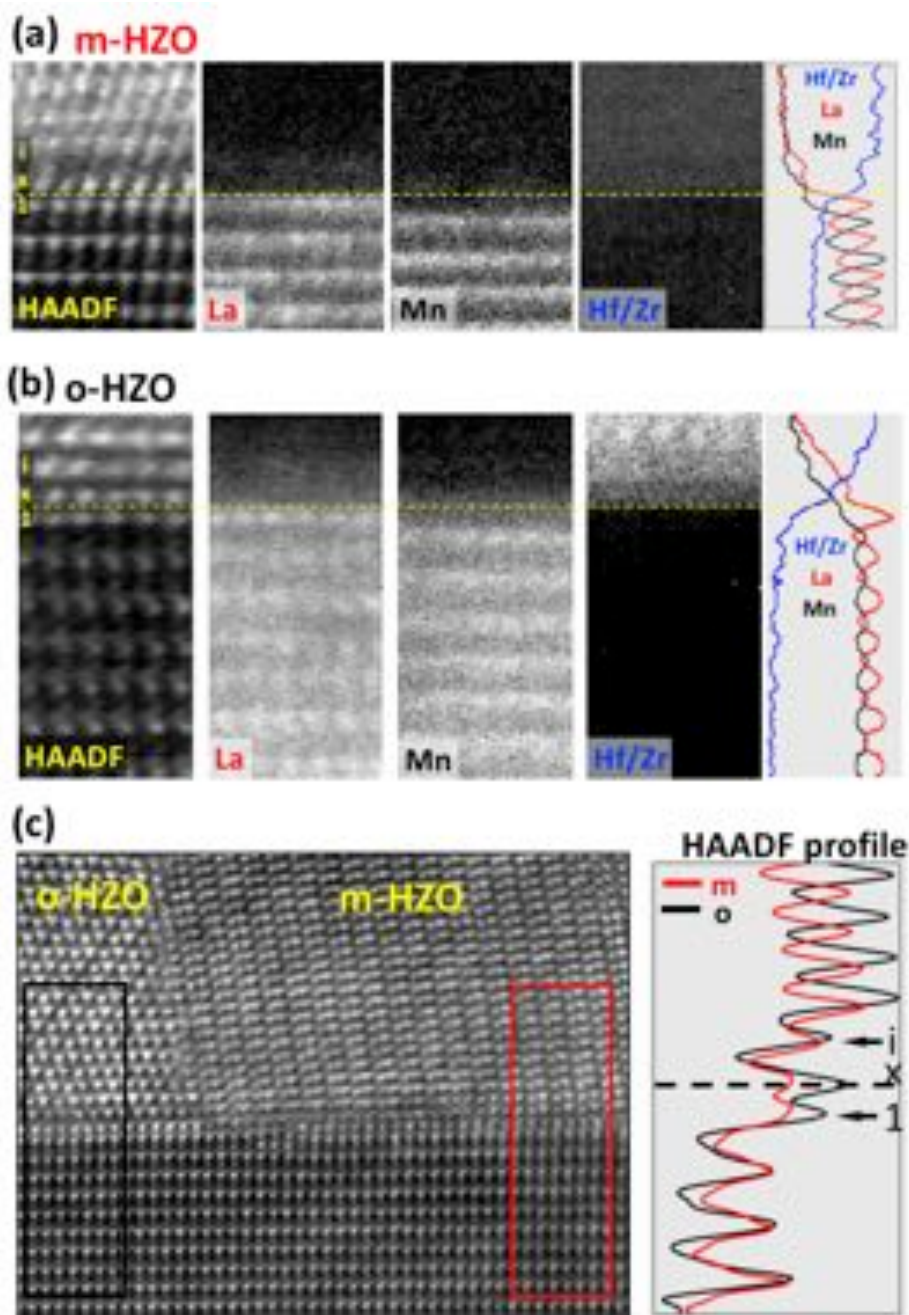


Figure 4.9: Comparison of the interfaces of o-HZO and m-HZO with the LSMO. (a) Interface with the monoclinic (HAADF image, La, Mn and Hf/Zr chemical maps and profiles). (b) Interface with the orthorhombic (HAADF image, La, Mn and Hf/Zr chemical maps and profiles). (c) HAADF showing the interface with the orthorhombic and monoclinic phases and intensity profiles across both interfaces in the highlighted regions.

account for the contrast observed in planes x and i of the Z-contrast images shown in Figure 4.6, and prove that a chemical reconstruction takes place at the HZO/LSMO interface.

Similar features are observed at the m-HZO/LSMO interface, with Hf/Zr occupying the Mn sites in layer x (Figure 4.9 (a) and (b)). However, HAADF images and EELS elemental maps of this interface show that the content of La and Hf/Sr in layers 1 and x, respectively, are lower (see Figure 4.9). The HAADF images show smaller intensity in layers 1 and x of the interface (Figure 4.9 (c)), suggesting that the chemistry may be slightly different compared with the one from the o-HZO/LSMO interface. Indeed, the profiles of the chemical composition show that layer 1 of the interface with the orthorhombic phase has an enhanced La content (Figure 4.9 (b)), while this is not observed at the interface with the monoclinic (Figure 4.9(a)). The observed differences may vary slightly depending on the explored location along the interface, but the features shown in Figure 4.9 are representative of the interface with the orthorhombic and monoclinic HZO phases.

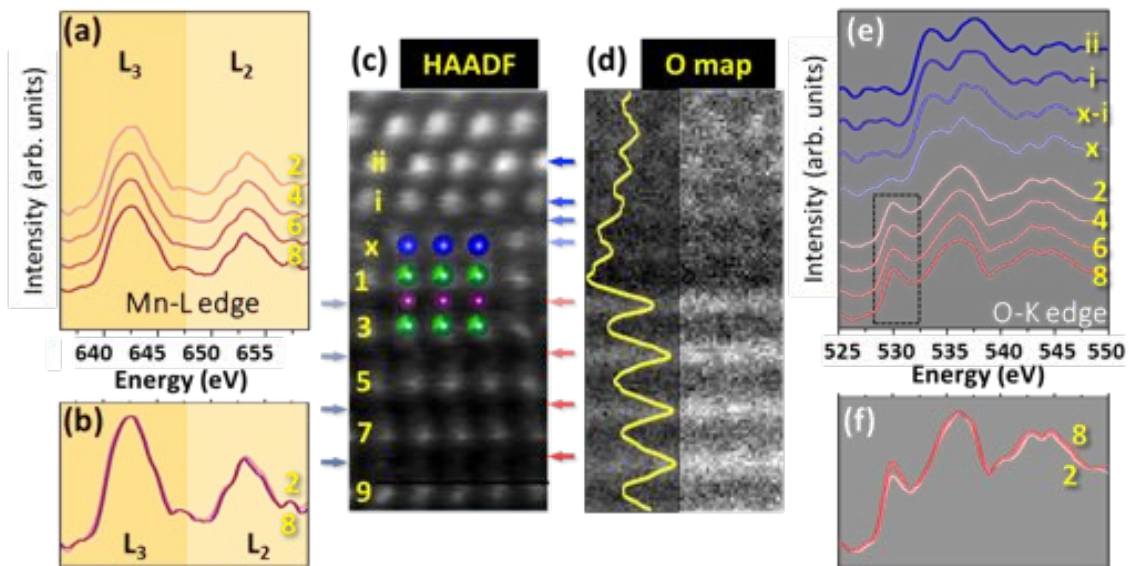


Figure 4.10: Change of electronic fine structure across the LSMO/o-HZO heterointerface tracked using row-averaged Mn L-edge (a) and O-K edge (e). (b) and (f) superimposed spectra of the uppermost (2) and lowermost (8) MnO_2 planes of Mn-L and O-K edges, respectively. (c) shows the HAADF image (acquired along the $[110]$ LSMO zone axis) from where spectra in (a) and (e) have been extracted, with the cation model structure superimposed (Mn (purple), Hf/Zr (blue), La (dark green) and Sr (light green)). The colors of the spectra (in (a), (b), (e) and (f)) and of the arrows (in (c)) indicate the element analyzed in each atomic plane, with Hf/Zr in blue, O in red and Mn in purple. The intensity ratio of the O pre-peak (at 527 eV) and the main peak (at 535 eV) is ~ 0.3 in the layers further from the interface, while this ratio becomes smaller (~ 0.2) at the interface, as shown in (f). (d) O elemental map across the LSMO/o-HZO heterointerface and the corresponding intensity profile (yellow background) shows a smaller O signal at the interface, indicating that a smaller quantity of O is present. The O map in (d) was obtained by integrating the O-K in each pixel from around 527 eV to around 540 eV.

EELS also allows tracking changes in the electronic structure across the interface. It is well known that Mn-L and O-K edges are very sensitive to changes in bonding, coordination and the oxidation state of Mn.¹¹⁷ Figure 4.10 shows the Mn-L and O-K edges from spectra acquired plane by plane (Figure 4.10 (a) and 4.10 (e)), starting far below the interface till the HZO layer (Figure 4.10 (c)). The Mn-L edge includes the L₃ and L₂ white lines at onset energies of about 640 and 650 eV, respectively. The intensity ratio of the L₃ and L₂ lines of the Mn L_{2,3} edge (the L₂₃ ratio) correlates with the oxidation state of Mn.¹¹⁷ The measured Mn L₂₃ ratio is close to that of LSMO compound, with a mix of Mn⁺² and Mn⁺³.¹¹⁷ But more importantly, the Mn L₂₃ ratio remains unchanged when shifting planes towards the interface, see Figure 4.10 (a) and (b). Hence, Mn does not change its oxidation state when approaching the HZO layer. Regarding the O-K edge (Figure 4.10 (e)), it shows a rather abrupt transition at the heterointerface, in agreement with the abrupt structural and chemical variations shown in Figure 4.6, 4.7 and 4.8. Within the LSMO layer, the O-K edge shows a pre-peak, with an energy onset at ~527 eV. The pre-peak disappears after the uppermost Mn plane, being present up to plane 1 but absent in plane x (the Hf/Zr monolayer that is present at the interface between LSMO and HZO), as shown in Figure 4.10 (e). This is not the only change that takes place in the O-K edge pre-peak, as its intensity decreases in the uppermost Mn plane as well; see Figure 4.10 (f), where two O-K edge spectra are compared, one from plane 1 and one from the lowermost MnO₂ plane shown (plane 8 in Figure 4.10 (c)). This pre-peak is sensitive to the partially filled 2p states of oxygen, which are hybridized with 3d states of manganese. Therefore, its variation in intensity is signaling either the presence of oxygen vacancies or transfer of electrons from Hf/Zr found in the perovskite plane x, or both; although the EELS oxygen elemental map, Figure 4.10 (d), reveals a weaker oxygen signal at the interface (especially at plane x), indicating that indeed oxygen is less abundant at the interface. Figure 4.11, acquired along the other inspected zone axis ([100] LSMO zone axis) also shows a decrease of the oxygen signal at the interface.

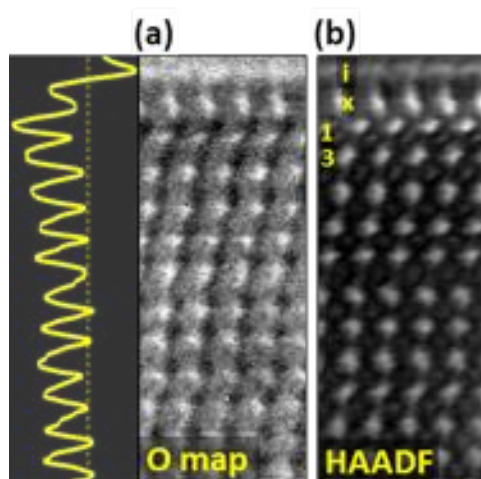


Figure 4.11. (a) Oxygen elemental map across the LSMO/o-HZO heterointerface with the averaged profile shown at the left. The shows a smaller O signal at the interface, indicating that a smaller quantity of O is present. (b) Corresponding HAADF image of the oxygen map in (a). The inspected area is the same as the one shown in Figure 4.8.

From the STEM-EELS experiments, we observe that the MnO_2 -terminated surface layer of LSMO undergoes a chemical reconstruction; specifically, Mn atoms are substituted by Hf/Zr atoms. The LSMO top surface is expected to exhibit MnO_2 termination,^{148,150} provided that the STO is mostly TiO_2 terminated, and the stoichiometry is expected to be maintained in films grown by pulsed laser deposition. Instead, we find Hf/Zr atoms at the said layer. Figure 4.12 shows the bottom LSMO interface with the STO substrate, revealing a TiO_2 -LaO interface, as opposed to a SrO - MnO_2 interface (note that the first monolayer containing Mn is found just above the first monolayer containing La). This supports a preferential MnO_2 termination at the top surface of the LSMO before the deposition of the HZO film. Moreover, an oxygen deficiency is detected at the interface, which indicates that the substitution of Mn atoms by Hf occurs under oxygen deprivation conditions. The presence of oxygen vacancies at the interface may also be relevant during the ferroelectric switching and screening,^{151,152} and electroresistance.^{124,153} Interfacial reconstructions leading to the formation of a hybrid atomic plane bridging two dissimilar structures have been reported to allow for heteroepitaxy of dissimilar oxides as binary oxides on perovskites.¹⁵⁴ These results rule out the presence of a tetragonal HZO phase at the LSMO/o-HZO interface of the explored specimen –the two atomic planes under the o-HZO structure contain La/Sr (plane 1) and Hf/Zr (plane x) cations at the perovskite A and M sites, respectively– contrary to what has been previously reported in an equivalent heterostructure.¹³⁵ Furthermore, the HZO cation sublattice shows structural features incompatible with the tetragonal phase, see Appendix 4-B. In brief, Figure A.4.3 shows that both the spacings and angles between atomic columns on the observation plane (corresponding to the (Hf/Zr) cation sublattice) reveal the expected “breathing” (periodic larger and smaller spacings and angles) of the orthorhombic phase, ruling out the presence of the tetragonal phase at the interface.

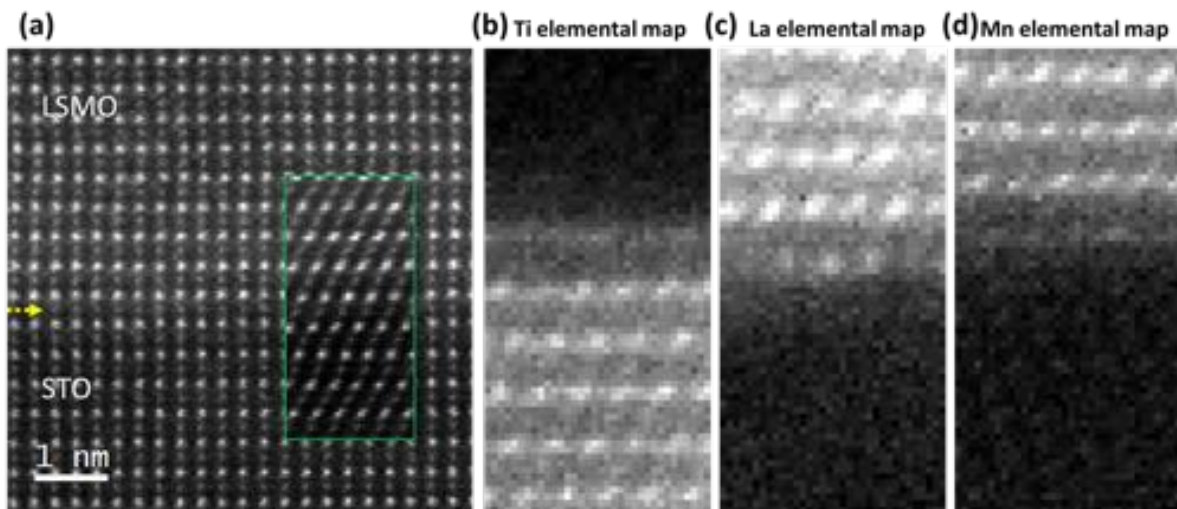


Figure 4.12: EELS elemental mapping of the LSMO/STO interface. (a) HAADF image of the LSMO/STO interface. The inset shows the simultaneously acquired HAADF image. The arrow marks the interface. (b-d) Ti L-edge, La M-edge and Mn L-edge elemental maps, respectively.

4.3.2 DFT calculations of the HZO/LSMO Interface

To understand the driving force for Hf substitution at the MnO_2 layer, we have simulated the initial growth process and compared the energetics of HfO_x ($x = 0, 1, 2$) clusters deposited as adatoms on MnO_2 as opposed to Hf substituting Mn. More complex HfO_x clusters ($x > 2$) on MnO_2 surface were not considered due to computational limitations. The adsorption and substitution of Hf, HfO and HfO_2 on MnO_2 are shown using atomic models in Figure 4.13(a-c), respectively. For classification, the structures with Hf adatom on the surface and Hf substituting Mn at the MnO_2 -terminated layer are referred to as Hf-A and Hf-E, respectively. The corresponding structures of HfO are labeled as HfO-A and HfO-E, and that of HfO_2 as HfO_2 -A and HfO_2 -E, respectively. For the adatom clusters, we find that the Hf atom tends to adsorb at the center of four neighboring Mn atoms of the MnO_2 surface. Subsequently, we exchange the positions of the Hf adatom and a Mn atom of the surface to get the Hf-E, HfO-E and HfO_2 -E configurations.

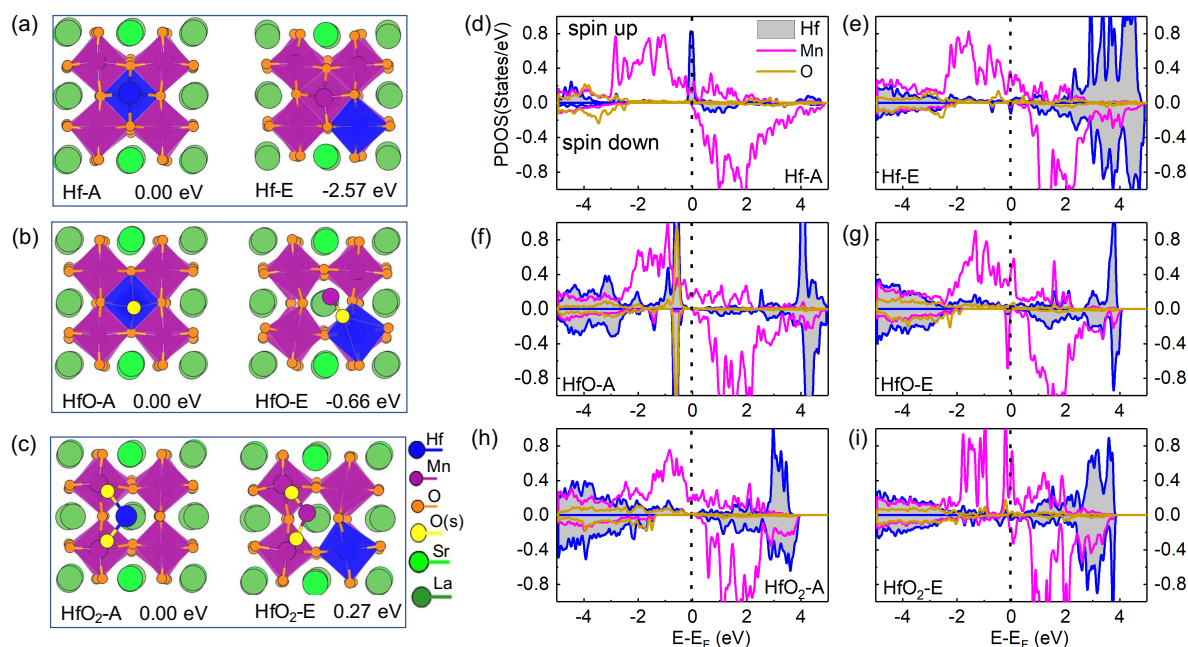


Figure 4.13: (a-c) Top view of $\text{La}_{0.75}\text{Sr}_{0.25}\text{MnO}_3$ slabs with Hf (Hf-A), HfO (HfO-A) or HfO_2 (HfO₂-A) clusters adsorbing on the MnO_2 -terminated surface, left panel, and the Hf atom exchanging position with a surface Mn atom and getting embedded in the LSMO matrix (Hf-E, HfO-E and HfO_2 -E), right panel. The conformations are represented by ball-and-stick models. Oxygen atoms adsorbing on LSMO surface are labeled as O(s). The relative energies with reference to the HfO_x -A configurations are also shown. (d-i) Spin-polarized, atom-projected density of states (PDOS) of surface atoms in Hf-A, Hf-E, HfO-A, HfO-E, HfO_2 -A and HfO_2 -E configurations.

For a single Hf atom, we find that the Hf-Mn exchange (Hf-E configuration) lowers the total energy by 2.57 eV from the Hf-A configuration, as shown in Figure 4.13 (a). Therefore, there is a significant thermodynamic driving force for the formation of Hf-E from Hf-A. To understand this

substitution, we analyze the electronic structure of the two configurations. The atom-projected density of states of the adatom and the top layer of LSMO for both Hf-A and Hf-E configurations are shown in Figure 4.13 (d, e), respectively. We find that the adsorption of Hf on the surface of MnO_2 results in large localized states around the Fermi energy, and these states are primarily derived from the Hf adatom. It indicates that Hf chemisorption induces surface dangling bonds, which leads to the higher energy of the Hf-A configuration. The electronic structure of Hf-E configuration in Figure 4.13 (e) shows that the Hf-Mn exchange leads to a significant reduction of the Hf-states near the Fermi energy due to the passivation of the dangling bonds.

The difference in the electronic structure of the Hf-A and Hf-E configurations, and the passivation of the dangling bonds with Hf_{Mn} substitution can be further understood from an analysis of the surface charges based on nominal oxidation states. The nominal oxidation state of Mn in $\text{La}_{0.67}\text{Sr}_{0.33}\text{MnO}_3$ is +3.33. In bulk, the two oxygen in a $\text{Mn}^{+3.33}\text{O}_2^{-2}$ unit need 4 electrons, and Mn only donates $3.33e$, so $\text{Mn}^{+3.33}\text{O}_2^{-2}$ plane has a charge of +0.67 per unit cell. Similarly, the $(\text{La}_{0.67}^{+3}\text{Sr}_{0.33}^{+2}\text{O}^{-2})$ plane has a net charge of -0.67 per unit cell. Along [001] direction in bulk LSMO, each $(\text{La}_{0.67}\text{Sr}_{0.33}\text{O})$ plane can be assumed as donating $0.335 e$ /unit cell to its two adjacent MnO_2 layers. The MnO_2 -terminated surface, therefore, has a charge of +0.335 per unit cell, as it receives $0.335 e$ /unit cell from only the underlying $(\text{La}_{0.67}\text{Sr}_{0.33}\text{O})$ layer. There are 4 MnO_2 units in the termination layer of the supercell, hence the total surface charge is +1.34. The preferred oxidation state of Hf is +4. Hence, the substitution of $\text{Mn}^{+3.33}$ by Hf^{+4} in MnO_2 contributes extra $0.67 e$ for the entire (2×2) MnO_2 layer, reducing the total surface charges from +1.34 to +0.67 for the MnO_2 layer. A Bader charge analysis¹⁵⁵— that partitions the valence electrons to atoms using a zero-flux surface where the electron density is minimum — of the two configurations, supports these results. We find that with the substitution of Mn by Hf in Hf-E, the Bader charge of the termination layer greatly reduces to $0.13 e$ from $1.10 e$ in Hf-A (Table 1). Apart from Hf on top of the MnO_2 layer, we have also analyzed the energetics of HfO and HfO_2 clusters on MnO_2 -terminated LSMO (Figure 4.13 (b-c)). For molecular HfO adsorption, its results are similar to Hf atom with the HfO-E configuration being $0.66 e\text{V}$ lower in energy than the HfO-A configuration. The mechanisms involved are similar to that of Hf atom. HfO chemisorption induces surface dangling bonds in HfO-A and drives its energy higher (Figure 4.13 (f)). Hf-Mn exchange leads to a significant reduction of the Hf-states near the Fermi energy due to passivation of the dangling bonds (Figure 4.13 (g)), and lowers the energy of the corresponding structure.

The behavior of HfO_2 cluster on MnO_2 -terminated LSMO (Figure 4.13 (c)) is different from that of Hf and HfO molecules, with the HfO_2 -A configuration being lower in energy by $0.27 e\text{V}$ from the HfO_2 -E configuration. The reason for the different behavior of HfO_2 is that the HfO_2 cluster

adsorbed on the MnO_2 surface does not have any surface dangling bonds, as observed from the density of states of Hf in Figure 4.13 (h). The exchange between Hf and Mn does not lead to any significant charge rebalance at the surface (Table 1). Moreover, in the HfO_2 -E configuration, surface Mn-O bonds are partly broken due to the embedding of Hf (see the increase in Mn-O bond lengths in Figure 4.14)). These broken bonds induce large localized states near the Fermi energy (Figure 4.13(i)) and increase the energy of the corresponding structure.

Table 4.1: Bader charges analysis of MnO_2 -terminated LSMO surface without and with Hf clusters.

Configuration ($2 \times 2 \text{ MnO}_2$)	Bader atomic charge (e)			
	Average surface Mn	Hf	Average surface O	Surface charge
Bare MnO_2 surface	5.40		7.06	2.08
Hf-A	5.49	2.26	7.11	1.10
Hf-E	5.42	1.81	7.08	0.13
HfO-A	5.45	1.90	7.09	1.51
HfO-E	5.50	1.73	7.08	1.45
HfO_2 -A	5.38	1.76	7.03	1.58
HfO_2 -E	5.40	1.75	7.02	1.55

The variation in adsorption energy of Hf, HfO and HfO_2 on LSMO with respect to the oxygen chemical potential are given in Figure 4.14. It is observed that Hf-E is the most stable configuration when $\mu_{\text{O}} < -6.99$ eV; i.e., under intermediate to Hf-rich (O-poor) growth conditions spanning a large range of μ_{O} values. For a small range of -6.99 eV $< \mu_{\text{O}} < -6.44$ eV, we find HfO-E to be most stable. When $\mu_{\text{O}} > -6.44$ eV, i.e., under oxygen-rich conditions HfO_2 -A becomes the most stable configuration on surface MnO_2 . These results showing the stability of Hf-E over a large range of μ_{O} values support the experimentally observed reduction in the EEL signal of the O-K edge at the interface due to formation of oxygen vacancies.

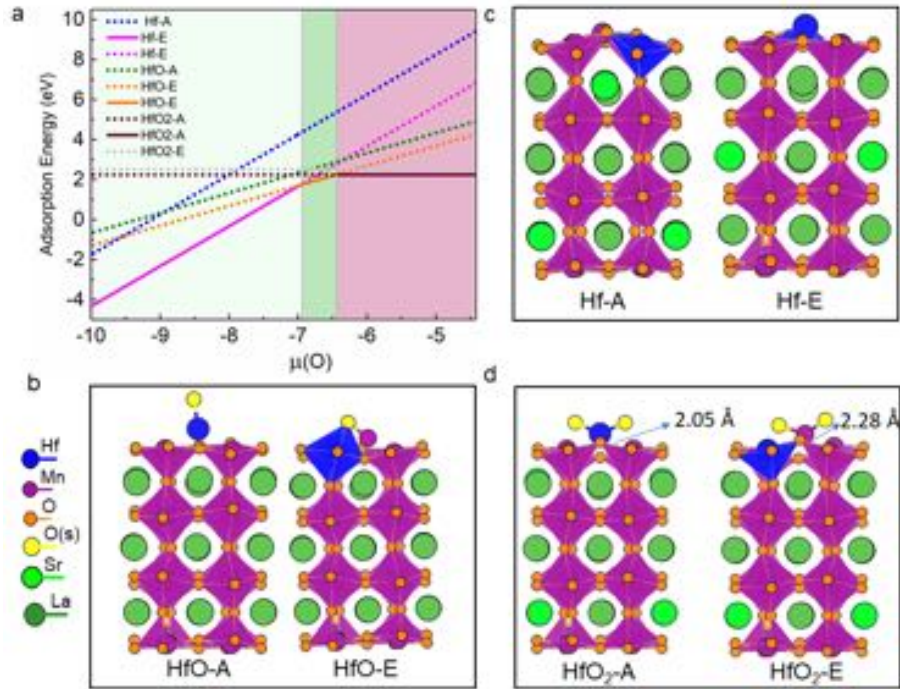


Figure 4.14: (a) Adsorption energy changes for Hf, HfO and HfO₂ with respect to the chemical potential of oxygen. The chemical potential range where Hf-E is most stable is indicated by light green shaded area, that for HfO-E by dark green shaded area, and for HfO₂-A by purple shaded area. (c - d) Side-views of Hf-A, Hf-E, HfO-A, HfO-E, HfO₂-A and HfO₂-E. The longest Mn-O bond length is highlighted in HfO₂-A and HfO₂-E.

In summary, the chemical and structural features of the HZO/LSMO heterointerface that allows epitaxial growth of ferroelectric HZO on perovskites have been revealed. Atomic resolution HAADF images and elemental maps show the chemical reconstruction of the MnO₂-terminated surface of LSMO occurs during the epitaxial growth of HZO on the LSMO, which is supported by DFT calculations of total energy and electronic structure. The reconstruction consists of the substitution of the Mn cations of the MnO₂ interface with HZO by a mixture of Hf/Zr atoms, with Hf/Zr occupying the sites of the Mn in the LSMO perovskite. Such a reconstruction occurs under oxygen deprivation conditions.

4.4 The Atomic Structure of the $\text{Hf}_{0.5}\text{Zr}_{0.5}\text{O}_2$ Interface with LaNiO_3 and SrRuO_3

The STEM analysis was extended to the HZO/LNO and HZO/SRO interfaces in order to try to identify potential differences between them and the HZO/LSMO interface. Figure 4.15 shows an HAADF image of the HZO and LNO layers. The LNO layer is found to contain stacking faults consisting of a missing NiO_2 plane (Figure 4.15, inset at the left). Moving laterally, on arriving to a region not lacking Ni, the defect becomes an antiphase boundary that propagates along the oop direction ($[001]$).¹⁵⁶ The HZO layer exhibits a monoclinic structure as the one observed in m-HZO/LSMO. Yet, some differences can be observed in the HZO layer near the interface. The HAADF intensity profile (inset at the right) reveals that layer x (first layer containing Hf/Zr, as will be shown later) shows a smaller intensity that smoothly increases over the four next planes (i - iii), as opposed to the abrupt HAADF increase observed at the HZO/LSMO interface. This suggests chemical or structural differences between both interfaces. To extract further structural information of the HZO film and the interface with LNO, the distances and angles between atomic columns were mapped on the observation plane of HAADF images across the HZO/LNO interface. In the same line as the HAADF intensity profile, the maps shown in Figure 4.16 reveal structural changes in the HZO layer close to the interface.

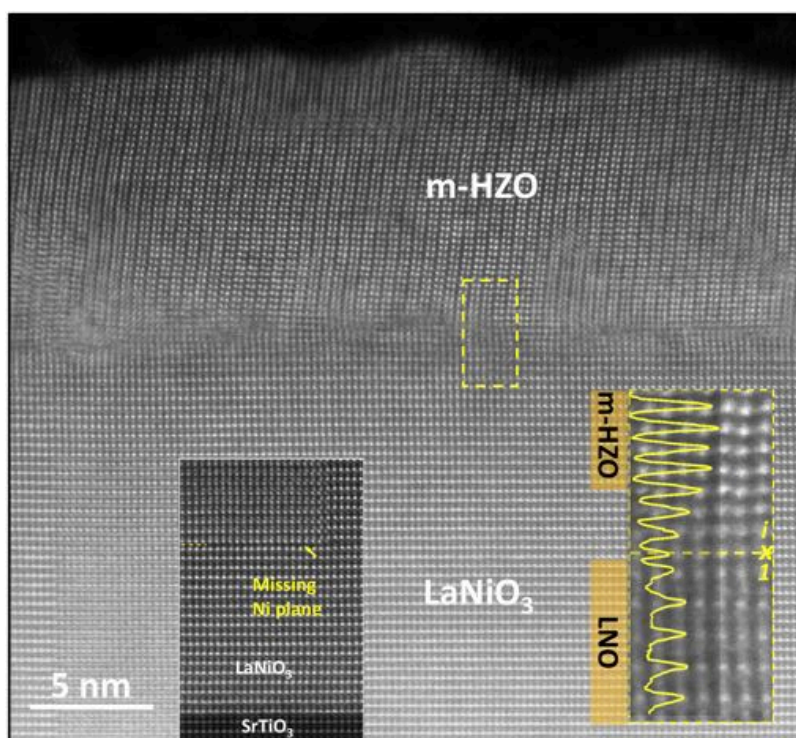


Figure 4.15: HAADF image of the HZO/LNO sample. The m-HZO film (001) oriented, viewed along $[010]$ and the LNO electrode, (001) oriented, viewed along $[110]$ zone axis, can be observed. The inset at the right shows a zoom of the area around the interface together with the corresponding HAADF intensity profile across the interface. The inset at the left shows one of the antiphase boundaries along $[001]$ found in the LNO electrode and the lower interface LNO/STO.

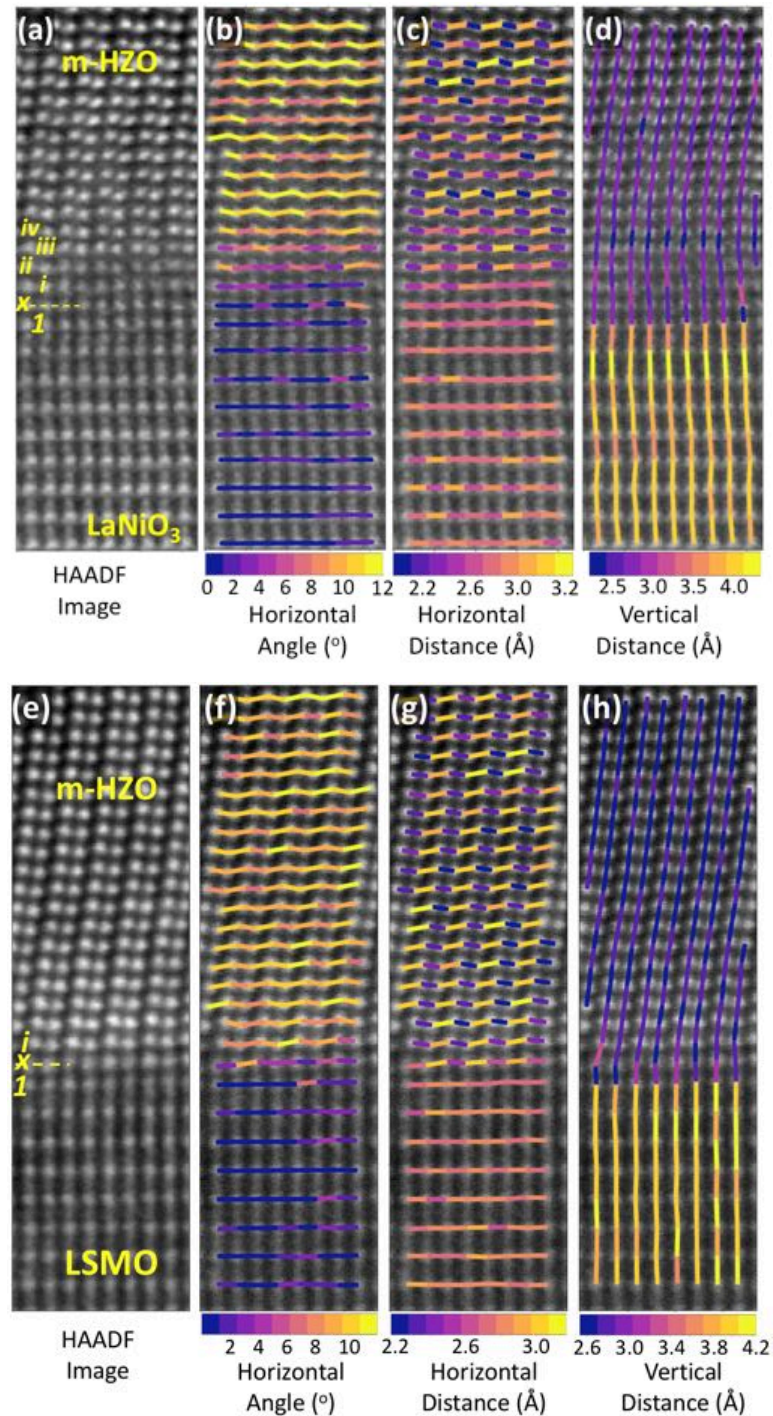


Figure 4.16: (a-d) structural mapping of angles and distances around the *m*-HZO/LNO interface. The color of the connecting sticks represents the angles or distances in the corresponding scale. The color scale is chosen to properly visualize the differences between SRO and HZO. Because of this, some horizontal angles may be out of the color scale (i.e. they are bigger than 14° and are displayed as 14, the maximum of the scale). (a) HAADF image of the analyzed area. (b) Absolute angle subtended by atomic columns horizontally connected. The angle refers to the angular distance from the horizontal direction. (c) Distance between columns horizontally connected (average direction corresponds to the $[100]$ direction in monoclinic HZO; (110) spacings in pseudocubic LNO). (d) Distance between columns vertically connected (along the $[001]$ direction in monoclinic HZO, corresponding to a distance of $c/2$; and (001) spacing in pseudocubic LNO). (e-h) equivalent angle and distance maps corresponding to the *m*-HZO/LSMO, for comparison.

In particular, the analysis reveals a structure that deviates from monoclinic HZO. The monoclinic structure shows an alternatively larger and smaller spacings and angles between atomic columns horizontally connected on the HAADF observation plane (see Figure 4.16 (b) and (c), at the center of the HZO film). After layer *l*, the vertical spacings abruptly change from the ones of the LNO(001) perovskite to those of HZO(001) (Figure 4.16 (d)). However, the horizontal angle and distances remain near zero in the closest atomic planes (*x* and *i*), start to appear in planes *ii* and *iii*, and only reach the monoclinic expected angles in plane *iv* and the following atomic planes. The horizontal spacings (Figure 4.16 (c)) show a similar trend, although the monoclinic distortions start to appear earlier. The spacings are basically constant in layers *x* and *i* and already follow the m-HZO spacings in layer *ii* and above. Such transition region separating layer *x* and the m-HZO spans over 3 planes (*i*, *ii* and *iii*), contrasting with the more abrupt HZO/LSMO interface (without transition region). For comparison, the maps of the m-HZO/LSMO are shown in Figure 4.16 (e-h). As can be appreciated, layer *i* already shows the monoclinic horizontal angles (Figure 4.16 (f)), while layer *x*, which is strained to the LSMO and occupies the Mn sites, already shows angle and distance breathing characteristic of m-HZO (although of much smaller amplitude), elucidating the perovskite-fluorite hybrid character of that atomic plane.

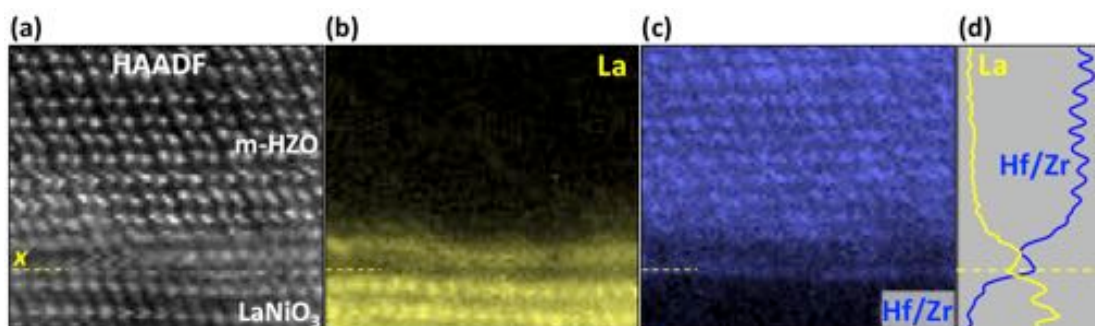


Figure 4.17: Chemical compositional maps around the m-HZO/LNO interface. (a) Simultaneous HAADF image of the analyzed area. (b) La chemical map. (c) Hf and Zr compositional map. (d) Averaged chemical profiles extracted from (b) and (c).

The compositional information of the HZO/LNO interface was extracted from EELS chemical maps. The chemical maps show important similarities as well as differences with the interface of both o-HZO and m-HZO with the LSMO layer. Similarly, Hf and Zr cations (5d and 4d transition metals, respectively) substitute the 3d transition metal, Ni in the present case, at the uppermost plane of the LNO perovskite, plane *x* (Figure 4.17 (a-d)). However, unlike the sharp La distribution of HZO/LSMO interface (the most stable interface for metastable o-HZO), here La can also be found in the HZO layer (Figure 4.17 (a-b)). The presence of La in the HZO film and the smaller oxygen content around the

interface (Figure 4.18) may also suggest an initial stage of formation of the existing $\text{La}_2\text{Hf}_2\text{O}_7$ and $\text{La}_2\text{Zr}_2\text{O}_7$ pyrochlores,^{157,158} a potential structure whose formation would be rapidly inhibited during the HZO film growth due to the lack of La in the subsequent atomic planes. The said pyrochlores have a similar cation ordering and lattice spacings to the one of the HZO fluorite, making difficult to discern between these and the tetragonal HZO phase (which admits La atoms in its structure¹⁵⁹). Anyhow, the chemistry and structure rapidly change from one atomic plane to the next close to the interface, and therefore I consider that the concept of a specific stoichiometry and repetitive unit cell is not the most adequate here. The pyrochlore structure is indeed similar to the fluorite-type structure of HfO_2 , and recently metallic pyrochlores have been used for the first time to epitaxially grow ferroelectric HZO with (001) orientation.¹³² In conclusion, the chemical and structural differences between HZO/LNO and HZO/LSMO interfaces affect the stabilization of o-HZO and m-HZO polymorphs. In particular, the chemically sharper HZO/LSMO interface is more stable for the o-HZO phase. It is relevant to point that the HAADF images of the HZO/LNO(1.2nm)/LSMO/STO sample (Figure 4.4, Section 4.2), with only a few LNO planes, show a similar interface with HZO.

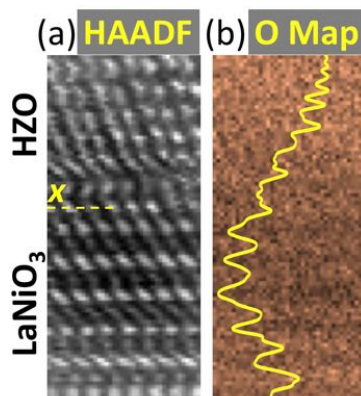


Figure 4.18: (a) simultaneous HAADF image and (b) oxygen K-edge map and corresponding integrated oxygen profile.

The analysis of the HZO/SRO interface also yields similarities and differences with the other explored interfaces. Figure 4.19 shows a HAADF image where the HZO film and the SRO electrode can be observed. The HAADF intensity profile takes around 4 atomic planes from plane x to reach the intensity observed in the HZO layer, suggesting a chemical compositional gradient. Therefore, this suggests that HZO/SRO interface is more abrupt than HZO/LNO, but slightly less than HZO/LSMO. Apart from the majority m-HZO epitaxial relationship with SRO, some grains show other epitaxial variations as a monoclinic grain with [100] aligned with [100] of SRO, (instead than with [110] of SRO, Figure 4.19 (b)), and a monoclinic grain (100) oriented (instead of (001), Figure 4.19 (c)).

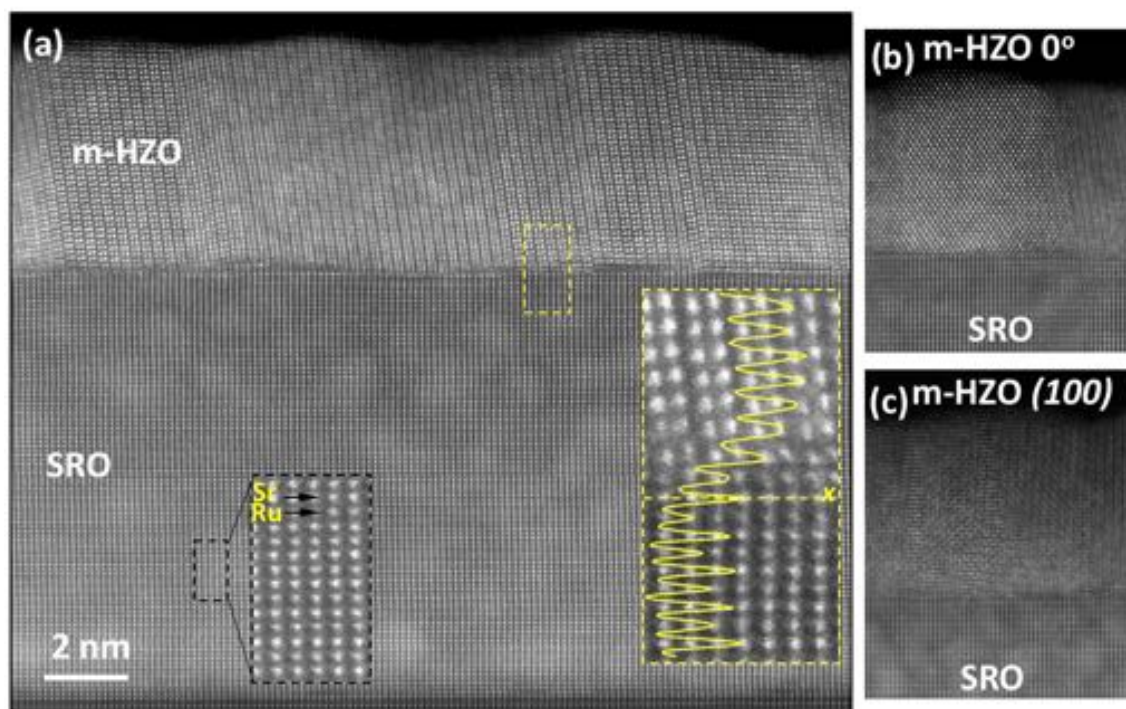


Figure 4.19: (a) HAADF image of the HZO/SRO sample. The m-HZO film ((001) oriented, [100] towards the right on the observation plane) and the SRO ((001) oriented, viewed along [110] zone axis) layers can be observed. The inset shows a zoom of the area around the interface together with the corresponding HAADF intensity profile across the interface. (b) m-HZO grain on SRO with unusual ip epitaxy ([100] of HZO aligned with [100] of SRO). (c) m-HZO grain on SRO (100) oriented.

Figure 4.20 shows the analysis of spacings across the m-HZO/SRO interface. The horizontal angles, horizontal and vertical distances (Figure 4.20 (b), (c) and (d), respectively) show that the monoclinic structure is already developed after plane x, similarly to the what is observed in m-HZO/LSMO and unlike m-HZO/LNO.

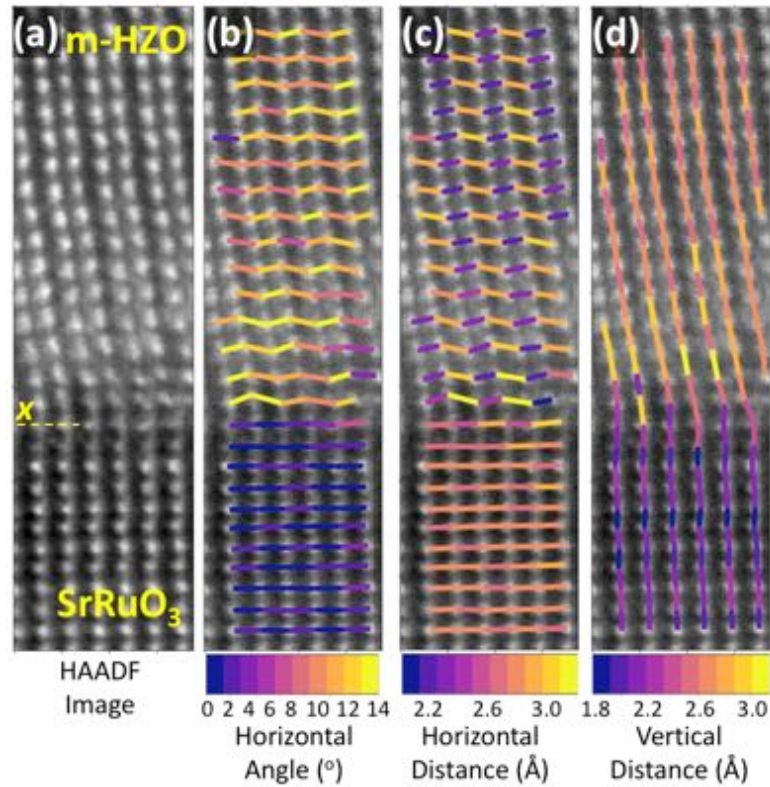


Figure 4.20: Structural mapping of angles and distances around the *m*-HZO/LNO interface. The color of the connecting sticks represents the angles or distances in the corresponding scale. (a) HAADF image of the analyzed area. (b) Absolute angle subtended by atomic columns horizontally connected. The angle refers to the angular distance from the horizontal direction. (c) Distance between columns horizontally connected (average direction corresponds to the $[100]$ direction in monoclinic HZO; (110) spacings in pseudocubic LNO). (d) Distance between columns vertically connected (along the $[001]$ direction in monoclinic HZO, corresponding to a distance of $c/2$; and (001) spacing in pseudocubic LNO). The color scale is chosen to properly visualize the differences between SRO and HZO. Because of this, some horizontal angles are out of the color scale (i.e. they are bigger than 14° and are displayed as 14, the maximum of the scale).

Regarding the chemical maps of *m*-HZO/SRO (Figure 4.21 (a-d)), again the uppermost plane of the SRO perovskite is observed to contain an important amount of Hf/Zr cations occupying the transition metal sites, Ru in the present case. Similarly to the HZO/LNO interface, a certain amount of Sr is observed to be present in the HZO film next to the interface (Figure 4.21 (b)), although in smaller quantities than the La in HZO/LNO.

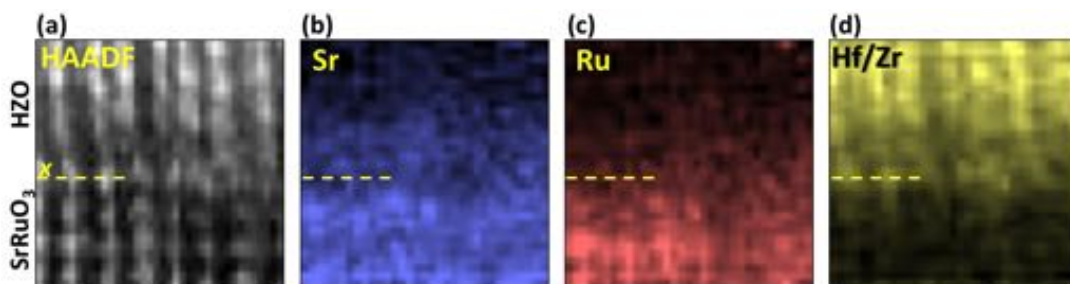


Figure 4.21: Chemical compositional maps around the *m*-HZO/LNO interface. (a) Simultaneous HAADF image of the analyzed area. (b) Sr chemical map. (c) Ru chemical map (d) Hf and Zr compositional map.

4.5 Conclusions

This study confirms that the interface chemistry influences critically the stabilization of the metastable orthorhombic phase and consequently the ferroelectric polarization in epitaxial HZO films.

Manganite electrodes as LSMO or LCMO are critical to epitaxially stabilize *o*-HZO. Engineering the interface with only a few LSMO mono-layers permits stabilizing the ferroelectric phase. The chemical and structural features of the HZO/LSMO heterointerface that allows epitaxial growth of ferroelectric HZO on perovskites have been revealed. Atomic resolution HAADF images and elemental maps show the chemical reconstruction of the MnO₂-terminated surface of LSMO occurs during the epitaxial growth of HZO on the LSMO, which is supported by DFT calculations of total energy and electronic structure. The reconstruction consists of the substitution of the Mn cations of the MnO₂ interface with HZO by a mixture of Hf/Zr atoms, with Hf/Zr occupying the sites of the Mn in the LSMO perovskite. Such a reconstruction occurs under oxygen deprivation conditions.

The interfaces of HZO/LNO and HZO/SRO interfaces were also explored, yielding similarities and differences with the HZO/LSMO interface. The 3d transition metal of each perovskite (Mn, Ni and Ru) is in each case substituted by the Hf/Zr 5d metals at the interface, allowing the epitaxial growth of either monoclinic (on LSMO, LNO and SRO) or orthorhombic (only on LSMO) HZO polymorphs. HZO/LSMO, the more stable interface for *o*-HZO, seems to be in terms of composition the most abrupt interface.

These results are a critical step towards understanding the decisive role of the LSMO buffer in the stabilization of the ferroelectric phase in thin films of (Hf,Zr)O₂. It is expected to encourage further studies owing to the critical role the interface plays on both the stabilization of the ferroelectric phase and its switching.

Appendix 4-A: Ferroelectric wake up of the HZO films with different bottom electrodes

In Figure A.4.1, representative I-V curves and loops collected during the first 10 cycles in films grown on LSMO, SRO, Nb:STO and BLSO are shown. The sample on LNO is not included due to its lack of hysteresis. Each panel shows the I-V curve or polarization loop for the first, second and tenth cycle of a pristine area of the sample. As reported,¹²³ epitaxial films can present a small wake-up effect. In Figure A.4.1(a), this small effect is observed by the different shape of the pristine and second cycled I-V curves and corresponding loops compared with the tenth. More prominent is the

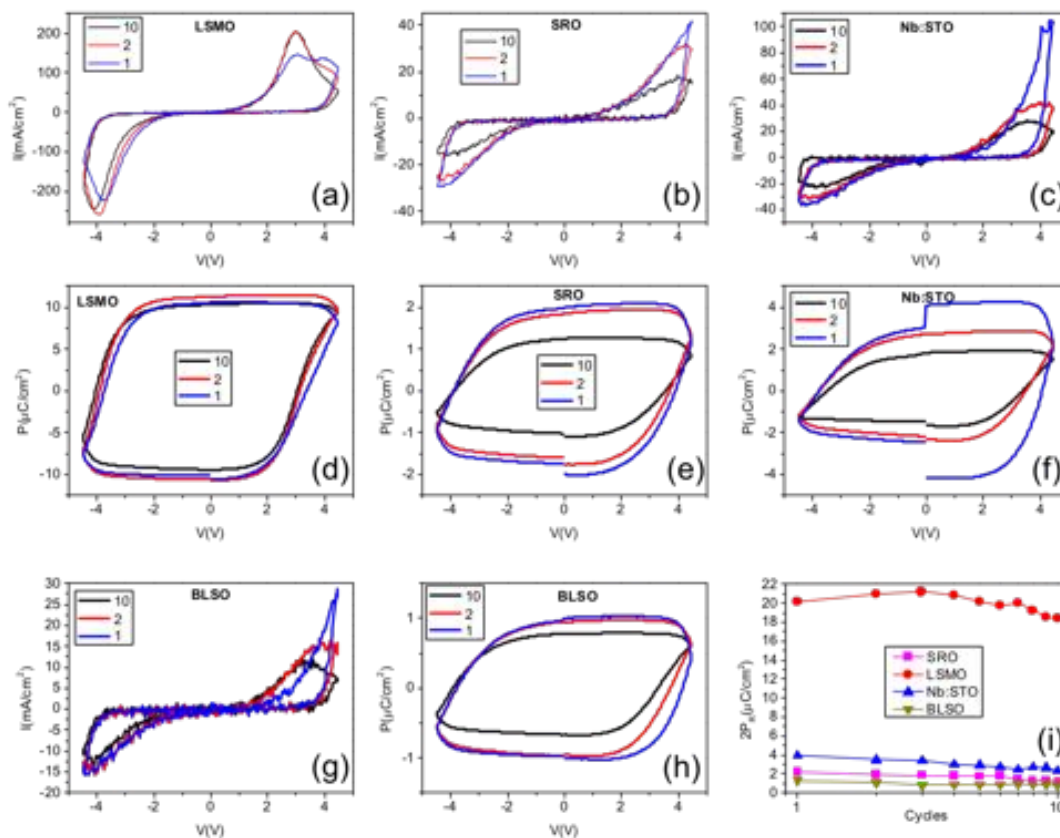


Figure A.4.1: (a-c) and (d-f) show the I-V and P-V curves of the HZO films on LSMO, Nb:STO, BLSO and SRO. Each panel shows polarization loop for the first, second and tenth cycle collected in a pristine junction of the sample. (e) and (f) show the I-V and P-V curves of the HZO film on BLSO. (i) shows the $2P_R$ of each of the four samples.

change upon cycling observed in the HZO film grown on NSTO (Figure A.4.1 (b)) and BLSO (Figure A.4.1 (c)). Whereas, the first loop (in blue) shows round shape, the successive cycling produces a reduction of integrated polarization and the loop gradually becomes more square-like. These results suggest that the pristine loop is dominated by residual leakage probably resulting from defects, which redistribute during the first cycles. The loops obtained for the HZO film on SRO also show important change, although those do not show saturated shape in any case. Figure A.4.1 (i) synthesizes these

results by plotting $2P_R$ of the loops as a function of the number of cycles of the HZO samples with LSMO, SRO, Nb:STO and BLSO electrodes.

Figure A.4.2 (a-h) shows representative I-V curves and loops collected during the first 10 cycles in films grown on the different manganites (LSMO, LCMO, LSMO-0.5 and LCMO-0.5). Figure A.4.2 (i) shows the corresponding $2P_R$ as a function of the number of cycles of the four samples. In all these four samples, the most noticeable change in the I-V curve occurs during the very first hysteresis loop. It can be observed that the change in the P-E shape and extracted $2P_R$ value in films on LCMO, LSMO-0.5 and LCMO-0.5 is a bit larger than on LSMO. Meanwhile, the integrated intensity does not change much during the first 10 cycles. Therefore, the wake-up in the HZO films on manganites is small.

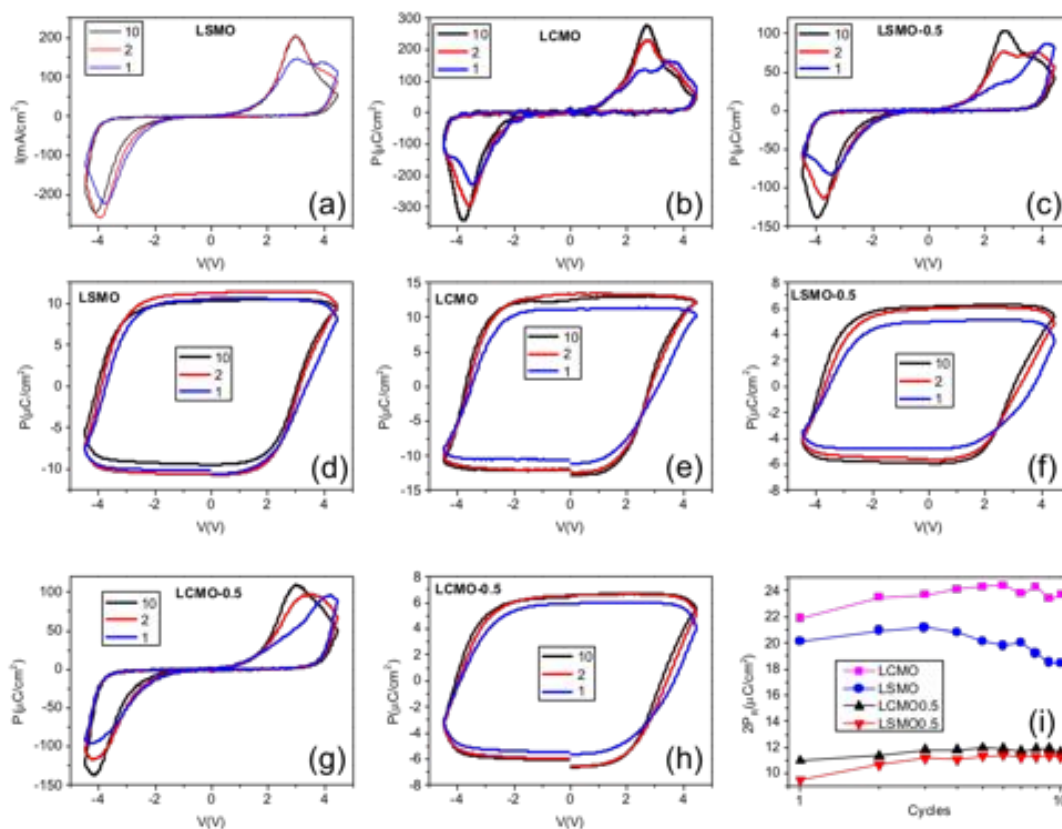


Figure A.4.2: (a-c) and (d-f) show the I-V and P-V curves of the HZO films on LSMO, Nb:STO, BLSO and SRO. Each panel shows polarization loop for the first, second and tenth cycle collected in a pristine junction of the sample. (e) and (f) show the I-V and P-V curves of the HZO film on BLSO. (i) shows the $2P_R$ of each of the four samples.

Appendix 4-B: Absence of the HZO Tetragonal Phase at the Interface

The cation sublattice can be used to explore the possibility of a tetragonal phase near the interface with the electrode, as observed in some cases.^{159,160} A grain containing one of the ([-211], [1-21], [11-2]) directions on the observation plane was studied for that purpose, given that the cation sublattice of the orthorhombic ($Pca2_1$) shows alternating bigger and smaller distances and angles between adjacent atomic columns on the observation, while the equivalent distances and angles are expected to be constant for the tetragonal phase ($P4_2nmc$). A high quality HAADF image of a grain showing the [11-2] direction was selected instead of [1-21] or [-211] because the modulation of distances and angles is greater than along the twin variants that show the [1-21] or [-211] directions. As can be appreciated in Figure A.4.3 (a-d), the distances map, such a occurs both along the [-111] and [-211] directions. The values are similar to those expected considering $Pca2_1$ ($a = 5.234$, $b = 5.010$ and $c = 5.043\text{\AA}$)¹⁶¹: approximately diagonal angles alternatively 67° and 75° (connecting projected consecutive columns along [112] direction) and horizontal ones -4° and 4° (connecting projected consecutive columns along [11-2] direction), and approximately diagonal distances of 2.97 and 3.23\AA (along [112]), and same horizontal distances of 2.97 and 3.23\AA (along [11-2]). Such modulated values are experimentally measured in Figure A.4.3 (a-d).

Interestingly, near the bottom interface with the LSMO (2-3 atomic planes directly above layer x), the alternative variation of the mapped distances and angles becomes smaller, approaching the average values (i.e 0° for horizontal angle, 71° for diagonal angle, and 3.1\AA for diagonal and horizontal distances). This cation ordering could suggest a more symmetric structure (i.e more similar to the higher symmetry tetragonal phase). Yet, the modulation of distances and angles does not completely disappear (in particular for the diagonal distance, for which the reduction of the modulation looks weak). In conclusion, although the analysis of the images reveals subtle structural differences in the first 2-3 atomic planes of HZO after the interface (plane x) that may indicate a tendency towards a more symmetric phase at the interface, the remaining distance and angle modulations are not compatible with the presence of the tetragonal phase.

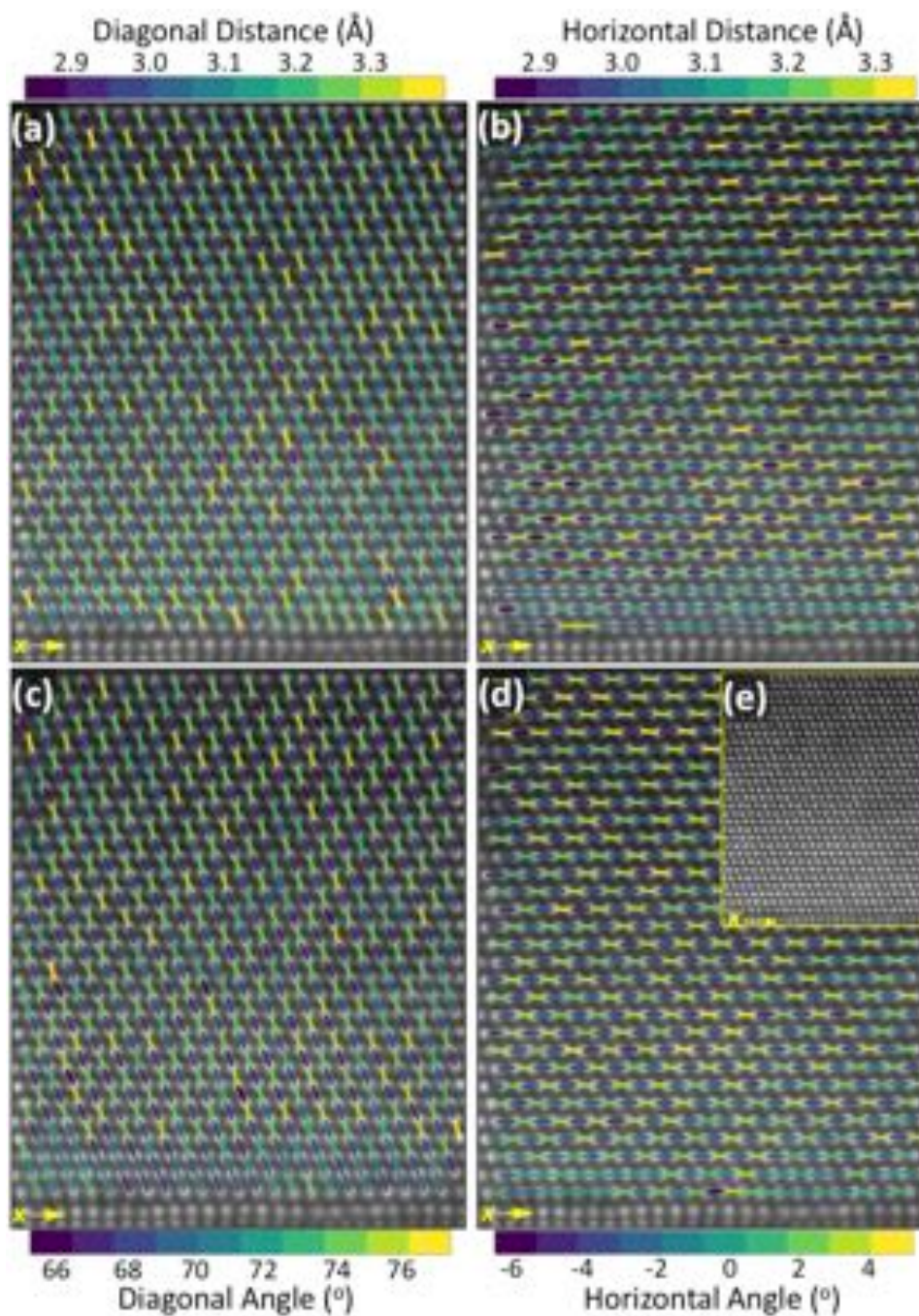
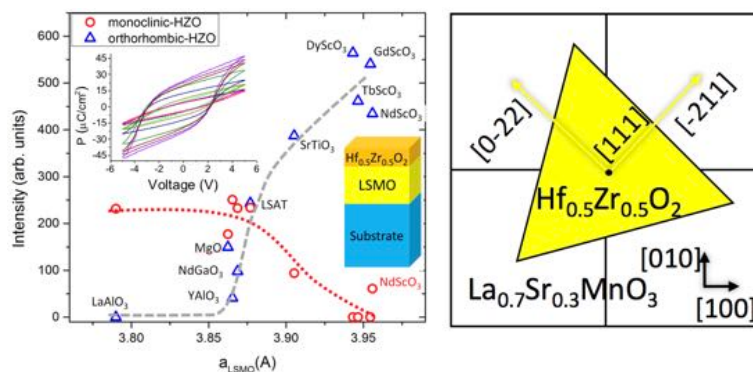


Figure A.4.3. Distance and angle maps of an o-HZO grain 111 oriented (upwards direction, and [11-2] rightwards direction) with colored sticks connecting the analyzed atomic columns showing the bigger (yellow) or smaller (blue) distances and angles. The angles are defined positive rotating clockwise from the left direction. (a) and (b) maps of the distance between adjacent columns connected along the diagonal ([112] direction) and horizontal ([11-2] direction) directions, respectively. (c) and (d) equivalent maps to (a) and (b) showing instead the angle of the sticks connecting atomic columns. (e) HAADF image of the analyzed o-HZO grain.

Chapter 5: Engineering Ferroelectric $\text{Hf}_{0.5}\text{Zr}_{0.5}\text{O}_2$ Thin Films by Epitaxial Stress

Beyond the chemistry of the bottom electrode, the lattice spacing of the template on which HZO grows can also be expected to affect the stabilization of o-HZO and m-HZO. In this chapter, we have gone further to explore the growth of HZO on LSMO templates in different strained states. For that, epitaxial HZO/LSMO bilayers were grown on a set of (001)-oriented single crystal substrates with lattice parameters going from 3.71 to 4.21 Å (cubic or pseudocubic setting). The impact of the epitaxial stress exerted by the LSMO layer on the HZO film, determined by the lattice mismatch with the substrate, is observed on the stabilization of the ferroelectric phase of hafnia. A monotonic increase (decrease) of the quantity of orthorhombic (monoclinic) phase is observed for HZO/LSMO grown on substrates with increasingly bigger lattice parameters. Hence, on LSMO electrodes under tensile strain most of the HZO film is orthorhombic, whereas the monoclinic phase is strongly favored when LSMO is relaxed or compressively strained. Consequently, the HZO films grown on scandate substrates, the latter having bigger lattice parameters, present substantially enhanced ferroelectric polarization in comparison to films on other substrates, including the commonly used SrTiO_3 . Moreover, a detailed analysis of the structures at the HZO/LSMO interface reveals that, among other possible cooperative mechanisms, domain matching epitaxy allows HZO epitaxial growth by accommodating the high lattice mismatch. The capability of controlling the phase in epitaxial doped HfO_2 films is of major interest since it can lead to films with superior ferroelectric properties and to a better understanding of these properties, thus paving the way for the fabrication of ferroelectric devices based on nanometric $(\text{Hf,Zr})\text{O}_2$.



5.1 Introduction

The epitaxial stress can be relevant for the growth of ferroelectric (Hf,Zr)O₂. First, epitaxial stress affects greatly the energy of a (semi)coherent interface between a substrate and a heteroepitaxial film, and it can favor the stabilization of a metastable phase that is in competition with other polymorphs. This epitaxial stabilization has been used to obtain unstable phases of a variety of complex oxides.^{162–165} Secondly, epitaxial stress can cause elastic lattice strain, which can modify the energy of the polymorphs^{166–168} and can also produce important effects on the polarization of ferroelectric oxides.^{169,170} The most common method to control stress in heteroepitaxial films is based on the selection of a substrate with particular lattice mismatch (review Chapter 1). However, this substrate engineering remains unexplored for ferroelectric (Hf,Zr)O₂ materials.

Aiming to investigate the effects of epitaxial stress, epitaxial Hf_{0.5}Zr_{0.5}O₂ (HZO) films were grown on a set of ten single crystalline oxide substrates presenting a wide range of lattice parameters. La_{0.67}Sr_{0.33}MnO₃ (LSMO) epitaxial electrodes and HZO films were sequentially deposited in a single process. Figure 5.1 (a) indicates the lattice parameter of each of the used substrates, as well as their lattice mismatch with LSMO, which is either positive or negative depending on the substrate. The used substrates are, increasing their lattice parameter, YAlO₃, LaAlO₃, NdGaO₃, LSAT, SrTiO₃, DyScO₃, TbScO₃, GdScO₃, NdScO₃ and MgO. The lattice parameters of LSMO are expected to vary according to the lattice mismatch with the used substrate and affect the epitaxial stabilization of HZO, given that LSMO is the epitaxial template on which HZO grows.

5.2 HZO Thin Films on Strained LSMO Templates

5.2.1 Structural Characterization

X-ray diffraction (XRD) θ - 2θ symmetric scans of the HZO/LSMO/substrate samples, Figure 5.1 (b), were measured. The substrate reflection is the most intense one and shifts monotonically from higher to smaller angles ($2\theta = 43$ - 49° range) as its lattice parameter increases (bottom-top direction in Figure 5.1 (b)). The position of the LSMO (002) reflection, in the $2\theta = 45$ - 48° range, depends strongly on the substrate lattice parameter. The corresponding LSMO out-of-plane (oop) lattice parameters are presented in Figure 5.1 (c) as a function of the lattice mismatch with the substrate. The in-plane (ip) lattice parameters, determined from reciprocal space maps (RSMs) around asymmetrical reflections (presented in Figure 5.2(a-j)), are also shown. Increasing lattice mismatch from around -2 to 2% (see the zoomed-in region in Figure 5.1 (d)), reduces the LSMO oop parameter monotonously from ~ 4.00 Å (on LaAlO_3) to ~ 3.80 Å (on TbScO_3), whereas the corresponding ip parameter increases from ~ 3.79 to ~ 3.95 Å. The RSMs in Figure 5.2 confirm that LSMO films, 25 nm thick, are elastically strained in the -2 to $+2\%$ lattice mismatch range. On the other hand, the LSMO relaxes plastically in those films having larger negative or positive lattice mismatch with the substrate, and the oop and ip parameters approach the bulk value, almost matching it on the greatly mismatched YAlO_3 (-4.1%) and ($+8.7\%$) MgO substrates. These results show that the strain state of LSMO is determined by its lattice mismatch with the substrate. The LSMO electrodes act as a template for the subsequent growth of HZO, and thus, their lattice strain, which depends on the substrate, can be relevant to the epitaxy of HZO. The XRD θ - 2θ scans in Figure 5.1 (b) show orthorhombic (o) HZO(111) at $2\theta \approx 30^\circ$ and/or monoclinic (m) HZO(002) at $2\theta \approx 34^\circ$ diffraction peaks. The m-HZO peak can include contribution of the (200), (020), and (002) reflections. The peaks are broad due to the nanometric thickness of the layers (~ 9.5 nm). The XRD θ - 2θ data show that the relative amount of o and m phases depends on the substrate used. In the case of substrates with a lattice parameter from 3.905 Å (SrTiO_3) to 4.01 Å (NdScO_3), the o-HZO(111) peaks have higher intensity, and Laue fringes can be seen around it. Figure 5.3 shows the Laue fringes around the o-HZO(111) of the sample grown on GdScO_3 , obtained with a longer acquisition time than the full scans.

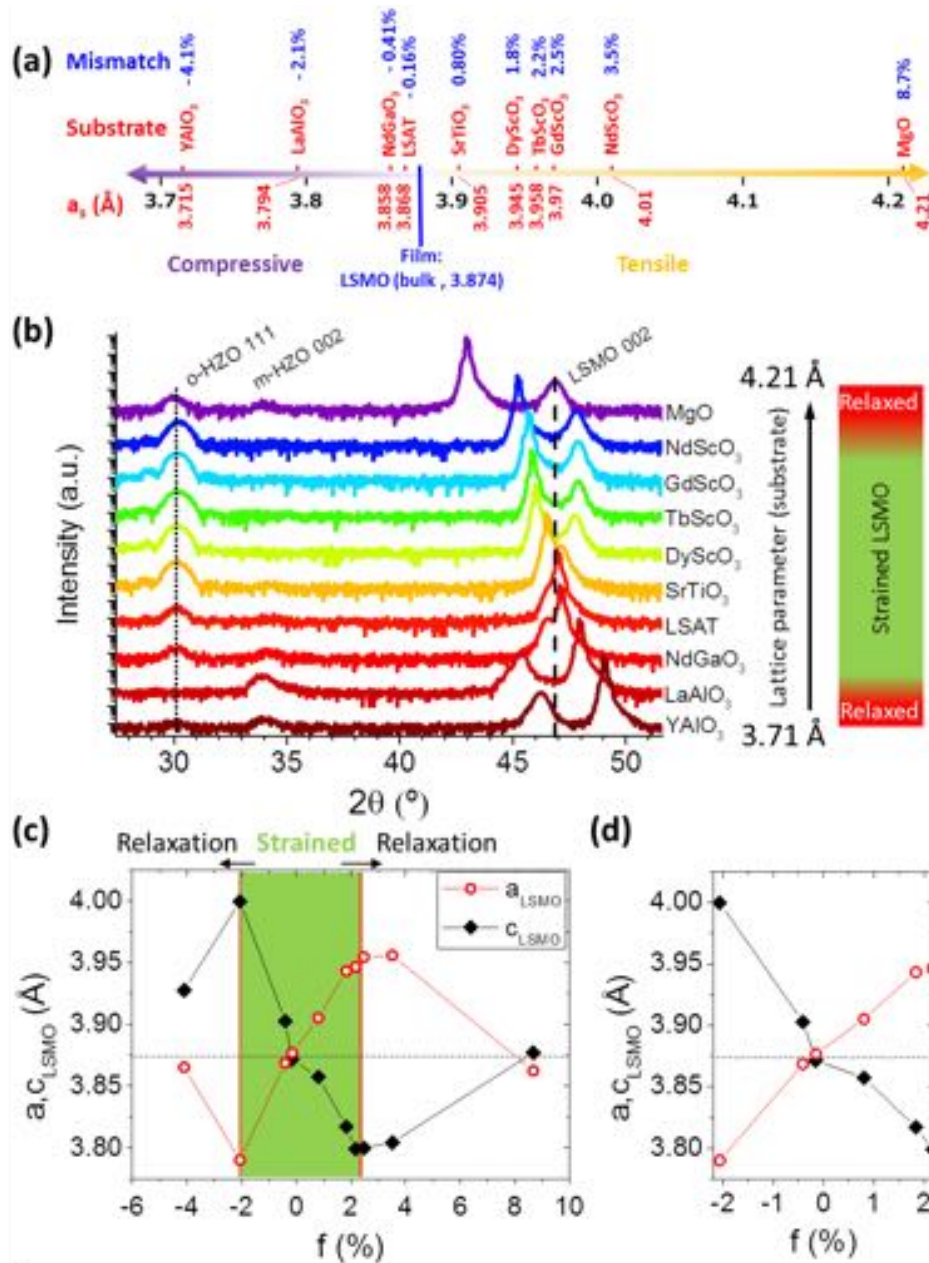


Figure 5.1: (a) Sketch showing the lattice mismatch between the LSMO electrode and the substrates used to deposit the HZO/LSMO bilayers. The lattice mismatch f between LSMO and the substrates is defined as $f = 100(a_s - a_{\text{LSMO}})/a_{\text{LSMO}}$, where a_{LSMO} and a_s are the lattice parameters of bulk LSMO and the substrate, respectively. A pseudocubic cell is used for rhombohedral LaAlO_3 and orthorhombic (NdGaO_3 and scandates) substrates. (b) XRD $\theta-2\theta$ symmetric scans of the HZO/LSMO bilayers. Scans are shifted vertically according to the lattice parameter of the substrate (see labels and arrow at the right). Vertical solid line at $2\theta = 30.1^\circ$ marks the positions of the $o\text{-HZO } 111$ peak in the film on $\text{SrTiO}_3(001)$. The vertical dashed line marks the position of the (002) reflection in bulk LSMO. Right: schematics of the strain state of LSMO depending on the lattice parameter of the substrate. (c) Out-of-plane and in-plane lattice parameters of LSMO as a function of the lattice mismatch with the substrate. (d) Zoom-in of the range of lattice mismatch where LSMO is elastically strained.

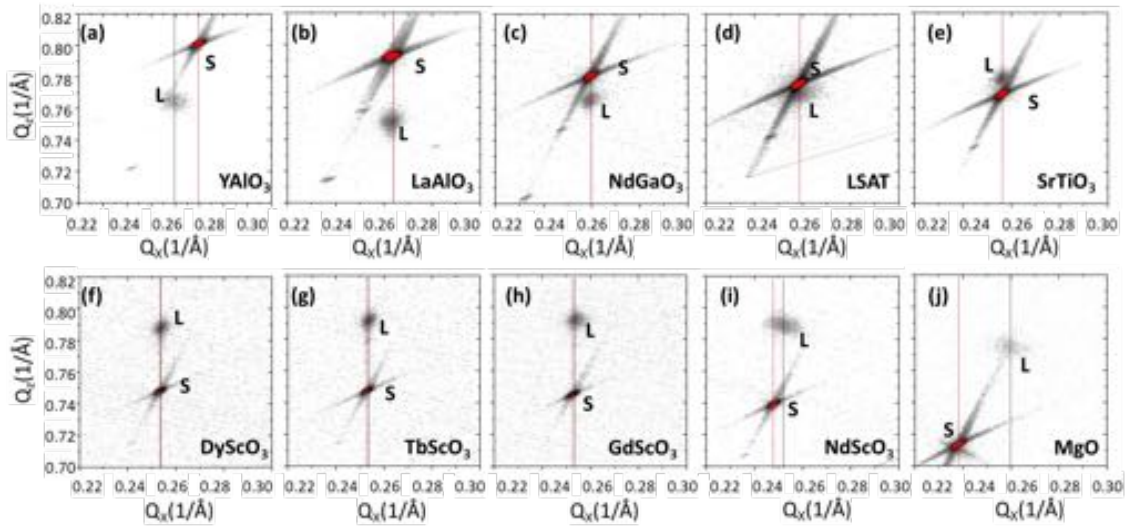


Figure 5.2: Reciprocal space maps of all samples (increasing substrate lattice parameters from (a) to (j)) showing the pseudocubic (103) substrate (denoted as S) and the LSMO layer (denoted as L) reflections. MgO is measured around the (113) cubic substrate reflection due to the systematic extinction of the 103 reflection, and thus the ip lattice parameter is $a_{100}=a_{110}/\sqrt{2}$. Q_x and Q_z are the ip and oop components of the reciprocal space coordinate. Vertical lines indicate the in-plane position of the substrate peaks. LSMO is strained to the substrate within the $-2 +2\%$ mismatch range (corresponding panels in the range (b)-(g)).

The positions of the fringes coincide with those from the model (see Figure 5.3), but they could also hide the monoclinic (-111) reflection, which is seen in other samples.¹²⁵

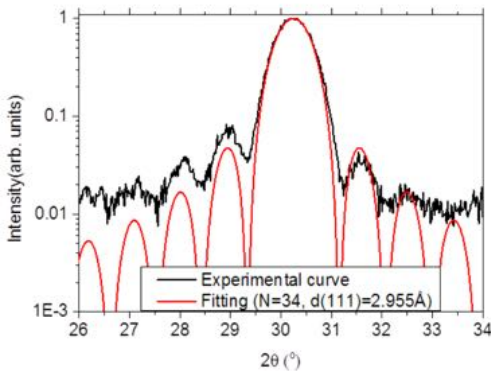


Figure 5.3: Laue fringes XRD (Cu $K\alpha$ radiation) θ - 2θ symmetric scan (red curve) around the o-HZO 111 reflection of the HZO/LSMO/GdScO₃(001) sample. The black curve corresponds to the experimental data. The red curve corresponds to the simulation according to the following equation¹⁷¹: $I(Q) = \left(\frac{\sin(QNd/2)}{\sin(Qd/2)}\right)^2$, where $Q=4\pi \cdot \sin(\theta)/\lambda$, with θ being the angle of the o-HZO 111 reflection, λ the x-ray wavelength, N the number of planes and d the interplanar spacing.

The XRD 2θ - χ frames of all samples, presented in Figure 5.4 (a), reflect the impact of the substrate on the growth of the o and m HZO phases. While the o-HZO 111 reflection is a bright circular spot, the m-HZO 002 reflection is generally elongated along χ , signaling higher mosaicity (excluding the film on LaAlO₃, in which m-HZO 002 reflection is a bright spot). In order to map the formation of

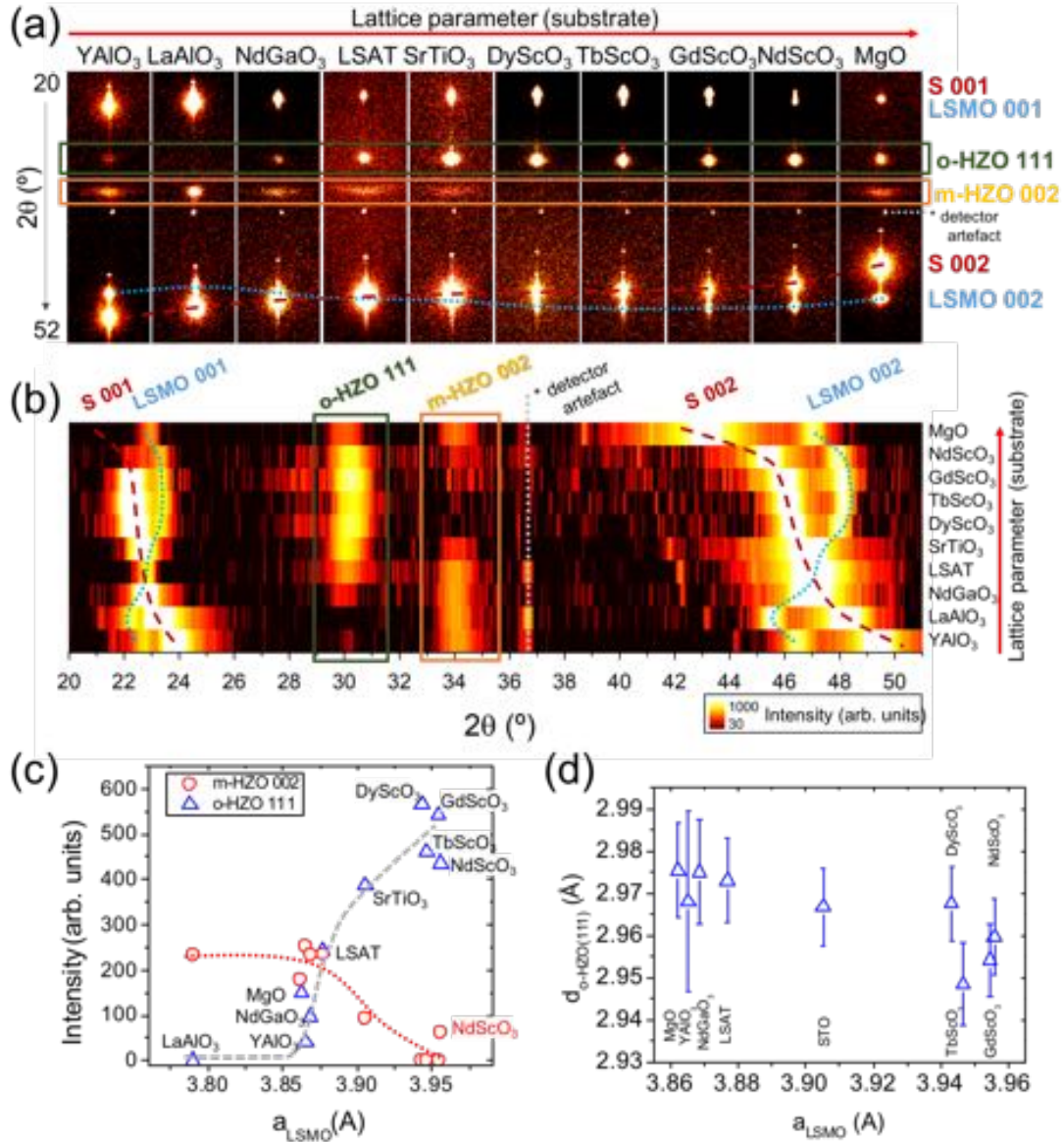


Figure 5.4: (a) XRD 2θ - χ frames of the HZO/LSMO bilayers. The 2θ and χ ranges are from 20 to 52° and from -8 to $+8^\circ$, respectively. (b) Mapping of the orthorhombic and monoclinic phases as a function of the substrate lattice parameter. The 2θ scans were integrated from $\chi = -10$ to $+10^\circ$, and the samples are ordered as the substrate lattice parameter increases. The change in the position of the LSMO peaks (marked with black dotted lines) on the used substrate (peak position marked with red dashed lines) is also visualized. (c) Intensity of the o-HZO(111) and m-HZO(002) peaks (calculated from Gaussian fits) and (d) interplanar $d_{\text{o-HZO}(111)}$ spacing as a function of the ip lattice parameter of the LSMO electrode. The $d_{\text{o-HZO}(111)}$ spacing was determined by Gaussian fits of the 2θ peak position, and the error bar is set to 1σ of the fit.

orthorhombic and monoclinic phases as a function of the substrate, the intensity at each 2θ was integrated from $\chi = -10$ to $+10^\circ$ for each frame (Figure 5.4 (b)). The intensity is plotted in a logarithmic color scale, and the 2θ scans are shifted vertically, ordered as the lattice parameter of the substrate increases (see labels at the right). The 001 reflections of the substrate (marked with red dashed line)

and LSMO electrode (marked with black dotted line) are at 2θ angles from around 20 to 26° , and the corresponding 002 reflections are from around 40 to 50° (Figure 5.4 (b)). The o-HZO 111 and the m-HZO 002 reflections are at around 30 and 34° , respectively. The map shows that the orthorhombic phase is mainly present on substrates with a lattice parameter from 3.905 \AA (SrTiO_3) to 4.01 \AA (NdScO_3) and that basically pure orthorhombic phase films are obtained on DyScO_3 , TbScO_3 , and GdScO_3 . Figure 5.4 (b) indicates that the orthorhombic phase is favored on substrates with a large lattice parameter, whereas the amount of monoclinic phase is greater when the lattice parameter of the substrate is smaller. The films on substrates with very large or very small lattice parameters do not follow this tendency, most probably due to the plastic relaxation of the LSMO electrode. Indeed, the intensities of the reflections of both phases show monotonic dependences as a function of the ip lattice parameter of LSMO (Figure 5.4 (c)). The orthorhombic phase starts to form when the ip parameter of the LSMO template is larger than $\sim 3.87 \text{ \AA}$, and the XRD o-HZO 111 spot intensity increases with the LSMO ip parameter. The monoclinic phase shows an opposite tendency, and it is only absent when the LSMO template has an elongated ip parameter around 3.95 \AA . As seen, the intensity of orthorhombic and monoclinic XRD reflections depends strongly on the ip parameter of the LSMO electrode (Figure 5.4 (c)), showing that depending on the strain of the LSMO electrode, either pure monoclinic phase, a mixture of both phases, or pure orthorhombic films are obtained. In contrast, the lattice parameter of the LSMO template has little influence on the interplanar $d_{\text{o-HZO}(111)}$ spacing (Figure 5.4 (d)), and only a slight $d_{\text{o-HZO}(111)}$ contraction, close to the detection limit, can be appreciated in the films on electrodes with the largest a_{LSMO} . This indicates plastic relaxation (further details can be found elsewhere ¹³⁹).

Polymorphs that are unstable in bulk can be stabilized in thin films due to the change in energy associated to elastic strain and the contributions from surface and interface energies. Density functional (DFT) calculations^{166–168} predict that compressive strain and surface energy contribution reduce the energy of the HfO_2 polar orthorhombic phase with respect to the monoclinic phase. Thus, the formation of the polar phase is more favorable in ultrathin films where the surface energy contribution is more relevant. These DFT calculations only considered films having $\{100\}$ ^{166,167} and $\{110\}$ ¹⁷² orientations, although DFT calculations were recently extended to the (111) orientation, and remarkably, it was found that the orthorhombic polar phase is energetically favored in (111)-oriented films over the monoclinic phase.¹⁶⁸ Therefore, the o-HZO(111) orientation in our epitaxial films can be a relevant factor on the stabilization of the ferroelectric phase, although in our films its formation is competing with the $\{100\}$ orientation of the monoclinic phase. On the other hand, strain is likely less relevant considering the low elastic strain (Figure 5.4 (d)) of the HZO films. Yet, strain could be relevant for the nucleation of orthorhombic and monoclinic grains during the first stages of the PLD growth, while

only the final state is accessed in the experiment. In addition, the interface between HZO and the bottom surface (the LSMO electrode in this case), for which the energy calculations are not reported, is shown to be determinant on the total energy of HZO polymorphs. The epitaxial stabilization of o-HZO with (111) orientation implies a change in crystal symmetry, being that the HZO film (111) oriented on the fourfold symmetry LSMO(001) surface. Heteroepitaxy with different symmetry between a top layer and a bottom layer (or the substrate) is relatively frequent.¹⁷³ Films can present either higher¹⁷⁴ or lower¹⁷⁵ symmetry than the substrate. Epitaxy requires matching between layer and substrate crystal lattices, which is intriguing when the surface symmetry of a layer and substrate is different. However, heteroepitaxy can happen in largely mismatched film–substrate systems by coincidence of m lattice planes of the film on n planes of the substrate (where m and n are different integers).¹⁷⁶ Such a possibility is assessed below, in section 5.3 of this chapter. This mechanism is often observed in heteroepitaxy of semiconductors¹⁷⁶ and oxides.¹⁷⁷ The change in symmetry usually causes formation of crystal variants, like in the case of o-HZO(111) films on LSMO(001) surfaces. Related examples are epitaxial growth of spinel NiFe_2O_4 (111) films on yttria-stabilized zirconia-YSZ(001)¹⁷⁸ or wurtzite ZnO (0001) on MgO (001).¹⁷⁵

XRD pole figures around asymmetrical o-HZO (–111) and m-HZO (–111) reflections in Figure 5.5 (a) and (b) confirm that both orthorhombic and monoclinic phases, when present in the films, are epitaxial. φ -scans around asymmetrical reflections of the orthorhombic and monoclinic phases, derived from the XRD pole figure corresponding to the film on SrTiO_3 show the epitaxial relationships of o and m phases with the substrate (Figure 5.5 (e-f)). The samples on GdScO_3 , STO and LSAT (Figure 5.5 (a)) show four sets of three o-HZO (–111) spots, indicating the existence of four crystal variants with 90° rotation in the plane. In Figure 5.5 (c), the epitaxial relationship is sketched. The rhombohedral distortion reported¹³⁵ in similar HZO films on LSMO(001) electrodes is not observed here within the sensitivity of the XRD measurements. In the films on substrates with a smaller lattice parameter than GdScO_3 , as SrTiO_3 and LSAT, the intensity of the o-HZO –111 reflections becomes increasingly smaller, and they are not observed in the film on LaAlO_3 . In contrast, the poles around m-HZO –111 show four intense spots in the film on LaAlO_3 , lower intensity spots on LSAT and SrTiO_3 , and barely detectable spots on GdScO_3 . The epitaxial relationship of this phase is sketched in Figure 5.5 (d).

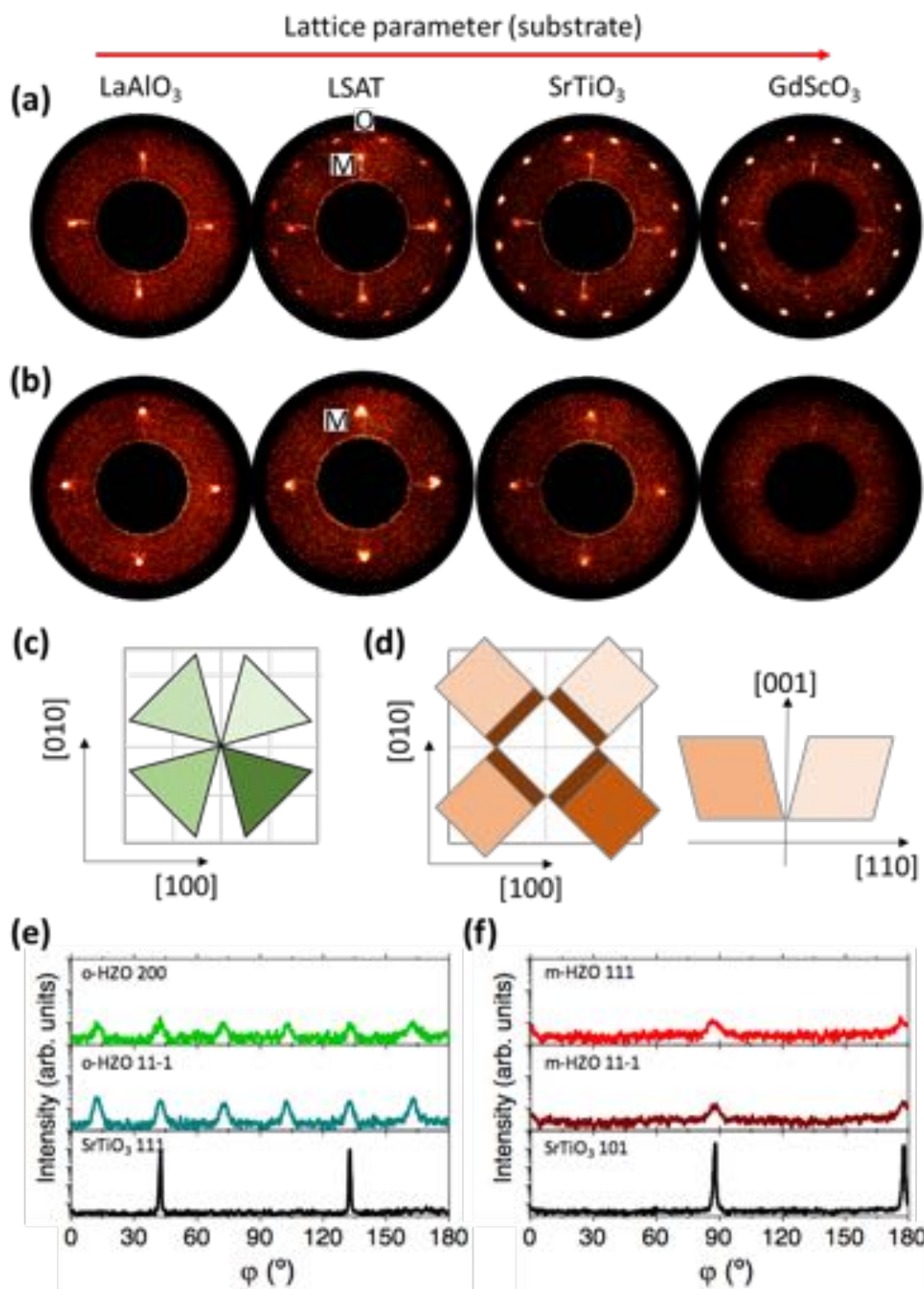


Figure 5.5: XRD pole figures of (a) $o\text{-HZO } -111$ (O) and $m\text{-HZO } -111$ (M), and (b) $m\text{-HZO } -111$ (M) reflections obtained for films on LaAlO_3 , LSAT, SrTiO_3 , and GdScO_3 . The pole figures were measured in the range of χ from 35 to 80°. (c) Sketch of the epitaxial relationship of the $o\text{-HZO}$ phase (top view). (d) Top and cross-sectional views of the epitaxial relationship of the $m\text{-HZO}$ phase. (e) XRD ϕ -scans around 200 and 11-1 reflections of $o\text{-HZO}$ and 111 pseudocubic reflections of the substrates. In (f) ϕ -scans of 111 and 11-1 reflections of $m\text{-HZO}$ and 101 pseudocubic reflections of the substrates. Intensity is plotted in logarithmic scale.

Topographic atomic force microscopy (AFM) images of HZO/LSMO bilayers on the ten substrates are shown in Figure 5.6 (a)-(j). All the films have a root mean square (rms) roughness of less than 5 Å, and a morphology of terraces and steps can be appreciated in some of the images. The surface flatness of all the films is remarkable considering the broad range of substrate lattice parameters. In Figure 5.6 (k) the rms roughness is plotted as a function of the lattice parameter of the substrate. It is seen that the roughness increases from around 2 to 4–5 Å with the substrate lattice parameter.

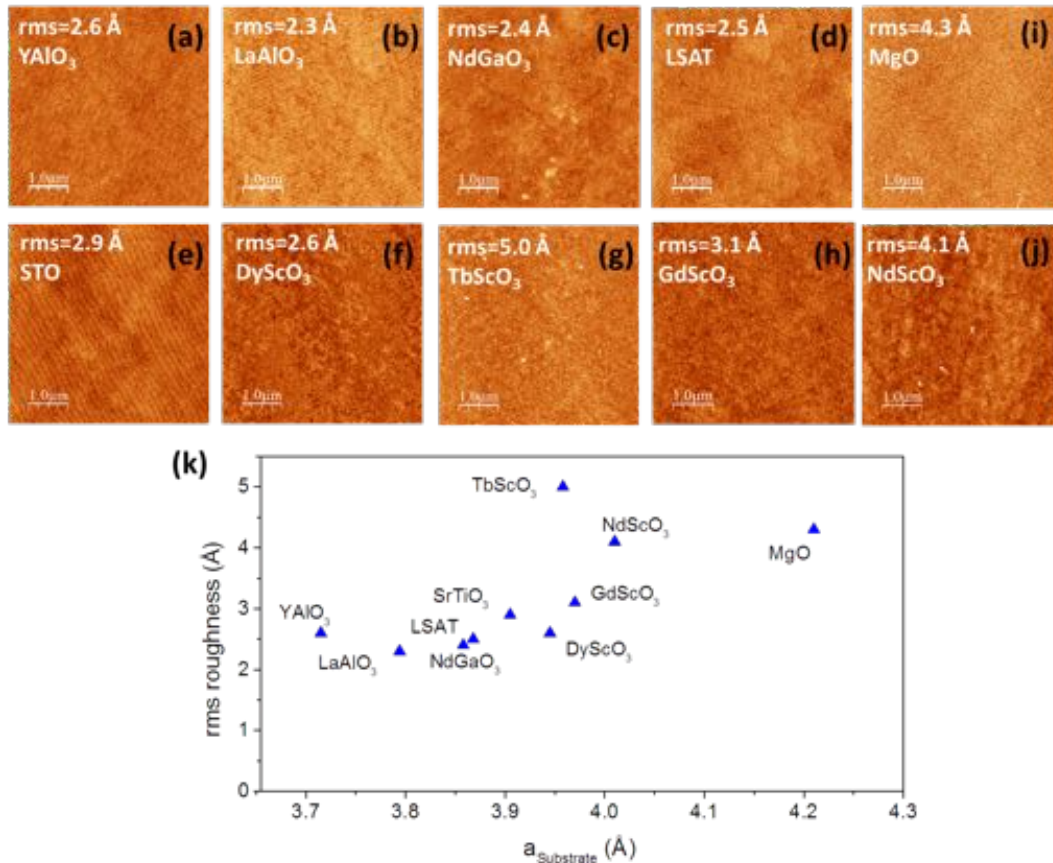


Figure 5.6: (a-j) Topographic AFM images, 5 μm x 5 μm scanned area, of all HZO/LSMO/substrate samples. The substrate and the rms roughness are indicated at the top left of each image. (k) shows the rms roughness of the HZO films plotted as a function of the substrate lattice parameter.

5.2.2 Microstructural Characterization by STEM

Scanning transmission electron microscopy (STEM) was used for structural characterization at the nanoscale and to identify the orthorhombic and monoclinic phases in the HZO films. Three samples with LSMO electrodes fully strained to the substrate were inspected: (i) LSAT, with a lattice parameter

$a_s = 3.868 \text{ \AA}$ and the best lattice matching with a bottom LSMO electrode; (ii) SrTiO_3 , with a larger lattice parameter $a_s = 3.905 \text{ \AA}$, which has been already used^{122,134,135} for epitaxial growth of o-HZO

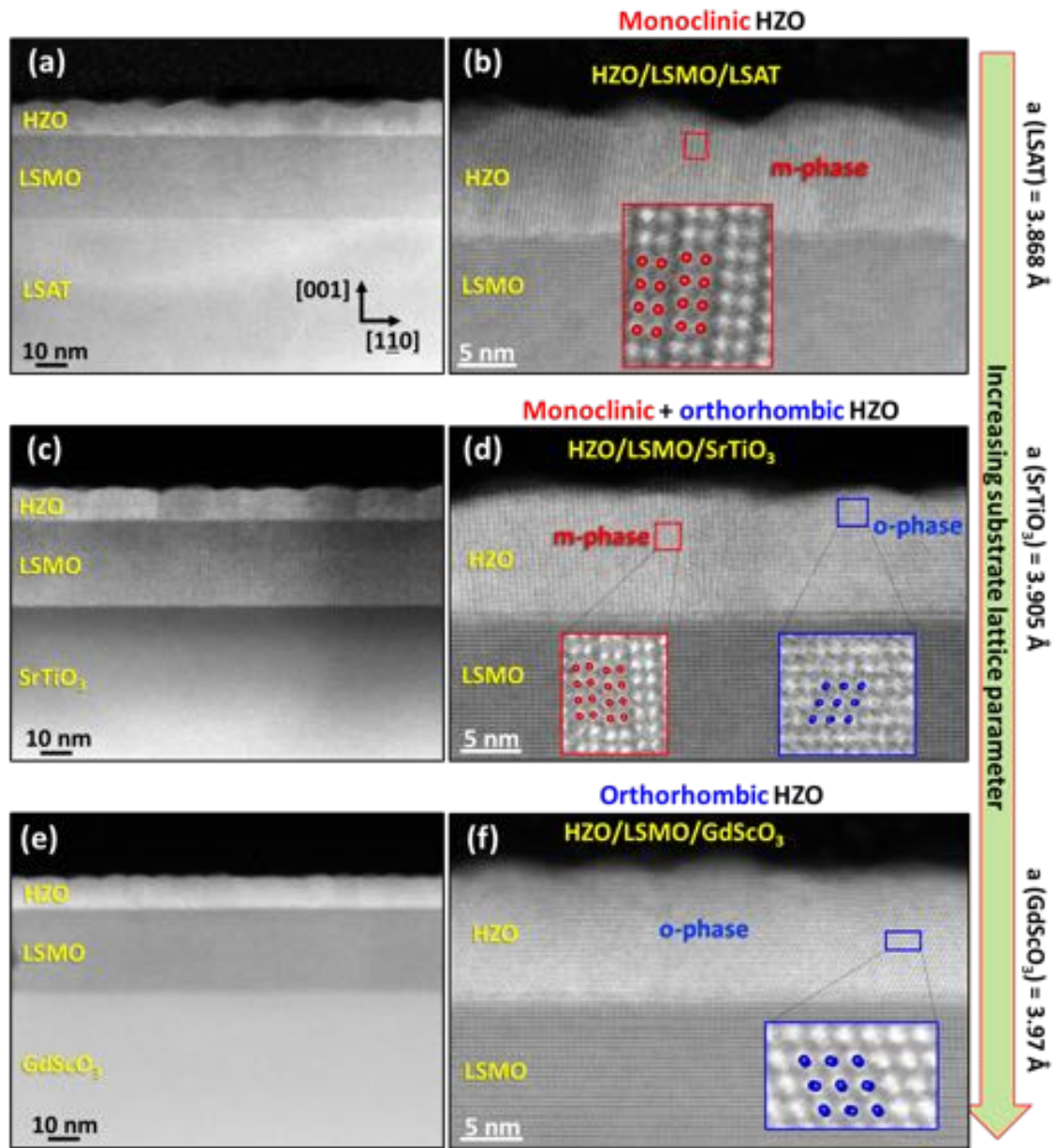


Figure 5.7: Cross-sectional HAADF images of HZO/LSMO films on (a-b) LSAT, (c-d) SrTiO_3 , and (e-f) GdScO_3 substrates. The images were acquired along the $[110]$ zone axes of the substrates. Left panels are low-magnification images showing the substrate, the LSMO, and the HZO films. Right panels are higher magnification images of the HZO and LSMO films. The insets show atomic-resolution images of the HZO films. Red and blue balls depict the monoclinic (space group $P2_1/c$) and orthorhombic (space group $Pca2_1$) structures, respectively.

(111), and (iii) GdScO_3 , with a much larger lattice parameter ($a_s = 3.97 \text{ \AA}$). The corresponding cross-sectional high-angle annular dark field (HAADF) images are presented in Figure 5.7 (a), (c) and (e), respectively. These images were obtained along the $[110]$ zone axes of the substrates, which allows

to access simultaneously suitable zone axes of all the layers, including the different epitaxial variants of HZO orthorhombic and monoclinic crystallites, given the epitaxial relationship revealed by pole figures in Figure 5.5. These low-magnification images show a clear contrast between the HZO film, LSMO electrode, and substrate. In order to properly identify the HZO phases, their orientation, and epitaxy in the HAADF images, the images in the HZO are compared with models of the orthorhombic and monoclinic cation structures projected along the corresponding zone axes. The models were implemented in VESTA⁶¹ considering $Pca2_1$ ($a=5.234$, $b=5.010$, $c=5.043$ Å)⁶¹ and $P2_1/c$ ($a=5.119$, $b=5.169$, $c=5.297$ Å) space groups. High-magnification images of the HZO film on LSAT (Figure 5.7 (b)) confirm the presence of the monoclinic phase (see the inset) and the absence of the orthorhombic phase in the imaged section. In contrast, orthorhombic and monoclinic HZO crystallites coexist in the film grown on SrTiO₃. Insets in Figure 5.7 (d) show enlarged views of the monoclinic and the orthorhombic grains, with the projected structures superimposed. Finally, the HZO film on GdScO₃ only presents orthorhombic grains (see the inset in Figure 5.7 (f)), with absence of monoclinic phase in the imaged section. The lateral size of orthorhombic grains is around 10 nm both in films grown on SrTiO₃ and GdScO₃, whereas the monoclinic phase tends to form grains with much larger lateral dimensions. Moreover, the increase in the relative amount of orthorhombic to monoclinic crystallites also fits the observations obtained by XRD, shown in Figures 5.1, 5.4 and 5.5. These results show the huge impact of the substrate lattice parameter in the formation of a monoclinic or orthorhombic HZO phase.

The epitaxial relationship for the orthorhombic phase is, as seen from STEM images, $[1-10]_o\text{-HZO}(111)//[1-10]_{\text{LSMO}}(001)//[1-10]_{\text{Substrate}}(001)$, where all the indices refer to the cubic or pseudocubic unit-cells. For the m-phase, the epitaxial relationship is seen to be $[010]_m\text{-HZO}(001)//[1-10]_{\text{LSMO}}(001)//[1-10]_{\text{Substrate}}(001)$. Thus, the epitaxial relationship as seen from STEM images agree with the one obtained in pole figures.

5.2.3 Ferroelectric Hysteresis

In agreement with the critical role of the substrate on the stabilization of the orthorhombic phase, the ferroelectricity is found to depend strongly on the substrate, as shown by the polarization loops, Figure 5.8.

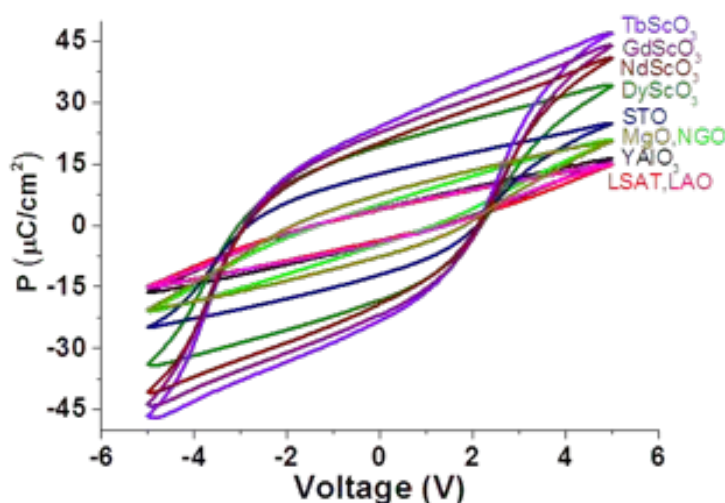


Figure 5.8: (a) Ferroelectric polarization loops of the HZO films on the different substrates.

Ferroelectric polarization loops and the corresponding J-V curves are shown separately in Figure 5.9 (a-j). The HZO films on the substrates with a smaller lattice parameter, YAlO_3 , LaAlO_3 , and NdGaO_3 , have a low ferroelectric polarization of about $4 \mu\text{C}/\text{cm}^2$. HZO films on substrates having a larger lattice parameter show an increasing remanent polarization (P_r) from around $5 \mu\text{C}/\text{cm}^2$ on LSAT to around $24 \mu\text{C}/\text{cm}^2$ on TbScO_3 . With further increase of the lattice parameter of the substrate, the polarization of HZO becomes progressively smaller, getting reduced to $9 \mu\text{C}/\text{cm}^2$ in the film on MgO .

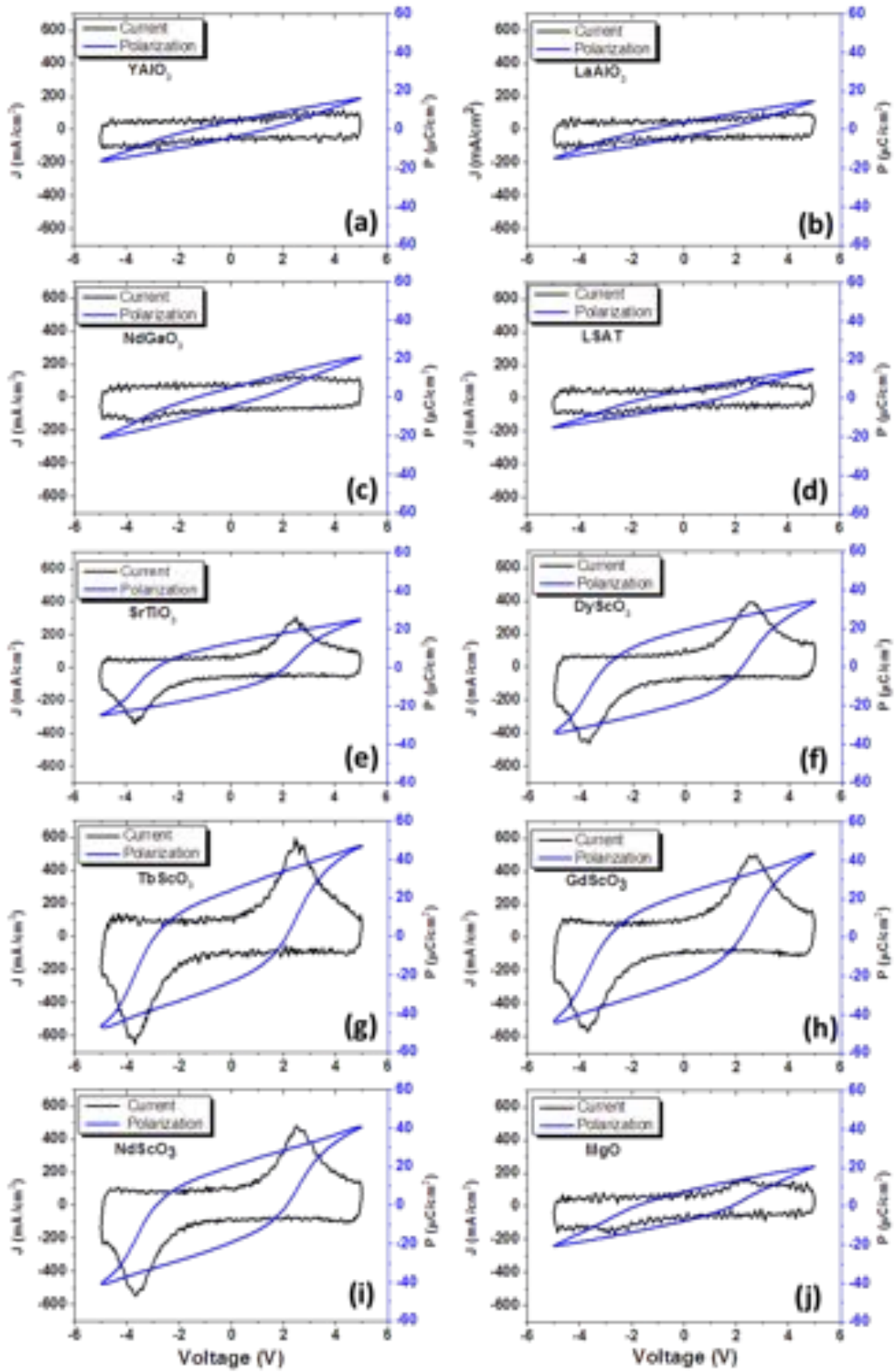


Figure 5.9: (a-j) ferroelectric polarization loops (in blue) and the corresponding current-voltage curves (in black) of the HZO films grown on the different substrates.

The remanent polarization is plotted against the substrate lattice parameter in Figure 5.10 (a), showing a peaked dependence with the largest polarization for HZO films on scandates with a lattice parameter around 3.96 Å. At this point, it is worth noting that the HZO films do not grow directly on the substrate but on the LSMO bottom electrode that is fully strained only on substrates with a lattice parameter in the 3.79–3.97 Å range. Indeed, the plot of the remanent polarization as a function of the a_{LSMO} parameter of the LSMO electrode shows very low polarization when a_{LSMO} is smaller than ~ 3.87 Å, and a continuous linear increase when the a_{LSMO} parameter is larger, Figure 5.10 (b).

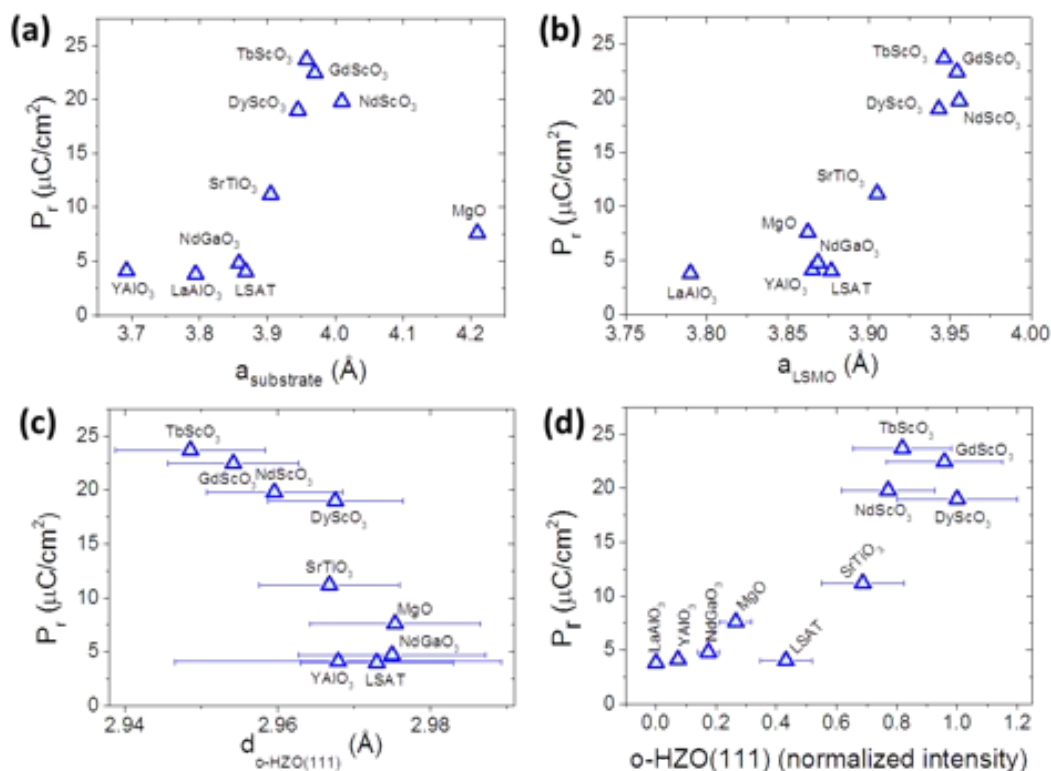


Figure 5.10: Remanent polarization as a function of (a) the lattice parameter of the substrate and (b) the a_{LSMO} parameter of the LSMO electrode. (c) Remanent polarization as a function of the interplanar $d_{\text{o-HZO}(111)}$ spacing. $d_{\text{o-HZO}(111)}$ was determined by Gaussian fits of the XRD 2θ peak position, and the error bar is set to 1σ of the fit. (d) Remanent polarization as a function of the normalized intensity of the XRD o-HZO (111) reflection. The intensity is normalized with respect to the intensity of the o-HZO (111) reflection of the film grown on DyScO_3 , which shows the biggest intensity.

Two potential contributions to the ferroelectric polarization can be considered: first, the amount of orthorhombic phase formed, and secondly, the strain state of the resulting o-HZO(111) phase (Figures 5.1, 5.4 and 5.5). These two contributions can ultimately determine the ferroelectric polarization. In order to assess the relevance of these two possible contributions, the remanent polarization is plotted as a function of the interplanar $d_{\text{o-HZO}(111)}$ spacing (Figure 5.10 (c)) and as a function of the normalized intensity of the XRD o-HZO 111 reflection (Figure 5.10 (d)). The films

with shorter interplanar $d_{\text{0-HZO}(111)}$ spacing appear to have larger polarization, but the graph does not show a clear dependence as error bars in the lattice parameter are comparable to its variation. In contrast, Figure 5.10 (d) clearly confirms that samples with the largest amount of orthorhombic phase (mainly on scandate substrates) also have the largest polarization. Thus, the role of epitaxial stress is unraveled: (1) it conditions the epitaxial stabilization of the orthorhombic phase, and (2) the amount of this phase determines the ferroelectric polarization. The impact is critical, and films on scandate substrates present greatly enhanced ferroelectric properties.

In summary, the role of epitaxial stress on the stabilization of the metastable orthorhombic phase of HZO has been unraveled. LSMO bottom electrodes are elastically strained in a range of lattice mismatch from around -2 to 2% , which allows to engineer the amount of orthorhombic and monoclinic phases present in the films. As long as the fully strained state of the LSMO is maintained, the amount of stabilized orthorhombic phase is enhanced on substrates with a pseudocubic lattice parameter larger than around 3.87 \AA , while the amount of monoclinic phase is reduced. TbScO_3 and GdScO_3 are optimal substrates to stabilize the orthorhombic HZO phase, with negligible amount of paraelectric phase and much higher polarization than that of films on SrTiO_3 or LSAT substrates. Epitaxial ultrathin HZO films with enhanced properties on TbScO_3 and GdScO_3 substrates could be used in emerging devices such as ferroelectric tunnel junctions, with superior performance than that of epitaxial films on SrTiO_3 (001).

5.3 Domain-Matching Epitaxy of $\text{Hf}_{0.5}\text{Zr}_{0.5}\text{O}_2$ (111) grown on $\text{La}_{0.7}\text{Sr}_{0.3}\text{MnO}_3$ (001)

The epitaxial relationship between (111) oriented orthorhombic and (001) oriented monoclinic crystallites, and the LSMO layer has been revealed, showing that depending on the lattice parameter of the LSMO, one or another phase and orientation are favored. Meanwhile, the mechanism allowing epitaxial growth is unknown and intriguing. Indeed, epitaxy was unexpected considering the symmetry dissimilarity and the large lattice mismatch between orthorhombic HZO(111) on LSMO(001), which naturally leads to the question: How does (111)-oriented orthorhombic HZO grow epitaxially on LSMO(001)? Covalent epitaxy requires crystal matching at the interface between film and substrate (or lower layer). Cube-on-cube epitaxy is common when lattice mismatch is low. Other simple cases, as 45° in-plane unit-cell rotation, are frequent.¹⁷⁹ However, these simple mechanisms of epitaxy are not feasible when substrate and film are more dissimilar. In these cases, films are generally polycrystalline, although some more unusual mechanisms can permit epitaxy. Examples include tilted epitaxy¹⁴³ and coincidence lattice epitaxy,¹⁷⁶ also called domain matching epitaxy (DME).¹⁸⁰

In this section, the possibility of the DME mechanism is investigated by analyzing STEM images of the sample grown on GdScO_3 (001), HZO/LSMO/ GdScO_3 . GdScO_3 (001) substrates are optimal to stabilize the orthorhombic phase: HZO/LSMO/ GdScO_3 films are free of the paraelectric monoclinic phase, permitting to achieve ferroelectric HZO films with a higher ferroelectricity with a remanent polarization slightly above $20 \mu\text{C}/\text{cm}^2$.

5.3.1 Analysis of the plane matching at the HZO/LSMO interface

Semicoherent interfaces between HZO and LSMO are observed by STEM. As shown previously, there are four basic domains of o-HZO(111) on LSMO. Figure 5.11 shows four GdScO_3 (111) poles and 12 o-HZO (-111) poles. Crystal domains form in heteroepitaxy when the symmetry of the film is lower than that of the substrate,^{181,182} and they can contribute to relieve elastic energy of the film.¹⁸³ One single o-HZO variant would produce three (-111) poles (i.e. (-111), (1-11) and (11-1)); therefore, the presence of 12 poles confirms the presence of four o-HZO epitaxial crystal variants. The four crystal domains are a natural consequence of the threefold symmetry of (111)-oriented HZO film grown on the fourfold symmetry LSMO(001). a , b and c are slightly different in the HZO orthorhombic cell, and so are the angles in the plane and oop directions. The latter entails that each (-111) pole should be made up of three poles corresponding to three similar but not equivalent domains, which are not resolved here due to the experimental resolution. Each of the four HZO domains on LSMO should then be split into another three kind of HZO domains, denoted as a , b and c domains are shown in top view in Figure 5.12. In the a , b and c kinds of domains, the projection along either a , b or c axis is aligned with the LSMO diagonal ($\langle 110 \rangle$).

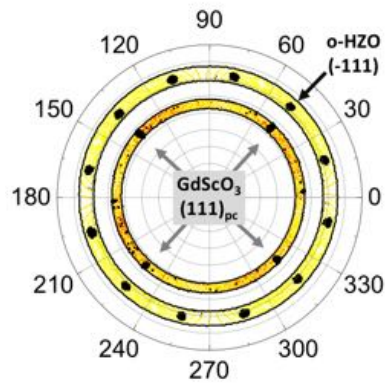


Figure 5.11: XRD pole figure around asymmetric $\text{GdScO}_3(111)$ and $\text{o-HZO}(-111)$ reflections of $\text{o-HZO}(111)$ crystallites.

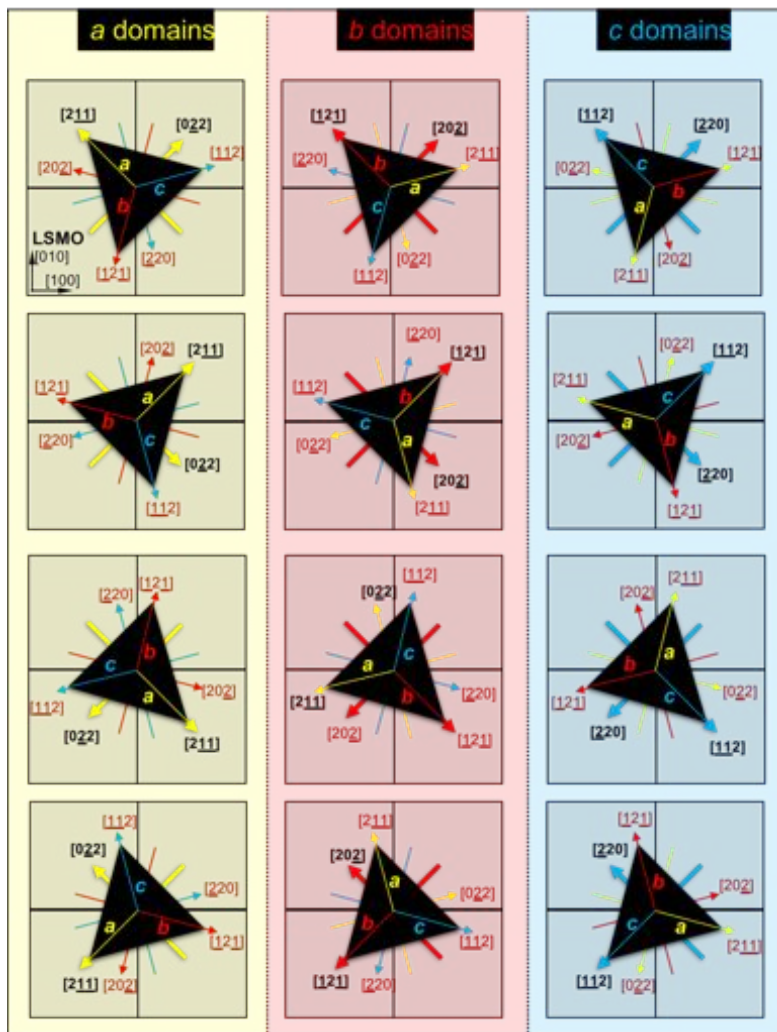


Figure 5.12: All possible $\text{o-HZO}(111)$ domains on LSMO according to the experimentally observed (111) oriented epitaxy. The HZO unit cell (black triangle) is observed projected along the $[111]$ direction (top view) on the LSMO surface (squares). The relative sizes of HZO and LSMO unit cells do not reproduce the real ones. The bold directions are the ones aligned with the LSMO $\langle 110 \rangle$ axis in each domain, with the projection of a , b and c aligned in a , b and c domains, respectively.

The a , b and c variants have a very similar cation pattern (Hf/Zr) on the observation plane of the used zone axis in HAADF imaging. The epitaxial relationship between the four crystal variants of o-HZO(111)film and the GdScO₃(001) (or the coherently strained LSMO(001) electrode), as well as the STEM observation direction, are sketched in Figure 5.13 (a). It is not obvious how lattice matching between the approximately four fold and three fold symmetries of LSMO(001) and o-HZO(111) surfaces occurs. Figure 5.13 (b) depicts the simulated structures of LSMO and o-HZO across the interface,⁶¹ projected on the HZO plane containing [111]_{op}/[11-2]_{ip} (op and ip subindices indicate out-of-plane and in-plane, respectively) and, correspondingly, the [001]_{op}/[110]_{ip} plane of LSMO. The same structure projected on the ip orthogonal direction of HZO, [111]_{op}/[-220]_{ip}, and [001]_{op}/[110]_{ip} of LSMO, is presented in Figure 5.13 (c). The atomic arrangement of LSMO implies an in-plane distance between cation columns parallel to the interface of approximately 2.807 Å, corresponding to the (110) interplanar distance. This distance is determined by the GdScO₃ substrate, since the LSMO layer grows fully strained on it. On the other hand, the atomic arrangement of o-HZO is more complex, and has been simulated using VESTA software considering calculated lattice constant for orthorhombic ($Pca2_1$) HfO₂ ($a=5.234\text{Å}$, $b=5.010\text{Å}$, $c=5.043\text{Å}$).^{61,161} The STEM results are in agreement with the simulations done considering the $Pca2_1$ space group. Since HZO has an orthorhombic unit-cell, cation distances are slightly different along variants of the same family of directions [1-21], [11-2] and [-211], with distances of 3.095, 3.105 and 3.163 Å, respectively. The projected structure of cations is similar in these different variants that can lie on the STEM observation plane when the substrates is seen along the [110] zone axis, making challenging to distinguish between them from the STEM images. I advance that the analysis that follows is quantitatively sensitive to the considered lattice parameters extracted from the bibliography, but it does not affect the extracted conclusions. The HZO cation columns appear positioned along the HZO[11-2] direction at a distance of approximately 3.105 Å. In order to analyze the lattice matching of HZO on LSMO, HZO (11-1) and LSMO (110) planes were used; see Figure 5.13(b). The HZO (11-1) planes are used (instead of the HZO (11-2) planes) because unlike the HZO (11-2) planes, they all end in the cations (Hf/Zr) located at the HZO/LSMO interface. The lattice mismatch (f) with LSMO ($f(\%) = 100 \times (d_{\text{LSMO}} - d_{\text{HZO}}) / d_{\text{HZO}}$, where d_{LSMO} and d_{HZO} are the horizontal distances between consecutive horizontally aligned cation columns in each material) is -9.60%. The matching of HZO (-220) and LSMO (110) planes along the orthogonal direction is shown in Figure 5.13 (c). The HZO cation columns are at a distance of approximately 1.811 Å (corresponding to the distance between (-220) planes), and the corresponding lattice mismatch with LSMO is 55.02%. Conventional epitaxy (coherent growth, followed by plastic relaxation above a critical thickness) is usual in systems where mismatch is low or moderate, but it is not possible in largely mismatched systems as occurs along HZO[-211]/LSMO[1-10] and along HZO[0-22]/LSMO[1-10], where mismatches are about -10% and 55%, respectively.

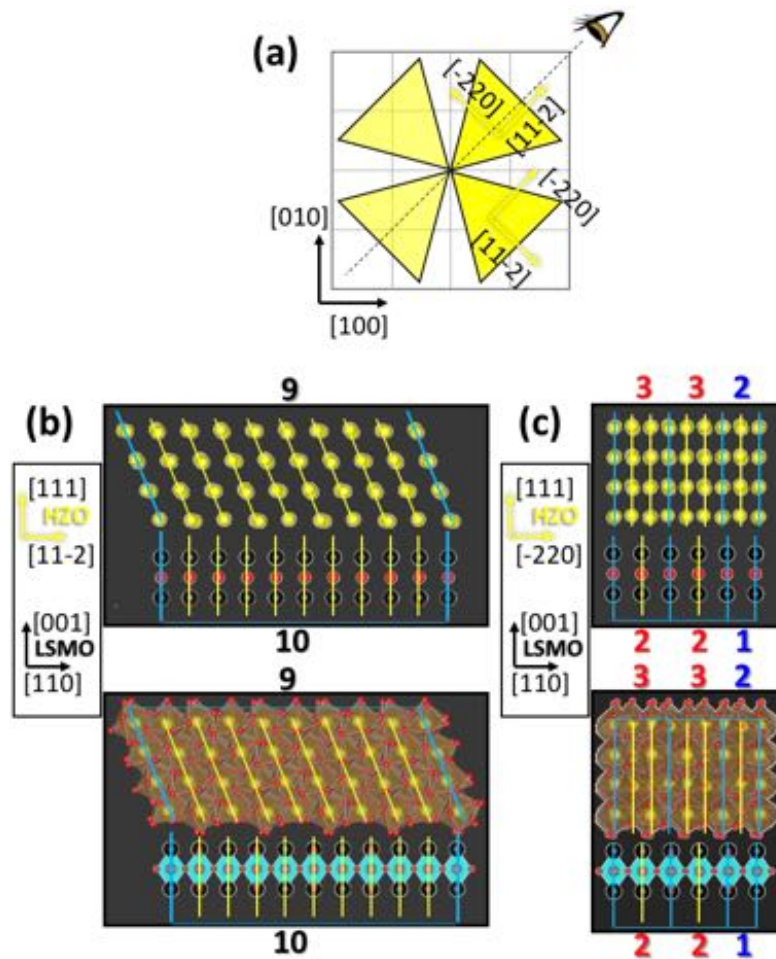


Figure 5.13: (a) Schematic showing a top view of HZO crystallites on the LSMO(001) surface and the observation direction (eye). The four existing in-plane orientation variants of HZO crystallites are schematized with four yellow triangles. (b) and (c) show predicted optimal domains for [11-2] and [-220] HZO variants, respectively, as seen laterally. For it, (11-1) (for [11-2] variants) and (-220) (for [-220] variants) HZO planes and LSMO(110) planes are marked. Only cations are shown in the sketches at the top, while both cations and oxygen atoms with the corresponding polyhedral sides are shown at the bottom. Planes delimiting the border of a domain are in light blue, while planes inside a domain are in yellow. In (b), the matching of 9 HZO (-111) with 10 LSMO (110) planes is shown (domain with smaller residual strain), while combinations of 3/2 (red) and 2/1 (blue) (-220)/(110) matching of planes is shown in (c) for [-220] variants. Hf/Zr cations (yellow balls) on the (001)-LSMO surface (La/Sr are black, while manganese and oxygen are in red).

Figure 5.14 shows a cross-section STEM image projected on the $[001]_{\text{op}}/[110]_{\text{ip}}$ plane of LSMO. Two grains corresponding to [11-2] and [-1-12] HZO crystal variants can be recognized, while a sharp contrast between HZO and LSMO layers can be seen. As visible (review Chapter 4 for a detailed characterization of the HZO/LSMO interface) the semicoherent interface develops after the Hf/Zr monolayer integrated into the LSMO structure. Despite the huge mismatch around -10%, the

interface is coherent (see zooms in Figure 5.14 (b) and (c)). The zoomed view (Figure 5.14 (c)) reveals the matching of $n=10$ atomic La/Sr planes of the LSMO electrode with $m=9$ atomic Hf/Zr planes of the HZO film. Note that the matching of n with m planes represents n and m times the distance between atomic columns; therefore, for $n=10$ and $m=9$, $n+1=11$ and $m+1=10$ columns are shown, respectively. Fast Fourier Transform (FFT) filtering of the images easily visualizes the additional planes, i.e. edge dislocations. In the case of grains with $[11-2]$ orientation, the domain size is deduced from the distance between these additional planes of LSMO, since they are more clearly visualized in the FFT filtered image. The STEM image (Figure 5.14 (b)) after FFT filtering (the FFT is presented in the inset) is shown in Figure 5.14 (d), displaying distances between adjacent additional planes of 9/10 and 10/11, indicating the presence of domains with the same periodicities. Figure 5.14 (e) shows the residual

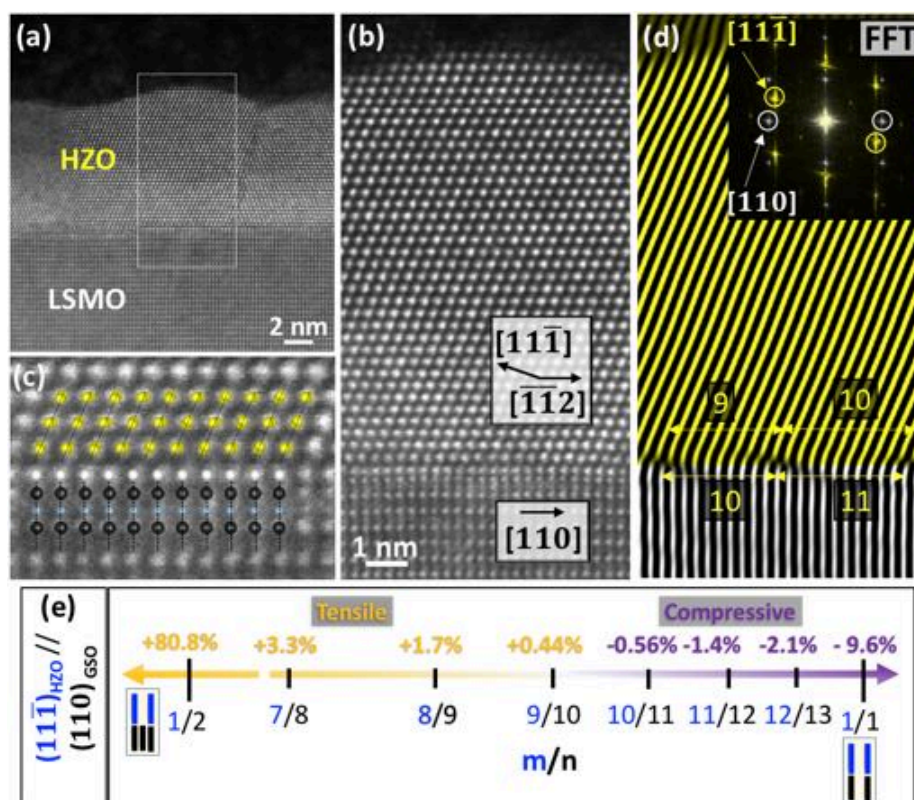


Figure 5.14: (a) Cross-sectional HAADF image of the HZO/LSMO heterostructure showing crystal variants of the $[11-2]$ type. (b) Zoomed image extracted from the region marked in (a). (c) Zoomed region around the interface with superimposed structural models of $[11-2]$ HZO and $[110]$ LSMO, showing a 9/10 domain. (d) Reconstructed image from reflections in the Fourier space corresponding to $[11-1]$ HZO and $[110]$ LSMO planes. (inset) The FFT of both HZO and LSMO. For the sake of clarity, planes in the HZO layer are shown in yellow, while planes in the LSMO are white. The same color code applies to the reflections present in the FFT inset. Two adjacent 9/10 and 10/11 domains are indicated in (d). (e) shows the residual strain along the $[11-2]$ for different periods.

lattice mismatch for different values of m and n calculated considering the $[11-2]$ direction (cation distance of 3.105\AA), with 9/10 having the smallest residual strain. Indeed, domains with m/n ratios

of 9/10 are found in all [11-2] crystal variants examined, Figure 5.15. Domains of close size, such as 6/7 (Figure 5.15 (a) and (b)) or 11/12 and 10/11 (Figure 5.14 and Figure 5.15 (c), (d) and (e)) are also found. Smaller domains as 6/7 can correspond to other variants of the same family (not clearly distinguished here, due to the very similar cation projected structure), particularly [-211] where smaller HZO domains are expected given the bigger interplanar distance of 3.163Å (with 8/9 domains having the smallest strain in this case) and can combine with other domains to produce an overall small strain. About 3 or 4 of such domains fit within one single crystallite, given the domains and grain sizes, the latter being ~10–12 nm.

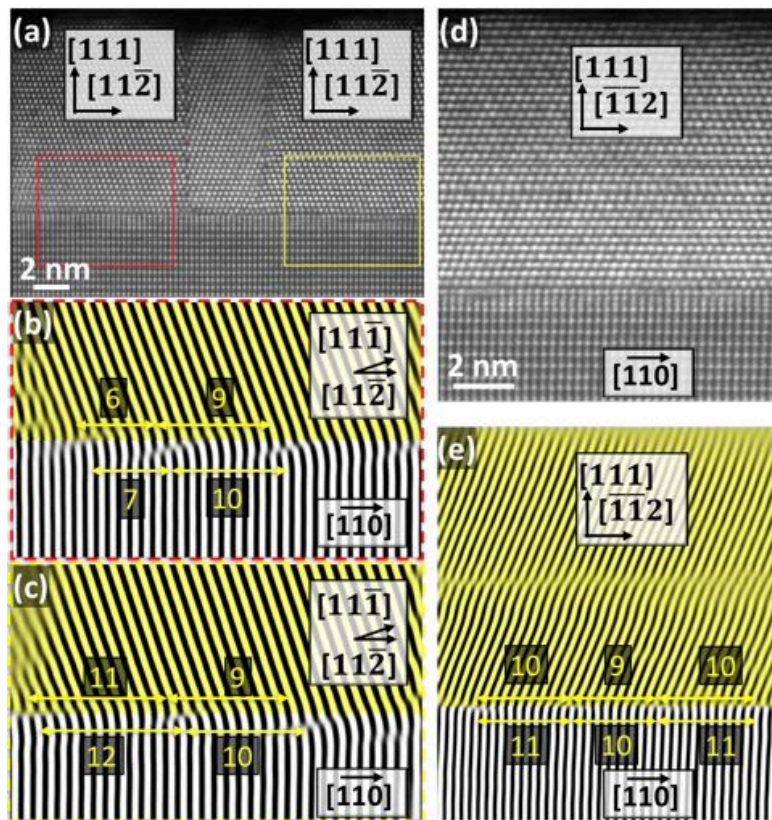


Figure 5.15: (a) shows a cross-sectional HAADF image of the HZO/LSMO heterostructure with three HZO grains with [11-2] in the observation plane. The analysis of HZO (11-1) and LSMO (110) planes of the grain at the left (marked in red) and the grain at the right (marked in yellow) reveals domains with m/n ratios above and below 9/10. (d) shows a bigger [11-2] type grain containing four misfit dislocations, as revealed in (e).

The STEM characterization of HZO[-220]/LSMO[1-10] interfaces, corresponding to the orthogonal direction of HZO[11-2], is summarized in Figure 5.16. The cross-sectional STEM view in Figure 5.16 (a) shows a [-220] grain variant occupying most of the imaged HZO film. There is also a second [-220] grain at its right. The zoom of the main [-220] grain shows a semicoherent interface, and its analysis reveals much smaller domains (Figure 5.15 (b) and (c)) than along the orthogonal [11-2] direction. Here, most of the domains correspond to the matching of 3 atomic Hf/Zr planes and 2

La/Sr planes. The FFT filtered image (Figure 5.16 (c)) also reveals the presence of an important number of 2/1 domains, appearing approximately 4 times less frequently than 3/2 domains.

DME of HZO(111) on LSMO(001) results in an effective lattice mismatch f^* (%) = $100 \times (n \cdot d_{\text{LSMO}} - m \cdot d_{\text{HZO}}) / n \cdot d_{\text{HZO}}$ that is much smaller than the lattice mismatch f of direct accommodation

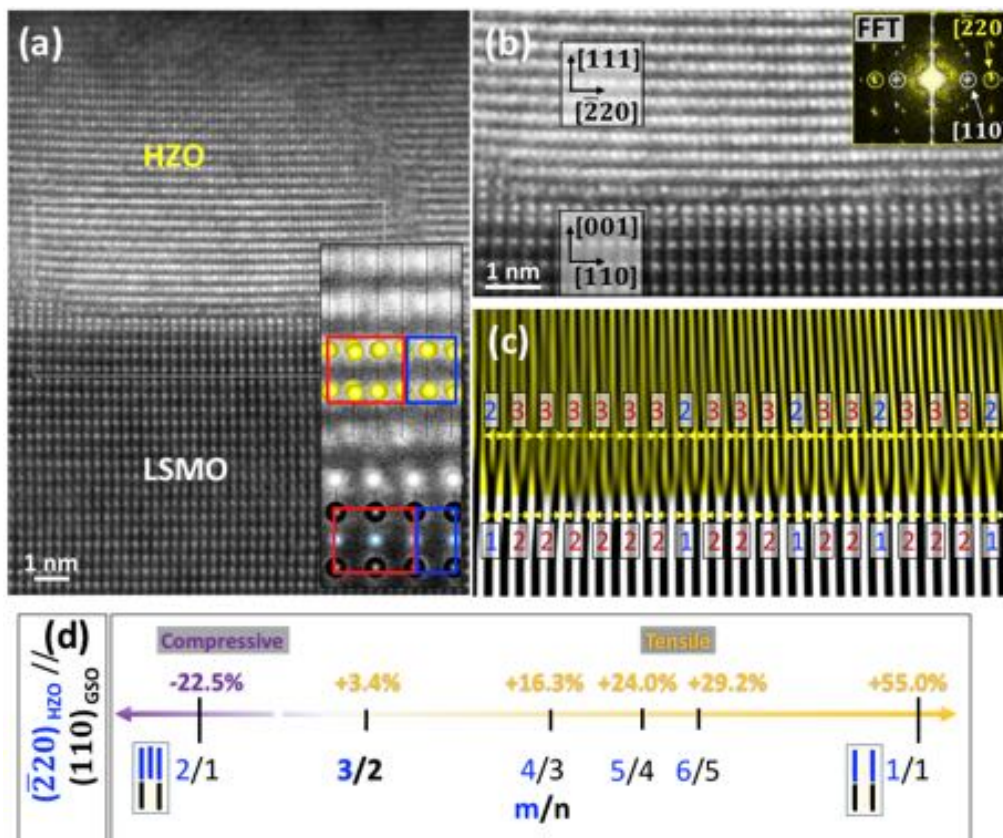


Figure 5.16: (a) Cross-sectional HAADF image of the HZO/LSMO heterostructure showing crystal variants of the $[-220]$ type. Bottom right inset shows a zoomed region around the interface with superimposed structural models of $[-220]$ HZO and $[110]$ LSMO, showing two adjacent 3/2 (red) and 2/1 (blue) domains. Yellow and white balls correspond to Hf/Zr atoms in the o-HZO and in the LSMO perovskite structures, respectively, while black and violet balls represent La and Mn. (b) Zoom extracted from the region marked in white in (a) and FFT of HZO layer (yellow) and LSMO (white) in the top right inset. (c) Equivalent filtered image extracted from (b) by only considering the FFT marked reflections in the inset in (b). 3/2 (red) and 2/1 (blue) domains are visible. From first 2/1 domain on the left to last 3/2 on the right there is a total ratio of 18 domains (14 of which are 3/2 and 4 are 2/1), indicating that in the imaged region around 77% of the present domains are 3/2, while around 23% are 2/1. (d) shows the residual strain along the $[-220]$ for different periods.

of one-to-one lattice planes. In the case of HZO(111)/LSMO(001), the m/n values that minimize f^* are 9/10 and 3/2 for HZO HZO $[11-2]$ /LSMO $[110]$ and $[-220]$ /LSMO $[110]$ interfaces, respectively (see Figures 5.14 (e) and 5.16 (d)). The residual mismatches after forming domains with these m/n are $f^*(\text{HZO}[11-2]/\text{LSMO}[110]) = 0.4\%$ and $f^*(\text{HZO}[-220]/\text{LSMO}[110]) = 3.4\%$. The residual

mismatch is still significant in the first case. However, domains with close m and n values can coexist to allow exact coincidence along a longer interface distance. In the case of the HZO[−220]/LSMO[110] interface, a minimal residual mismatch can be achieved from the combination of about 15% of 2/1 domains with 85% of 3/2 domains. For other variants of the same family, the ratio of 2/1 and 3/2 domains that minimizes the mismatch is slightly different. In the case of the HZO[11−2]/LSMO[110] interface, most of the domains are 9/10, and the observed presence of domains producing tensile (6/7) or compressive (10/11 or 11/12) strain can combine to minimize the residual stress.

The formation of a semicoherent interface in HZO above a monolayer differs from the nucleation and glide of misfit dislocations above a critical film thickness that occurs in conventional epitaxy. Films grown by conventional epitaxy mechanism are elastically strained before plastic relaxation occurs, and the elastic energy, proportional to the thickness and the square of strain, can be high.¹⁸⁴ The stoichiometry of strained films can change locally,¹⁸⁵ and other defects can form also to relieve the elastic energy,¹⁸⁶ and/or threading dislocations will be generated when the films relax plastically above the critical thickness.¹⁸⁷ These strain relief mechanisms can result in severe degradation of properties. In contrast, in films grown by the DME, dislocations are expected to form at the interface during the early stages of grain nucleation, permitting unstrained growth without formation of strain-driven defects. When the film is cooled after growth, differences in thermal expansion coefficients between film and substrate, or a possible phase transition, would also introduce a small amount of residual elastic strain or some dislocations, but with much lower amount of strain-driven defects than in conventional high-mismatch epitaxy. Therefore, the advantage of DME is twofold: it permits epitaxy in largely mismatched systems, and it results in a low-defect film. The occurring changes in surface symmetry, threefold in HZO(111) and fourfold in LSMO(001), are similar to others that are frequent in heteroepitaxy.^{174,181} The (111) growth of HZO occurs because of the lower HZO/LSMO interfacial energy compared to that between LSMO(001) and other low-index planes of HZO. Moreover, *ab initio* calculations of the energy of HZO films of different orientations concluded that the (111)-orientation made the orthorhombic phase thermodynamically stable with respect to the monoclinic one.¹⁶⁸ Thus, the (111)-orientation would be optimal considering both HZO(111) film and HZO(111)/LSMO(001) interface energies. Beyond DME, it is important to remark that several contributions may also be very relevant to minimize the total energy in the complex epitaxy of o-HZO(111) on LSMO(001), namely, interface energy, surface energy of o-HZO(111) and strain relief at domain and grain boundaries.

In the case of the m-HZO phase, the grains have (001) orientation with the following epitaxial relationship m-HZO[010]/LSMO[110]. The plane matching at the interface between m-HZO and LSMO grown on LSAT is analyzed in Figure 5.17.

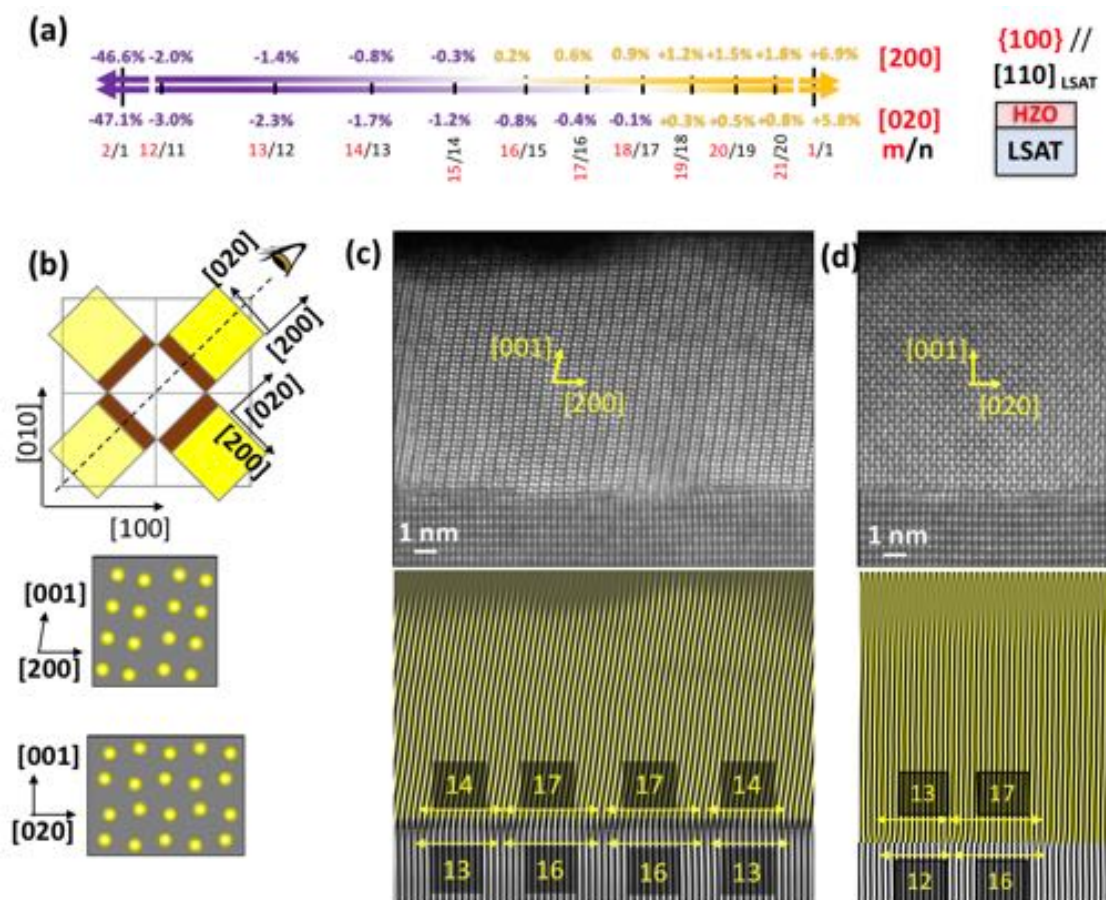


Figure 5.17: (a) monoclinic lattice mismatch along $[100]$ ((200) planes) and $[010]$ ((020) planes) directions for different values of m and n on the different substrates inspected by STEM. (b) sketch of crystallographic variants (top view) and the cation pattern expected along each one. (c) and (d) show the plane matching in $[200]$ and $[020]$ variants.

Figure 5.17 (a) shows the strain for different values of m and n along $[100]_{\text{HZO}}$ and $[010]_{\text{HZO}}$ directions. It can be appreciated that changing m and n by one unit changes the residual strain changes much less than in the o-HZO(111) case. Figure 5.17 (b) shows the possible crystallographic variants on the LSMO surface, with two orthogonal directions ($[100]$ and $[010]$) being accessible in STEM images obtained along the substrate $[110]$ zone axis. Figure 5.17 (c) and (d) show images that contain monoclinic grains with the two orthogonal directions and their corresponding plane analysis across the m-HZO/LSMO interface. m-HZO (200) and (020) (with distances of 2.56\AA and 2.58\AA , respectively; considering monoclinic unit-cell: $a=5.119\text{\AA}$, $b=5.169\text{\AA}$ ¹⁸⁸) planes, which end in consecutive cations at the interface, and LSMO (110) (2.74\AA , corresponding to the (110) spacing in LSAT) are used. Figure 5.17 (c) and (d) bottom panels show a mixture of tensile and compressive domains in the m-HZO film.

In conventional epitaxy (one-to-one plane matching), the lattice mismatch of m-HZO would be 6.9% and 5.8% along [100] and [010] directions (Figure 5.17(a)). In GSO, the equivalent mismatch would be 9.7% and 8.6% along [100] and [010] directions, which would require a larger density of extra planes in the HZO layer to make the HZO strain vanish. This fact could favor the (111) over the (001) orientation on bigger substrates. In the case of the (111) orientation, o-HZO is expected to have lower energy than m-HZO,¹⁶⁸ so the positive strain might favor the (111) and as a consequence the stabilization of o-HZO. Therefore, as far as the LSMO stays strained, the substrates with largest lattice parameters could be expected to favor the formation of the o-HZO over the m-HZO, as is experimentally observed.

Wrapping up, it is argued that the large lattice mismatch of o-HZO(111), about -10% along [11-2]HZO/[110]LSMO and about 55% along [-220]HZO/[110]LSMO, is accommodated by DME. In DME, m lattice planes of the upper layer match with n lattice planes of the lower layer (where m and n are different natural numbers), instead of the one-to-one matching of conventional epitaxy. The formation of domains, with m/n values of $\sim 9/10$ along [-211] and $3/2$ along [0-22] HZO directions, would then permit the relief of the epitaxial stress and the growth of high crystal quality orthorhombic films.

5.4 Conclusions

The huge effect of the epitaxial stress on the epitaxial stabilization of the metastable orthorhombic phase of HZO has been demonstrated. First, it has been shown that o-HZO is strongly favored over the m-HZO when the LSMO ip lattice parameter is larger than around 3.87 Å, which can be achieved by using substrates with appropriate lattice parameters. Secondly, it has been shown that the amount of orthorhombic phase determines the polarization of the HZO films, evidenced by the fact that TbScO_3 and GdScO_3 are both optimal substrates to stabilize the o-HZO phase and these films have much higher polarization than that of films grown on SrTiO_3 or LSAT substrates. Finally, it has been proposed that DME, through the formation of domains with m/n values of $\sim 9/10$ along [11-2] and a combination of $3/2$ and $2/1$ along [-220] HZO directions, is an important factor permitting the relief of the epitaxial stress in the HZO film, resulting in the epitaxial stabilization of the o-HZO(111) phase in high-quality epitaxial films.

Summary and Perspective

This thesis has addressed the study of ferroelectric dipoles topology in BaTiO₃/SrTiO₃ SPLs and the effects of different epitaxial conditions on the phase stabilization and ferroelectricity of Hf_{0.5}Zr_{0.5}O₂ thin films. In both cases, intimate links between the macroscopic ferroelectric properties and the nanoscale structure have been established.

The study of ferroelectric dipoles topology carried out in a set of BaTiO₃/SrTiO₃ symmetric SPLs by STEM reveals notable differences at the unit cell level. The ferroelectric distortion (δ_{Ti}) maps of 2 and 4-SPLs indicate that the polarization is highly oriented along the oop direction, as expected from the lattice strain induced by the SrTiO₃ substrate and its coupling to the polarization. Moreover, high δ_{Ti} distortions are observed, reaching up to 40 pm in 2-SPL and up to 30 pm in 4-SPL in the BaTiO₃ layers right next to the LSMO electrode, and acquiring more moderate values around the center of the SPL (down to around 10 pm). On the other hand, 10-SPL shows smooth rotations of the polarization inside the BaTiO₃ layers that are not next to the LSMO electrode or the top surface of the SPL. In 10-SPL the δ_{Ti} values are around or below 10 pm. Decreasing δ_{Ti} values are observed as the SPLs layers become thicker, indicating an also decreasing spontaneous polarization, in agreement with the macroscopic polarization. The observation of smooth polarization rotations in BaTiO₃ is the experimental verification of the feasibility of such rotations under what is regarded as unfavorable conditions, as it is the fixed direction of the unit-cell tetragonal axis. Additionally, such polarization configurations are found to remain stable during the probed time scale.

Regarding the research carried out in Hf_{0.5}Zr_{0.5}O₂ thin films, the ferroelectricity of epitaxial Hf_{0.5}Zr_{0.5}O₂ (HZO) thin films is found to depend mainly on the ferroelectric to non-polar phases fraction (i.e. orthorhombic to monoclinic fraction). The following different strategies have been demonstrated to control the fraction of orthorhombic phase:

- (1) The effect of the electrode on which HZO is deposited:
 - i. Only LSMO or similar manganites as LCMO are suitable for the stabilization of o-HZO on perovskites.
 - ii. The HZO/bottom electrode interfacial chemistry was revealed to play a fundamental role on the epitaxy of HZO and the stabilization of o-HZO. The growth of HZO on LSMO induces a chemical reconstruction on the surface of the latter, basically consisting in the substitution of Mn by Hf/Zr cations.

(2) Besides, the lattice parameters of the LSMO bottom electrode greatly affects the competition between orthorhombic and monoclinic phases. Continuous tuning of the LSMO lattice parameters by epitaxial strain permits to tune the microstructure of the HZO films: it allows to obtain either pure m-HZO films, coexisting m/o-HZO or pure o-HZO films. Domain matching epitaxy is argued to be a mechanism that permits the strain relief and epitaxial growth of the fluorite-HZO on the dissimilar perovskite-LSMO structure.

This thesis' interest also lies in the new questions and potential research lines that may arise from it. In the case of BaTiO₃/SrTiO₃, the results presented in Chapter 3 are the first of its kind in BaTiO₃, and therefore new studies are needed. Apart from studies assessing the feasibility of the polarization domains under different conditions, it could be interesting to probe how the domains evolve under externally variable electric fields. Such kind of studies are been carried on magnetic skyrmions, where the sizes of such topological structures are bigger though. Indeed, the nanometer scale of the revealed BaTiO₃ topologies makes these studies more challenging, but already feasible with the new in-situ electrical biasing TEM holders, which will allow researchers to investigate the electrical response of materials inside the transmission electron microscope.

In the case of HZO, the stabilization of the orthorhombic phase seems a complex process that depends on an interplay of conditions, not always easy to identify and reproduce. New studies are needed to improve the understanding of formation of the metastable o-HZO phase and the associated ferroelectric properties. Currently, different research groups including ourselves, are designing and performing new experiments with epitaxial (Hf,Zr)O₂ thin films, as the use of different dopants. Furthermore, epitaxial films are grown primarily by PLD, which allows to adjust the thermodynamics/kinetics balance using growth temperature, growth rate and plasma energy. These studies have yet to be addressed, as well as the use of other deposition techniques, including Molecular Beam Epitaxy and Atomic Layer Deposition, for instance. Epitaxial HZO films have allowed the achievement of simultaneous high polarization, retention, and endurance up to 10¹¹ cycles, however they appear to suffer pronounced fatigue. Different causes have been attributed to the phenomenon, including domain walls, oxygen vacancies and other charged defects and paraelectric-ferroelectric phase changes, which suggests that that the microstructure of the film, and the changes that may take place at the atomic scale, may be critical. For this reason, operando atomic scale electron microscopy investigations can provide important clues. As mentioned before, the new in-situ electrical biasing TEM holders are expected to make such studies possible.

Besides, the results on HZO presented in this thesis have contributed positively to other research lines within our research group. The knowledge acquired about the microstructure of the films has helped to untangle the role of ferroelectric and microstructure contributions to the electroresistance in HZO ferroelectric junctions,¹²⁴ later leading to engineered HZO ferroelectric junctions with larger voltage operation window and improved homogeneity and endurance.¹⁸⁹ Moreover, it has contributed to realize of the unexpected positive side of the presence of the HZO monoclinic phase, which enhances the ferroelectric endurance of the HZO films (results submitted to *Advanced Electronic Materials*).

Bibliography

- 1 N. Setter, D. Damjanovic, L. Eng, G. Fox, S. Gevorgian, S. Hong, A. Kingon, H. Kohlstedt, N. Y. Park, G. B. Stephenson, I. Stolitchnov, A. K. Taganstev, D. V. Taylor, T. Yamada and S. Streiffer, *J. Appl. Phys.*, 2006, **100**, 051606.
- 2 S. Pandya, J. Wilbur, J. Kim, R. Gao, A. Dasgupta, C. Dames and L. W. Martin, *Nat. Mater.*, 2018, **17**, 432.
- 3 D. Damjanovic, P. Muralt and N. Setter, *IEEE Sens. J.*, 2001, **1**, 191–206.
- 4 T. S. Böске, J. Müller, D. Bräuhaus, U. Schröder and U. Böttger, *Appl. Phys. Lett.*, 2011, **99**, 102903.
- 5 T. Mikolajick, S. Slesazek, M. H. Park and U. Schroeder, *MRS Bull.*, 2018, **43**, 340–346.
- 6 M. H. Park, Y. H. Lee, T. Mikolajick, U. Schroeder and C. S. Hwang, *MRS Commun.*, 2018, **8**, 795–808.
- 7 S. E. Reyes-Lillo, K. F. Garrity and K. M. Rabe, *Phys. Rev. B - Condens. Matter Mater. Phys.*, 2014, **90**, 140103.
- 8 N. A. Spaldin, *J. Solid State Chem.*, 2012, **195**, 2–10.
- 9 R. E. Cohen, *Nature*, 1992, **358**, 136–138.
- 10 V. Garcia and M. Bibes, *Nat. Commun.*, 2014, **5**, 4289.
- 11 Fujitsu FRAM Guide Book, 2008, MN05-00009.
- 12 T. Eshita, W. Wang, K. Nakamura, S. Ozawa, Y. Okita, S. Mihara, Y. Hikosaka, H. Saito, J. Watanabe, K. Inoue, H. Yamaguchi and K. Nomura, *J. Phys. Sci. Appl.*, 2015, **5**, 29–32.
- 13 M. J. Pan and C. Randall, *IEEE Electr. Insul. Mag.*, 2010, **26**, 44–50.
- 14 F. Eltes, C. Mai, D. Caimi, M. Kroh, Y. Popoff, G. Winzer, D. Petousi, S. Lischke, J. Elliott Ortmann, L. Czornomaz, L. Zimmermann, J. Fompeyrine and S. Abel, *J. Light. Technol.*, 2019, **37**, 1456–1462.
- 15 S. V. Ushakov, A. Navrotsky, Y. Yang, S. Stemmer, K. Kukli, M. Ritala, M. A. Leskelä, P. Fejes, A. Demkov, C. Wang, B. Y. Nguyen, D. Triyoso and P. Tobin, *Phys. Status Solidi Basic Solid State Phys.*, 2004, **241**, 2268–2278.
- 16 T. D. Huan, V. Sharma, G. A. Rossetti and R. Ramprasad, *Phys. Rev. B - Condens. Matter Mater. Phys.*, 2014, **90**, 064111.
- 17 M. H. Park, Y. H. Lee, H. J. Kim, Y. J. Kim, T. Moon, K. Do Kim, J. Müller, A. Kersch, U. Schroeder, T. Mikolajick and C. S. Hwang, *Adv. Mater.*, 2015, **27**, 1811–1831.
- 18 G. Sharma, S. V. Ushakov and A. Navrotsky, *J. Am. Ceram. Soc.*, 2017, **101**, 31–35.
- 19 U. Schroeder, S. Mueller, J. Mueller, E. Yurchuk, D. Martin, C. Adelman, T. Schloesser, R. Van Bentum and T. Mikolajick, *ECS J. Solid State Sci. Technol.*, 2013, **2**, N69.
- 20 S. S. Cheema, D. Kwon, N. Shanker, R. dos Reis, S. L. Hsu, J. Xiao, H. Zhang, R. Wagner, A. Datar, M. R. McCarter, C. R. Serrao, A. K. Yadav, G. Karbasian, C. H. Hsu, A. J. Tan, L. C. Wang, V. Thakare, X. Zhang, A. Mehta, E. Karapetrova, R. V. Chopdekar, P. Shafer, E. Arenholz, C. Hu, R. Proksch, R. Ramesh, J. Ciston and S. Salahuddin, *Nature*, 2020, **580**, 478–482.
- 21 S. Dünkel, M. Trentzsch, R. Richter, P. Moll, C. Fuchs, O. Gehring, M. Majer, S. Wittek, B. Müller, T. Melde, H. Mulaosmanovic, S. Slesazek, S. Müller, J. Ocker, M. Noack, D. A. Löhr, P. Polakowski, J. Müller, T. Mikolajick, J. Höntschel, B. Rice, J. Pellerin and S. Beyer, in *Technical Digest - International Electron Devices Meeting, IEDM*, 2017, pp. 19.7.1-19.7.4.
- 22 J. Müller, T. S. Böске, U. Schröder, S. Mueller, D. Bräuhaus, U. Böttger, L. Frey and T. Mikolajick, *Nano Lett.*, 2012, **12**, 4318–4323.
- 23 C. Richter, T. Schenk, M. H. Park, F. A. Tschardtke, E. D. Grimley, J. M. LeBeau, C. Zhou, C. M. Fancher, J. L. Jones, T. Mikolajick and U. Schroeder, *Adv. Electron. Mater.*, 2017, **3**, 1700131.

- 24 A. Zenkevich, Y. Matveyev, K. Maksimova, R. Gaynutdinov, A. Tolstikhina and V. Fridkin, *Phys. Rev. B - Condens. Matter Mater. Phys.*, 2014, **90**, 161409.
- 25 N. Balke, B. Winchester, W. Ren, Y. H. Chu, A. N. Morozovska, E. A. Eliseev, M. Huijben, R. K. Vasudevan, P. Maksymovych, J. Britson, S. Jesse, I. Kornev, R. Ramesh, L. Bellaiche, L. Q. Chen and S. V. Kalinin, *Nat. Phys.*, 2012, **8**, 81–88.
- 26 G. Sanchez-Santolino, J. Tornos, D. Hernandez-Martin, J. I. Beltran, C. Munuera, M. Cabero, A. Perez-Muñoz, J. Ricote, F. Mompean, M. Garcia-Hernandez, Z. Sefrioui, C. Leon, S. J. Pennycook, M. C. Muñoz, M. Varela and J. Santamaria, *Nat. Nanotechnol.*, 2017, **12**, 655–662.
- 27 K. H. Chew, M. Iwata, F. G. Shin and Y. Ishibashi, *Integr. Ferroelectr.*, 2008, **100**, 79–87.
- 28 K. G. Lim, K. H. Chew, L. H. Ong and M. Iwata, *Epl*, 2012, **99**, 46004.
- 29 J. Junquera and P. Ghosez, *Nature*, 2003, **422**, 506–509.
- 30 P. Aguado-Puente, P. García-Fernández and J. Junquera, *Phys. Rev. Lett.*, 2011, **107**, 217601.
- 31 S. Lisenkov and L. Bellaiche, *Phys. Rev. B - Condens. Matter Mater. Phys.*, 2007, **76**, 020102.
- 32 A. P. Levanyuk and I. B. Misirlioglu, *J. Appl. Phys.*, 2011, **110**, 114109.
- 33 V. A. Stephanovich, I. A. Luk'yanchuk and M. G. Karkut, *Phys. Rev. Lett.*, 2005, **94**, 047601.
- 34 C. Kittel, *Phys. Rev.*, 1946, **70**, 965–971.
- 35 K. H. Chew, *Solid State Phenom.*, 2012, **189**, 145–167.
- 36 N. A. Pertsev, A. G. Zembilgotov and A. K. Tagantsev, *Phys. Rev. Lett.*, 1998, **80**, 1988.
- 37 D. G. Schlom, L.-Q. Chen, C.-B. Eom, K. M. Rabe, S. K. Streiffer and J.-M. Triscone, *Annu. Rev. Mater. Res.*, 2007, **37**, 589–626.
- 38 D. Fuchs, E. Arac, C. Pinta, S. Schuppler, R. Schneider and H. V. Löhneysen, *Phys. Rev. B - Condens. Matter Mater. Phys.*, 2008, **77**, 014434.
- 39 S. W. Bedell, A. Khakifirooz and D. K. Sadana, *MRS Bull.*, 2014, **39**, 131–137.
- 40 D. G. Schlom, L. Q. Chen, C. J. Fennie, V. Gopalan, D. A. Muller, X. Pan, R. Ramesh and R. Uecker, *MRS Bull.*, 2014, **39**, 118–130.
- 41 J. Lyu, I. Fina, R. Solanas, J. Fontcuberta and F. Sánchez, *Sci. Rep.*, 2018, **8**, 495.
- 42 M. A. Moram and M. E. Vickers, *Reports Prog. Phys.*, 2009, **72**, 036502.
- 43 I. Fina Martínez, *Dissertation*, 2012, UAB.
- 44 I. Fina, L. Fábrega, E. Langenberg, X. Mart, F. Sánchez, M. Varela and J. Fontcuberta, *J. Appl. Phys.*, 2011, **109**, 074105.
- 45 D. B. Williams and C. B. Carter, *Transmission electron microscopy: A textbook for materials science*, 2009.
- 46 P. D. Pennycook, Stephen J. Nellist, *Scanning Transmission Electron Microscopy: Imaging and Analysis*, Springer, 2011.
- 47 R. F. Egerton, *Electron Energy-Loss Spectroscopy in the Electron Microscope*, 2011.
- 48 M. F. M. Ondrej L. Krivanek, Niklas Dellby, *Handbook of Charged Particle Optics*, 2017.
- 49 A. R. Lupini, S. N. Rashkeev, M. Varela, A. Y. Borisevich, M. P. Oxley, K. Van Benthem, Y. Peng, N. De Jonge, G. M. Veith, T. J. Pennycook, W. Zhou, R. Ishikawa, M. F. Chisholm, S. T. Pantelides and S. J. Pennycook, in *RSC Nanoscience and Nanotechnology*, 2015.
- 50 F. Hosokawa, H. Sawada, Y. Kondo, K. Takayanagi and K. Suenaga, *J. Electron Microsc. (Tokyo)*. 2013, **62**, 23–41.
- 51 C. Ophus, *Microsc. Microanal.*, 2019, **25**, 563–582.
- 52 I. T. Joliffe and B. Morgan, *Stat. Methods Med. Res.*, 1992, **1**, 69–95.

- 53 C. Hill and C. Hill, in *Learning Scientific Programming with Python*, 2016.
- 54 M. Nord, P. E. Vullum, I. MacLaren, T. Tybell and R. Holmestad, *Adv. Struct. Chem. Imaging*, 2017, **3**, 9.
- 55 T. Nakatani, A. Yoshiasa, A. Nakatsuka, T. Hiratoko, T. Mashimo, M. Okube and S. Sasaki, *Acta Crystallogr. Sect. B Struct. Sci. Cryst. Eng. Mater.*, 2016, **72**, 151–159.
- 56 E. Bousquet, M. Dawber, N. Stucki, C. Lichtensteiger, P. Hermet, S. Gariglio, J. M. Triscone and P. Ghosez, *Nature*, 2008, **452**, 732–736.
- 57 J. Gazquez, M. Stengel, R. Mishra, M. Scigaj, M. Varela, M. A. Roldan, J. Fontcuberta, F. Sánchez and G. Herranz, *Phys. Rev. Lett.*, 2017, **119**, 106102.
- 58 Y. Liu, Y. L. Zhu, Y. L. Tang and X. L. Ma, *J. Mater. Res.*, 2017, **32**, 947–956.
- 59 P. Gao, A. Kumamoto, R. Ishikawa, N. Lugg, N. Shibata and Y. Ikuhara, *Ultramicroscopy*, 2018, **184**, 177–187.
- 60 R. Ishikawa, A. R. Lupini, Y. Hinuma and S. J. Pennycook, *Ultramicroscopy*, 2015, **151**, 122–129.
- 61 K. Momma and F. Izumi, *J. Appl. Crystallogr.*, 2011, **44**, 1272–1276.
- 62 M. P. Singh, C. Simon, B. Raveau and W. Prellier, *Phase Transitions*, 2006, **79**, 973–990.
- 63 K. Ueda, H. Tabata and T. Kawai, *Science*, 1998, **280**, 1064–1066.
- 64 H. Tabata and T. Kawai, *Appl. Phys. Lett.*, 1997, **70**, 321–323.
- 65 R. Tsu, *Superlattice to Nanoelectronics*, 2011.
- 66 J. Ravichandran, A. K. Yadav, R. Cheaito, P. B. Rossen, A. Soukiassian, S. J. Suresha, J. C. Duda, B. M. Foley, C. H. Lee, Y. Zhu, A. W. Lichtenberger, J. E. Moore, D. A. Muller, D. G. Schlom, P. E. Hopkins, A. Majumdar, R. Ramesh and M. A. Zurbuchen, *Nat. Mater.*, 2014, **13**, 168–172.
- 67 A. Ohtomo and H. Y. Hwang, 2004, **427**, 423–427.
- 68 A. I. Lebedev, *Phys. Solid State*, 2010, **52**, 1448–1462.
- 69 A. K. Yadav, C. T. Nelson, S. L. Hsu, Z. Hong, J. D. Clarkson, C. M. Schlepütz, A. R. Damodaran, P. Shafer, E. Arenholz, L. R. Dedon, D. Chen, A. Vishwanath, A. M. Minor, L. Q. Chen, J. F. Scott, L. W. Martin and R. Ramesh, *Nature*, 2016, **534**, 138.
- 70 Z. Hong, A. R. Damodaran, F. Xue, S. L. Hsu, J. Britson, A. K. Yadav, C. T. Nelson, J. J. Wang, J. F. Scott, L. W. Martin, R. Ramesh and L. Q. Chen, *Nano Lett.*, 2017, **17**, 2246–2252.
- 71 H. W. Wu, S. Lu, T. Aoki, P. Ponath, J. Wang, C. Young, J. G. Ekerdt, M. R. McCartney and D. J. Smith, *Adv. Mater. Interfaces*, 2020, **7**, 2000555.
- 72 W. Zhicheng, C. Hui, L. Qixin, C. Zhangzhang, X. Hui, Z. Hua, Z. Xiaofang and L. Yalin, *J. Phys. D. Appl. Phys.*, 2020, **53**, 314004.
- 73 S. Kobayashi, K. Inoue, T. Kato, Y. Ikuhara and T. Yamamoto, *J. Appl. Phys.*, 2018, **123**, 064102.
- 74 D. Karpov, Z. Liu, T. dos S. Rolo, R. Harder, P. V Balachandran, D. Xue, T. Lookman and E. Foftung, *Nat. Commun.*, 2017, **8**, 280.
- 75 J. B. Neaton and K. M. Rabe, *Appl. Phys. Lett.*, 2003, **82**, 1586–1588.
- 76 W. Tian, J. C. Jiang, X. Q. Pan, J. H. Haeni, Y. L. Li, L. Q. Chen, D. G. Schlom, J. B. Neaton, K. M. Rabe and Q. X. Jia, *Appl. Phys. Lett.*, 2006, **89**, 23–25.
- 77 P. Aguado-Puente and J. Junquera, *Phys. Rev. B - Condens. Matter Mater. Phys.*, 2012, **85**, 184105.
- 78 N. Strkalj, G. De Luca, M. Campanini, S. Pal, J. Schaab, C. Gattinoni, N. A. Spaldin, M. D. Rossell, M. Fiebig and M. Trassin, *Phys. Rev. Lett.*, 2019, **123**, 147601.
- 79 B. Bein, H.-C. Hsing, S. J. Callori, J. Sinsheimer, P. V Chinta, R. L. Headrick and M. Dawber, *Nat. Commun.*, 2015, **6**, 10136.
- 80 C. T. Nelson, B. Winchester, Y. Zhang, S. J. Kim, A. Melville, C. Adamo, C. M. Folkman, S. H. Baek, C. B.

- Eom, D. G. Schlom, L. Q. Chen and X. Pan, *Nano Lett.*, 2011, **11**, 828–834.
- 81 E. Khestanova, N. Dix, I. Fina, M. Scigaj, J. M. Rebled, C. Magén, S. Estradé, F. Peiró, G. Herranz, J. Fontcuberta and F. Sánchez, *Adv. Funct. Mater.*, 2016, **26**, 6446–6453.
- 82 Y. L. Li, S. Y. Hu, D. Tenne, A. Soukiassian, D. G. Schlom, X. X. Xi, K. J. Choi, C. B. Eom, A. Saxena, T. Lookman, Q. X. Jia and L. Q. Chen, *Appl. Phys. Lett.*, 2007, **91**, 112914.
- 83 A. Visinoiu, R. Scholz, S. Chattopadhyay, M. Alexe and D. Hesse, *Japanese J. Appl. Physics, Part 1 Regul. Pap. Short Notes Rev. Pap.*, 2002, **41**, 6633–6638.
- 84 A. I. Lebedev, *Phys. Solid State*, 2010, **52**, 1448–1462.
- 85 C. L. Jia, V. Nagarajan, J. Q. He, L. Houben, T. Zhao, R. Ramesh, K. Urban and R. Waser, *Nat. Mater.*, 2007, **6**, 64–69.
- 86 P. Zubko, N. Jecklin, A. Torres-Pardo, P. Aguado-Puente, A. Gloter, C. Lichtensteiger, J. Junquera, O. Stéphan and J. M. Triscone, *Nano Lett.*, 2012, **12**, 2846–2851.
- 87 F. Lan, H. Chen, H. Lin, Y. Bai, Y. Yu, T. Miao, Y. Zhu, T. Z. Ward, Z. Gai, W. Wang, L. Yin, E. W. Plummer and J. Shen, *Proc. Natl. Acad. Sci. U. S. A.*, 2019, **116**, 4141–4146.
- 88 S. Prosandeev, I. I. Naumov, H. Fu, L. Bellaiche, M. P. D. Campbell, R. G. P. McQuaid, L.-W. Chang, A. Schilling, L. J. McGilly, A. Kumar and J. Marty Gregg, *Nanoscale Ferroelectr. Multiferroics*, 2016, 700–728.
- 89 M. Á. García-March, A. Ferrando, M. Zacarés, S. Sahu and D. E. Ceballos-Herrera, *Phys. Rev. A - At. Mol. Opt. Phys.*, 2009, **79**, 053820.
- 90 D. Peng, X. Yang and W. Jiang, *J. Appl. Phys.*, 2019, **126**, 244101.
- 91 L. Lu, Y. Nahas, M. Liu, H. Du, Z. Jiang, S. Ren, D. Wang, L. Jin, S. Prokhorenko, C. L. Jia and L. Bellaiche, *Phys. Rev. Lett.*, 2018, **120**, 177601.
- 92 *J. Phys. C Solid State Phys.*, 1973, **6**, 1181–1203.
- 93 R. Desbuquois, L. Chomaz, T. Yefsah, J. Léonard, J. Beugnon, C. Weitenberg and J. Dalibard, *Nat. Phys.*, 2012, **8**, 645–648.
- 94 J. Y. Choi, S. W. Seo and Y. Il Shin, *Phys. Rev. Lett.*, 2013, **110**, 22–26.
- 95 Y. Ivry, D. Chu, J. F. Scott, E. K. H. Salje and C. Durkan, *Nano Lett.*, 2011, **11**, 4619–4625.
- 96 X. Tian, X. Yang, P. Wang and D. Peng, *Appl. Phys. Lett.*, 2013, **103**, 242905.
- 97 X. B. Tian, X. H. Yang and P. Wang, *J. Electron. Mater.*, 2015, **44**, 3795–3800.
- 98 X. B. Tian, X. H. Yang and W. Z. Cao, *J. Electron. Mater.*, 2013, **42**, 2504–2509.
- 99 W. J. Chen, Y. Zheng, B. Wang, D. C. Ma and F. R. Ling, *Phys. Chem. Chem. Phys.*, 2013, **15**, 7277–7285.
- 100 W. J. Chen, Y. Zheng and B. Wang, *Appl. Phys. Lett.*, 2012, **100**, 062901.
- 101 S. Das, A. Ghosh, M. R. McCarter, S. L. Hsu, Y. L. Tang, A. R. Damodaran, R. Ramesh and L. W. Martin, *APL Mater.*, 2018, **6**, 100901.
- 102 S. Kobayashi, K. Inoue, T. Kato, Y. Ikuhara and T. Yamamoto, *J. Appl. Phys.*, 2018, **123**, 064102.
- 103 C. Zhao, H. Wu, F. Li, Y. Cai, Y. Zhang, D. Song, J. Wu, X. Lyu, J. Yin, D. Xiao, J. Zhu and S. J. Pennycook, *J. Am. Chem. Soc.*, 2018, **140**, 15252–15260.
- 104 C. Lichtensteiger, J. M. Triscone, J. Junquera and P. Ghosez, *Phys. Rev. Lett.*, 2005, **94**, 047603.
- 105 B. K. Lai, I. Ponomareva, I. A. Kornev, L. Bellaiche and G. J. Salamo, *Phys. Rev. B - Condens. Matter Mater. Phys.*, 2007, **75**, 1–7.
- 106 J. Lyu, S. Estandía, J. Gazquez, M. F. Chisholm, I. Fina, N. Dix, J. Fontcuberta and F. Sánchez, *ACS Appl. Mater. Interfaces*, 2018, **10**, 25529–25535.
- 107 L. Li, X. Cheng, J. R. Jokisaari, P. Gao, J. Britson, C. Adamo, C. Heikes, D. G. Schlom, L. Q. Chen and X. Pan,

- Phys. Rev. Lett.*, 2018, **120**, 137602.
- 108 S. Prokhorenko, Y. Nahas and L. Bellaïche, *Phys. Rev. Lett.*, 2017, **118**, 147601.
- 109 K. Du, M. Zhang, C. Dai, Z. N. Zhou, Y. W. Xie, Z. H. Ren, H. Tian, L. Q. Chen, G. Van Tendeloo and Z. Zhang, *Nat. Commun.*, 2019, **10**, 4864.
- 110 A. K. Yadav, K. X. Nguyen, Z. Hong, P. García-Fernández, P. Aguado-Puente, C. T. Nelson, S. Das, B. Prasad, D. Kwon, S. Cheema, A. I. Khan, C. Hu, J. Íñiguez, J. Junquera, L. Q. Chen, D. A. Muller, R. Ramesh and S. Salahuddin, *Nature*, 2019, **565**, 468–471.
- 111 P. Shafer, P. García-Fernández, P. Aguado-Puente, A. R. Damodaran, A. K. Yadav, C. T. Nelson, S.-L. Hsu, J. C. Wojdeł, J. Íñiguez, L. W. Martin, E. Arenholz, J. Junquera and R. Ramesh, *Proc. Natl. Acad. Sci.*, 2018, **115**, 201711652.
- 112 R. Negrea, M. Hoffmann, M. Herzig, P. Lucian, F. P. G. Fengler, T. Mittmann, T. Mikolajick, B. Max, U. Schroeder and S. Slesazeck, *Nature*, 2019, **565**, 464–467.
- 113 J. Kim, M. You, K. Kim, K. Chu and C. Yang, 2019, **4**, 29.
- 114 A. Fert, V. Cros and J. Sampaio, *Nat. Nanotechnol.*, 2013, **8**, 152–156.
- 115 X. Zhang, M. Ezawa and Y. Zhou, *Sci. Rep.*, 2015, **5**, 9400.
- 116 R. D. Leapman, L. A. Grunes and P. L. Fejes, *Phys. Rev. B*, 1982, **26**, 614–635.
- 117 M. Varela, M. P. Oxley, W. Luo, J. Tao, M. Watanabe, A. R. Lupini, S. T. Pantelides and S. J. Pennycook, *Phys. Rev. B - Condens. Matter Mater. Phys.*, 2009, **79**, 085117.
- 118 Q. Qiao, Y. Zhang, R. Contreras-Guerrero, R. Droopad, S. T. Pantelides, S. J. Pennycook, S. Ogut and R. F. Klie, *Appl. Phys. Lett.*, 2015, **107**, 201604.
- 119 A. S. Sefat, G. Amow, M.-Y. Wu, G. A. Botton and J. E. Greedan, *J. Solid State Chem.*, 2005, **178**, 1008–1016.
- 120 J. Zhang, A. Visinoiu, F. Heyroth, F. Syrowatka, M. Alexe, D. Hesse and H. S. Leipner, *Phys. Rev. B - Condens. Matter Mater. Phys.*, 2005, **71**, 064108.
- 121 M. Aoki, Y. Sato, R. Teranishi and K. Kaneko, *Appl. Microsc.*, 2018, **48**, 27–32.
- 122 J. Lyu, I. Fina, R. Solanas, J. Fontcuberta and F. Sánchez, *ACS Appl. Electron. Mater.* 2019, 2019, **1**, 220–228.
- 123 T. Song, R. Bachelet, G. Saint-Girons, R. Solanas, I. Fina and F. Sanchez, *ACS Appl. Electron. Mater.*, 2020, **2**, 3221–3232.
- 124 M. C. Sulzbach, S. Estandía, X. Long, J. Lyu, N. Dix, J. Gàzquez, M. F. Chisholm, F. Sánchez, I. Fina and J. Fontcuberta, *Adv. Electron. Mater.*, 2020, **6**, 1900852.
- 125 J. Lyu, T. Song, I. Fina and F. Sánchez, *Nanoscale*, 2020, **12**, 11280.
- 126 P. Nukala, J. Antoja-Lleonart, Y. Wei, L. Yedra, B. Dkhil and B. Noheda, *ACS Appl. Electron. Mater.*, 2019, **1**, 2585–2593.
- 127 T. Li, N. Zhang, Z. Sun, C. Xie, M. Ye, S. Mazumdar, L. Shu, Y. Wang, D. Wang, L. Chen, S. Ke and H. Huang, *J. Mater. Chem. C*, 2018, **6**, 9224–9231.
- 128 L. Bégon-Lours, M. Mulder, P. Nukala, S. De Graaf, Y. A. Birkhölzer, B. Kooi, B. Noheda, G. Koster and G. Rijnders, *Phys. Rev. Mater.*, 2020, **4**, 043401.
- 129 T. Mimura, T. Shimizu, T. Kiguchi, A. Akama, T. J. Konno, Y. Katsuya, O. Sakata and H. Funakubo, *Jpn. J. Appl. Phys.*, 2019, **58**, SBBB09.
- 130 T. Shimizu, K. Katayama, T. Kiguchi, A. Akama, T. J. Konno and H. Funakubo, *Appl. Phys. Lett.*, 2015, **107**, 032910.
- 131 K. Katayama, T. Shimizu, O. Sakata, T. Shiraishi, S. Nakamura, T. Kiguchi, A. Akama, T. J. Konno, H. Uchida and H. Funakubo, *J. Appl. Phys.*, 2016, **119**, 134101.

- 132 Z. Zhang, S. L. Hsu, V. A. Stoica, H. Paik, E. Parsonnet, A. Qualls, J. Wang, L. Xie, M. Kumari, S. Das, Z. Leng, M. McBriarty, R. Proksch, A. Gruverman, D. G. Schlom, L. Q. Chen, S. Salahuddin, L. W. Martin and R. Ramesh, *Adv. Mater.*, 2021, **33**, 2006089.
- 133 T. Li, M. Ye, Z. Sun, N. Zhang, W. Zhang, S. Inguva, C. Xie, L. Chen, Y. Wang, S. Ke and H. Huang, *ACS Appl. Mater. Interfaces*, 2019, **11**, 4139–4144.
- 134 J. Lyu, I. Fina, R. Solanas, J. Fontcuberta and F. Sánchez, *Appl. Phys. Lett.*, 2018, **113**, 082902.
- 135 Y. Wei, P. Nukala, M. Salverda, S. Matzen, H. J. Zhao, J. Momand, A. S. Everhardt, G. Agnus, G. R. Blake, P. Lecoeur, B. J. Kooi, J. Iñiguez, B. Dkhil and B. Noheda, *Nat. Mater.*, 2018, **17**, 1095–1100.
- 136 H. Y. Yoong, H. Wu, J. Zhao, H. Wang, R. Guo, J. Xiao, B. Zhang, P. Yang, S. J. Pennycook, N. Deng, X. Yan and J. Chen, *Adv. Funct. Mater.*, 2018, **28**, 1806037.
- 137 J. Lyu, I. Fina, R. Bachelet, G. Saint-Girons, S. Estandía, J. Gázquez, J. Fontcuberta and F. Sánchez, *Appl. Phys. Lett.*, 2019, **114**, 222901.
- 138 J. Lyu, I. Fina, J. Fontcuberta and F. Sánchez, *ACS Appl. Mater. Interfaces*, 2019, **11**, 6224–6229.
- 139 S. Estandía, N. Dix, J. Gazquez, I. Fina, J. Lyu, M. F. Chisholm, J. Fontcuberta and F. Sánchez, *ACS Appl. Electron. Mater.*, 2019, **1**, 1449–1457.
- 140 S. Estandía, N. Dix, M. F. Chisholm, I. Fina and F. Sánchez, *Cryst. Growth Des.*, 2020, **20**, 3801–3806.
- 141 M. Dawber, K. M. Rabe and J. F. Scott, *Rev. Mod. Phys.*, 2005, **77**, 1083.
- 142 J. Schwarzkopf and R. Fornari, *Prog. Cryst. Growth Charact. Mater.*, 2006, **52**, 159–212.
- 143 R. F. C. Farrow, S. S. P. Parkin and V. S. Speriosu, *J. Appl. Phys.*, 1988, **64**, 5315.
- 144 S. Estandía, J. Gazquez, M. Varela, N. Dix, M. Qian, R. Solanas, I. Fina and F. Sanchez, *J. Mater. Chem. C*, 2021, **9**, 3486–3492.
- 145 G. Herranz, F. Sánchez, J. Fontcuberta, M. V. García-Cuenca, C. Ferrater, M. Varela, T. Angelova, A. Cros and A. Cantarero, *Phys. Rev. B - Condens. Matter Mater. Phys.*, 2005, **71**, 174411.
- 146 F. Sánchez, G. Herranz, I. C. Infante, J. Fontcuberta, M. V. García-Cuenca, C. Ferrater and M. Varela, *Appl. Phys. Lett.*, 2004, **85**, 1981.
- 147 D. Gutiérrez, G. Radaelli, F. Sánchez, R. Bertacco and J. Fontcuberta, *Phys. Rev. B - Condens. Matter Mater. Phys.*, 2014, **89**, 075107.
- 148 P. Yu, W. Luo, D. Yi, J. X. Zhang, M. D. Rossell, C. H. Yang, L. You, G. Singh-Bhalla, S. Y. Yang, Q. He, Q. M. Ramasse, R. Erni, L. W. Martin, Y. H. Chu, S. T. Pantelides, S. J. Pennycook and R. Ramesh, *Proc. Natl. Acad. Sci. U. S. A.*, 2012, **109**, 9710–9715.
- 149 N. Strkalj, C. Gattinoni, A. Vogel, M. Campanini, R. Haerdi, A. Rossi, M. D. Rossell, N. A. Spaldin, M. Fiebig and M. Trassin, *Nat. Commun.*, 2020, **11**, 5815.
- 150 F. Sánchez, C. Ocal and J. Fontcuberta, *Chem. Soc. Rev.*, 2014, **43**, 2272–2285.
- 151 P. Nukala, M. Ahmadi, Y. Wei, S. de Graaf, E. Stylianidis, T. Chakraborty, S. Matzen, H. W. Zandbergen, A. Björling, D. Mannix, D. Carbone, B. Kooi and B. Noheda, *Science*, 2021, eabf3789.
- 152 Y. M. Kim, A. Morozovska, E. Eliseev, M. P. Oxley, R. Mishra, S. M. Selbach, T. Grande, S. T. Pantelides, S. V. Kalinin and A. Y. Borisevich, *Nat. Mater.*, 2014, **13**, 1019–1025.
- 153 C. Ferreyra, M. Rengifo, M. J. Sánchez, A. S. Everhardt, B. Noheda and D. Rubi, *Phys. Rev. Appl.*, 2020, arXiv:2006, Submitted: 18 Jun 2020.
- 154 X. Gao, S. Lee, J. Nichols, T. L. Meyer, T. Z. Ward, M. F. Chisholm and H. N. Lee, *Sci. Rep.*, 2016, **6**, 38168.
- 155 W. Tang, E. Sanville and G. Henkelman, *J. Phys. Condens. Matter*, 2009, **21**, 084204.
- 156 F. Wrobel, A. F. Mark, G. Christiani, W. Sigle, H. U. Habermeier, P. A. Van Aken, G. Logvenov, B. Keimer and

- E. Benckiser, *Appl. Phys. Lett.*, 2017, **110**, 041606.
- 157 B. Paul, K. Singh, T. Jaroń, A. Roy and A. Chowdhury, *J. Alloys Compd.*, 2016, **686**, 130–136.
- 158 V. G. Sevast'Yanov, E. P. Simonenko, N. P. Simonenko, K. A. Sakharov and N. T. Kuznetsov, *Mendeleev Commun.*, 2013, **23**, 17–18.
- 159 U. Schroeder, C. Richter, M. H. Park, T. Schenk, M. Pešić, M. Hoffmann, F. P. G. Fengler, D. Pohl, B. Rellinghaus, C. Zhou, C. C. Chung, J. L. Jones and T. Mikolajick, *Inorg. Chem.*, 2018, **57**, 2752–2765.
- 160 E. D. Grimley, T. Schenk, X. Sang, M. Pešić, U. Schroeder, T. Mikolajick and J. M. LeBeau, *Adv. Electron. Mater.*, 2016, **2**, 1600173.
- 161 L. L. Tao, T. R. Paudel, A. A. Kovalev and E. Y. Tsymbal, *Phys. Rev. B*, 2017, **95**, 245141.
- 162 O. Y. Gorbenko, S. V. Samoilenkov, I. E. Graboy and A. R. Kaul, *Chem. Mater.*, 2002, **14**, 4026–4043.
- 163 A. R. Kaul, O. Y. Gorbenko and A. A. Kamenev, *Russ. Chem. Rev.*, 2004, **73**, 861–880.
- 164 N. Dix, R. Muralidharan, M. Varela, J. Fontcuberta and F. Sánchez, *Appl. Phys. Lett.*, 2012, **100**, 122905.
- 165 M. Gich, I. Fina, A. Morelli, F. Sánchez, M. Alexe, J. Gàzquez, J. Fontcuberta and A. Roig, *Adv. Mater.*, 2014, **26**, 4645–4652.
- 166 R. Batra, T. D. Huan, J. L. Jones, G. Rossetti and R. Ramprasad, *J. Phys. Chem. C*, 2017, **121**, 4139–4145.
- 167 R. Materlik, C. Kunneth and A. Kersch, *J. Appl. Phys.*, 2015, **117**, 134109.
- 168 S. Liu and B. M. Hanrahan, *Phys. Rev. Mater.*, 2019, **3**, 054404.
- 169 D. G. Schlom, L. Q. Chen, C. B. Eom, K. M. Rabe, S. K. Streiffner and J. M. Triscone, *Annu. Rev. Mater. Res.*, 2007, **37**, 589–626.
- 170 K. J. Choi, M. Biegalski, Y. L. Li, A. Sharan, J. Schubert, R. Uecker, P. Reiche, Y. B. Chen, X. Q. Pan, V. Gopalan, L. Q. Che, D. C. Schlom and C. B. Eom, *Science*, 2004, **306**, 1005–1009.
- 171 D. Pesquera, X. Marti, V. Holy, R. Bachelet, G. Herranz and J. Fontcuberta, *Appl. Phys. Lett.*, 2011, **99**, 221901.
- 172 R. Batra, H. D. Tran and R. Ramprasad, *Appl. Phys. Lett.*, 2016, **108**, 172902.
- 173 M. Grundmann, T. Böntgen and M. Lorenz, *Phys. Rev. Lett.*, 2010, **105**, 146102.
- 174 M. Scigaj, N. Dix, M. Cabero, A. Rivera-Calzada, J. Santamaria, J. Fontcuberta, G. Herranz and F. Sánchez, *Appl. Phys. Lett.*, 2014, **104**, 251602.
- 175 H. Zhou, H. Q. Wang, Y. Li, K. Li, J. Kang, J. C. Zheng, Z. Jiang, Y. Huang, L. Wu, L. Zhang, K. Kisslinger and Y. Zhu, *ACS Appl. Mater. Interfaces*, 2014, **6**, 13823–13832.
- 176 A. Trampert and K. H. Ploog, *Cryst. Res. Technol.*, 2000, **35**, 793–806.
- 177 F. Sánchez, R. Bachelet, P. De Coux, B. Warot-Fonrose, V. Skumryev, L. Tarnawska, P. Zaumseil, T. Schroeder and J. Fontcuberta, *Appl. Phys. Lett.*, 2011, **99**, 211910.
- 178 S. Venzke, R. B. Van Dover, J. M. Phillips, E. M. Gyorgy, T. Siegrist, C. H. Chen, D. Werder, R. M. Fleming, R. J. Felder, E. Coleman and R. Opila, *J. Mater. Res.*, 1996, **11**, 1187–1198.
- 179 M. Scigaj, N. Dix, I. Fina, R. Bachelet, B. Warot-Fonrose, J. Fontcuberta and F. Sánchez, *Appl. Phys. Lett.*, 2013, **102**, 112905.
- 180 J. Narayan and B. C. Larson, *J. Appl. Phys.*, 2003, **93**, 278.
- 181 M. Grundmann, *Phys. Status Solidi Basic Res.*, 2011, **248**, 805–824.
- 182 X. Marti, V. Skumryev, A. Cattoni, R. Bertacco, V. Laukhin, C. Ferrater, M. V. García-Cuenca, M. Varela, F. Sánchez and J. Fontcuberta, *J. Magn. Magn. Mater.*, 2009, **321**, 1719–1722.
- 183 S. Little and A. Zangwill, *Phys. Rev. B*, 1994, **49**, 16659.
- 184 J. W. Matthews, D. C. Jackson and A. Chambers, *Thin Solid Films*, 1975, **26**, 129–134.
- 185 S. Estradé, J. M. Rebled, J. Arbiol, F. Peiró, I. C. Infante, G. Herranz, F. Sánchez, J. Fontcuberta, R. Córdoba, B.

Bibliography

- G. Mendis and A. L. Bleloch, *Appl. Phys. Lett.*, 2009, **95**, 072507.
- 186 J. W. Matthews and A. E. Blakeslee, *J. Cryst. Growth*, 1974, **27**, 118–125.
- 187 I. B. Misirlioglu, A. L. Vasiliev, M. Aindow, S. P. Alpay and R. Ramesh, *Appl. Phys. Lett.*, 2004, **84**, 1742.
- 188 R. RUH, H. J. GARRETT, R. F. DOMAGALA and N. M. TALLAN, *J. Am. Ceram. Soc.*, 1968, **51**, 23–28.
- 189 M. C. Sulzbach, S. Estandía, J. Gàzquez, F. Sánchez, I. Fina and J. Fontcuberta, *Adv. Funct. Mater.*, 2020, **30**, 2002638.

List of Publications

1. Jike Lyu, Saúl Estandía, Jaume Gazquez, Matthew F. Chisholm, Ignasi Fina, Nico Dix, Josep Fontcuberta, Florencio Sánchez. “Control of Polar Orientation and Lattice Strain in Epitaxial BaTiO₃ Films on Silicon”. *ACS Appl. Mater. Interfaces* 2018, 10, 30, 25529-25535.
2. Saúl Estandía, Florencio Sánchez, Matthew F. Chisholm and Jaume Gazquez. “Rotational polarization nanotopologies in BaTiO₃/SrTiO₃ superlattices”. *Nanoscale*, 2019, 11, 21275-21283.
3. Saúl Estandía, Nico Dix, Jaume Gazquez, Ignasi Fina, Jike Lyu, Matthew F. Chisholm, Josep Fontcuberta, Florencio Sánchez. “Engineering Ferroelectric Hf_{0.5}Zr_{0.5}O₂ Thin Films by Epitaxial Stress”. *ACS Appl. Electron. Mater.* 2019, 1, 8, 1449-1457.
4. Jike Lyu, Ignasi Fina, Romain Bachelet, Guillaume Saint-Girons, Saúl Estandía, Jaume Gázquez, Josep Fontcuberta and Florencio Sánchez. “Enhanced ferroelectricity in epitaxial Hf_{0.5}Zr_{0.5}O₂ thin films integrated with Si(001) using SrTiO₃ template”. *Applied Physics Letters*, 2019, 114 (22), 222901.
5. Milena Cervo Sulzbach, Saúl Estandía, Xiao Long, Jike Lyu, Nico Dix, Jaume Gazquez, Matthew F. Chisholm, Florencio Sánchez, Ignasi Fina and Josep Fontcuberta. “Unraveling Ferroelectric Polarization and Ionic Contributions to Electroresistance in Epitaxial Hf_{0.5}Zr_{0.5}O₂ Tunnel Junctions” *Adv. Electron. Mater.* 2020, 6, 1900852.
6. Milena Cervo Sulzbach, Saúl Estandía, Jaume Gázquez, Florencio Sánchez, Ignasi Fina, Josep Fontcuberta “Blocking of Conducting Channels Widens Window for Ferroelectric Resistive Switching in Interface-Engineered Hf_{0.5}Zr_{0.5}O₂ Tunnel Devices” *Advanced Functional Materials*, 2020, 30 (32), 2002638.
7. Saul Estandía, Nico Dix, Matthew F. Chisholm, Ignasi Fina, and Florencio Sánchez. “Domain-Matching Epitaxy of Ferroelectric Hf_{0.5}Zr_{0.5}O₂(111) on La_{2/3}Sr_{1/3}MnO₃ (001)” *Crystal Growth & Design*, 2020, 20 (6), 3801-3806.
8. Saúl Estandía, Jaume Gázquez, María Varela, Nico Dix, Mengdi Qian, Raúl Solanas, Ignasi Fina and Florencio Sánchez “Critical effect of the bottom electrode on the ferroelectricity of epitaxial Hf_{0.5}Zr_{0.5}O₂ thin films” *J. Mater. Chem. C*, 2021, 9, 3486.

9. Tingfeng Song, Saúl Estandía, Huan Tan, Nico Dix, Jaume Gàzquez, Ignasi Fina, and Florencio Sánchez “*Positive Effect of Parasitic Monoclinic Phase of $Hf_{0.5}Zr_{0.5}O_2$ on Ferroelectric Endurance*” Submitted to Advanced Electronic Materials.
10. Cervo Sulzbach, Milena; Tan, Huan; Estandía, Saúl; Gàzquez, Jaume; Sanchez, Florencio; Fina, Ignasi; Fontcuberta, Josep “*Ferroelectric and resistive switching in epitaxial 2 nm $Hf_{0.5}Zr_{0.5}O_2$ tunnel junctions*” Submitted to ACS Applied Electronic Materials.
11. Saúl Estandía, Tengfei Cao, Rohan Mishra, Ignasi Fina Florencio Sánchez, and Jaume Gazquez “*Insights into the Atomic Structure of the Interface of Ferroelectric $Hf_{0.5}Zr_{0.5}O_2$ grown epitaxially on $La_{2/3}Sr_{1/3}MnO_3$* ” Submitted to Physical Review Materials.

Other Communications

1. Saúl Estandía, Florencio Sánchez, Matthew F. Chisholm, Jaume Gàzquez. Observation of Rotational Polarization Nanotopologies in $BaTiO_3/SrTiO_3$ Superlattices. **Oral**, Acropolis Congress Centre, Spring Meeting 2019 EMRS, Nice (France), 27th-31st May 2019.
2. Saúl Estandía, Florencio Sánchez, Matthew F. Chisholm, Jaume Gàzquez. Rotational Polarization Topologies in $BaTiO_3/SrTiO_3$ Superlattices. **Poster**, International School of Oxide Electronics (ISOE2019), Cargèse (France), 25th June - 5th July 2019.
3. Saúl Estandía, Florencio Sánchez, Matthew F. Chisholm, Jaume Gàzquez. Rotational Polarization Nanotopologies in $BaTiO_3/SrTiO_3$ Superlattices. **Oral**, 4th Scientific Meeting of BNC-b Students (JPhD 2019), Bellaterra (Catalonia, Spain), 6th-7th June 2019.
4. Saúl Estandía, Florencio Sánchez, Matthew F. Chisholm, Jaume Gàzquez. Observation of Rotational Polarization Nanotopologies in $BaTiO_3/SrTiO_3$ Superlattices. **Poster**, 25th International Workshop on Oxide Electronics (iWOE25), Les Diablerets (Switzerland), 1st-3rd October 2018.

5. *Saúl Estandía, Florencio Sánchez, Matthew F. Chisholm, Jaume Gázquez.* Mapping the Polarization in BaTiO₃/SrTiO₃ Superlattices by STEM. **Poster**, Spring 2018 Meeting of the TO-BE COST Action, Sant Feliu de Guíxols (Catalonia, Spain), 12th-14th March 2018.